University of Alberta

Three dimensional simulation and magnetic decoupling
of the linac in a linac-MR system

by

Joël St. Aubin

A thesis submitted to the Faculty of Graduate Studies and Research
in partial fulfillment of the requirements for the degree of

Doctor of Philosophy

in

Medical Physics

Department of Physics

Examining Committee

Dr. Gino Fallone, Physics/Oncology, University of Alberta

Dr. Stephen Steciw, Oncology, University of Alberta

Dr. Richard Sydora, Physics, University of Alberta

Dr. Satyapal Rathee, Oncology, University of Alberta

Dr. Sharon Morsink, Physics, University of Alberta

Dr. Charlie Ma, Radiation Oncology/Radiation physics, Fox Chase Cancer Center

Abstract

Real time image guided radiotherapy has been proposed by integrating an in-line 6 MV linear accelerator (linac) to a magnetic resonance (MR) imager in either a parallel or transverse configuration. In either configuration, magnetic interference in the linac is caused by its immersion in the magnetic fringe fields of the MR imager. Thus in order to minimize the effect of the magnetic interference, investigations on linac performance in external magnetic fields was completed through various simulations.

Finite difference and finite element methods as well as particle simulations were performed in order to design an electron gun and an in-line 6 MV linac waveguide. Monte Carlo simulations provided calculations of dose distributions in a water tank from the derived electron phase space at the linac target. The entire simulation was validated against measurements taken from a commercial medical in-line 6 MV linac, other simulation programs, and theory.

The validated linac simulation was used to investigate linac performance in external magnetic fields. The results of this investigation showed that the linac had a much lower tolerance to transverse magnetic fields compared to longitudinal fields. While transverse magnetic fields caused a global deflection of the electron beam away from the central axis of the waveguide, longitudinal fields changed the optics of the electron gun in a suboptimal way. Both transverse and longitudinal magnetic fields caused excessive beam loss if the field strength was large enough. Heating caused by excessive beam loss in external magnetic fields was shown to have little effect on the resonant frequency of the waveguide, and

any change in dosimetry, if it existed, was shown to be easily corrected using the jaws or multileaf collimators (MLCs). It was determined that the low-field parallel configuration linac-MR system investigated did not require any magnetic shielding, so the focus was on shielding the transverse configuration. Using beam loss, MLC motor tolerance to magnetic fields, and MR imager homogeneity as constraints, passive and active magnetic shielding was designed and optimized. Thus through the parallel configuration, or using magnetic shielding, magnetic interference has been reduced to within the linac operational tolerance.

Acknowledgements

Table of Contents

List of Tables

List of Figures

List of Abbreviations

AC	Accelerating cavity
BBU	Beam break up
BPMDC	Brushed permanent magnetic direct current
CBCT	Cone beam computed tomography
CDF	Cumulative distribution function
CIC	Cloud-in-cell
CSDA	Continuous slowing down approximation
CT	Computed tomography
CTV	Clinical tumor Volume
D_{10}	Dose at 10 cm depth
DBS	Directional bremsstrahlung splitting
D_{CAX}	Central axis dose
DCS	Differential cross section
DD	Depth dose
DSV	Diameter spherical volume
ECUT	Electron cut off energy
EPID	Electronic portal imaging device
FD	Finite difference
FEM	Finite element method
FWHM	Full width half maximum
GTV	Gross tumor volume
ICCG	Incomplete Cholesky conjugate gradient

ICRU	International commission on radiological units and measurements
IGRT	Image guided radiation therapy
IM	Internal margin
IMRT	Intensity modulated radiation therapy
ITV	Internal target volume
linac	Linear accelerator
MLC	Multileaf collimator
MR	Magnetic resonance
OR	Organ at risk
PCUT	Photon cut off energy
PDE	Partial differential equation
PDF	Probability distribution function
PIC	Particle-in-cell
PRV	Planning organ at risk volume
PTV	Planning target volume
RF	Radio-frequency
RPM	Revolutions per minute
SC	Side cavity
SM	Setup margin
SSD	Source to surface distance
SW	Standing wave
TM	Transverse magnetic
VSWR	Voltage standing wave ratio

CHAPTER 1: Introduction

1.1   HISTORY OF EXTERNAL BEAM RADIATION THERAPY

External beam radiation therapy began with the discovery of X-rays by Wilhelm C. Roentgen in 1895 using a Hittorf-Crookes tube at the University of Wurzburg.[1] Cathode rays, or electrons, were accelerated in vacuum using an electrostatic field and the abrupt change in acceleration upon impacting the outer glass tube generated the X-rays through bremsstrahlung production[2]. Treatments using the newly discovered X-rays were performed within a month of their discovery by Emil Grubbé and continued to treat cancer and other malignancies with equipment whose peak voltage was 250 kV or less. It was recognized that the scope of radiation therapy would be limited until higher energy X-rays could be produced.[3] In 1937 a megavoltage 1 MV X-ray unit was installed for patient treatments in St. Bartholomew's Hospital (Barts) in London England. It was a 30 foot long evacuated X-ray tube using two Cockcroft-Walton high voltage generators each capable of generating 600 kV.[3] This unit at Barts represented a major technical development since it also included a variable field size for collimation, an adjustable height patient couch, and a built in parallel plate monitoring system. Clinical studies throughout World War II using the megavoltage treatment unit[4, 5] left no doubt as to the benefits of X-ray treatments with energies of at least 1 MV.

The next development in particle acceleration technology came in 1924 when Gustaf Ising proposed a resonance method for particle acceleration.[6] The theory was that a low voltage could be applied to a particle repeatedly such that the particle gained energy larger than any one voltage. This reduced the required voltages applied to the accelerator overcoming electrical breakdown issues. In 1928 Rolf Wideroe applied Ising's theory and built the first accelerator using the resonance method to accelerate potassium ions.[7] In his work, Wideroe proposed a beam transformer which was essentially the magnetic induction section of a betatron. In 1932, Ernest Lawrence developed the particle accelerator known as the cyclotron.[8] Whereas Wideroe's accelerator provided linear acceleration, the

cyclotron provided acceleration as the particles traveled in circular orbits. In 1933, the Van de Graaff accelerator was developed[9] by its name sake, and was applied clinically producing 2 MV X-rays. The first application of the Van de Graaff accelerator in radiation therapy allowed for both a megavoltage photon and electron beam. The accelerator could be rotated to provide different treatment angles, but only with significant difficulty.[3] In 1940, Donald Kerst, at the University of Illinois, developed the betatron[10] which exclusively accelerated electrons to high energy in a similar fashion as a cyclotron. The first betatron developed by Kerst accelerated electrons to 2.3 MeV, the second to 20 MeV and the third to 300 MeV.[3] A target was placed on the betatron injector assembly which provided high energy X-rays and the electron beam was so well collimated that the X-rays generated in the target had a sharply defined radiation field with no penumbra. A thirty field treatment using the betatron was performed on a graduate student with glioblastoma in 1948 at the University of Illinois. The treatment required the development of dosimetry, monitoring and collimation of the various fields. All of the thirty fields were non-coplanar such that multi-arc rotational therapy was achieved.[11, 12] The betatron, with improvements for medical use, was installed in at the Saskatoon Cancer Clinic in 1948[13], and in 1949 at the University of Illinois College of Medicine. Treatments in the range of 6 – 22 MeV began in 1950 at the University of Illinois.[14]

A big technological advancement that lead to the medical linear accelerator (linac) came with the development of klystrons and magnetrons during World War II to produce high power microwaves for radar. These microwave power sources were applied in radiation therapy to provide the power necessary to accelerate charged particles with smaller equipment. Smaller medical linacs were subsequently developed as an efficient method of particle acceleration using klystron or magnetron technology.[15, 16] The first linac was an 8 MV unit installed at the Hammersmith Hospital in England in 1953. Later in the same year 4 MV units were installed at the Christie and Newcastle General Hospitals. The linac installed at the Christie hospital capable of a 120° rotation. A 6 MV unit was

installed at Stanford on which the first patient was treated in 1956. A prototype compact 6 MV linac which allowed a full 360° gantry rotation was installed at the UCLA medical center and the first production model was installed at the Stanford University School of Medicine; both in 1962.

As an alternative to linear accelerator external beam radiation therapy, a ^{60}Co unit was used in 1951 at the Saskatoon Clinic in Canada. The ^{60}Co source was generated through the activation of ^{59}Co in the high flux NRX reactor at the Oak Ridge National Laboratory in Chalk River, Ontario in 1949. ^{60}Co was also used starting in 1951 at MD Anderson Hospital in Houston, Texas.[13] ^{60}Co has the major advantage in that it does not have the large power requirements of the linac, and the entire treatment unit is simple compared to the complex nature of the linac. With its mean energy of 1.25 MeV, ^{60}Co provides significant improvements over kilovoltage X-ray units, but compared to the linac, it has a larger source size leading to a larger penumbra, less skin sparing due to its lower energy, and a lower dose rate set by the source size and the specific activity of ^{60}Co. The drawbacks of ^{60}Co are all overcome with the use of linear accelerators making them the predominant treatment modality of the western world. However, the simplicity of ^{60}Co units makes them ideal for many locations worldwide.

1.2 IMAGE-GUIDED RADIATION THERAPY (IGRT)

The delivery of external beam radiation therapy has uncertainties related to geometric errors such as patient setup variations from day to day[17-19], and inter- and intrafraction organ and tumor motion[17, 20-23]. Due to these uncertainties, in 1993 the International Commission of Radiation Units and Measurements (ICRU) developed the report entitled ICRU 50[24] in an attempt to account for the uncertainties in radiation therapy. The report defined the gross tumor volume (GTV) to be the volume seen from the diagnostic image. The size of the GTV is then increased to a clinical tumor volume (CTV) to account for microscopic spread. A setup margin (SM) is then provided to account for the uncertainties in radiation delivery creating the planning target volume (PTV). In 1999, a

supplement protocol ICRU 62[25] further added the definition of the internal target volume (ITV) to account for target motion. The ITV is determined through the addition of an internal margin (IM) to the CTV. The PTV is then determined by addition of the SM to the ITV. New from the ICRU 62 report was the definition of organs at risk (OR) and the planning organ at risk volume (PRV). The definitions given above from the ICRU 50 and ICRU 62 reports are presented in Figure 1.1.
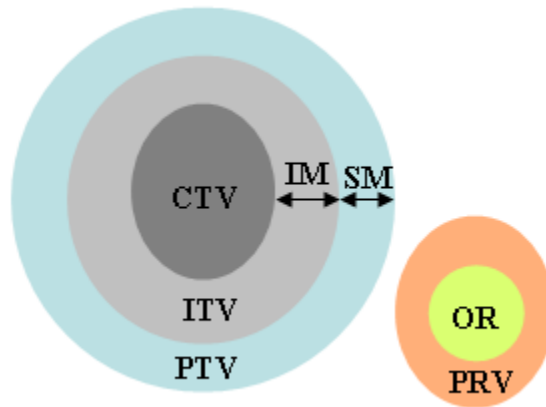
Figure 1.1 Definitions set by reports ICRU 50 and ICRU 62 for use in radiation therapy treatment planning.

Image-guided radiation therapy (IGRT) aims to eliminate, or at the very least minimize the PTV through the reduction of the IM and SM. Image-guided radiation therapy began as early as 1959 but didn't become a common practice at that time.[26] In 1982 Brahme[27] introduced the idea of intensity modulated radiation therapy (IMRT) to deliver a more conformal dose to the PTV while reducing the dose to sensitive critical structures. The use of IMRT with its steep dose gradients that are unforgiving to positioning errors and motion aided in the revitalization of IGRT. The following sections outline current IGRT techniques.

1.2.1   Kilovoltage (kV) imaging

In-room diagnostic quality kV imaging with the kV X-ray source mounted within the linac head began as early as 1959 by Weissbluth[26] and was revitalized

in 1985 by Biggs[28]. The X-ray source within the linac head retracted during treatments and the images were acquired with either radiographic film or an X-ray image intensifier. Currently, most in-room kV images for on-line corrections use electronic kV-imagers to obtain near instantaneous images. In addition to the setup of Weissbluth and Biggs with the X-ray tube mounted in the linac head, room based systems have been developed that use two X-ray sources that create two projections of the patient to provide better localization.[29] Real-time tracking with use of fluoroscopic X-rays has also been proposed in order to determine tumor motion through internal fiducial markers that are opaque to X-rays.[30] However, the fiducial markers do not yield volumetric information, so the outline of the tumor is unavailable. Although kV imaging deposits a small fraction of the treatment dose, daily imaging over the course of treatment can add up to a significant dose, especially for fluoroscopic procedures. With X-ray sources not mounted in the linac head, a common isocenter between the linac and the X-ray imaging equipment must normally be maintained and verification of patient setup can become more complicated. Kilovoltage X-ray generation along the treatment axis during treatment is impossible since the X-ray source would be in the treatment beam thus preventing real-time motion tracking from the beam's eye view.

1.2.2   Megavoltage (MV) imaging

In 1986, Leong developed a method of producing on-line high quality portal images using a fluorescent screen and a silicon-intensified target camera.[31] The system produced real-time images from the 10 MV X-rays used for treatment. Currently, the electronic portal imaging device (EPID)[32-34] is the most common form of imager for use with on-line planar MV imaging. Typically the EPID is an active matrix flat panel imager using thin film transistors fabricated from hydrogenated amorphous silicon (a-Si:H).[35] Using the EPID to image the treatment beam also allows for a verification of the delivered dose compared to the treatment plan and for quality assurance.[36, 37] Current MV imaging techniques

are not real-time and require a separate image to be taken. This can increase the patient dose, especially for daily imaging. MV imaging also suffers from poor soft tissue contrast as compared to kV imaging. The poor soft tissue contrast of the MV images can prevent this technique from providing real-time motion tracking, especially in areas where the tumor and background have similar contrast. In addition, due to the 2D nature of the image, other structures are superimposed on the region of interest, further decreasing contrast.

1.2.3   Cone beam computed tomography (CBCT)

The use of volumetric imaging allows for a 3D image to be generated. Initially volumetric imaging was performed using a 'CT on rails' system. The patient was first imaged on a CT scanner prior to each treatment and then transferred to the linac via a couch that moved on rails in the floor.[38, 39] The systems generated diagnostic quality images but were large and expensive. In contrast to these large systems, volumetric imaging can be performed using a CBCT system comprised of an X-ray source and an electronic imager integrated onto the linac gantry. Typically hundreds of projections are acquired on the electronic imager as the linac gantry rotates around the patient.[40, 41] A 3D volumetric image is generated through a reconstruction process using each of the cone beam projections.[42] The reconstructed images have been shown to produce images with good spatial resolution and soft tissue contrast.[43] CBCT reconstructed images have been effectively used to verify patient setup misalignments compared to treatment planning images.[44, 45] However, CBCT is not optimal for real-time motion tracking since it requires a rotation of the gantry during treatment, which is slow, and since scatter radiation from the patient can significantly degrade the image.[46] CBCT has the same additional drawback that all the other X-ray imaging modalities do in that it deposits a greater dose to the patient above the treatment plan.

1.2.4   Tomotherapy

Tomotherapy (Madison, WI)[47] is essentially a CT scanner with a linac for
a source instead of a standard X-ray tube. The linac is capable of generating a 6
MV beam for treatments, and a 3 MV beam used for daily MVCT imaging prior
to treatment. The MVCT acquires a volumetric image using spiraling fan beam
projection data. The daily MVCT image can be used to verify patient positioning,
dose, and tumor alignment.[48] A drawback of using daily MVCT images is the
dose deposited to the patient in addition to the treatment dose. Tomotherapy, with
MVCT, is not used for real-time motion tracking since the imaging source,
required to rotate to obtain a CT image, is also the treatment source.

1.2.5   Ultrasound

Ultrasound has been shown to provide superior soft tissue contrast
compared to CT in a limited number of areas such as the prostate.[41] Ultrasound is
non-ionizing and as such does not add to the total dose given to a patient during
treatment. The use of ultrasound for prostate IGRT has been investigated and
found to be functionally equivalent to using CT simulation.[49, 50] However, other
studies have shown that the results using ultrasound depend greatly on the skill of
the user creating a great deal of user variability.[51, 52] Ultrasound is limited in its
use for real-time motion tracking to areas where soft tissue contrast is good (such
as the prostate) as well as to areas accessible to an ultrasound probe.

1.2.6   Radio-frequency (RF) tracking

RF tracking requires the insertion of a RF transponder into the patient.[53, 54]
An external antenna array is then used to track the position and motion of the RF
transponders and this information is relayed to the treatment unit. The RF
transponders act as a tumor surrogate similar to an implanted fiducial marker that
is opaque to X-rays. The significant advantage of RF tracking is that no ionizing
radiation is used reducing the total dose to the patient. RF tracking can also be

used for real-time motion tracking, but no volumetric information on the actual tumor is available, nor is information on any organ at risk.

1.2.7   Optical tracking

Optical tracking consists of using an infrared camera to image reflective markers placed on the patient surface during treatment. The surface markers are assumed to act as a tumor surrogate to estimate tumor motion. The accuracy of the reflective markers acting as a tumor surrogate has been questioned[55] bringing into question its use for real-time motion tracking.

1.3   MAGNETIC RESONANCE (MR) IMAGING GUIDED RADIATION THERAPY FOR REAL-TIME IGRT

Current IGRT systems and techniques all lack in one or more critical aspects making them unsuitable to perform real-time IGRT. An optimal real-time IGRT system may be one that possesses the following capabilities. The imaging system should provide real-time images using non-ionizing radiation so no increase in dose is given to the patient over the course of treatment. The imaging system should create a 3D image or at least a 'beam's eye view' image with high soft tissue contrast for clear delineation of the tumor and all OR (ICRU 62). The imaging system should be independent of the treatment beam allowing for dose adaptation required by the observed tumor or organ motion. The full IGRT system, imaging system and treatment unit, should function independently with no interference between the two. The requirements of an optimal real-time IGRT system are met by a treatment unit coupled to a magnetic resonance (MR) imager. To this date, three separate MR guided radiation therapy designs have been proposed; two linac-MR systems and one cobalt-MR system.

Our group at the Cross Cancer Institute in Edmonton, AB Canada proposed the integration of a low field MR imager to an in-line side-coupled 6 MV linac. The proposed design of our linac-MR system has two configurations. The transverse configuration is shown in Figure 1.2 with the linac attached to the

side of the MR imager. The linac and MR imager both rotate together on the same gantry. A small scale prototype system of the transverse configuration consisting of an in-line 6 MV linac coupled to a 27.9 cm MR bore 0.2 T bi-planar MR imager was built and tested in 2009, proving the feasibility of such a design. This system was the first in the world to produce MR images during irradiation.[56] The parallel configuration is shown in Figure 1.3 where the linac is attached to the MR imager on its symmetry axis. Again, the linac and MR imager both rotate together on the same gantry. This configuration uses an open MR imager instead of a superconducting solenoid imager since many open MR imagers have an opening around which the current carrying wires are wound. This allows for an X-ray beam to pass through the MR imager without interacting with any structures, provided a redesign of the gradient coils is performed. Technical and dosimetric issues that arise due to the integration of the linac and MR imager have been investigated by our group in depth providing many solutions.[57-70]
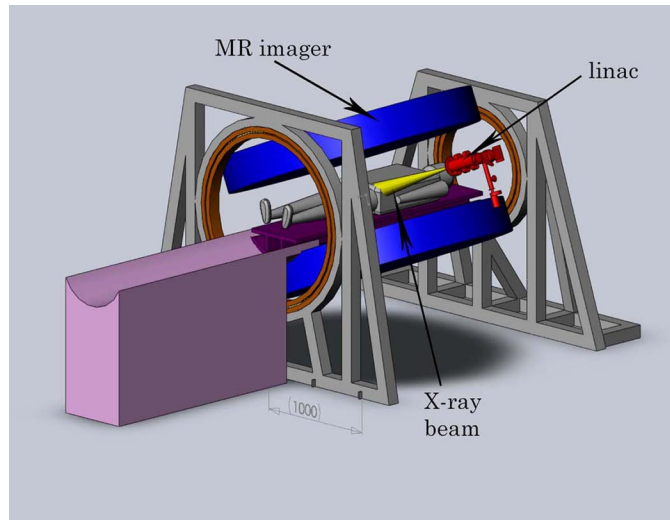
Figure 1.2: The transverse configuration linac-MR system proposed by our group at the Cross Cancer Institute in Edmonton AB, Canada. The linac rotates with the bi-planar MR imager on the same gantry. With permission of Emanuel Blosser.
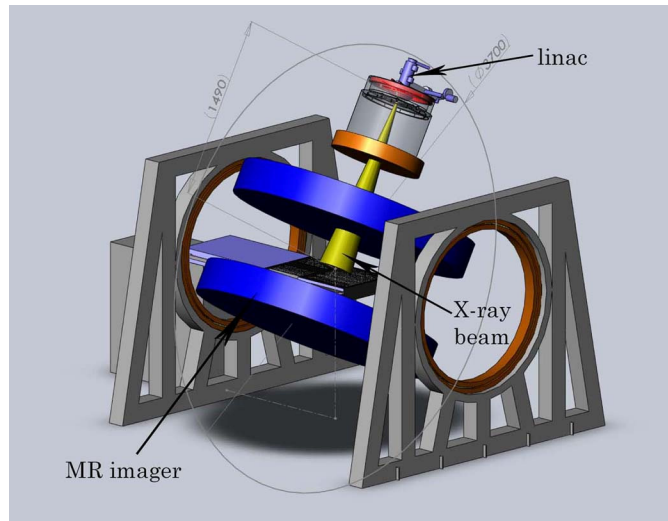
Figure 1.3: The parallel configuration linac-MR system proposed by our group at the Cross Cancer Institute in Edmonton AB, Canada. The linac rotates with the open MR imager on the same gantry. With permission of Emanuel Blosser.

A group at the Universitair Medisch Centrum in Utrecht, Netherlands has proposed the coupling of a superconducting 1.5 T solenoid MR imager with a 6 MV linac.[71] The MR imager had to be redesigned to provide a path for the X-ray beam to pass without interacting with the superconducting coils or gradients. However, the X-ray beam still passes through the outer shell of the MR imager. The linac rotates around the stationary MR imager on a gantry in a low magnetic field zone created through active shielding. A great deal of work on dosimetry as well as technical achievements has been published by the Netherlands group.[72-77] An advantage of using a 1.5 T main magnetic field is the increased signal to noise ratio achievable. However, a drawback of the system is the hot and cold spots in the dose distribution at tissue-air interfaces caused by the curling of electrons traveling perpendicular to the high strength magnetic field.[57]

A cobalt-MR system was proposed by Dempsey in Gainsville FL, USA[78, 79]. His design uses a superconducting 0.3 T open MR imager in conjunction with three ^{60}Co sources mounted on a ring circling the open section of the MR imager. The ^{60}Co sources produce no RF that would degrade the MR image. However, ^{60}Co is ferromagnetic and rotating the ring containing the three sources in the

magnetic fringe field of the MR imager could cause perturbations of the main magnetic field leading to geometric distortions. Additional drawbacks include the large penumbra due to the large source size of ^{60}Co, and the low dose rate leading to longer treatment times.

Using higher magnetic field strength MR imagers would allow for greater spatial or temporal resolution. However, the creation of hot and cold spots in the dosimetry cannot be ignored for fields of 1.5 T and greater.[57, 70] For the parallel linac-MR configuration, the greatest field strength which minimized the hot and cold spots has been found to be around 0.5 T.[70] Using ^{60}Co as the radiation source circumvents any magnetic interference issues at the linac, but in addition to the drawbacks listed above, also has a disadvantage in that it is an open radioactive source. A greater amount of safety, security and documentation is required for the use of ^{60}Co. Higher energy linacs are longer which increases their sensitivity to magnetic fields making magnetic shielding design more difficult. In some cases of very long linacs (e.g 1.5 m) simple shielding may not be sufficient and further beam modifying systems may be required.

The benefit of a linac-MR system is clearly the reduction of the SM and IM through real-time imaging during treatment. The reduction of these margins could lead to dose escalation increasing tumor control while minimizing the damage to the surrounding tissues. In this way, the linac-MR system is well suited to perform treatments on a variety of sites within the body. For example, the radiation beam could be adapted in real-time to treat moving lung or breast tumors. It would also be well suited to treat prostate cancer due to its motion and deformation caused by changes in the bladder and rectum. In addition to the more precise treatment of sites that are currently treated with radiation therapy, sites not currently treated with radiation therapy could be treated. Real-time, high contrast imaging of the abdomen (not possible with X-rays) would allow a more conformal dose to be delivered to the kidneys, or pancreas sparing the large number of adjacent critical structures. However, a drawback to linac-MR systems is that not everyone is a candidate for MR imaging. Metal workers with slivers in

their eye are an example of someone who would not be treatable with a linac-MR system.

1.4   RESEARCH MOTIVATION

One of the major issues that arise from the integration of a linac with an MR imager is magnetic interference. The fringe magnetic fields intersect the linac in a direction perpendicular to its length for the transverse configuration, or parallel/antiparallel to its length for the parallel configuration. For the transverse configuration, the transverse magnetic field creates a force on the accelerating electrons deflecting them from their straight course to the target. Due to the close proximity of the linac to the MR imager, the magnetic fringe field strengths are large enough to cause all the electrons to be deflected before reaching the target. With no electrons incident on the target, the linac is no longer useful for clinical radiation therapy treatments. In the parallel case, no global beam deflection away from the beam axis is caused by the longitudinal magnetic fringe fields, but the electron gun optics is altered causing large beam losses at the anode and a non-laminar beam.

The electron deflections in the waveguide or electron gun caused by the magnetic fringe fields of the MR imager can be reduced through the use of passive or active magnetic shielding. Materials with a high relative permeability can be used to deflect magnetic field lines creating pockets of low field.[2] However the relative permeability of a material is a function of field strength and at lower fields it becomes increasingly difficult to reduce the field to even lower values. Thus even though it may seem straight forward to shield the linac to below 0.5 G, which it currently operates in due to earth's magnetic field, the design of passive shielding to accomplish this is sub-optimal requiring large amounts of steel, the introduction of mu-metal™ and a larger than necessary target-isocenter distance.[80] In addition, the design of active shielding to achieve fields of less than 0.5 G over the entire linac maybe impractical for the transverse configuration, if not impossible due space restrictions around the linac. Therefore, an investigation

was required to quantitatively determine the performance of an in-line side-coupled 6 MV linac in the presence of a magnetic field. From these results, the linac tolerance to magnetic fields was determined and more optimal magnetic shielding was designed when it was determined that the linac needed to be magnetically decoupled from the MR imager.

1.5 THESIS OUTLINE

In order to determine linac performance in a magnetic field and design optimal magnetic shielding, the full simulation of an in-line side-coupled 6 MV linac waveguide and electron gun was required. The waveguide was designed to emulate a Varian (Palo Alto, CA) 600C linac operating at 2998.5 MHz in a $\pi/2$ mode. The RF solution within the waveguide was determined using the finite difference (FD) program SUPERFISH (Los Alamos National Lab, NM)[81] and the finite element method (FEM) program COMSOL Multiphysics (Burlington, MA). The electron gun was designed first using EGN2w (Stanford Linear Accelerator Center, CA)[82] and replicated in 3D using the FEM program OPERA-3d/SCALA (Kidlington, UK) to emulate the electron gun used with the Varian 600C based on measurements. The particle-in-cell (PIC) program PARMELA (Los Alamos National Lab, NM)[83] then calculated the electron trajectories within the linac. The entire linac simulation, the electron gun and the waveguide, was validated against electrical and dosimetric measurements taken from a Varian 600C. This linac simulation was then used to investigate the effect of magnetic fields on the accelerating electron beam, dose distributions in a water tank, and heating of the waveguide caused by additional beam losses. These investigations lead to a determination of the maximum magnetic field in which the linac could operate providing the required constraint to optimize magnetic shielding.

The breakdown of the chapters in this thesis is as follows. Chapter two discusses the theory and techniques used throughout this work. It begins with classical electromagnetic theory and leads into computational electromagnetism where the FD programs EGN2w and SUPERFISH are explained as well as the

FEM programs COMSOL and OPERA-3d/SCALA. Basic linear accelerator theory is discussed next followed by an explanation of the numerical particle simulations performed in EGN2w, OPERA-3d/SCALA and PARMELA. Lastly a discussion of the Monte Carlo technique as applied to the program EGSnrc (National Science and Research Council of Canada, Winnipeg)[84] is given. Chapter three discusses the details of the design of an in-line side-coupled 6 MV linac waveguide. Details on the effects of the side and port coupling irises on the electron beam and dose distributions are highlighted. Chapter four provides the details on the integrated linac simulation including the design of the electron gun (EGN2w). Simulated dose distributions are generated from the full linac simulation using the EGSnrc Monte Carlo programs (BEAMnrcMP 2007[85] and DOSXYZnrc 2007). The full linac simulation is validated against electrical and dosimetric measurements from a Varian 600C. Chapter five discusses the inability of EGN2w to simulate the transverse orientation of the MR magnetic fringe fields and provides the solution using the 3D electron gun program OPERA-3d/SCALA. The 3D electron gun, together with the waveguide solution of chapters three and four is used to investigate the electron beam and dosimetric effects of a transverse magnetic field crossing through the linac. Chapter six investigates the effect of a longitudinal magnetic field on the simulated linac highlighting the effects on the electron gun and dosimetry. Chapter sevens details an investigation of waveguide detuning caused by beam losses in a transverse magnetic field. Resonant frequency changes as a result of waveguide heating caused by the deflected electrons impacting the waveguide instead of the target are calculated. Chapter eight provides measurements of brushed permanent magnet DC (BPMDC) motor operation in a magnetic field. This information is required for the design of optimal magnetic shielding. Chapter nine outlines the design and optimization of both passive and active magnetic shielding. Chapter ten summarizes and concludes all the work performed.

1.6   REFERENCES

[1] W. C. Roentgen, "Eine neue art con Strahlen. Sitzungs-berichte," Phys. Med. Ges. Wurzburg, **137**, 132-141 (1895).

[2] D. J. Jackson, *Classical Electrodynamics* (John Wiley & Sons, Inc., USA, 1999).

[3] J. S. Laughlin, "Development of the technology of radiation therapy," RadioGraphics, **9**, 1245-1266 (1989).

[4] A. Jones, "The development of megavoltage x-ray therapy at St. Bartholomew's hospital," Br. J. Radiol., **22 (suppl)**, 3-10 (1988).

[5] G. S. Innes, "The one million volt x-ray therapy equipment at St. Bartholomew's hospital," Br. J. Radiol., **22(suppl)**, 11-16 (1988).

[6] G. Ising, "Prinzip einer methode zur herstellung von kanalstrahlen hoher voltzahl," Ark. Mat. Fys. , **18**, 1-4 (1924).

[7] R. Wideroe, "Über ein neues Prinzip zur Herstellung hoher Spannungen," Arch. Electrotech., **21**, 387-406 (1928).

[8] E. Q. Lawrence, and M. S. Livingston, "The production of high speed light ions without the use of high voltages," Phys. Rev., **40**, 19-35 (1932).

[9] R. J. Van de Graaff, K. T. Compton, and L. C. Van Atta, "The electrostatic production of high voltage for nuclear investigations," Phys. Rev., **43**, 149-157 (1933).

[10] D. W. Kerst, "The acceleration of electrons by magnetic induction," Phys. Rev., **60**, 47-53 (1941).

[11] G. D. Adams, G. M. Almy, S. M. Dancoff, A. O. Hanson, D. W. Kerst, H. W. Koch, E. F. Lanzl, L. H. Lanzl, J. S. Laughlin, H. Quastler, D. E. Riesen, C. S. Robinson, and L. S. Skaggs, "Techniques for the application of the betatron to medical therapy," AJR, **60**, 153-157 (1948).

[12] H. Quastler, G. D. Adams, G. M. Almy, S. M. Dancoff, A. O. Hanson, D. W. Kerst, H. W. Koch, L. H. Lanzl, J. S. Laughlin, D. E. Riesen, C. S. Robinson, V. T. Austin, T. G. Kerley, E. F. Lanzl, G. Y. McClure, E. A. Thompson, and L. S.

Skaggs, "Techniques for the application of the betatron to medical therapy - with report of one case," AJR, **61**, 591-625 (1949).

[13] H. E. Johns, "The physicist in cancer treatment and detection," Int. J. Radiat. Oncol. Biol. Phys., **7**, 801-808 (1981).

[14] J. S. Laughlin, "Consideration of the use of a 23 MeV - medical betatron," Nucleonics, **8**, 5-16 (1951).

[15] E. L. Ginzton, W. W. Hansen, and W. R. Kennedy, "A linear electron accelerator," Rev. Sci. Instrum., **19**, 89-108 (1948).

[16] D. W. Fry, R. Harvie, L. B. Mullett, and W. Walkinshaw, "Travelling-wave linear accelerator for electrons," Nature, **160**, 351-353 (1947).

[17] L. Ekberg, O. Holmberg, L. Wittgren, G. Bjelkengren, and T. Landberg, "What margins should be added to the clinical target volume in radiotherapy treatment planning for lung cancer?," Radiother. Oncol., **48**, 71-77 (1998).

[18] C. W. Hurkmans, P. Remeijer, J. V. Lebesque, and B. J. Mijnheer, "Set-up verification using portal imaging; review of current clinical practice," Radiother. Oncol., **58**, 105-120 (2001).

[19] A. Tinger, J. M. Michalski, A. Cheng, D. A. Low, R. Zhu, W. R. Bosch, J. A. Purdy, and C. A. Perez, "A critical evaluation of the planning target volume for 3-D conformal radiotherapy of prostate cancer," Int. J. Radiat. Oncol. Biol. Phys., **42**, 213-221 (1998).

[20] J. T. Booth, and S. F. Zavgorodni, "Set-up error & organ motion uncertainty: a review," Aust. Phys. Eng. Sci. Med., **22**, 29-47 (1999).

[21] C. L. Hector, S. Webb, and P. M. Evans, "The dosimetric consequences of inter-fractional patient movement on conventional and intensity-modulated breast radiotherapy treatments," Radiother. Oncol., **54**, 57-64 (2000).

[22] K. M. Langen, and D. T. L. Jones, "Organ motion and its management," Int. J. Radiat. Oncol. Biol. Phys., **50**, 265-278 (2001).

[23] E. Rietzel, S. J. Rosenthal, D. P. Gierga, C. G. Willett, and G. T. Y. Chen, "Moving targets: detection and tracking of internal organ motion for treatment planning and patient set-up," Radiother. Oncol., **73**, S68-S72 (2004).

[24] ICRU, "Prescribing, recording and reporting photon beam therapy," *Report 50*, (ICRU,Bethesda) 1993

[25] ICRU, "Prescribing, recording and reporting photon beam therapy," *ICRU 62*, (ICRU,Bethesda) 1999

[26] M. Weissbluth, C. J. Karzmark, R. E. Steele, and A. H. Selby, "The Stanford medical linear accelerator. 2. Installation and physical measurements," Radiol., **72**, 242-253 (1959).

[27] A. Brahme, J. E. Roos, and I. Lax, "Solution of an integral equation encountered in rotation therapy," Phys. Med. Biol., **27**, 1221-1229 (1982).

[28] P. J. Biggs, M. Goitein, and M. D. Russell, "A diagnostic X-ray field verification device for a 10 MV linear accelerator," Int. J. Radiat. Oncol. Biol. Phys., **11**, 635-643 (1985).

[29] J. E. Schewe, K. L. Lam, J. M. Balter, and R. K. Ten Haken, "A room-based diagnostic imaging system for measurement of patient setup," Med. Phys., **25**, 2385-2387 (1998).

[30] H. Shirato, S. Shimizu, K. Kitamura, T. Nishioka, K. Kagei, S. Hashimoto, H. Aoyama, T. Kunieda, N. Shinohara, H. Dosaka-Akita, and K. Miyasaka, "Four-dimensional treatment planning and fluoroscopic real-time tumor tracking radiotherapy for moving tumor," Int. J. Radiat. Oncol. Biol. Phys., **48**, 435-442 (2000).

[31] J. Leong, "Use of digital fluoroscopy as an online verification device in radiation-therapy," Phys. Med. Biol., **31**, 985-992 (1986).

[32] M. G. Herman, J. M. Balter, D. A. Jaffray, K. P. McGee, P. Munro, S. Shalev, M. Van Herk, and J. W. Wong, "Clinical use of electronic portal imaging: Report of AAPM radiation therapy committee Task Group 58," Med. Phys., **28**, 712-737 (2001).

[33] W. De Neve, H. Van den, F.,, M. De Beukeleer, M. Coghe, L. Thon, P. De Roover, Van Lancker M., and G. Storme, "Routine clinical on-line portal imaging followed by immediate field adjustment using a tele-controlled patient couch," Radiother. Oncol., **24**, 45-54 (1992).

[34] A. Ezz, P. Munro, A. T. Porter, J. Battista, D. A. Jaffray, A. Fenster, and S. Osborne, "Daily monitoring and correction of radiation-field placement using a video-based portal imaging system - a pilot study," Int. J. Radiat. Oncol. Biol. Phys., **22**, 159-165 (1992).

[35] L. E. Antonuk, "Electronic portal imaging devices: a review and historical perspective of contemporary technologies and research," Phys. Med. Biol., **47**, R31-R65 (2002).

[36] V. N. Hansen, P. M. Evans, and W. Swindell, "The application of transit dosimetry to precision radiotherapy," Med. Phys., **23**, 713-721 (1996).

[37] M. van Zijtveld, M. L. P. Dirkx, H. C. J. de Boer, and B. J. M. Heijmen, "Dosimetric pre-treatment verification of IMRT using an EPID; clinical experience," Radiother. Oncol., **81**, 168-175 (2006).

[38] Y. Aoki, A. Akanuma, K. Karasawa, K. Sakata, K. Nakagawa, N. Muta, Y. Onogi, and M. Lio, "An integrated radiotherapy treatment system and its clinical application," Radiat. Med., **5**, 131-141 (1987).

[39] K. Kuriyama, H. Onishi, N. Sano, T. Komiyama, Y. Aikawa, Y. Tateda, T. Araki, and M. Uematsu, "A new irradiation unit constructed of self-moving gantry-CT and linac," Int. J. Radiat. Oncol. Biol. Phys., **55**, 428-435 (2003).

[40] L. A. Dawson, and M. B. Sharpe, "Image-guided radiotherapy: rationale, benefits, and limitations," Lancet Oncol., **7**, 848-858 (2006).

[41] M. B. Sharpe, T. Craig, and D. J. Moseley, "Image guidance: Treatment target localization systems,"in *Imrt, Igrt, Sbrt: Advances in the Treatment Planning and Delivery of Radiotherapy*, eds. J. L. Meyer *et al.* (Karger, Basel, 2007), pp. 72-93.

[42] L. A. Feldkamp, L. C. Davis, and J. W. Kress, "Practical cone-beam algorithm," Journal of the Optical Society of America a-Optics Image Science and Vision, **1**, 612-619 (1984).

[43] D. A. Jaffray, J. H. Siewerdsen, J. W. Wong, and A. A. Martinez, "Flat-panel cone-beam computed tomography for image-guided radiation therapy," Int. J. Radiat. Oncol. Biol. Phys., **53**, 1337-1349 (2002).

[44] D. J. Godfrey, F. F. Yin, M. Oldham, S. Yoo, and C. Willett, "Digital tomosynthesis with an on-board kilovoltage imaging device," Int. J. Radiat. Oncol. Biol. Phys., **65**, 8-15 (2006).

[45] C. A. McBain, A. M. Henry, J. Sykes, A. Amer, T. Marchant, C. M. Moore, J. Davies, J. Stratford, C. McCarthy, B. Porritt, P. Williams, V. S. Khoo, and P. Price, "X-ray volumetric imaging in image-guided radiotherapy: The new standard in on-treatment imaging," Int. J. Radiat. Oncol. Biol. Phys., **64**, 625-634 (2006).

[46] D. Verellen, M. De Ridder, and G. Storme, "A (short) history of image-guided radiotherapy," Radiother. Oncol., **86**, 4-13 (2008).

[47] T. R. Mackie, T. Holmes, S. Swerdloff, P. Reckwerdt, J. O. Deasy, J. Yang, B. Paliwal, and T. Kinsella, "Tomotherapy - a new concept for the delivery of dynamic conformal radiotherapy," Med. Phys., **20**, 1709-1719 (1993).

[48] K. M. Langen, S. L. Meeks, D. O. Poole, T. H. Wagner, T. R. Willoughby, P. A. Kupelian, K. J. Ruchala, J. Haimerl, and G. H. Olivera, "The use of megavoltage CT (MVCT) images for dose recomputations," Phys. Med. Biol., **50**, 4259-4276 (2005).

[49] E. J. Holupka, I. D. Kaplan, E. C. Burdette, and G. K. Svensson, "Ultrasound image fusion for external beam radiotherapy for prostate cancer," Int. J. Radiat. Oncol. Biol. Phys., **35**, 975-984 (1996).

[50] J. Lattanzi, S. McNeeley, W. Pinover, E. Horwitz, I. Das, T. E. Schultheiss, and G. E. Hanks, "A comparison of daily CT localization to a daily ultrasound-based system in prostate cancer," Int. J. Radiat. Oncol. Biol. Phys., **43**, 719-725 (1999).

[51] K. M. Langen, J. Pouliot, C. Anezinos, M. Aubin, A. R. Gottschalk, I. C. Hsu, D. Lowther, Y. M. Liu, K. Shinohara, L. J. Verhey, V. Weinberg, and M. Roach, "Evaluation of ultrasound-based prostate localization for image-guided radiotherapy," Int. J. Radiat. Oncol. Biol. Phys., **57**, 635-644 (2003).

[52] X. Artignan, M. H. P. Smitsmans, J. V. Lebesque, D. A. Jaffray, M. van Her, and H. Bartelink, "Online ultrasound image guidance for radiotherapy of prostate

cancer: Impact of image acquisition on prostate displacement," Int. J. Radiat. Oncol. Biol. Phys., **59**, 595-601 (2004).

[53] P. G. Seiler, H. Blattmann, S. Kirsch, R. K. Muench, and C. Schilling, "A novel tracking technique for the continuous precise measurement of tumour positions in conformal radiotherapy," Phys. Med. Biol., **45**, N103-N110 (2000).

[54] D. W. Litzenberg, T. R. Willoughby, J. M. Balter, H. M. Sandler, J. Wei, P. A. Kupflian, A. A. Cunningham, A. Bock, M. Aubin, M. Roach, K. Shinohara, and J. Pouliot, "Positional stability of electromagnetic transponders used for prostate localization and continuous, real-time tracking," Int. J. Radiat. Oncol. Biol. Phys., **68**, 1199-1206 (2007).

[55] J. D. P. Hoisak, K. E. Sixel, R. Tirona, P. Cheung, and J. P. Pignol, "Correlation of lung tumour motion with surrogates of respiration," Med. Phys., **31**, 1759-1759 (2004).

[56] B. G. Fallone, B. Murray, S. Rathee, T. Stanescu, S. Steciw, S. Vidakovic, E. Blosser, and D. Tymofichuk, "First MR images obtained during megavoltage photon irradiation from a prototype integrated linac-MR system," Med. Phys., **36**, 2084-2088 (2009).

[57] C. Kirkby, T. Stanescu, S. Rathee, M. Carlone, B. Murray, and B. G. Fallone, "Patient dosimetry for hybrid MRI-radiotherapy systems," Med. Phys., **35**, 1019-1027 (2008).

[58] B. Burke, M. Lamey, S. Rathee, B. Murray, and B. G. Fallone, "Radio frequency noise from clinical linear accelerators," Phys. Med. Biol., **54**, 2483-2492 (2009).

[59] B. Burke, B. G. Fallone, and S. Rathee, "Radiation induced currents in MRI RF coils: application to linac/MRI integration," Phys. Med. Biol., **55**, 735-746 (2010).

[60] M. Lamey, B. Burke, E. Blosser, S. Rathee, N. De Zanche, and B. G. Fallone, "Radio frequency shielding for a linac-MRI system," Phys. Med. Biol., **55**, 995-1006 (2010).

[61] M. Lamey, J. Yun, B. Burke, S. Rathee, and B. G. Fallone, "Radio frequency noise from an MLC: a feasibility study of the use of an MLC for linac-MR systems," Phys. Med. Biol., **55**, 981-994 (2010).

[62] C. Kirkby, T. Stanescu, and B. G. Fallone, "Magnetic field effects on the energy deposition spectra of MV photon radiation," Phys. Med. Biol., **54**, 243-257 (2009).

[63] J. St. Aubin, S. Steciw, and B. G. Fallone, "The design of a simulated in-line side-coupled 6 MV linear accelerator waveguide," Med. Phys., **37**, 466-476 (2010).

[64] J. St. Aubin, S. Steciw, and B. G. Fallone, "An integrated 6 MV linear accelerator model from electron gun to dose in a water tank," Med. Phys., **37**, 2279-2288 (2010).

[65] J. St. Aubin, S. Steciw, and B. G. Fallone, "Effect of transverse magnetic fields on a simulated in-line 6 MV linac," Phys. Med. Biol., **55**, 4861-4869 (2010).

[66] J. St. Aubin, D. M. Santos, S. Steciw, and B. G. Fallone, "Effect of longitudinal magnetic fields on a simulated 6 MV linac," Med. Phys., **37**, 4916-4923 (2010).

[67] J. St. Aubin, S. Steciw, and B. G. Fallone, "Waveguide detuning caused by transverse magnetic fields on a simulated in-line 6 MV linac," Med. Phys., **37**, 4751-4754 (2010).

[68] J. St. Aubin, S. Steciw, and B. G. Fallone, "Magnetic decoupling of the linac in a low field bi-planar linac-MR system," Med. Phys., **37**, 4755-4761 (2010).

[69] J. Yun, J. St. Aubin, S. Rathee, and B. G. Fallone, "Brushed permanent magnet DC MLC motor operation in an external magnetic field," Med. Phys., **37**, 2131-2134 (2010).

[70] C. Kirkby, B. Murray, S. Rathee, and B. G. Fallone, "Lung dosimetry in a linac-MRI radiotherapy unit with a longitudinal magnetic field," Med. Phys., **37**, 4722-4732 (2010).

[71] B. W. Raaymakers, J. J. W. Lagendijk, J. Overweg, J. G. M. Kok, A. J. E. Raaijmakers, E. M. Kerkhof, R. W. van der Put, I. Meijsing, S. P. M. Crijns, F. Benedosso, M. van Vulpen, C. H. W. de Graaff, J. Allen, and K. J. Brown,

"Integrating a 1.5 T MRI scanner with a 6 MV accelerator: proof of concept," Phys. Med. Biol., **54**, N229-N237 (2009).

[72] J. G. M. Kok, B. W. Raaymakers, J. J. W. Lagendijk, J. Overweg, C. H. W. de Graaff, and K. J. Brown, "Installation of the 1.5 T MRI accelerator next to clinical accelerators: impact of the fringe field," Phys. Med. Biol., **54**, N409-N415 (2009).

[73] A. J. E. Raaijmakers, B. Hardemark, B. W. Raaymakers, C. P. J. Raaijmakers, and J. J. W. Lagendijk, "Dose optimization for the MRI-accelerator: IMRT in the presence of a magnetic field," Phys. Med. Biol., **52**, 7045-7054 (2007).

[74] A. J. E. Raaijmakers, B. W. Raaymakers, and J. J. W. Lagendijk, "Experimental verification of magnetic field dose effects for the MRI-accelerator," Phys. Med. Biol., **52**, 4283-4291 (2007).

[75] A. J. E. Raaijmakers, B. W. Raaymakers, and J. J. W. Lagendijk, "Magnetic-field-induced dose effects in MR-guided radiotherapy systems: dependence on the magnetic field strength," Phys. Med. Biol., **53**, 909-923 (2008).

[76] A. J. E. Raaijmakers, B. W. Raaymakers, S. van der Meer, and J. J. W. Lagendijk, "Integrating a MRI scanner with a 6 MV radiotherapy accelerator: impact of the surface orientation on the entrance and exit dose due to the transverse magnetic field," Phys. Med. Biol., **52**, 929-939 (2007).

[77] B. W. Raaymakers, A. J. E. Raaijmakers, and J. J. W. Lagendijk, "Feasibility of MRI guided proton therapy: magnetic field dose effects," Phys. Med. Biol., **53**, 5615-5622 (2008).

[78] J. F. Dempsey, D. Benoit, J. R. Fitzsimmons, A. Haghighat, J. G. Li, D. A. Low, S. Mutic, J. R. Palta, H. E. Romeijn, and G. E. Sjoden, "A Device for Realtime 3D Image-Guided IMRT," Int. J. Radiat. Biol., **63**, S202-S202 (2005).

[79] J. F. Dempsey, and J. L. Patrick, http://www.viewray.com/index.php, (visited March 12, 2010)

[80] S. Steciw, T. Stanescu, M. Carlone, and B. G. Fallone, "Magnetic shielding of a coupled MRI-Linac system," Med. Phys., **34**, 2623-2623 (2007).

[81] J. H. Billen, and L. M. Young, "Poisson Superfish," *LA-UR-96-1834*, (L.A.N.L.,Los Alamos) 2006

[82] W. B. Herrmannsfeldt, "EGUN - An electron optics and gun design program," *SLAC-331-UC-28(A)*, 1988

[83] L. M. Young, "Parmela," *LA-UR-96-1835*, (L.A.N.L.,Los Alamos) 2005

[84] I. Kawrakow, E. Mainegra-Hing, D. W. O. Rogers, F. Tessier, and B. R. B. Walters, "The EGSnrc code system: Monte Carlo simulation of electron and photon transport," *report PIRS-701*, (National Research Council of Canada,Ottawa) 2009

[85] D. W. O. Rogers, B. A. Faddegon, G. X. Ding, C. M. Ma, J. We, and T. R. Mackie, "BEAM - A Monte Carlo code to simulate radiotherapy treatment units," Med. Phys., **22**, 503-524 (1995).

CHAPTER 2: Theory and Techniques

2.1 ELECTROMAGNETIC THEORY

Particle accelerators deliver energy to charged particle beams through an electric field. The first accelerators used a constant electrostatic field to deliver this energy where the charged particle beam received the maximum energy corresponding to the maximum potential drop produced. Electric field strengths, and hence particle energies were limited in these accelerators due to electrical breakdown. Radiofrequency (RF) accelerators overcame this issue by using time varying fields which are excited in coupled resonant cavities comprising a waveguide. A familiarity with electromagnetic theory and in particular Maxwell's equations and their application in electrodynamics is required to understand linear accelerator theory.

2.1.1 Maxwell's equations

The theoretical framework of classical electromagnetic theory is described by Maxwell's equations,

$$\nabla \cdot \mathbf{D} = \rho \tag{2.1}$$

$$\nabla \cdot \mathbf{B} = 0 \tag{2.2}$$

$$\nabla \times \mathbf{E} = -\frac{\partial \mathbf{B}}{\partial t} \tag{2.3}$$

$$\nabla \times \mathbf{H} = \mathbf{J} + \frac{\partial \mathbf{D}}{\partial t} \tag{2.4}$$

where ρ represents charge density, $\mathbf{J}$ represents the current density vector, $\mathbf{E}$, $\mathbf{B}$, $\mathbf{D}$ and $\mathbf{H}$ represent the electric field, magnetic flux density, electric displacement field, and magnetic field vectors respectively. Maxwell's equations given in Eqs. $2.1 - 2.4$ require supplementation with the constitutive relations, which for linear media are

$$\mathbf{D} = \varepsilon_o \varepsilon_r \mathbf{E} \tag{2.5}$$

$$\mathbf{B} = \mu_o \mu_r \mathbf{H} \tag{2.6}$$

where ε_o and μ_o are the permittivity and permeability of free space respectively while ε_r and μ_r are the relative permittivity and permeability of the media through which the electromagnetic field permeates. For completeness, a full characterization of electromagnetic theory requires a force law which outlines electromagnetic effects on charged particles. The force law is described by the Lorentz force,

$$\mathbf{F} = q\left(\mathbf{E} + \mathbf{v} \times \mathbf{B}\right). \tag{2.7}$$

Solving Maxwell's coupled partial differential equations (PDEs) in the form given in Eqs. 2.1 – 2.4 is difficult and often unnecessary. Decoupling of Maxwell's first order PDEs can be performed through the generation of a second order PDE. This technique is applied in order to obtain the solution for the RF field within a linac cavity. In a source free and current free region with a conductivity of zero, by taking the curl of Eq. 2.3 and using Eqs. 2.1, 2.4, 2.5, and 2.6, Maxwell's equations can be decoupled to yield,

$$\nabla \times \mu_r^{-1} \nabla \times \mathbf{E} - k_o^{\,2} \varepsilon_r \mathbf{E} = 0 \tag{2.8a}$$

$$k_o^2 = \varepsilon_o \mu_o \omega^2 \,. \tag{2.8b}$$

Eq. 2.8 is known as the Helmholtz equation, an uncoupled elliptic second order PDE. After solving Eq. 2.8 for the electric field, the magnetic field can be found by solving Eq. 2.4 using Eq. 2.5 to give a full characterization of the RF field within a linac cavity.

The solution to Eq. 2.8 is only unique provided appropriate boundary conditions are specified. In the case of a linac cavity made of copper or other finite conductive material, the RF field penetrates into the material a small distance. This effect is known as the skin effect and can be approximated through the use of an impedance boundary condition when the refractive index of the material is large compared to the medium[1,2]

$$\sqrt{\frac{\mu_o \mu_r}{\varepsilon_c}} \hat{\mathbf{n}} \times \mathbf{H} + \mathbf{E} - \left(\hat{\mathbf{n}} \cdot \mathbf{E}\right)\hat{\mathbf{n}} = 0 \,. \tag{2.9}$$

In Eq. 2.9 ε_c is the complex permittivity of the material. Thus the electric field solution to Eq. 2.8 is uniquely determined through application of the boundary condition in Eq. 2.9.

Poission's equation, and its homogeneous form, the Laplace equation was used in two instances in this work. The first instance was the solution of the electrostatic potential within the designed electron gun. In this case the electric field can be represented as

$$\mathbf{E} = -\nabla\Phi_e \tag{2.10}$$

where Φ_e represents the electrostatic potential. By taking the gradient of Eq. 2.10, Poisson's equation is obtained

$$-\nabla \cdot \varepsilon_o \varepsilon_r \nabla\Phi_e = \rho. \tag{2.11}$$

Laplace's equation is simply Eq. 2.11 with $\rho=0$,

$$-\nabla \cdot \varepsilon_o \varepsilon_r \nabla\Phi_e = 0. \tag{2.12}$$

The electrostatic potential within the electron gun resulting from a known cathode-anode potential was solved using Laplace's equation (Eq. 2.12) while the electrostatic field solution due to the space charge potential was solved using Poisson's equation (Eq. 2.11).

The second instance in which Laplace's equation was used came about in order to solve for the magnetostatic potential in and around the MR imager in the presence of materials with high relative permeabilities. In this case there are no external currents and the curl of the magnetic field is zero (as with the electrostatic case) so the procedure in determining the magnetic field H from the magnetostatic potential Φ_m is identical to above.

$$\mathbf{H} = -\nabla\Phi_m \tag{2.13}$$

$$-\nabla \cdot \mu_o \mu_r \nabla\Phi_m = 0. \tag{2.14}$$

Eq. 2.14 is the Laplace equation for the magnetic potential. In order for a unique solution to be obtained from Eq. 2.14, an appropriate boundary condition, which typically requires the potential to drop to zero at infinity, needs to be set. The magnetic field can then be calculated from Eq. 2.13.

In the case where currents exist in the problem boundaries, Eqs. 2.13 and 2.14 no longer hold true. An alternative approach is then to use the magnetic vector potential **A**, where

$$\mathbf{B} = \nabla \times \mathbf{A} \qquad (2.15)$$

follows from Eq. 2.2. With a constant current I, the magnetic vector potential can be found from

$$\mathbf{A} = \frac{\mu_o I}{4\pi} \int \frac{dl}{R}. \qquad (2.16)$$

For a loop of wire of radius a centered about the z axis, parallel to the xy plane at a height h above the plane, the solution to Eq. 2.16 can be expressed in a cylindrical coordinate system (r,φ,z). The integration of Eq. 2.16 over the current loop results in,

$$\mathbf{A} = \frac{\mu_o I}{2\pi} \sqrt{\frac{a}{r}} \left[\left(\frac{2}{k} - k \right) K(k) - \frac{2}{k} E(k) \right] \hat{\varphi} \qquad (2.17a)$$

with $K(k)$ and $E(k)$ representing complete elliptic integrals of the first and second kind[3] respectively and with

$$k = \sqrt{\frac{4ar}{(r+a)^2 + (z-h)^2}}. \qquad (2.17b)$$

After substituting Eq. 2.17 into Eq. 2.16 it can be shown that

$$B_r = \frac{-\mu_o I(z-h)}{2\pi\sqrt{(r+a)^2 + (z-h)^2}} \left[F + \frac{2aE(k)}{\left[(r+a)^2 + (z-h)^2\right]\left(1-k^2\right)} \right] \qquad (2.18a)$$

where

$$F = \frac{4a}{(r+a)^2 + (z-h)^2} \int_0^{\pi/2} \frac{\sin^2\alpha - 1}{\left(1-k^2\right)\sqrt{1-k^2\sin^2\alpha}}, \qquad (2.18b)$$

and

$$B_z = \frac{\mu_o I}{2\pi\sqrt{(r+a)^2 + (z-h)^2}} \times$$

$$\left[K(k) + E(k) \left(\frac{2a(r+a)}{\left[(r+a)^2 + (z-h)^2\right]\left(1-k^2\right)} - \frac{1}{1-k^2} \right) \right]. \qquad (2.19)$$

A transformation can be applied to Eq. 2.18 and Eq. 2.19 in order to define the magnetic flux density in Cartesian *xyz* coordinates,

$$B_x = \pm B_r \frac{1}{\sqrt{1+(y/x)^2}} \tag{2.20a}$$

$$B_y = \pm B_r \frac{y}{x\sqrt{1+(y/x)^2}} \tag{2.20b}$$

$$r = \sqrt{x^2 + y^2} \,. \tag{2.20c}$$

It is recognized that the solution **B** of Eqs. 2.18 and 2.19 is the magnetic flux density measured in Tesla (T). However, in order to conform to current nomenclature in the literature, these fields will be referred to as 'magnetic field' throughout this manuscript. The only exception is in chapter 3 where the true magnetic field **H** measured in A/m is discussed in terms of the RF field in the waveguide.

2.1.2   Waveguides

Waveguides are structures that contain and direct electromagnetic fields along a required path. For a cylindrical waveguide, the lowest order standing wave that can exist with an electric field directed along the waveguide length is the TM_{01} mode. For simplicity in the following analysis, the assumption is that the waveguide walls are made from perfect electrical conductors with infinite conductivity. For a cylindrical waveguide of radius *a*, the TM_{01} mode means the only nonzero electric field component is the $\mathbf{E}_z$ component and the only nonzero magnetic field component is the $\mathbf{H}_\varphi$ component. The electric field component $\mathbf{E}_z$ can be found by solving Eq. 2.8 in cylindrical coordinates (r,φ,z) which gives

$$\mathbf{E}_z = E_o J_o(k_{01}r) e^{-j(\beta_{01}z - \omega t)} \, \hat{\mathbf{z}} \tag{2.21a}$$

$$k_{01} = \frac{2.405}{a} \tag{2.21b}$$

$$\beta_{01}^2 = k_o^2 - k_{01}^2 \tag{2.21c}$$

where J_o is the zeroth order Bessel function of the first kind[3]. The circumferential magnetic field can then be found by solving Eq. 2.3 through a separation of the

transverse and longitudinal components of the electric and magnetic fields, and with the assumption of a sinusoidal variation in time and in propagation (with propagation constant β_{01}). By further separating the Del operator into its transverse and longitudinal components, it follows that Eq. 2.3 can be written as

$$\nabla_t \times \mathbf{E}_t = -j\omega\mu_o \mathbf{H}_z \tag{2.22}$$

$$\hat{\mathbf{z}} \times \nabla_t \mathbf{E}_z + j\beta(\hat{\mathbf{z}} + \mathbf{E}_t) = j\omega\mu_o \mathbf{H}_t . \tag{2.23}$$

For the TM_{01} mode, $\mathbf{H}_z = \mathbf{E}_t = 0$ and $\mathbf{H}_t = \mathbf{H}_\varphi$. Thus by substituting Eq. 2.21 into Eq. 2.23 it follows that

$$\mathbf{H}_\varphi = \frac{jE_o}{z} J_1(k_{01}r)e^{-j(\beta_{01}z - \omega t)} \, \hat{\boldsymbol{\varphi}} . \tag{2.24}$$

where J_1 is the first order Bessel function of the first kind[3]. A more detailed and rigorous account of the separation of Maxwell's equations into transverse and longitudinal components and its general application to guided waves can be found in Collins[4].

For a wave with a propagation constant β, the dispersion relation for a waveguide becomes

$$k_c^2 = k_o^2 - \beta^2 . \tag{2.25}$$

At the cutoff between wave propagation and exponential decay, $\beta=0$ and according to Eq. 2.25, $k_o = k_c$. With this relation, k_c can be defined as $k_c^2 = \omega_c^2/c^2$ where ω_c defines the cutoff frequency of the waveguide. The graph of Eq. 2.25 is known as a dispersion curve and is shown in Figure 2.1. As is seen in Figure 2.1, the dispersion curve lies above the 45°, $v=c$ line for all frequencies. Thus the slope for a line connecting the origin to any point on the dispersion curve will always be greater than 45°, or have a phase velocity v_{ph} greater than the speed of light c.

A mathematical representation of the phase velocity of a guided wave in a uniform waveguide can be obtained from Eq. 2.25

$$v_{ph} = \frac{\omega}{\beta} = \frac{c}{\sqrt{1 - (\omega_c/\omega)^2}} \tag{2.26}$$

and the group velocity is

$$v_{gr} = \frac{d\omega}{d\beta} = c\sqrt{1 - (\omega_c / \omega)^2} \ . \tag{2.27}$$

With $\omega_c < \omega$ for a propagating wave, Eq. 2.26 shows that the phase velocity of a guided wave is always greater than c in a uniform waveguide. Therefore, a uniform waveguide cannot be used as an accelerator since efficient particle acceleration requires a phase matching between the particles and electromagnetic wave. Since particle velocities can never reach or exceed the speed of light, the charged particle will continuously change phases with respect to the wave receiving less acceleration over time and eventually experience a decelerating field. It is therefore required to lower the phase velocity of the guided waves for particle acceleration.
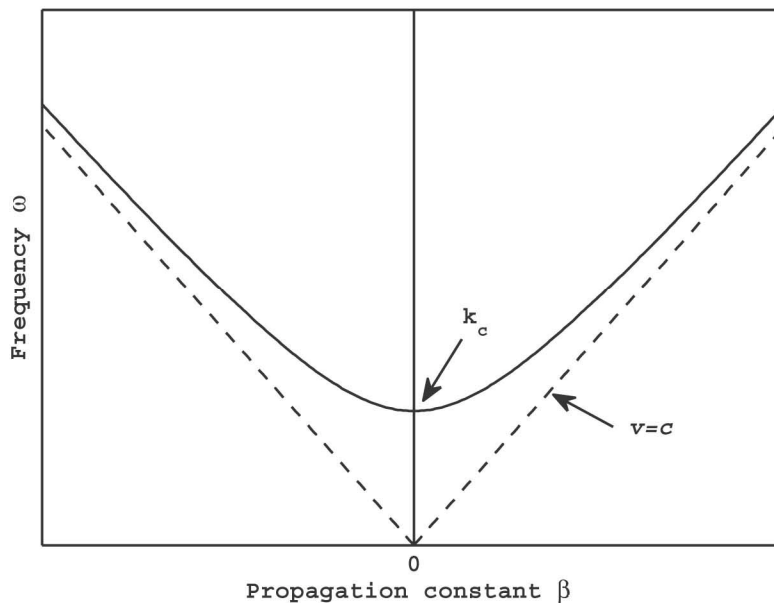
Figure 2.1: Theoretical dispersion curve for a uniform waveguide. The dispersion curve lies above the *v=c* line illustrating the phase velocity *v$_{ph}$* is always greater than the speed of light in a uniform waveguide.

2.1.3   Slow wave structures

Slow wave structures define structures within which the phase velocity of the electromagnetic wave is below the speed of light. The theoretical foundation outlined in this section follows from the work of Slater[5], and Wangler[6]. The

reduction in the phase velocity comes about by loading the cylindrical waveguide with periodically spaced irises or tees. The theoretical foundation for wave propagation in these periodically loaded waveguides is based on Floquet's theorem[6] which states that for a given oscillation mode, and at a given frequency, the wave function at two different cross sections separated by one period d, only differ by a constant factor which is in general complex. Mathematically stated, Floquet's theorem becomes

$$\mathbf{E}(r, z + d) = \mathbf{E}(r, z)e^{\pm j\beta d}.$$ (2.28)

With each cavity in the waveguide being identical, intuitively one expects the time-independent solution to the field in one cavity to be identical to the solution in the other cavity apart from a difference in phase. The propagation constant for wave propagation within the periodic structure can thus be expressed,

$$\beta_n = \beta + \frac{2\pi n}{d}.$$ (2.29)

Further, with $E_d(r,z)$ being periodic, it can be expanded as a Fourier series

$$E_d(r, z) = \sum_{n=-\infty}^{\infty} a_n(r)e^{-j2\pi nz/d}.$$ (2.30)

Since the coefficients $a_n(r)$ of Eq. 2.30 must satisfy Eq. 2.8, the TM_{01} electric field solution within a periodically loaded waveguide becomes

$$E_z(r, z, t) = \sum_{n=-\infty}^{\infty} E_n J_o(k_n r)e^{-j(\beta_n z - \omega t)}$$ (2.31a)

$$k_n^2 = k_o^2 - \beta_n^2$$ (2.31b)

 which is similar to what was derived in Eq. 2.21. In Eq. 2.31, $n>0$ represents waves propagating in the $+z$ direction and $n<0$ represents waves propagating in the $-z$ direction. Thus the electric field within the periodic waveguide given by Eq. 2.31 represents an infinite sum of forward and backward propagating waves, or space harmonics, who's amplitudes are given by the coefficients $a_n(r)$ of Eq. 2.30. The space harmonic with the largest Fourier coefficient and hence amplitude is the $n=0$, or principle space harmonic. The principle harmonic is what is used for acceleration in electron linacs[7]. The phase velocity for the nth space harmonic

v_{ph}^{n} can be derived from the phase velocity of the principle space harmonic v_{ph}^{0}

according to Eq. 2.26 by dividing the wave angular frequency by Eq. 2.29 and

simplifying using $\beta = 2\pi/\lambda$

$$v_{ph}^{n} = \frac{v_{ph}^{o}}{1 + (n\lambda_{o}/d)}.$$
(2.32)

Thus a space harmonic with an arbitrarily large n will yield an arbitrarily low

phase velocity. In addition, the principle space harmonic has its phase velocity

modified in loaded waveguides due to the increased reflections at the loading

structures (e.g. at the irises). If the reflections are large enough through use of

small irises, the phase velocity of the principle wave can also be lowered below

the speed of light. The drawback however with small irises, is that higher order

space harmonics also obtain significant amplitudes due to the reflections at the

irises which absorb power and contribute to heat dissipation on waveguide walls

with finite conductivity.

The changes in wave propagation within the loaded waveguide changes

the characteristics of the dispersion curve as seen in Figure 2.2. The multiple

bands shown in Figure 2.2 are a result of the waveguide's multiple cutoff

wavelengths, each at a higher and higher frequency. Figure 2.2 also illustrates the

stop band between two pass bands where, at these frequencies, only exponential

decay of the wave is possible. The different bands, caused by the different modes

of the waveguide, may not be exclusively independent of each other due to the

multiple reflections within the waveguide. This can lead to mode mixing at higher

frequencies with the higher order spatial harmonics draining power. This in turn

leads to increased Joule heating of the waveguide walls and defocusing effects on

an accelerating charged particle beam. The lowest order TM mode, with its

circular symmetry in cylindrical waveguides, is independent of other modes for a

large range of frequencies avoiding mode mixing and making it ideal for use in

linear accelerators.
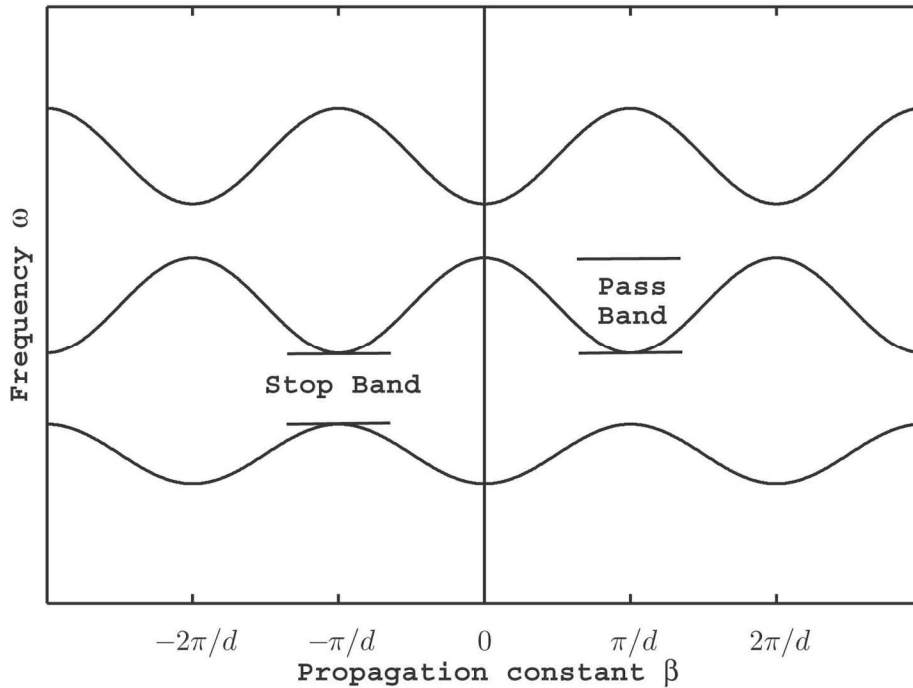
Figure 2.2: The dispersion relation for a loaded waveguide is shown with the stop band and pass band emphasized.

2.1.4   Lumped circuit theory

Many electrical properties of a periodically loaded waveguide made up of a chain of resonant cavities can be described by lumped circuit theory. The foundations for this section are taken from the work of Nagle *et al*[8]. The waveguide under investigation is assumed to be bi-periodic whose cavities are resonantly coupled at the location of high magnetic field strength. The coupled circuit diagram for a bi-periodic structure is given in Figure 2.3 where *R* represents resistance due to the finite conductivity of the waveguide walls, *L* represents the cavity inductance, and *C* the cavity capacitance. The *k* variables represent the coupling coefficients between cavities, with k_1 being the nearest neighbor coupling coefficient, and k_2 and k_3 being the next nearest neighbor coupling coefficients for the accelerating and coupling cavities respectively. The cavities with *n=0,2,...,2N* represent accelerating cavities and cavities with *n=1,3,...,2N-1* represent coupling cavities. The following derivation implicitly

assumes the first and last cavities in the chain are half cavities terminated in perfectly conducting surfaces.
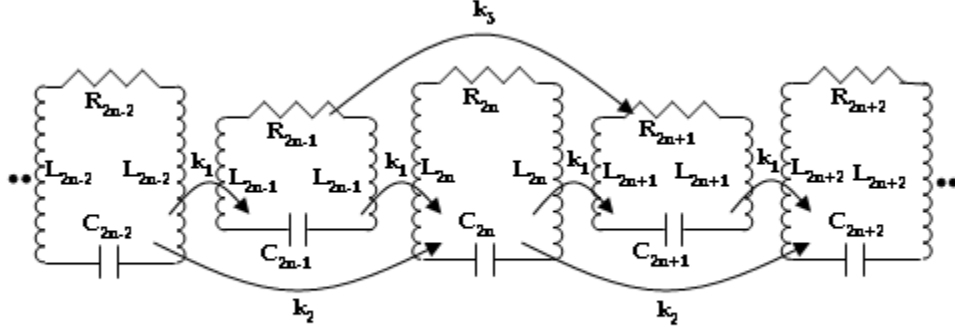
Figure 2.3: Circuit diagram for the lumped circuit theory. k_1 represents the nearest neighbor coupling coefficient, and k_2 and k_3 represent the next nearest neighbor coupling coefficient for the accelerating and coupling cavities respectively.

The circuit equation for cavity 2n is

$$V_{2n} = R_{2n}I_{2n} + 2L_{2n}\frac{dI_{2n}}{dt} + \frac{1}{C_{2n}}\int_0^t I(\tau)d\tau +$$

$$M_{2n-1}\frac{dI_{2n-1}}{dt} + M_{2n+1}\frac{dI_{2n+1}}{dt} + M_{2n-2}\frac{dI_{2n-2}}{dt} + M_{2n+2}\frac{dI_{2n+2}}{dt} \qquad (2.33)$$

where V is the voltage in the circuit and I is the current and M is the mutual inductance defined as $M_{2n\pm m} = k_m\sqrt{L_{2n}L_{2n\pm m}}$ and $m=1,2$ in this case. Taking the Laplace transform[3] of Eq. 2.33 gives

$$E_{2n} = i_{2n}\left[2j\omega L_{2n} + R_{2n} + \frac{1}{j\omega C_{2n}}\right] +$$

$$j\omega k_1\left[\sqrt{L_{2n}L_{2n-1}}i_{2n-1} + \sqrt{L_{2n}L_{2n+1}}i_{2n+1}\right] + \qquad (2.34)$$

$$j\omega k_2\left[\sqrt{L_{2n}L_{2n-2}}i_{2n-2} + \sqrt{L_{2n}L_{2n+2}}i_{2n+2}\right]$$

Dividing by $j\omega\sqrt{2L_{2n}}$ and simplifying the result with the relations

$$X_{2n} = i_{2n}\sqrt{2L_{2n}} \qquad (2.35a)$$

$$\omega_1^{-2} = 2L_{2n}C_{2n} \tag{2.35b}$$

$$Q_1 R_{2n} = 2\omega_1 L_{2n} \tag{2.35c}$$

Eq. 2.34 becomes

$$0 = X_{2n}\left[1 - \frac{\omega_1^2}{\omega^2}\right] + \frac{k_1}{2}\left[X_{2n-1} + X_{2n+1}\right] + \frac{k_2}{2}\left[X_{2n-2} + X_{2n+2}\right] \tag{2.36}$$

where the driving term E_{2n} was set to zero for investigations near resonance and the assumption that Q_1 is very large was used (which is valid for linac cavities). In Eq. 2.36, ω_1 represents the resonant frequency of the accelerating cavity and ω is the frequency of the electromagnetic wave. By following the same procedure outline above, the equation for the coupled cavities is found to be

$$0 = X_{2n+1}\left[1 - \frac{\omega_2^2}{\omega^2}\right] + \frac{k_1}{2}\left[X_{2n} + X_{2n+2}\right] + \frac{k_3}{2}\left[X_{2n-1} + X_{2n+3}\right]. \tag{2.37}$$

The solution to the homogeneous Eqs. 2.36 and 2.37 are

$$X_{2n} = A\cos 2n\varphi \tag{2.38}$$

$$X_{2n+1} = B\cos(2n+1)\varphi \tag{2.39}$$

where $\varphi = \pi q/2N$ representing the phase shift per cavity with $q=0,1,...,2N$. Substituting the homogeneous solutions into 2.36 gives

$$\frac{A}{B} = \frac{k_1 \cos\varphi}{\left[(\omega_1/\omega)^2 - 1 - k_2 \cos 2\varphi\right]} \tag{2.40}$$

while substituting them into Eq. 2.37 gives

$$\frac{A}{B} = \frac{\left[(\omega_2/\omega)^2 - 1 - k_3 \cos 2\varphi\right]}{k_1 \cos\varphi} \tag{2.41}$$

The dispersion relation for a bi-periodic chain of cavities is found by equating Eqs. 2.40 and 2.41,

$$k_1^2 \cos^2\varphi = \left(1 - \omega_1^2/\omega^2 + k_2 \cos 2\varphi\right) \times \left(1 - \omega_2^2/\omega^2 + k_3 \cos 2\varphi\right). \tag{2.42}$$

A plot of Eq. 2.42 is given in Figure 2.4 with $k_2 = k_3 = 0$ and with $\omega_1 \neq \omega_2$.
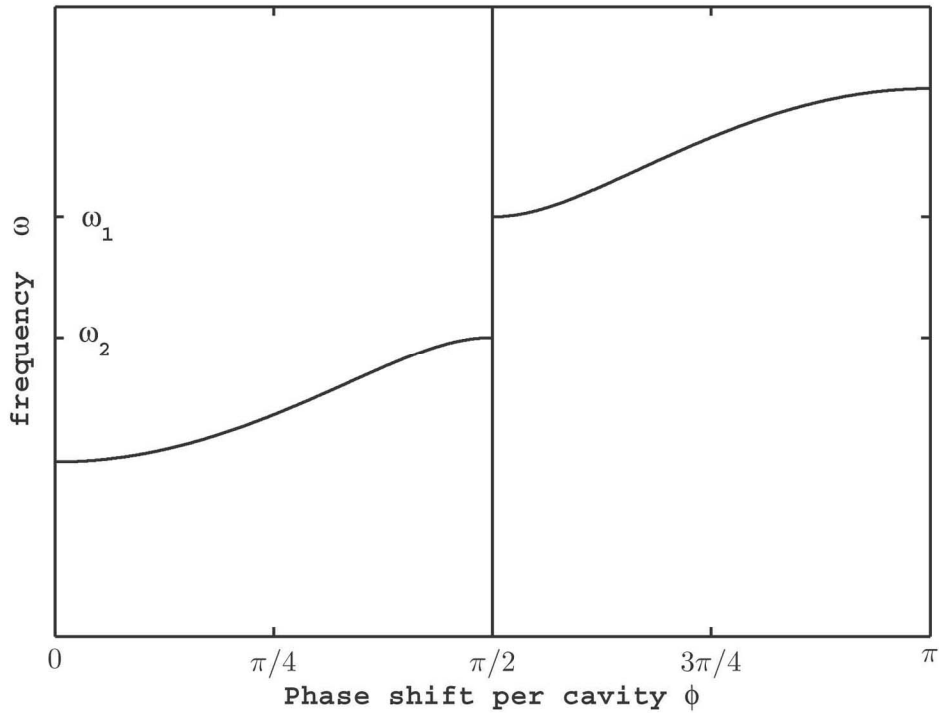
Figure 2.4: Theoretical bi-periodic waveguide dispersion curve for $k_2=k_3=0$ and with $\omega_1 \neq \omega_2$. A stop band forms between ω_1 and ω_2 when the accelerating and coupling cavities have different resonant frequencies.

The stop band that forms between ω_1 and ω_2 can be removed by setting both frequencies to be equal as seen in Figure 2.5. The joining of the passbands is known as the creation of confluence at the π mode for each of the individual bands. After the creation of confluence, a stable $\pi/2$ operating mode exists at one frequency. The $\pi/2$ mode has many desirable features, and is the mode in which the medical linac waveguide under investigation operates. Figure 2.4 and Figure 2.5 show dispersion curves plotted against phase shift per cavity instead of propagation constant β. This comes as a result of the waveguide under investigation being a standing wave structure that is closed at both ends. The standing wave can be described through the phase shift per cavity as compared to the propagation constant for a traveling wave. The finite bandwidth of the dispersion curve shown in Figure 2.5 would be broken up into $N+1$ discrete normal modes corresponding to different phase shifts per cavity for a waveguide

comprised of $N+1$ resonant cavities. Each resonant mode has a finite linewidth Γ caused by the finite conductivity of the waveguide walls[9] which is given by $\Gamma=\omega_\varphi/Q$. Since the bandwidth of the dispersion curve is fixed, a waveguide with twice as many cavities would have twice as many modes over the same frequency range. If the number of cavities is large enough that the modes are spaced close together, the mode linewidths can overlap causing mode mixing. Even, if the modes don't initially overlap, resonant frequency errors caused in the manufacturing process can cause frequency shifts in the modes resulting in mode mixing.
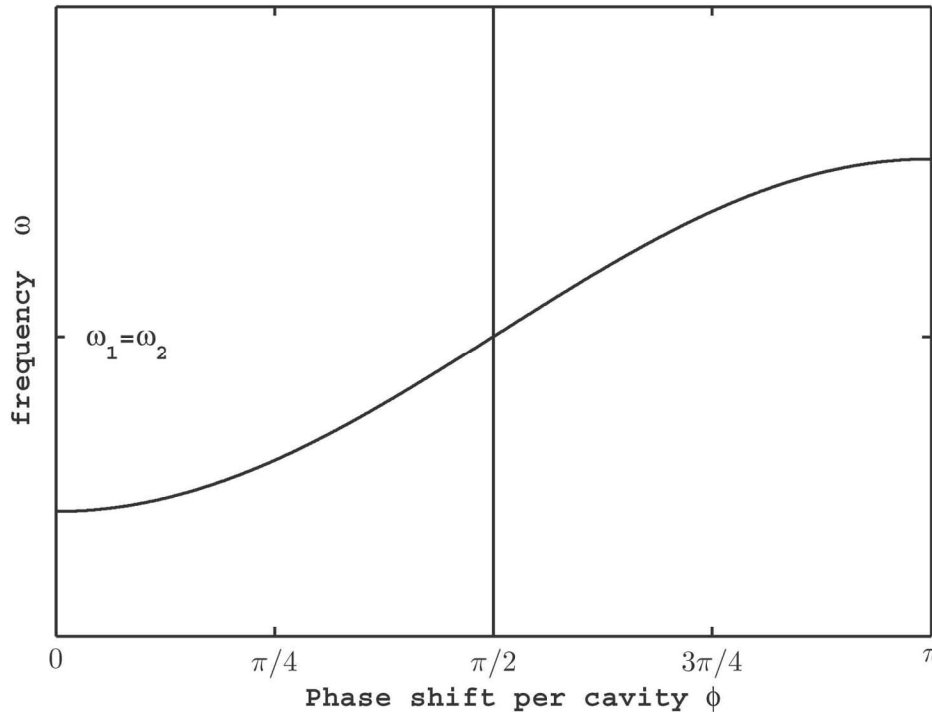
Figure 2.5: The bi-periodic waveguide dispersion curve with the creation of confluence at the resulting π/2 mode is shown. This is a result of accelerating and coupling cavities having the same resonant frequency

2.1.5   Resonant frequency changes

Since the slope of the $\pi/2$ mode is the steepest, its separation from the other modes is the largest which makes it more resistant to resonant frequency

errors. Through first order perturbation analysis of *N+1* bi-periodically coupled

cavities, it can be shown that[8]

$$\delta\omega_p^2 = \omega_p^2 \cdot \sum_{n=0}^{N} W(n) \cdot \left[\delta\omega_{on}^2 / \omega_o^2\right] \cdot \cos^2\left(\pi q n / N\right).$$

(2.43)

In Eq. 2.43, $\delta\omega_q$ represents the change in operating frequency ω_q of the waveguide

for the *q* mode as a result of the resonant frequency errors $\delta\omega_{on}$ of cavity *n* with

nominal frequency ω_o. *W(n)* = ½ for half accelerating cavities and *W(n)* = 1 for

full cavities. Cavity resonant frequency changes result from geometric errors of

the waveguide cavity due to manufacturing, or even the planned introduction of a

coupling iris providing a means for power transfer from one cavity to the next.

The resultant resonant frequency changes caused by a perturbation that depresses

part of the wall into the cavity is treated by Slater[5] who derives

$$\omega^2 = \omega_1^2\left(1 + \int_V \left(H^2 - E^2\right)dV\right).$$

(2.44)

Thus if the perturbation occurs in a region of high magnetic field and low electric

field the resultant resonant frequency increases. If however the perturbation

causes a part of wall in the same region described above to bulge outwards, it

results in a lower resonant frequency. This is what is experienced when a coupling

iris is introduced into a waveguide cavity. A thorough treatment on the analytical

calculation of coupling coefficients between resonant cavities is not treated here,

but has been investigated previously by other authors[4, 10, 11].

2.2 COMPUTATIONAL ELECTROMAGNETICS

Numeric computational techniques for solving electromagnetic problems

are useful for complex problem geometries. Linac cavity, electron gun, and MR

imager geometries are examples of complex geometries that required the use of

computational techniques such as finite difference (FD) and the finite element

method (FEM) in this work. These numeric techniques used in solving

electromagnetic problems are typically broken down into steps. The first step,

known as meshing, breaks up the main geometric volume into many sub-volumes.

Next, the PDE being investigated is discretized and formulated onto the mesh resulting in a matrix for implicitly formulated problems. For the particle simulations, the implicit formulation is a result of the temporal discretization, while for the electromagnetic simulations it is due to the spatial discretization. Lastly the solution is found on the discrete mesh points by solving the matrix. Specifically, the 2D axisymmetric electron gun program EGN2w used a simple Taylor expansion FD approach to solve Eqs. 2.11 and 2.12. The 2D axisymmetric linac cavity program Superfish used a more complex conformal FD method to solve Eq. 2.8 for the magnetic field (**H**). The FEM electron gun program OPERA-3d/SCALA was used to solve Eqs. 2.11 and 2.12 in 3D. COMSOL Multiphysics (COMSOL) used the FEM to solve Eq. 2.8 for the RF field in the coupled linac waveguide, as well as Eq. 2.14 for the magnetostatic potential of the bi-planar MR imager modeled.

2.2.1   Finite Difference

2.2.1.1   EGN2w

The simplest form of FD approximations of differentials comes from a Taylor expansion of the dependent variables. This FD method replaces the continuous derivatives of the PDE under investigation with corresponding FD formulas. This was the approach used by the electron gun program EGN2w. It used a simple mesh to divide up the problem geometry with a square grid as shown in Figure 2.6. Meshing with a square grid permits a simple mathematical form of the Taylor expansion leading to simple FD formulas. Its drawback however, is it inability to conform to curved surfaces to a high degree of accuracy.

The Taylor expansion of the dependent variable u about the point (i,j) in the x direction is

$$u(i+1,j) = u(i,j) + h\, u_x(i,j) + \frac{h^2}{2!} u_{xx}(i,j) + \frac{h^3}{3!} u_{xxx}(i,j) + \dots \tag{2.45}$$

and the Taylor expansion in the y direction is performed in the same manner. By solving Eq. 2.45 for u_x and neglecting terms of second order and higher, a forward difference formula is obtained. Through a similar Taylor expansion as Eq. 2.45,

but for *u(i-1,j)*, solving for u_x and neglecting second order and higher terms, a backward difference formula is obtained. Both the forward and backward difference formulas explained have errors on the order of *Δx*. EGN2w uses the more accurate central difference formula which is obtained through use of higher order terms in Eq. 2.45. By adding the Taylor expansions in both the forward and backward directions, solving for u_x and keeping the second order term, the central difference formula is obtained with errors on the order of $(\Delta x)^2$.
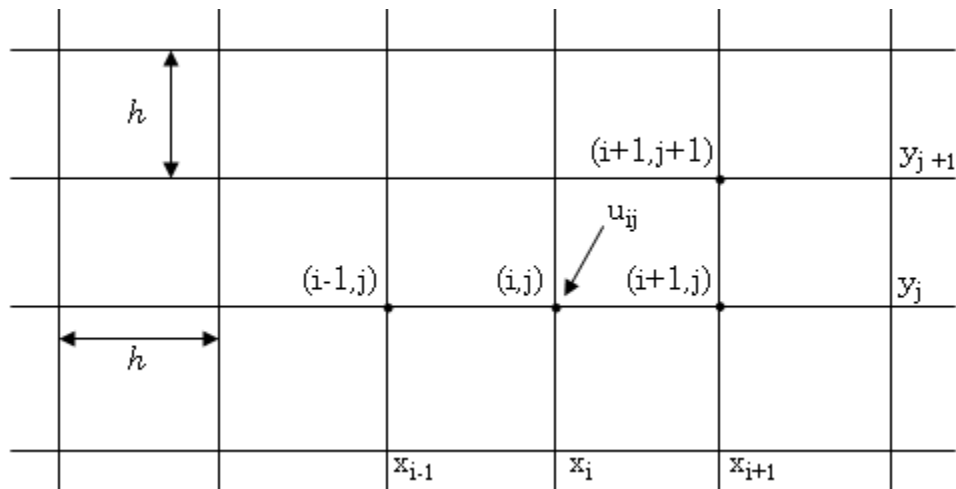
Figure 2.6: A typical regular square grid used to mesh the EGN2w problem geometry using the standard FD method.

The simplicity of the above formulation of the FD method relies on the ability to Taylor expand the dependent variables solely along a coordinate direction, either the x or y direction in Figure 2.6. However, many problem geometries cannot be meshed with a high degree of accuracy using a square grid (or box in 3D).

2.2.1.2   Superfish

Superfish makes use of triangular elements which enables the mesh to conform to the geometry to a greater degree. However, Taylor expansion along an arbitrary direction corresponding to the mesh lines of the triangular mesh is complicated and instead Superfish uses a conformal FD approach. The conformal FD approach taken by the program Superfish[12] was initially given by Winslow[13].
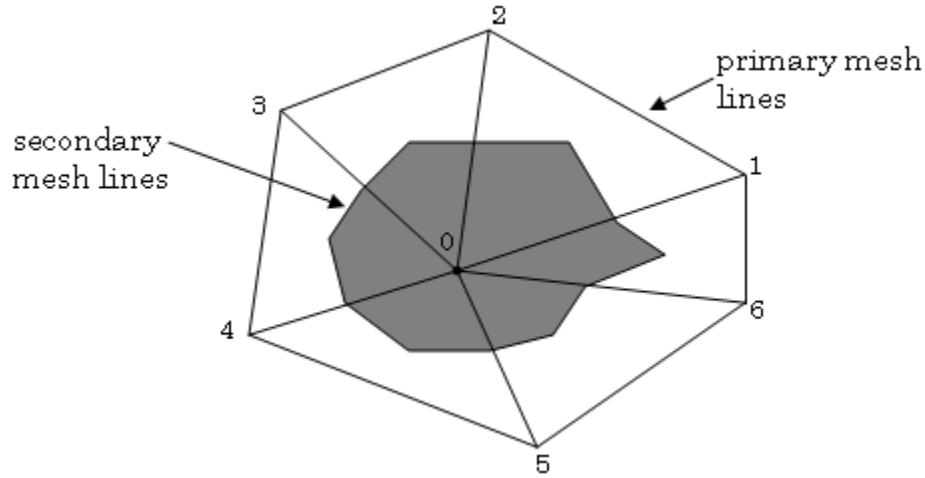
Figure 2.7: Primary and secondary mesh used in the conformal FD program Superfish.

An interior mesh point '0' in a triangular mesh is surrounded by six triangles (Figure 2.7). A secondary mesh (seen in grey in Figure 2.7) is defined whose vertices are located at the primary mesh triangle centroid for each triangle and the midpoints of the triangle sides. The conformal FD approach taken by Superfish solves Eq. 2.8 for the magnetic field (instead of the electric field) in vacuum giving,

$$\nabla \times \nabla \times \mathbf{H} = k_o^2 \mathbf{H} .$$
(2.46)

Integrating Eq. 2.46 over the area of the secondary mesh gives

$$\oint \nabla \times \mathbf{H} \cdot d\mathbf{s} = k_o^2 \int \mathbf{H} \cdot d\mathbf{a} .$$
(2.47)

after Stoke's theorem[9] has been applied. By further assuming that **H** varies linearly within every triangle, the magnetic field is uniquely determined by the solutions at the three primary triangle vertices. Equation 2.47 can thus be expressed discretely as

$$\sum_{p=0}^{6} H_p \left(V_p + k_o^2 W_p \right)$$
(2.48)

with V_p and W_p depending only on the vertex coordinates.

2.2.2   Finite element method

2.2.2.1   Meshing

The finite element method applied to electromagnetic problems is described in detail by Jin[2]. The first step in finding a numerical solution to any problem is the dividing up of the main geometry surface in 2D or volume in 3D into many smaller sub-surfaces or sub-volumes. This is done by 'meshing' the main geometry with small elements. Examples of basic elements for 2D and 3D geometries are given in Figure 2.8 (a) and (b) respectively. The vertices of one element are always required to correspond to vertices of other elements, with a vertex never being positioned along an element edge. After the mesh is generated, optimization is performed using the Delauney triangulation[14] to achieve greater accuracy in the FEM solution. Both OPERA-3d/SCALA and COMSOL use this approach for meshing.

The geometry of an electron gun, linac cavity and bi-planar MR imager has a large number of curved surfaces. Using the straight edges elements given in Figure 2.8 (a) and (b) to describe a curved surface requires a large number of elements to be used to minimize the geometric errors. An alternative solution is to allow the construction of elements with curved edges which would more accurately conform to arbitrary boundaries. An example of a tetrahedron element with curved edges is given in Figure 2.8 (c). Each node on the curved element in the xyz-space problem geometry is mapped into a $\xi\eta\zeta$-space which transforms the curved edges into straight edges. In the example of Figure 2.8 (c) the mapping is performed using a quadratic transformation which requires the additional nodes placed at the center of the edges. If the transformation function matches the finite element basis functions (explained in section 2.2.2.2), the curved elements are known as isoparametric elements. Further detail on the application of isoparametric elements to the finite element method is given by Zienkiewicz[15]. Isoparametric elements were used in both OPERA-3d/SCALA and COMSOL to better conform to the geometric boundaries.
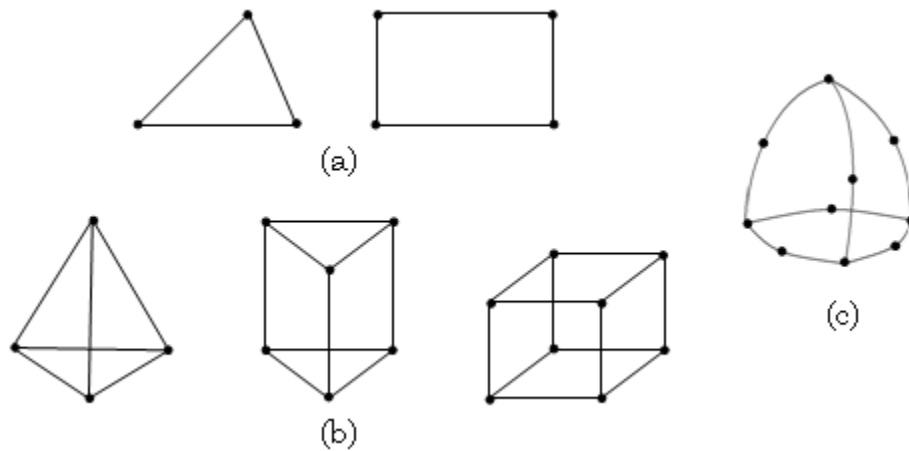
Figure 2.8: Basic elements for (a) 2D problem geometries and (b) 3D problem geometries. A tetrahedron with curved edges is shown in (c)

With the generation of the mesh, numbering systems are required for each node. Each element is assigned an element number and local node numbers are generated. In addition to the local node numbers, each node is also assigned a global node number running from $1,..,N$ where N is the total number of nodes in the entire problem domain. An array known as a 'T array' keeps track of the element number e, the local node number and its corresponding global node number. The T array can be separated into one array that indexes the interior node numbers to the global node numbers, as well as one that indexes boundary nodes numbers to global node numbers. The separation of the T array in this manner can simplify the formulation of the elemental equation (section 2.2.2.3). Another array known as a 'P array' keeps track of the global number and its global (x,y,z) position. The T and P arrays are necessary for the matrix assembly step (section 2.2.2.4) and for the determination of the global solution.

2.2.2.2   *Basis functions*

With a mesh generated that conforms to the problem geometry, the next step in the finite element method is to choose approximations to the dependent variables. The approximation functions chosen are known as basis functions and are defined at each node of the mesh. The most common type of basis function

which is used by OPERA-3d/SCALA and COMSOL to solve Poisson's and Laplace's equation (Eqs. 2.11, 2.12 and 2.14) is the Lagrange basis function. It has a value of one at the node point for which it is defined, is identically zero at all the other nodes, and varies across the element according to its element order. Linear order elements are the most straightforward to use and understand, but higher order elements can achieve a greater accuracy[2]. OPERA-3d/SCALA uses both first and second order Lagrange elements, while COMSOL uses up to fifth order Lagrange elements.

Lagrange basis functions which are defined at the nodes are not ideal for electromagnetic calculations requiring a full vector formulation such as the solution to Eq. 2.8, since in general only the basis function itself is required to be continuous. Discontinuities in the derivatives of the basis functions cause the divergence condition (Eq. 2.2) to not be satisfied leading to spurious, or non-physical solutions. In addition, natural, or Neumann boundary conditions that should automatically be satisfied, sometimes require explicit enforcement which makes the problem construction more difficult. Lastly, sharp corners which cause large electromagnetic field enhacements[9] are treated poorly with nodal based basis functions. In order to overcome the deficiencies associated with Lagrange and other nodal basis functions, a vector element formulation can be used[16]. Instead of the approximation to the dependent variables being defined at node points, it is defined along an edge. The formulation of vector elements automatically satisfies the divergence condition eliminating spurious solutions, and also inherently enforces Neumann boundary conditions[2]. Since field singularities are determined analytically at sharp edges, some difficulties still arise even with the formulation of vector elements, but the effects are reduced. The vector Helmholtz equation (Eq. 2.8) was solved in COMSOL Multiphysics using cubic vector elements for the RF field solution within the waveguide.

2.2.2.3   Formulation of the elemental equations

After the selection of basis functions, the PDE is discretized locally over each element yielding an elemental equation. The discretization of the PDE performed by the OPERA-3d/SCALA and COMSOL programs is done by Galerkin's method[2]. Galerkin's method is a subset of the more general method of weighted residuals. The method of weighted residuals admits a weak solution to the PDE being solved since it requires the approximate solution to be identical to the true solution times a weighting factor. In Galerkin's method, the weighting factor is the chosen basis function.

With a general PDE defined as $L=ug$, with L representing the differential operator, Galerkin's method states that the best approximation $\tilde{u}$ is the one that gives the least residual. This amounts to minimizing the L_2 norm of the residual r over the element Ω_e,

$$\|r\|^2 = \langle r,.r \rangle = \int_{\Omega_e} \left| L\tilde{u}^e - g \right|^2 d\Omega_e \ . \tag{2.49}$$

Thus Galerkin's general formulation of the weak solution becomes,

$$\left\langle \varphi_i^e , L\tilde{u}^e \right\rangle - \left\langle \varphi_i^e , g \right\rangle = 0 \ . \tag{2.50}$$

where φ_i^e is the basis function. The approximate solution $\tilde{u}^e$ in Eqs. 2.49 and 2.50 is defined as

$$\tilde{u}^e = \sum_{j=1}^{N} u_j^e \varphi_j^e \tag{2.51}$$

The formulation of the elemental equations is the major component of the PDE discretization for the finite element method. As such, formulation of the elemental equations for Poisson's equation (Eq. 2.11) and for the Helmholtz equation (Eq. 2.8) is given below.

The differential operator L for Poisson's equation is

$$L = -\nabla \cdot \lambda \nabla \tag{2.52}$$

where $\lambda = \varepsilon_o \varepsilon_r$. Substituting Eq. 2.52 into Eq. 2.50 gives

$$- \int_{\Omega_e} \varphi_i^e \nabla \cdot \left(\lambda \nabla \tilde{u}^e \right) d\Omega_e - \int_{\Omega_e} \rho \varphi_i^e d\Omega_e = 0 \ . \tag{2.53}$$

Performing integration by parts on the first integral in Eq. 2.53 yields

$$\int_{\Omega_e} \nabla \varphi_i^e \cdot \lambda \nabla \tilde{u}^e d\Omega_e - \int_{\Gamma_e} \varphi_i^e \lambda \nabla \tilde{u}^e \cdot d\hat{\mathbf{n}} - \int_{\Omega_e} \rho \varphi_i^e d\Omega_e = 0 . \tag{2.54}$$

The second integral (a surface integral) can be ignored in our simulations for two reasons. First, on all interior elements the integral is always zero satisfying the natural Neumann boundary condition. Second, the integral is either zero on the surface satisfying natural Neumann boundary conditions, or it is specified explicitly though Dirichlet boundary conditions. A natural Neumann boundary condition is when the normal derivative of the dependent variable is zero, and a Dirichlet boundary condition is when the dependent variable is set (input) explicitly. Substituting the approximate solution of Eq. 2.51 into Eq. 2.54 gives

$$\sum_{j=1}^{N} u_j^e \int_{\Omega_e} \nabla \varphi_i^e \cdot \lambda \nabla \varphi_j^e d\Omega_e - \int_{\Omega_e} \rho \varphi_i^e d\Omega_e = 0 . \tag{2.55}$$

Equation 2.55 can be rewritten in matrix form to give

$$\left[K^e \right] \mathbf{u}^e - \left[b^e \right] = 0 \tag{2.56}$$

where

$$K_{ij}^e = \int_{\Omega_e} \nabla \varphi_i^e \cdot \lambda \nabla \varphi_j^e d\Omega_e \tag{2.57}$$

$$b_i^e = \int_{\Omega_e} \rho \varphi_i^e d\Omega_e . \tag{2.58}$$

As an example of the FEM discretization process, the solution of the elemental equation (Eq. 2.56) will be given using linear Lagrange basis functions on 2D triangular elements for simplicity and clarity.

Linear Lagrange elements can be defined through the use of barycentric coordinates. The jth barycentric coordinate of the point p shown in Figure 2.9 is

$$N_j = \frac{\Delta_j}{\Delta^e} , \, j = i, i+1, i+2 . \tag{2.59}$$

where the Δ_j represents the area of a sub-triangle seen in Figure 2.9 and Δ^e represents the total area of the triangle. Each barycentric coordinate N_j in Eq. 2.59 represents a linear Lagrange basis function. The nodes of the triangle are always

numbered in a local fashion maintaining a counterclockwise cyclic permutation to ensure that Δ_j is always positive.
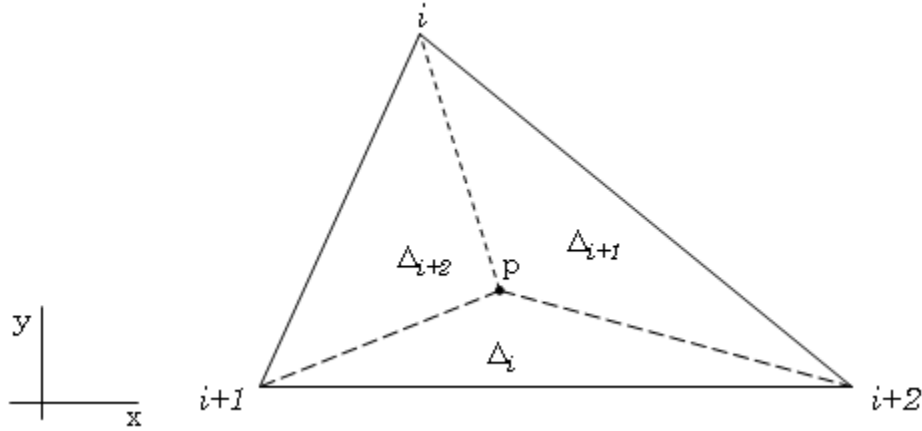
Figure 2.9: Triangular element with a point p inside. The coordinates of the point p is expressed in barycentric coordinates.

Equation 2.59, together with Figure 2.9 for node i becomes,

$$N_i = \frac{1}{2\Delta^e}\left(a_i x + b_i y + c_i\right)$$ (2.60a)

$$a_i = y_{i+1} - y_{i+2}.$$ (2.60b)

$$b_i = x_{i+2} - x_{i+1}$$ (2.60c)

$$c_i = x_{i+1}y_{i+2} - x_{i+2}y_{i+1}$$ (2.60d)

Equation 2.57 can be solved using Eq. 2.60 to give

$$K_{ij}^e = \frac{\lambda}{4\Delta^e}\left(a_i a_j + b_i b_j\right)$$ (2.61)

while Eq. 2.58 can be solved using Gauss-Legendre quadrature[2] giving

$$b_i^e = \rho\frac{\Delta^e}{3}.$$ (2.62)

The FEM solution to Poisson's equation given in Eqs. 2.61 and 2.62 is easily adapted to Laplace's equation by setting $\rho=0$ in Eq. 2.62. In addition, these solutions can be adapted for magnetostatic problems by again setting $\rho=0$ and by setting $\lambda=\mu_0\mu_r$. The results given in Eqs. 2.61 and 2.62 are strictly for linear basis functions. Higher order basis functions can be used in Eqs. 2.57 and 2.58 to

achieve higher accuracy in the solution, but with added complexity. An nth order Lagrange basis function is defined as

$$\varphi^e = \xi_o f_o + \xi_1 f_1 + \ldots + \xi_n f_n \tag{2.63a}$$

$$\xi_k = \frac{\prod\limits_{j=0,j\neq k}^{n}\left(x - x_j\right)}{\prod\limits_{j=0,j\neq k}^{n}\left(x_k - x_j\right)} \tag{2.63b}$$

where f is the FEM field solution at the nodes of element e.

Galerkin's formulation of the Helmholtz equation (Eq. 2.8) using vector basis functions $\mathbf{N}_i^e$ is

$$\int\limits_{\Omega_e}\left(\mathbf{N}_i^e \cdot \nabla \times \mu_r^{-1}\nabla \times \widetilde{\mathbf{E}}^e - \mathbf{N}_i^e \cdot k_o^2 \varepsilon_r \widetilde{\mathbf{E}}^e\right)d\Omega_e \;. \tag{2.64}$$

The vector basis functions are described in detail by Jin.[2] Applying Green's second theorem for vectors, Eq. 2.64 becomes

$$\int\limits_{\Omega_e}\left(\nabla \times \mathbf{N}_i^e\right)\cdot\left(\mu_r^{-1}\nabla \times \widetilde{\mathbf{E}}^e\right)d\Omega_e - k_o^2 \int\limits_{\Omega_e}\varepsilon_r\left(\mathbf{N}_i^e \cdot \widetilde{\mathbf{E}}^e\right)d\Omega_e \tag{2.65}$$

$$-\int\limits_{\Gamma_e}\left(\mathbf{N}_i^e \times \mu_r^{-1}\nabla \times \widetilde{\mathbf{E}}^e\right)\cdot\hat{\mathbf{n}}\,d\Gamma_e = 0$$

where the approximate solution $\widetilde{\mathbf{E}}^e$ is

$$\widetilde{\mathbf{E}}^e = \sum_{j}^{n}\mathbf{N}_j^e E_j^e = \left\{\mathbf{N}^e\right\}^{\mathrm{T}}\left\{E^e\right\}. \tag{2.66}$$

Substituting Eq. 2.66 into Eq. 2.65

$$\int\limits_{\Omega_e}\left\{\nabla \times \mathbf{N}^e\right\}\cdot\left\{\mu_r^{-1}\nabla \times \mathbf{N}^e\right\}^{\mathrm{T}}\left\{E^e\right\}d\Omega_e - k_o^2 \int\limits_{\Omega_e}\varepsilon_r\left\{\mathbf{N}^e\right\}\cdot\left\{\mathbf{N}^e\right\}^{\mathrm{T}}\left\{E^e\right\}d\Omega_e \tag{2.67}$$

$$-\int\limits_{\Gamma_e}\left\{\mathbf{N}^e \times \left\{\mu_r^{-1}\nabla \times \mathbf{N}^e\right\}^{\mathrm{T}}\right\}\left\{E^e\right\}\cdot\hat{\mathbf{n}}\,d\Gamma_e = 0$$

Eq. 2.67 can be expressed in matrix form as

$$\left[K^e\right]\mathbf{E}^e = k_o^2\left[b^e\right]\mathbf{E}^e + \left[g^e\right]\mathbf{E}^e \tag{2.68}$$

where

$$\left[K^e\right] = \int\limits_{\Omega_e}\left\{\nabla \times \mathbf{N}^e\right\}\cdot\left\{\mu_r^{-1}\nabla \times \mathbf{N}^e\right\}^{\mathrm{T}}d\Omega_e \tag{2.69}$$

$$\left[b^e\right] = \int_{\Omega_e} \varepsilon_r \{\mathbf{N}^e\} \cdot \{\mathbf{N}^e\}^{\mathrm{T}} \, d\Omega_e \tag{2.70}$$

$$\left[g^e\right] = \int_{\Gamma_e} \{\mathbf{N}^e \times \{\mu_r^{-1} \nabla \times \mathbf{N}^e\}^{\mathrm{T}}\} \cdot \hat{\mathbf{n}} \, d\Gamma_e \tag{2.71}$$

It is clear that the impedance boundary condition in Eq. 2.9 cannot be applied directly to Eq. 2.67 since Eq. 2.9 requires knowledge of the magnetic field **H** in addition to the electric field **E**. This can be performed in two ways. The first is to use the FEM to solve for **H** at the boundary from the **E** field, or a dual-field formulization[2] can be used for higher accuracy which solves both the **E** and **H** fields simultaneously at the boundary. Once the impedance boundary condition has been applied by either of the two methods, the matrix $[g^e]$ can in general be absorbed into matrices $[K^e]$ and $[b^e]$ leaving[2]

$$\left[K^e\right]\mathbf{E}^e = k_o^2 \left[b^e\right]\mathbf{E}^e \tag{2.72}$$

which is an eigenvalue equation.

2.2.2.4   *Matrix assembly and solution*

After the elemental equations are determined for each element (Eq. 2.56 or Eq. 2.72), all the elemental equations are assembled together into global matrices from which the total solution is found. Matrix assembly simply builds the global matrix from the elemental equations using the local to global node number index stored in the T array. The generation of the global stiffness matrix $[K]$ amounts to the following,

$$K_{n(i,e),n(j,e)} = K_{n(i,e),n(j,e)} + K_{ij}^e \tag{2.73}$$

where the index $n(i,e)$ or $n(j,e)$ is obtained from the T array. A similar operation is performed to generate the global source vector $[b]$. After the global stiffness matrix and source vector has been assembled, a method to solve the large number of linear equations is required. There are a large number of methods and techniques available to perform this task as outlined by Jin[2], but the solution to Eq. 2.56 in COMSOL used the direct solver PARDISO[17, 18]. Eq. 2.72 represents an eigenvalue problem which was solved iteratively using the ARPACK

algorithm[19]. However, if a source term is added to Eq. 2.72, representing power flow into the waveguide, PARDISO was the only algorithm required. OPERA-3d/SCALA solely used the Incomplete Cholesky conjugate gradient iterative solver[20] to solve Eq. 2.56. With the solution obtained at every node (or edge for vector elements), the basis functions serve as an interpolation method to obtain the solution at any point within the problem geometry.

2.3 LINEAR ACCELERATORS

The use of RF fields to accelerate charged particles has provided the means for very large particle energies to be obtained. However, due to the constantly changing polarity of the RF field, the interactions between the charged particles and the electromagnetic field must be understood to design an accelerator which efficiently captures and accelerates the particles to high energies. The theory behind charged particle acceleration within RF linear accelerators is well understood and has been thoroughly discussed by many authors[5-7, 21, 22]. The discussion outlined here will follow their descriptions closely.

2.3.1 Transit time factor and shunt impedance

Two important concepts for RF linear accelerators are the transit time factor and the shunt impedance. The transit time factor accounts for the time varying nature of the RF field and how much acceleration can be derived from it and the shunt impedance is a metric to quantify the efficiency of a slow wave structure to act as a linear accelerator. The transit time factor is defined as

$$T = \frac{\int_{-L/2}^{L/2} E(0,z)\cos(2\pi\, z/\beta\lambda)dz}{\int_{-L/2}^{L/2} E(0,z)dz} \tag{2.74}$$

within an accelerating cavity of length L. In Eq. 2.74 β is the normalized charged particle velocity and λ is the wavelength of the RF wave. Implicit assumptions in Eq. 2.74 are that the geometric center of the cavity corresponds to the electrical center and that the axial electric field $E(0,z)$ is an even function. Both of these

assumptions hold true in general for the linac cavities being investigated in this thesis. The transit time factor always runs from zero to one, measuring the reduction in charged particle energy gain due to the sinusoidal time variation of the RF wave. The transit time factor is an important concept when considering the maximum charged particle energy gain through a linac. The total energy gain ΔW of a particle with charge q, expressed in terms of the maximum axial electric field strength E_o is

$$\Delta W = qE_oT\cos\varphi\,L \tag{2.75}$$

which is sometimes known as the Panofsky equation. The angle φ refers to the synchronous phase. If a charged particle is injected into a linac at the synchronous phase, the particle will maintain that exact phase throughout its acceleration. If a particle is injected with any other phase, the acceleration the particle experiences will cause it to either advance on the wave crest, or slip behind depending on when it was injected and on the phase velocity of the RF wave.

The shunt impedance of a cavity or waveguide structure, measured per unit length, is a measure of how efficiently power is transferred to the charged particle from the RF wave. It is defined as

$$Z = \frac{E_o^2}{P_l/L} \tag{2.76}$$

where P_l is the power dissipated on the waveguide walls. Equation 2.76 is defined from the maximum axial electric field value, but considering the time variation of the RF field, a more representative metric is the effective shunt impedance, which is defined as

$$ZT^2 = \frac{(E_oT)^2}{P_l/L}. \tag{2.77}$$

2.3.2   Longitudinal particle dynamics for standing-wave linacs

The maximum efficiency of a linear accelerator not only depends on the cavity geometry and the RF field which together define the transit time factor and the effective shunt impedance, but also depends on the charged particle injection.

All of the above concepts assume injection on the synchronous phase which yields the maximum possible efficiency. However, the evolution of the charged particle beam as it accelerates within the linac is of critical importance to minimize beam loss, and maximize energy gain. The discussion of particle dynamics for standing-wave (SW) linacs is presented here since the linac under investigation accelerates electrons using RF standing-waves.
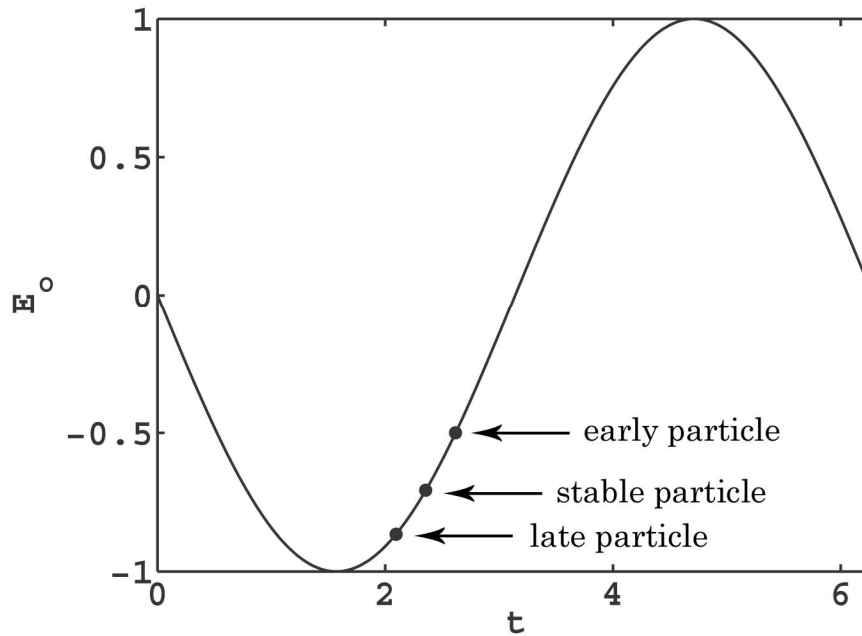
Figure 2.10: Graphical representation of different particle phases on an RF wave crest.

Figure 2.10 shows three particles at different phases of the accelerating RF wave. The stable particle represents the synchronous phase as explained previously. The 'early particle' entered the cavity as the RF wave is building up and therefore experiences a lower electric field strength and receives less acceleration. The 'late particle' enters the cavity after the standing-wave has almost obtained its maximum and therefore experiences larger electric field strength and more acceleration. As the particles progress through the cavity, the early particle is overtaken by both the stable and late particles and enters the next cavity late due to its lower acceleration. The late particle, having the greatest acceleration enters the next cavity early. Thus oscillations around the stable

particle occur as the charged particle beam progresses through the linac for RF phase velocities less than *c*. As the phase velocity of the RF wave approaches *c*, these oscillations decrease in magnitude and at the speed of light, no oscillations occur at all since no particle can travel at the speed of light and can therefore not advance on the wave crest. The particles undergoing these motions, oscillatory or asymptotically approaching the wave crest, are considered to be captured within an RF bucket because they will continue to accelerate through the linac. However, the different particle phases on the RF wave as seen in Figure 2.10 leads to different energy gains. The differential equation that describes the change in energy gain with respect to the stable particle (subscript s) over an axial distance *l* is

$$\frac{d(W - W_s)}{dl} = qE_oT(\cos\varphi - \cos\varphi_s).$$

(2.78)

Another important concept is the longitudinal motion of a low energy beam injected into a linac with an RF phase velocity of *c*. The charged particle beam injected at low energies slips back on the RF wave as it gains momentum. If the particles are electrons which can achieve ultrarelativistic velocities, they approach a stable phase on the RF wave as their velocities nearly match the RF phase velocity of *c*. Thus the electrons undergo longitudinal bunching as a large number of particles over a relatively wide phase range approach the same stable phase on the RF wave. The maximum phase slip of the electrons can be shown to occur if they are injected at an RF phase of $\varphi \approx 90°$.[6] However, since the electrons have speeds lower than *c* upon injection from an electron gun, there is a restriction as to the minimum axial electric field strength required to give the injected electrons the impulse required to achieve the required acceleration before the RF polarity reverses. The minimum axial electric field strength is given in Eq. 2.79 with β_i representing the normalized particle injection velocity and λ representing the RF wavelength

$$E_o = \frac{2\pi mc^2}{q\lambda}\sqrt{\frac{1 - \beta_i}{1 + \beta_i}}.$$

(2.79)

Equation 2.79 shows that the lower the initial particle velocity, the larger the axial electric field is required to be.

2.3.3   Transverse particle dynamics

The cavity geometry for a linear accelerator is typically designed to maximize the effective shunt impedance. These optimized cavity geometries have the effect of producing radial RF fields that tend to create transverse focusing and defocusing fields as seen in Figure 2.11.
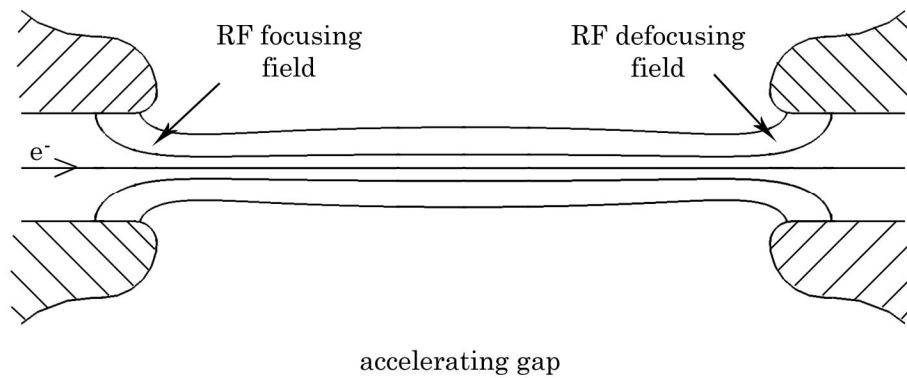
Figure 2.11: Transverse RF fields due to the cavity geometry maximizing shunt impedance.

Three mechanisms play a role when considering the net radial impulse imparted to a charged particle beam as it traverses a linac cavity. First, the radial fields vary with the radial particle displacement. Second, the fields vary in time as the particle crosses the cavity, and third, particle velocities change over the course of one cavity so the charged particles spend different amounts of time in the first half of the cavity compared to the second. The third mechanism has the exception of electrons within the ultrarelativistic regime ($\gamma \gg 1$) where their velocities do not change appreciably over the course of one cavity. In fact, by considering Laplace's equation, it can be shown that if there is longitudinal focusing at a point, the two transverse components cannot also be focusing at that point.

For electron linacs, which are of most concern for this thesis, the electrons gain a large amount of momentum over the accelerating gap at the beginning of

the linac. With a negative synchronous phase, the RF field is rising in time creating longitudinal bunching or focusing. The radial focusing field experienced by the electron as it enters the cavity will be smaller than the defocusing field experienced at the cavity exit due to the time varying nature of the RF field. However, since the electron gains a large amount of momentum, it spends less time at the exit than at the entrance creating a net focusing force. This is called electrostatic focusing.

    A description of the transverse dynamics of a charged particle beam at a point in time or space can be expressed through the use of a phase space plot which is generated with the beams position x on the abscissa and the divergence parameter x' on the ordinate axis. The phase space plot of a real charged particle beam has ill defined edges making it difficult to fully quantify analytically. However, an approximation to its shape in a phase space plot can be performed by outlining an ellipse based on the beam's root-mean-square (rms) values. An example of this type of ellipse is given in Figure 2.12.
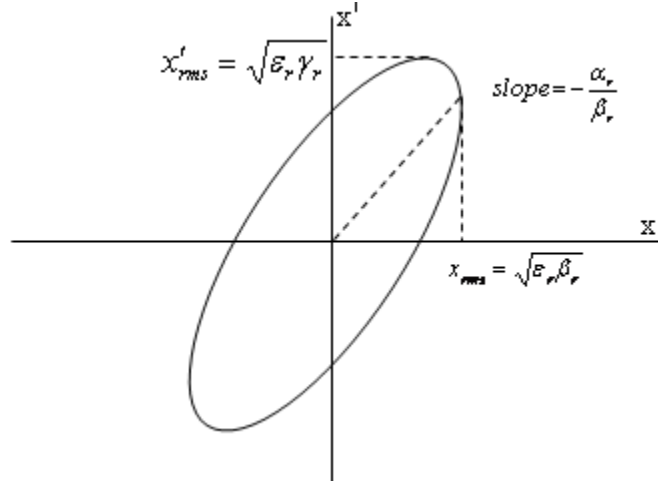
Figure 2.12: A transverse phase space ellipse defined by the Courant-Snyder parameters.

In Figure 2.12, α_r, β_r, γ_r, and ε_r are Courant-Snyder parameters. The first three parameters are related through the following,

$$1 = \gamma_r \beta_r - \alpha_r^2 \qquad\qquad (2.80)$$

and the parameter ε_r, known as the rms emittance, is defined as

$$\varepsilon_r = \sqrt{\overline{x^2 x'^2} - \overline{xx'}^2} \ .$$

(2.81)

The rms emittance can be understood geometrically as being proportional to the area of the ellipse in a 2D phase space plot.

With emittance quantified another important concept is emittance growth. Emittance growth can arise from two main factors in addition to RF defocusing. The first can be explained through the following example. If at one location within the linac the charged particle beam has an rms emittance of ε_1 and is diverging away from the central axis, further down the linac, the emittance will have grown to ε_2 where $\varepsilon_1 < \varepsilon_2$. This form of emittance growth is simply caused by the trajectories of the charged particle beam. The second factor contributing to emittance growth arises from space charge forces. A beam of identical particles accelerating within a linear accelerator is confined in space. Since the beam is composed of particles of like charge, they will repel each other according to Coulomb's law. This repulsive force is known as a space charge force and is non negligible for all but ultrarelativistic electrons where their beam generated magnetic field cancels the space charge repulsive force. Emittance growth in general needs to be reduced to minimize beam loss as the charge particle beam accelerates within the linac. Minimization of emittance growth can be performed through external focusing elements such as solenoids, quadrupoles, and RF quadrupole elements. However, if high intensity, high brightness beams are not required, no external focusing may be necessary provided the linac is sufficiently short.

2.3.4   Beam loading and wakefields

The general idea behind beam loading and wakefield generation comes from the charged particle beam generating its own electric and magnetic fields. These fields interact with the generator induced fields changing the net field within an accelerating cavity. The presence of the charged particle beam induces charges on the cavity walls which then generate their own fields that work back on the beam. The induced fields can resonate at the accelerating mode, and at

higher order modes. Resonance of higher order modes can lead to mode mixing and increase power loss through Joule heating of the cavity walls. Beam loading is the effect of the induced field on the accelerating mode. The net accelerating field is then a superposition of the generator induced field minus the beam loading field. The fundamental theorem of beam loading states that the induced voltage experienced by a charge is half of the induced voltage the particle leaves in the cavity. Thus beam loading tends to reduce the maximum energy gain of a charged particle beam in a SW linac according to

$$\Delta W = \frac{2\sqrt{\beta_c \, \mathrm{ZLP_1}}}{1+\beta_c} - \frac{IZL}{1+\beta_c} \tag{2.82}$$

where I is the charged particle beam current and β_c is the waveguide-cavity coupling coefficient. The waveguide-cavity coupling coefficient β_c is equivalent to the voltage standing wave ratio (VSWR) in the over-coupled regime.[6] The VSWR is calculated in the simulation of the linac waveguide using the FEM (section 3.2.3).

Wakefields are more of a concern for ultrarelativistic electrons since at $v<c$ the major concern is the space charge fields. However at $v\approx c$, space charge fields are largely canceled due to beam generated magnetic fields. The beam generated electric field is highly Lorentz contracted and scatters when encountering geometric variations such as when the electrons leave the accelerating gap seen in Figure 2.11 and enter the drift tube. This scattered radiation interacts with electrons trailing in the same bunch as well as with electrons in subsequent bunches. The scattered radiation (wakefield) can be broken up into short range and long range effects. Short range wakefields are of high frequency and act on the trailing electrons of the bunch that generated the wakefields. Short range wakefields lead to parasitic losses in energy, increased energy spread and may lead to single bunch beam break up (BBU). Single bunch BBU is caused when the wakefields induce betatron oscillations in trailing off axis electrons. Since these wakefields are of high frequency, they are above the frequency cutoff of the drift tube meaning they continue to trail the same electron

bunch throughout the linac over time. Thus the oscillations can continue to grow in magnitude over time until the electrons are lost on the cavity walls. Long range wakefields are of lower frequency and are below the cutoff frequency of the drift tube and so cannot continue to trail the same electron bunch. They can however be carried from cavity to cavity through the strong cavity to cavity coupling. Long range wakefields are long lasting since they resonate for a time

$$\tau = \frac{2Q}{\omega} \tag{2.83}$$

where Q is the cavity Q factor and ω is the cavity resonant frequency. Thus long range wakefields can affect subsequent bunches leading to multibunch BBU.

2.3.5   Electron injectors

The characteristics of the beam injected into a linac can have a great effect on its evolution through the linac. For medical linacs, electron guns are used as injectors. A current is run through a resistive wire in the cathode giving the electrons sufficient energy to overcome the work function of the metal ejecting them into the electron gun. When a large negative potential is placed on the cathode, the electrons accelerate towards the linac being focused by the electrostatic fields shaped by the gun geometry. As greater numbers of electrons are ejected from the cathode, a larger Coulomb repulsive force at the cathode appears due to the existence of a space charge 'cloud'. When a sufficient amount of current exists in front of the cathode, further increases in cathode temperature yield no greater emission of electrons since the repulsive space charge force dominates. At this point, the electron gun is said to be space charge limited and Child's law completely describes the electron current density j_e emitted from the cathode based solely on the potential V and the normal sampling distance d which is much smaller than the radius of curvature of the cathode,

$$j_e = \frac{4\varepsilon_o}{9} \sqrt{\frac{2q}{m_e}} \frac{V^{3/2}}{d^2} . \tag{2.84}$$

In Eq. 2.84, m_e is the electron mass and q is the electronic charge. Child's law is a common emission model for electron guns, specifically when exact information

about cathode temperature and work function is unknown (which is the case for this work). It was found that the difference between Child's law, and the more accurate Fowler-Nordheim field emission model[23] (which required an estimate of cathode temperature and work function) was less than 1% for the simulations performed in OPERA-3d/SCALA (section 2.4.3). Electron gun geometries come in many forms depending on its application, but many, including the gun designed for this work, are based on the Pierce diode[22, 24].

2.4   NUMERICAL PARTICLE SIMULATIONS

Numerical particle simulations were an important part of this work. The numerical methods applied by the various particle simulation programs used in this work can all be categorized as a form of Particle Mesh (PM) simulation. The programs used ranged from the axisymmetric 2D FD beamlet electron gun program EGN2w[25] to the 3D FEM beamlet program Opera-3d/SCALA, to the particle-in-cell (PIC) program 'phase and radial motion in electron linear accelerators' (PARMELA)[26]. The general algorithm for each program will be discussed separately.

2.4.1   Governing equations

The general equations that describe an ideal plasma model are Maxwell's equations (Eq. 2.1 – 2.4), Poisson's equation (Eq. 2.12), the Lorentz force equation (Eq. 2.7), and the Vlasov equation

$$\frac{df}{dt} = \frac{\partial f}{\partial t} + \mathbf{v} \cdot \frac{\partial f}{\partial \mathbf{x}} + \frac{\mathbf{F}}{m} \cdot \frac{\partial f}{\partial \mathbf{v}} = 0 . \tag{2.85}$$

Although the variable $f=f(x,v,t)$ in Eq. 2.85 corresponds to a generic particle probability distribution, the work presented in this thesis assumes it to be an electron distribution. The distribution describes the probability of an electron being near the position $\mathbf{x}$ with approximately the velocity $\mathbf{v}$ at a time t. The self-consistent electromagnetic field depends in a complex way on the electron distribution function. The above mentioned system of equations is known as the Vlasov-Maxwell system of equations.

If the x-v phase space is divided up into a regular array of infinitesimal volume cells such that not more than one electron exists within a cell, then *f(x,v,t)dxdv* gives the probability that the cell is occupied at a given time. If an electron is in a cell (**x**,**v**) at time *t* then there will be one in the cell (**x'**,**v'**) at time *t'* according to the equations of motion

$$\mathbf{x'} = \mathbf{x} + \int_t^{t'} \mathbf{v}\, dt \tag{2.86}$$

$$\mathbf{v'} = \mathbf{v} + \int_t^{t'} \frac{\mathbf{F}}{m}\, dt \tag{2.87}$$

and

$$f(\mathbf{x'}, \mathbf{v'}, t') = f(\mathbf{x}, \mathbf{v}, t). \tag{2.88}$$

Equations 2.86 and 2.87 are nothing more than a restatement of the Vlasov equation (Eq. 2.85) as can be seen by Taylor expanding Eq. 2.88 and taking the limit as *(t'-t)* goes to zero. Mapping *f* for every infinitesimal cell is computationally impossible, so instead sample points of the distribution function are used each of which represents an element *i* of the phase fluid corresponding to $N_s = \int_i f\, d\mathbf{x} d\mathbf{v}$ plasma electrons per unit volume. The governing equations of motion for the ensemble of plasma electrons per unit volume (given by Eqs. 2.86 and 2.87) are rewritten below in relativistic differential form

$$\mathbf{v}_i = \frac{d\mathbf{x}_i}{dt}\Big|_i ,$$

$$\mathbf{F}_i = M_i \frac{d(\gamma_i \mathbf{v}_i)}{dt} \tag{2.89a}$$

$$\gamma_i = \frac{1}{\sqrt{1 - \dfrac{v_i^2}{c^2}}}. \tag{2.89b}$$

In Eq. 2.89 $M_i = N_s m_e$, with m_e representing the electron rest mass, $\mathbf{F}_i$ is the Lorentz force (Eq. 2.7) and γ_i is the relativistic factor. Equation 2.89 is the 'superparticle' representation of the equations of motion for electron plasmas. However, in the simulations performed in this work, the calculations are performed in a space

charge dominated regime where the collective plasma effects are minimal. This is not the case in general when electron plasmas undergo oscillations due to a restoring force (e.g. from lattice ions in a conductor).

2.4.2 EGN2w

The electron gun program EGN2w performs a simple central difference approach on square grids (section 2.2.1.1) to discretized Poisson's (or Laplace's) equation[25]. With a defined geometry and boundary conditions, EGN2s first solves Laplace's equation (Eq. 2.12). Then, the current density for a user specified number of macroparticles (or 'beamlets') is calculated using Child's law (Eq. 2.84) from the solved electrostatic potential. Each beamlet is associated with an area of the cathode surface which depends on the radial distance of the beamlet. The current associated with the beamlet is simply found by multiplying the current density with its associated area. The total current in the beam is then found by simply summing the current of each beamlet together. The electric field is calculated from the solved potential using a central difference approximation to Eq. 2.10 with the radial component of the electric field reduced by a factor of 2 for the first iteration. This avoids over-focusing the beam since no space charge is initially calculated. The relativistic kinematic equations (Eq. 2.89) are solved using an explicit fourth-order Runge-Kutta method[27, 28],

$$
\begin{aligned}
\mathbf{k}_1 &= f\left(t^n, \mathbf{x}^n\right) \\
\mathbf{k}_2 &= f\left(t^n + \frac{1}{2}\Delta t, \mathbf{x}^n + \frac{1}{2}\mathbf{k}_1\right) \\
\mathbf{k}_3 &= f\left(t^n + \frac{1}{2}\Delta t, \mathbf{x}^n + \frac{1}{2}\mathbf{k}_2\right) \\
\mathbf{k}_4 &= f\left(t^n + \Delta t, \mathbf{x}^n + \mathbf{k}_3\right) \\
\mathbf{x}^{n+1} &= \mathbf{x}^n + \frac{1}{6}\left(\mathbf{k}_1 + 2\mathbf{k}_2 + 2\mathbf{k}_3 + \mathbf{k}_4\right).
\end{aligned}
\tag{2.90}
$$

From the second iteration onwards, space charge is calculated and used for the subsequent determination of emission current and beamlet trajectories. Space charge is calculated through a charge assignment scheme that interpolates a

fraction of the total current within a square cell (from all beamlets crossing that cell) to the cell vertices. The fraction of the total current at each vertex is proportional to the inverse distance from the beamlet. The space charge density can then be derived at each vertex from the fractional current I_i[25]

$$\rho_i = \frac{I_i}{a_i \cdot v_{z,i}}$$ (2.91)

from which an updated electrostatic potential including space charge is found by solving Poisson's equation (Eq. 2.12). In Eq. 2.91, a_i represents the area associated with each beamlet and $v_{z,i}$ is the z velocity. The updated electrostatic potential (including space charge) is used in Child's law for to solve for the emission current and the process repeats for a set number of iterations. It was found that after nine iterations, the beam current converged to a stable solution.

2.4.3   OPERA-3d/SCALA

The foundation of the OPERA-3d/SCALA algorithm is the FEM. Once the geometry is defined and the boundary conditions are set, OPERA-3d/SCALA solves Laplace's equation (Eq. 2.12) for the electrostatic potential using the FEM (given in section 2.2.2). The electric field is then calculated from the solved potential Φ_i^e using Galkerkin's method to discretized Eq. 2.10

$$\int_{\Omega_e} \varphi_i^e E_i^e d\Omega_e = \int_{\Omega_e} \varphi_i^e \nabla\left(\varphi_j^e \Phi_j^e\right) d\Omega_e$$ (2.92)

where φ_i^e is the same basis function used in calculating the potential (section 2.2.2.2).

The current density for each beamlet emitted off the cathode is calculated using Child's law (Eq. 2.84) and the current is calculated by multiplying the result with the cathode area associated with each beamlet (in the same manner as EGN2w). The beamlets trajectories are then determined by solving Eq. 2.89 subject to the electric fields using a Runge-Kutta-Merson fifth order integration scheme[29, 30] initially with no space charge. The value R in Eq. 2.93d provides an estimate of the error in the integration which is used for automatic selection of the integration step. If the desired integration accuracy is ε the algorithm for

determining the integration step is as follows. If $R > \varepsilon$, divide the integration step by 2, if $R < \varepsilon/64$ double it, otherwise the integration step is satisfactory. Once the integration step has been chosen, Eq. 2.93c is used to performing the actual integration.

$$\mathbf{k}_1 = f\left(t^n, \mathbf{x}^n\right)$$

$$\mathbf{k}_2 = f\left(t^n + \frac{1}{3}\Delta t, \mathbf{x}^n + \frac{1}{3}\mathbf{k}_1\right)$$

$$\mathbf{k}_3 = f\left(t^n + \frac{1}{3}\Delta t, \mathbf{x}^n + \frac{1}{6}\mathbf{k}_1 + \frac{1}{6}\mathbf{k}_2\right) \tag{2.93a}$$

$$\mathbf{k}_4 = f\left(t^n + \frac{1}{2}\Delta t, \mathbf{x}^n + \frac{1}{8}\mathbf{k}_1 + \frac{3}{8}\mathbf{k}_3\right)$$

$$\mathbf{k}_5 = f\left(t^n + \Delta t, \mathbf{x}^n + \frac{1}{2}\mathbf{k}_1 - \frac{3}{2}\mathbf{k}_3 + 2\mathbf{k}_4\right)$$

$$\mathbf{x}_1^{n+1} = \mathbf{x}^n + \frac{1}{6}\mathbf{k}_1 + \frac{2}{3}\mathbf{k}_4 + \frac{1}{6}\mathbf{k}_5 \tag{2.93b}$$

$$\mathbf{x}_2^{n+1} = \mathbf{x}^n + \frac{1}{10}\mathbf{k}_1 + \frac{3}{10}\mathbf{k}_3 + \frac{2}{5}\mathbf{k}_4 + \frac{1}{5}\mathbf{k}_5 \tag{2.93c}$$

$$R = 0.2\left|\mathbf{x}_2^{n+1} - \mathbf{x}_1^{n+1}\right|. \tag{2.93d}$$

Once the initial beamlet trajectories have been calculated, space charge is solved by calculating the current that intersects a 'dual grid' of the FEM mesh. The dual grid is produced by generated normal bisectors of all the edges in the mesh element where the bisectors all meet at the circumcenter of the element. An example of a 2D FEM mesh element and the dual grid is shown in Figure 2.13. The dual grid divides up each element into sub-elements (A, B and C in Figure 2.13). The charge density ρ_i resulting from the beamlet current I_i is calculated from

$$\rho_i = \frac{1}{\Delta^{sub}}\int_1^2 \frac{I_i}{|\mathbf{v}_i|}ds \tag{2.94}$$

where Δ^{sub} is the volume of the sub-element and $\mathbf{v}_i$ is the velocity of the beamlet as it crosses the sub-element. The total charge density within the sub-element ρ_{sub}

is found by summing all the beamlet charge densities together. Eq. 2.58 is then obtained by

$$\int_{\Omega_e} \rho \varphi_i^e \, d\Omega_e = \sum_{sub-elements} \int_{\Omega_{sub}} \rho_{sub} \varphi_i^e \, d\Omega_{sub} \, . \tag{2.95}$$

The calculation of space charge and beamlet trajectory is continued until the emission current calculated from Child's law for the current iteration is identical to the last iteration within a predefined value.
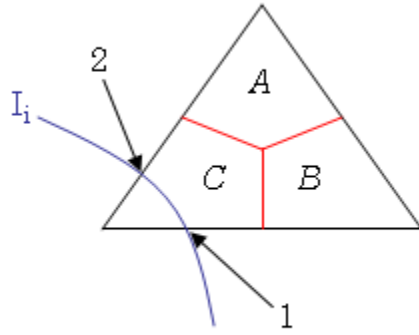
Figure 2.13: The dual grid (in 2D) used for the SCALA space charge calculations is given along with a representative beamlet intersecting a sub element.

2.4.4 PARMELA

Unlike EGN2w and OPERA-3d/SCALA, PARMELA uses a PIC approach[31] to calculate space charge and electron trajectories. PARMELA discretizes Eq. 2.89 using the leapfrog approach,

$$\mathbf{v}_i^{n+1/2} \Delta t = \mathbf{x}_i^{n+1} - \mathbf{x}_i^n$$

$$\left(\frac{q_i}{M_i} \mathbf{E}_i^n + \mathbf{v}_i^n \times \Omega_i^n \right) \Delta t = \gamma_i^{n+1/2} \mathbf{v}_i^{n+1/2} - \gamma_i^{n-1/2} \mathbf{v}_i^{n-1/2} \tag{2.96a}$$

$$\Omega_i^n = \frac{q_i \mathbf{B}_i^n}{M_i} \tag{2.96b}$$

where the superscript n refers to time, and the subscript i refers to position.

Before Eq. 2.96 can be applied to determine the particle motions, the space charge field needs to be calculated in order to obtain self consistent forces.

The PIC algorithm applied by PARMELA for its 3D space charge calculation can be separated into three parts. The first is charge assignment where the charge density is determined at specified cell points. The second is field solution in which the space charge electric field generated by the calculated charge density is obtained. The third is force interpolation and electron trajectory calculation. Force interpolation is where the force calculated at the cell points is interpolated back to the original particle positions. The leap-frog scheme (Eq. 2.96) is then used to calculate the particle trajectories subject to the self consistent forces generated by the space charge field and any other external fields.

The 3D space charge routine used in PARMELA is based on the PIC algorithm by Qiang *et al.*[32] Charge assignment is performed using the assignment function *W(x)*

$$W(x) = \prod\left(\frac{x}{H}\right) * S(x). \tag{2.97}$$

Eq. 2.97 represents a 1D charge assignment function where *H* is the mesh size and *S(x)* is the cloud shape function and $\prod$ is the top hat function[31]. The 3D charge assignment function is simply

$$W(x, y, z) = W(x)W(y)W(z). \tag{2.98}$$

The cloud shape function *S(x)* used by PARMELA is a cloud-in-cell (CIC) function defined by

$$S(x) = \frac{1}{H}\prod\left(\frac{x}{H}\right). \tag{2.99}$$

The charge assignment function using a CIC shape function, known as a CIC scheme, is a continuous piecewise linear function used to distribute charge between eight cell points in 3D. The forces calculated using the CIC scheme are fairly smooth reducing amplitude fluctuations in interparticle forces as electrons move with respect to each other and the mesh. Any errors that do arise are localized spatially to a large extent reducing their global effects. Higher order charge assignment schemes exist that further reduce interparticle force

fluctuations, but at the expense of greater complexity, and need to assign charge to a greater number of cell points.

The errors that can arise due to the discrete nature of the simulation place two major constraints on the simulation. The first constraint is the long range constraint which amounts to the minimization of electric potential fluctuations (leading to force fluctuations) for particles with large separations. The second constraint is the smoothness constraint which requires the minimization of potential fluctuations for small particle separations. This constraint amounts to a requirement for continuous assignment functions and their derivatives. Although both of these constraints are more easily met through the use of higher order assignment functions, the simple CIC scheme used by PARMELA meets the above constraints sufficiently to produce an accurate solution[33] and has been used to design accelerators in the past.[34, 35]

Charge assignment can be described as a convolution (as seen in Eq. 2.97) and sampling. The Fourier transform of the charge density within a cell shows aliasing in k space since it is not infinite in extent and is only defined over a finite number of cell points (eight in 3D). The aliasing causes a loss of displacement invariance which causes fluctuations in the total mesh defined charge density. Depending on the exact aliasing present, too much or too little total charge can be defined at one cell point while the opposite effect appears at a near cell point. These fluctuations lead to non-physical charge fluctuations and interparticle forces. This aliasing effect is known as mode coupling which leads to a violation of the long range and smoothness constraints to some extent. The application of the assignment function leads to a widening of the charge density ρ. If ρ is band limited, the application of a sharpening operator $L = \left[\hat{W}(k) \right]^{-1}$ can almost completely recover the physical charge density provided the mesh spacing is not too large to cause further aliasing. Unfortunately a band limited charge density would require assignment to all cell points, which is impractical. Thus the accuracy of the numerical solution is directly related to the degree of aliasing in the solution placing a constraint on the maximum mesh size.

After charge assignment, PARMELA calculates the space charge potential through the use of Green's function[9] using the convolution method[31]. The potential at a mesh point (x,y,z) can always be written as a sum of contributions from all other sources at points (x',y',z'),

$$\varphi_{x,y,z} = \sum G_{x-x',y-y',z-z'} \rho_{x',y',z'} \ .$$ (2.100)

The Fourier transform of Eq. 2.100 gives

$$\hat{\varphi}_{k,l,m} = \hat{G}_{k,l,m} \hat{\rho}_{k,l,m} .$$ (2.101)

The interaction potential G (Green's function) is written on the mesh at each cell point for a unit charge at the origin and the solution is saved in memory. At each time step $\hat{\rho}$ is determined from which $\hat{\varphi}$ is calculated. The potential φ is then obtained through the inverse Fourier transform of $\hat{\varphi}$. It should be noted that when solving for an isolated system requiring open boundary conditions, eight times more mesh is required to calculate G initially to ensure it approximately goes to zero at infinity. Even though only one quarter of the mesh generated is actually used for charge assignment and calculation purposes, this method requires eight times more storage for G. The space charge electric field is then solved from the space charge potential using a central difference scheme.

Force interpolation is performed using the same CIC scheme in order to conserve momentum and eliminate the generation of unphysical self forces[31]. After the application of the CIC scheme to interpolate the forces back to the particle positions, the same sharpening operator L is used and Eq. 2.96 is then used to determine the particle motions.

2.5 MONTE CARLO SIMULATIONS

The name "Monte Carlo" was set by physicists working on the Manhattan Project in the 1940's to describe a class of numerical techniques that rely on the use of random numbers. In Monte Carlo simulations of radiation transport, a particle track is considered to be a random sequence of free motion with an interaction event at a location where the particle changes direction, losses energy,

or creates a secondary particle. The interaction events are determined by the differential cross sections (DCS) which form the probability distribution functions (PDF). Radiation transport can be broken down into three distinct categories, (1) the free path between interactions, (2) type of interaction event, and (3) energy loss and angular deflection of the primary particle along with the initial state of any secondary particles if they were created. The Monte Carlo method gives the same information as the solution to the Boltzmann transport equation but is easier to implement, especially for complex geometries.[36] Not all interactions are calculated in most Monte Carlo simulation in order to improve the calculation efficiency. For the work presented here for example, Rayleigh scattering and atomic relaxations were not simulated since their effect is only significant for low energy applications (< 1 MeV).[37]

2.5.1   Sampling techniques

A key component in the Monte Carlo simulation process is the sampling of the PDF that describe the DCS. A cumulative distribution function (CDF) is defined by

$$CDF = \int_{x_{min}}^{x} PDF(x')dx'.$$

(2.102)

The CDF is defined as a monotonically increasing function where $0 \leq CDF \leq 1$ which is always true when $PDF \geq 0$. Sampling of the CDF can be performed using the inverse-transform method which requires the inverse of the CDF to be calculated. Thus

$$\xi = CDF(x)$$
$$x = CDF^{-1}(\xi)$$

(2.103)

and $0 \leq \xi \leq 1$. In this method ξ can be represented by a uniform random number. The calculation of the CDF and its inverse can only be done analytically for simple PDF. For more complex PDF, a numerical integration is required to define the CDF, and more importantly its inverse. The numeric solution is typically pre-calculated for speed and stored in a table in memory. When a numerical solution

to the inverse CDF is pre-calculated and stored, an interpolation method is also required to sample between the discrete values stored in memory. The interpolation method is required to have sufficient accuracy to ensure its error is negligible, and should be fast.

An alternative to the numeric integration of complex PDF together with the data storage and interpolation requirements of the inverse transform method is the rejection method. This method is used in the EGSnrc Monte Carlo algorithm. The foundation of the rejection method is the sampling a PDF π which is different and much simpler than the originally complex PDF p. An additional sampling of the function r is then performed to determine whether the result of sampling π is accepted or not. Mathematically the rejection method is

$$p = C \pi \, r \tag{2.104}$$

where C is a positive constant that satisfies $C\pi \geq p$ and $0 \leq r \leq 1$. The rejection method algorithm is as follows:

(1) generate a random value x from π using a random number ξ_1

(2) generate another random number ξ_2

(3) if $\xi_2 > r(\xi_1)$ go back to (1)

(4) otherwise deliver x

The advantage of the rejection method is that it's simple and no interpolation is required reducing the error. The drawbacks however are its poorer efficiency, calculated to be 1/C and the requirement for two random numbers to sample one PDF.

2.5.2   EGSnrc photon transport

The first step of photon transport is to decide the distance to the next interaction site. The distance to the interaction site is determined from the Beer–Lambert law

$$N = N_o e^{-\mu x} \tag{2.105}$$

where μ is the linear attenuation coefficient and x is the path length. The photon is considered to undergo free motion with no interactions along the path length. At

the interaction site, which interaction takes place is determined by sampling the relevant DCS. The main DCS in EGSnrc which are relevant are: (1) Rayleigh scattering, (2) photoelectric absorption, (3) Compton scattering, and (4) pair/triplet production. A thorough discussion of these DCS is given in the book by Johns and Cunningham[38] and their application to EGSnrc is given by Kawrakow[37]. The photon energy and the initial state of secondary particles (if any) are then set according to the relevant DCS.

2.5.3   EGSnrc charged particle transport

Charged particle transport makes use of a 'condensed history' where multiple small interactions causing the particle's random walk are set into a single interaction. At this interaction, the energy and direction of the charged particle are altered by sampling the appropriate multiple scattering distributions. EGSnrc (based on the EGS4 code)[39] implements a Class II condensed history in which bremsstrahlung photons created with an energy above k_c and inelastic collisions that set in motion atomic electrons with energy above T_c are modeled explicitly. Both k_c and T_c are user defined parameters and interactions with energies greater than these are known as catastrophic interactions. Sub-threshold energy losses are described by the continuously slowing down approximation (CSDA)[38] in EGSnrc. Thus the process for charged particle transport is as follows: (1) sample the energy at which the next catastrophic event takes place, (2) modify the particle energy, position and direction caused by multiple 'soft' interactions using the CSDA and multiple scattering theory[40, 41], (3) at the catastrophic interaction site, select the interaction type from the total interaction cross section, and (4) at the current position and energy, determine energy and direction changes of the parent particle as well as the initial state of any secondary particles by sampling the appropriate DCS.

The default charged particle transport algorithm in EGSnrc is divided into two sub-steps where the scattering angles θ_1, φ_1 and θ_2, φ_2 are sampled according to the multiple scattering theory. The final scattering angle is determined from the scattering angles at each of the sub-steps and the particle positions and energy

losses are altered accordingly. When spin effects are included in the scattering calculations, if the step size between catastrophic interactions is restricted to 25% energy loss, the accuracy of the multiple scattering algorithm is better than 0.1%.[37] Although the accuracy of the EGSnrc code has been proven in the literature in the past through multiple validations against measurement, its accuracy in a magnetic field (as applied to linac-MR systems) is yet unknown since no direct measurement has been made. However, through comparison with other Monte Carlo radiation transport programs, it has been shown to be highly accurate.[42] It should be noted that in this work, no magnetic field was placed on the Monte Carlo simulations in order to focus on its effect on the linac.

Since multiple scattering theory assumes the scattering occurs in one medium, boundary crossings between media have to be treated differently. EGSnrc uses an exact boundary crossing algorithm which switches from multiple scattering theory to single elastic scattering at a distance of t_{min}, chosen to be three elastic mean free paths for efficiency[37]. The smaller step size of the single scattering mode reduces the error as the charged particle crosses the boundary from one medium to another.

2.5.4   Variance reduction

Variance reduction describes a class of techniques that reduces the statistical variance of the Monte Carlo solution in efficient ways. The statistical noise, or variance, in a Monte Carlo solution is reduced by generating larger and larger numbers of particles in the region of interest. A review of variance reduction techniques in radiation transport has been given by Bielajew and Rogers[43]. Directly tracking more and more particles is computationally expensive and time consuming. An alternative to this computationally expensive operation is particle splitting. Particle splitting is one class of variance reduction techniques and was used in the Monte Carlo simulations presented in this work. Specifically, in the EGSnrc code, directional bremsstrahlung splitting (DBS) was used[44]. When a bremsstrahlung photon is generated, DBS generates not one, but NBRSPL

photons, set by the user, each of whose direction is determined by sampling the leading term of the Koch-Motz distribution[37, 41]. The user also defines the field of interest, and the photons not directed into this field are eliminated through Russian roulette. All the photons directed into the field of interest are given a weight 1/NBRSPL while the photons directed outside the field of interest that survive the Russian roulette are fat (i.e. given a weight of one). To improve the efficiency of the DBS routine, instead of looping over each NBRSPL photon, a subroutine is called that pre-calculates the number of photons directed into the field and only simulates these photons. It also samples the angle of a photon from the full distributions and if that angle is not directed into the field, a single fat photon is created and tracked.

If a photon generated through the DBS routine is about to undergo a Compton interaction, Russian roulette is played on the photon, and if it survives, becomes a fat photon. The treatment is different if the Compton interaction occurs in a gas to prevent the creation of a large number of fat photons just above the region of interest[44]. The fat photon creates a fat electron, and Russian roulette is played on the scattered photon if it is directed outside the field of interest. With this method, all electrons created through Compton scattering of DBS created photons are fat, and thus electron splitting is also used to split each fat electron into NBRSPL electrons with a weight of 1/NBRSPL. Russian roulette is played on electrons that are directed away from the field on interest. A more detail description of the DBS routine is given by Kawrakow *et al*[44].

2.6   REFERENCES

[1] T. B. A. Senior, "Impedance boundary conditions for imperfectly conducting surfaces," Appl. Sci. Res., **8**, 418-436 (1960).

[2] J. Jin, *The finite element method in electromagnetics* (John Wiley & Sons Inc., New York, 2002).

[3] G. B. Arfken, and H. J. Weber, *Mathematical methods for physicists* (Academic Press, San Diego, 1995).

[4] R. E. Collins, *Field theory of guided waves* (McGraw-Hill, New York, 1960).

[5] J. C. Slater, *Microwave electronics* (D. Van Nostrand Company Inc., New York, 1950).

[6] T. P. Wangler, *RF linear accelerators* (Wiley-VCH, Weinheim, 2008).

[7] R. H. Helm, and R. Miller, "Particle dynamics,"in *Linear Accelerators*, eds. P. M. Lapostolle, and A. L. Septier (North Holland Pub. Co., Amsterdam, 1970).

[8] D. E. Nagle, E. A. Knapp, and B. C. Knapp, "Coupled resonator model for standing wave accelerator tanks," Rev. Sci. Instrum., **38**, 1583-1587 (1967).

[9] D. J. Jackson, *Classical Electrodynamics* (John Wiley & Sons, Inc., USA, 1999).

[10] H. A. Bethe, "Theory of diffraction by small holes," Phys. Rev., **66**, 163-182 (1944).

[11] J. Gao, "Analytical formulas for the resonant frequency changes due to opening aperatures on cavity walls," Nucl. Instrum. Methods Phys. Res. Sect. A-Accel. Spectrom. Dect. Assoc. Equip., **311**, 437-443 (1992).

[12] H. Halbach, and R. F. Holsinger, "Superfish - a computer program for evaluation of RF cavities with cylindrical symmetry," Part. Accel., **7**, 213-222 (1976).

[13] A. M. Winslow, "Numerical solution of the quasilinear Poisson equation in a nonuniform triangle mesh," J. Comput. Phys., **1**, 149-172 (1966).

[14] B. Delaunay, "Sur la sphére vide," Izvestia Akademii Nauk SSSR, Otdelenie Matematicheskikh i Estestvennykh Nauk, **7**, 793-800 (1934).

[15] O. C. Zienkiewicz, and D. V. Phillips, "An automatic mesh generation scheme for plane and curved surfaces by lsquoisoparametricrsquo co-ordinates," International Journal for Numerical Methods in Engineering, **3**, 519-528 (1971).

[16] J. C. Nedelec, "A new family of mixed finite-elements in R3," Numerische Mathematik, **50**, 57-81 (1986).

[17] O. Schenk, and K. Gärtner, "Solving unsymmetric sparse systems of linear equations with PARDISO," Future Generation Computer Systems, **20**, 475-487 (2004).

[18] O. Schenk, and K. Gartner, "On fast factorization pivoting methods for sparse symmetric indefinite systems," ETNA, **23**, 158-179 (2006).

[19] R. B. Lehoucq, D. C. Sorensen, and C. Yang, "ARPACK Users' Guide: Solution of Large-Scale Eigenvalue Problems with Implicitly Restarted Arnoldi Methods", http://www.caam.rice.edu/software/ARPACK, 1997

[20] D. S. Kershaw, "Incomplete cholesky-conjugate gradient method for iterative solution of systems of linear equations," J. Comput. Phys., **26**, 43-65 (1978).

[21] S. Humphries, *Principles of charged particle acceleration* (John Wiley & Sons, USA, 1986).

[22] S. Humphries, *Charged particle beams* (John Wiley & Sons, USA, 1990).

[23] R. H. Fowler, and L. Nordheim, "Electron Emission in Intense Electric Fields," Proceedings of the Royal Society of London **119**, 173-181 (1928).

[24] J. R. Pierce, *Theory and design of electron beams* (D. Van Nostrand Co., New York, 1949).

[25] W. B. Herrmannsfeldt, "EGUN - An electron optics and gun design program," *SLAC-331-UC-28(A)*, 1988

[26] L. M. Young, "Parmela," *LA-UR-96-1835*, (L.A.N.L.,Los Alamos) 2005

[27] C. Runge, "Über die numerische Auflösung von Differentialgleichungen," Math. Ann., **46**, 167-178 (1895).

[28] W. Kutta, "Beitrag zur näherungsweisen Integration totaler Differentialgleichungen," Z. Math. Phys., **46**, 435-453 (1901).

[29] R. H. Merson, "An operational method for the study of integration processes" in Proc. Symp. Data processing, (Weapons Research Establishment, Salisbury, S. Australia, 1957).

[30] J. C. Butcher, *The numerical analysis of ordinary differential equations: Runge-Kutta and general linear methods* (John Wiley & Sons Ltd., Chichester, UK, 1987).

[31] R. W. Hockney, and J. W. Eastwood, *Computer simulations using particles* (Taylor & Francis Group, New York, 1988).

[32] J. Qiang, R. D. Ryne, S. Habib, and V. Decyk, "An object-oriented parallel particle-in-cell code for beam dynamics simulation in linear accelerators," J. Comput. Phys., **163**, 434-451 (2000).

[33] C. Limborg, P. R. Bolton, J. E. Clendenin, D. Dowell, S. Gierman, B. F. Murphy, and J. F. Schmerge, "Comparison of parmela simulations with longitudinal emittance measurements at the SLAC gun test facility,"in *Proceedings of the 2003 Particle Accelerator Conference, Vols 1-5*, eds. J. Chew, P. Lucas, and S. Webber (IEEE, Portland, OR, 2003), pp. 3216-3218.

[34] J. C. Goldstein, T.-S. F. Wang, and R. L. Sheffield, "INEX simulations of the optical performance of the AFEL," Nucl. Instrum. Methods Phys. Res. Sect. A-Accel. Spectrom. Dect. Assoc. Equip., **318**, 617-622 (1992).

[35] P. G. O'Shea, S. C. Bender, B. E. Carlsten, J. W. Early, D. W. Feldman, A. H. Lumpkin, R. B. Feldman, J. C. Goldstein, K. F. McKenna, R. Martineau, E. J. Pitcher, M. J. Schmitt, W. E. Stein, M. D. Wilke, and T. J. Zaugg, "Performance of the APEX free-electron laser at Los Alamos National Laboratory," Nucl. Instrum. Methods Phys. Res. Sect. A-Accel. Spectrom. Dect. Assoc. Equip., **331**, 62-68 (1993).

[36] M. J. Berger, "Monte Carlo calculation of the penetration and diffusion of fast charged particles,"in *Methods in Computational Physics*, eds. B. Alder, S. Fernbach, and M. Rotenberg (Academic Press, New York, 1963), pp. 135-215.

[37] I. Kawrakow, E. Mainegra-Hing, D. W. O. Rogers, F. Tessier, and B. R. B. Walters, "The EGSnrc code system: Monte Carlo simulation of electron and photon transport," *report PIRS-701*, (National Research Council of Canada,Ottawa) 2009

[38] H. E. Johns, and J. R. Cunningham, *The physics of radiology* (Charles C Thomas, Springfield, IL, 1983).

[39] W. R. Nelson, H. Hirayama, and D. W. O. Rogers, "The EGS4 code system," *SLAC-UC-32*, (Stanford Linear Accelerator Center,Stanford, CA) 1985

[40] I. Kawrakow, and A. F. Bielajew, "On the representation of electron multiple elastic-scattering distributions for Monte Carlo calculations," Nucl. Instrum. Methods Phys. Res. B, **134**, 325-336 (1998).

[41] I. Kawrakow, "Accurate condensed history Monte Carlo simulation of electron transport. I. EGSnrc, the new EGS4 version," Med. Phys., **27**, 485-498 (2000).

[42] C. Kirkby, T. Stanescu, S. Rathee, M. Carlone, B. Murray, and B. G. Fallone, "Patient dosimetry for hybrid MRI-radiotherapy systems," Med. Phys., **35**, 1019-1027 (2008).

[43] A. F. Bielajew, and D. W. O. Rogers, "Variance-reduction techniques,"in *Monte Carlo Transport of Electrons and Photons*, eds. T. M. Jenkins, W. R. Nelson, and A. Rindi (Plenum, New York, 1988), pp. 407-419.

[44] I. Kawrakow, D. W. O. Rogers, and B. R. B. Walters, "Large efficiency improvements in BEAMnrc using directional bremsstrahlung splitting," Med. Phys., **31**, 2883-2898 (2004).

CHAPTER 3: The design of a simulated in-line side-coupled 6 MV linear accelerator waveguide

3.1   INTRODUCTION

The modeling and optimization of linear accelerator cavities has been performed numerically for many decades using various software[1], however to date, this is the only full 3D electron linac medical waveguide simulation published. Before numeric calculations were performed, sections of the waveguide could be machined and redesigned numerous times before the optimal parameters were achieved. When considering numeric design programs, a common and popular choice is the axisymmetric 2D finite difference (FD) program Superfish. Superfish has been used in the design of axisymmetric waveguide systems[2-5] and through benchmarking has been shown to be highly accurate[6, 7]. This 2D software however is unable to fully model side-coupled waveguide systems due to its requirement for axisymmetric cavity designs. With the increasing power of personal computers, full 3D simulations have become available with a variety of numerical methods to solve Maxwell's equations which are capable of solving side-coupled systems. In many cases however, the design and optimization of a full waveguide from a 3D numerical simulation is unnecessary and impractical due to extremely large computational requirements of memory and time for long structures with many beamline components. In these cases, only a section of the waveguide is investigated through simulation[4, 8-12], and the results are typically compared to measurements using a prototype waveguide built from aluminum or 'cold model'. When modeling only sections of the linac waveguide at a time, the electron beam characteristics can only be determined within each section of the waveguide modeled separately. Since in this work the

electron dynamics within the entire waveguide is needed, a full 3D model
incorporating all aspects of waveguide design and coupling is required.

In order to accurately determine the electron trajectories within an in-line
side-coupled 6 MV medical linac waveguide, a full 3D waveguide model was
designed to ensure the simulated structure resonated at the appropriate frequency.
The design of the 3D waveguide began by creating an accelerating cavity which
emulates the characteristics of a commercial medical waveguide. The theory for
coupled cavity waveguide design as linear accelerators[13-16] and its coupling
effects[17-19] has been applied for a proton linac previously[8, 20-22], and now is
applied practically for the electron medical linac modeled here. This work
provides a concise 3D simulation design for an in-line side-coupled 6 MV linac
waveguide, and produces an RF field solution incorporating the effects of side
coupling.

3.2   METHODS AND MATERIALS

3.2.1   Theoretical foundation for waveguide cavity design

The theoretical foundation for designing each cavity to resonate at a
nominal frequency was taken from the lumped circuit model of a side-coupled
linear accelerator derived by Nagle[13] and explained in section 2.1.4. A side-
coupled linac is resonantly coupled with its coupling irises at a location of high
magnetic field and low electric field, where power is transferred from one cavity
to the next through mutual inductance. According to Slater's perturbation
formula[15] (Eq. 2.44) the introduction of a coupling iris in the location of a strong
magnetic field causes a decrease in the resonant frequency of the cavity, and more
generally any geometric change to the cavity will cause a shift in its resonant
frequency. As a simple approximation, referring to Eq. 2.35b of the lumped
circuit model in section 2.1.4, each cavity's resonant frequency squared is
inversely proportional to the inductance of the cavity L, and the cavity's
capacitance C. Slater's perturbation theory can then be simply understood by
considering that the introduction of a coupling iris increases the inductance which

in turn decreases the resonant frequency. In general, in order to recover a resonant frequency of 2998.5±0.1 MHz after the introduction, removal, or alteration of a coupling iris, the capacitance of the accelerating cavities was adjusted by changing the length of the nose cones, and the inductance was changed by altering the cavity diameter. In the side coupling cavities the only change required was to the capacitance of the cavity which was achieved by adjusting the post lengths.

3.2.2   Two-dimensional FD simulations

This work was aimed at emulating a Varian 600C linac waveguide. The dimensions of a single accelerating cavity published by Roy *et al.* in 1993[23] was redesigned using the 2D FD program Superfish which offered very fast simulations but was restricted to axisymmetric cavities. The Superfish mesh consisted of 7428 nodes of which 474 resided on the boundary where the nodes specify the triangles of the domain discretization with an average area of 5.25×10^{-4} cm^2. Using the exact dimensions from Roy *et al.*, it was found that the beam tube diameter as well as the effective shunt impedance (a measure of how well a waveguide works as a linear accelerator) was not identical to the Varian 600C waveguide. The accelerating cavity was thus redesigned by our group in order to achieve a beam tube diameter and approximate effective shunt impedance of 5 mm and 115 MΩ/m respectively,[1] which is consistent with a Varian 600C waveguide that achieves a nominal electron energy of 6 MeV. Since the effective shunt impedance of a simulated accelerating cavity is approximately 15% greater than a manufactured waveguide[1], the simulated accelerating cavity was designed to have an effective shunt impedance of 115 MΩ/m instead of the published 100 MΩ/m. Using this slightly larger value, the cavity geometry would give cavity dimensions that more closely approximated the manufactured waveguide.

3.2.3   Three-dimensional FEM waveguide simulation

The modified and optimized 2D design of the accelerating cavity was then reproduced in 3D using the finite element method (FEM) program COMSOL

Multiphysics. The 3D mesh was generated using isoparametric tetrahedral elements with cubic vector shape functions to obtain smooth field solutions with increased accuracy[24] and a port power of 2.3 MW was used. The resonant frequency of the side-coupled in-line linac waveguide was chosen to be 2998.5 MHz which is within the frequency range of a standard e2V tunable S-band magnetron and will hereafter be referred to as the nominal resonant frequency. The reference 3D accelerating cavity solution compared to the 2D Superfish solution contained 55 501 mesh elements while the full in-line side-coupled linac waveguide model used 368 625 elements. With the reference cavity having 55 501 mesh elements, it had a very similar mesh to the full model meaning the accuracy of the solution within the reference cell could be extrapolated to the solution of the full waveguide model. Using cubic vector elements, these mesh values translated into 255 305 nodes for the reference cavity mesh and just under 1.6 million nodes on which the RF field solution was calculated. The FEM RF field solution for the full waveguide model required 115 GB of RAM and took just over an hour on a PC possessing 128 GB of RAM running on 4 2.0 GHz quad-core AMD Opteron 8350 processors.

Figure 3.1: The dimensions and geometry of the basic unit comprising one side coupled cavity and two half accelerating cavities is shown. Dimensions indicated by bold Greek letters were optimized for the simulated in-line side-coupled 6 MV linac waveguide and all dimensions given are in mm.

The full 3D linac waveguide simulation was completed in five design stages. Before each stage was complete, all the cavities were required to resonate at the nominal resonant frequency. The first design stage was of the 'basic unit' shown in Figure 3.1. With an overlap between the side coupling and accelerating cavities of 6 mm (in accordance to a 2998 MHz frequency of Roy *et al.*[23]), the Superfish designed cavity diameter was adjusted slightly to account for the frequency reduction caused by the coupling irises. The numbers given in Figure 3.1 represent dimensions published by Roy *et al.* which were kept identical in this model while the Greek letters correspond to dimensions that required optimization. The geometry of the basic unit, although not respecting the staggered up-down sequence seen in Figure 3.2, is sufficient in order to design each cavity to resonate at the nominal frequency. The second design stage had the basic unit repeated five times, staggering the coupling cavities above and below the beam tube axis as seen in Figure 3.2. This created a waveguide terminated in half accelerating cavities at both ends. Since the basic unit was initially designed to resonant at 2998.5 ± 0.1 MHz for the TM_{010} mode, no additional redesign of the waveguide shown in Fig. 2 was required. The third design stage required designing a full end cavity with only one coupling iris. This was performed to ensure the simulated 3D linac waveguide emulated a manufactured one with a full end cavity. The fourth design stage required shifting the first side cavity (SC1 in Figure 3.2) towards the front end of the waveguide where the electron gun is located. By shifting SC1 towards the front end of the waveguide, iris 1 becomes larger and iris 2 becomes smaller. This asymmetry in the coupling irises causes the RF field magnitude in the first accelerating cavity (AC1) to become smaller than in the second accelerating cavity (AC2). The larger the asymmetry in the coupling irises, the smaller the RF field in AC1 becomes compared to AC2 (for the same input power). Thus through the design of the first side cavity shift, control of the RF field magnitude in AC1 can be achieved. This is important since the RF field magnitude in AC1 plays a critical role in the extent of the injected electron beam blooming. Two different side cavity shifts of 0.5 mm and 1.5 mm

will be examined in this paper. The fifth and last design stage is the design of a

coupling port that feeds power from the magnetron, through the transmission

waveguide into the linac waveguide. In 1995 Zhao *et al.*[25] published a formula

that determines the optimal coupling coefficient from a known input power with

the goal of maximizing dose rate. With an input power of 2.3 MW, the optimal

coupling coefficient was calculated to be 2.11. Since the coupling coefficient

between the transmission waveguide and the linac waveguide is identical to the

voltage standing wave ratio (VSWR) in the over-coupled regime (coupling

coefficient greater than 1), the VSWR was calculated in the simulations. The

VSWR measured is in fact a sum of two traveling waves, the power emission

from the field within the linac waveguide at resonance and the reflected power at

the port.[14]
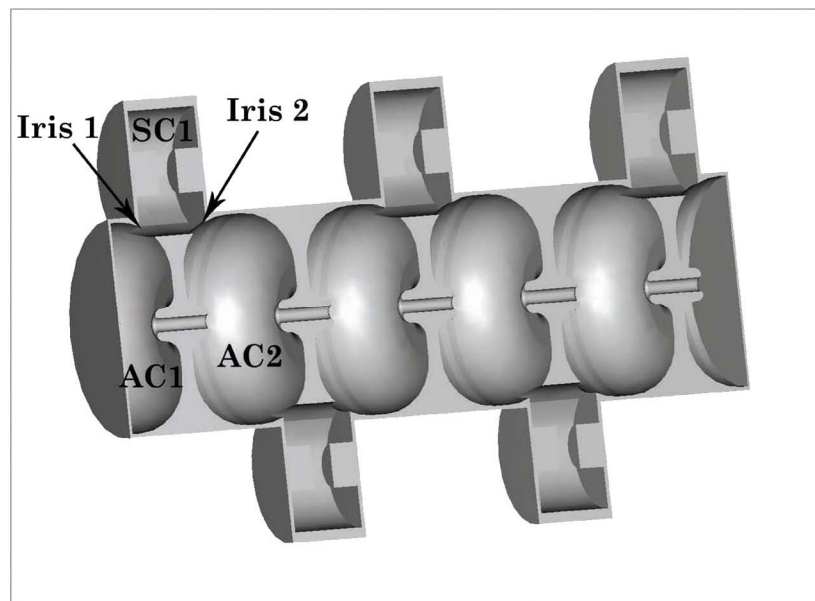
**Figure 3.2: A cutaway section of the waveguide terminated in half cavities is given. This
geometry is created by repeating the basic unit (Figure 3.1) five times ensuring the side
cavities are staggered above and below the beam tube axis. Iris 1 and 2 along with side cavity
1 (SC1) and accelerating cavities 1 and 2 (AC1 and AC2 respectively) are emphasized.**

3.2.4   Determining the effects of the coupling and port irises on the

**   RF field solution**

The effect of the asymmetrically placed coupling and port irises in a side coupled waveguide on the RF field was investigated next. In order to remove any numerical noise resulting from different FEM meshes in the comparison between coupled and non-coupled cavities, the RF field solution was solved on the same mesh for both the coupled and non-coupled cavities. Once the initial mesh was generated, the coupled solution was found using an eigenvalue solver with the boundary conditions at the irises set to require continuity in the field solution across the boundary. With the continuity condition enforced, power is transferred from an accelerating cavity to a side cavity or from the magnetron into the linac waveguide just as in true operation. When the non-coupled cavity was solved, the iris boundary condition was simply changed from a continuity condition to a perfect electrical conductor which fully contained the RF field within the cavity. A difference map was then made with the coupled solution subtracted from the non-coupled solution such that any increases in field due to coupling resulted in positive values in the difference map. The coupled and non-coupled solutions were initially normalized to the average electric field on axis to remove any differences in field magnitudes due to the eigenvalue solver. The normalized difference field was multiplied by a factor of 26 MV/m to obtain a representative field magnitude that would accelerate the electrons to 6 MeV and the difference maps were generated in each cavity at the same phase of the RF field for consistency in the analysis.

In order to determine that the difference maps generated as explained above were strictly due to the introduction of the irises and not due to the inherent differences in the field distributions caused by the RF at different frequencies (comparing the cavity frequency with and without irises), COMSOL was used to calculate changes in the field distributions due to the changes in frequency. The same cavity geometry and mesh was used in the analysis with the RF frequency simply changed to the cavity frequency determined with and without irises.

3.2.5   Particle simulations

The electron phase space at the target of the in-line 6 MV linac waveguide model was calculated using PARMELA. The PARMELA simulation includes the effects of space charge (fields generated by the electron beam itself) as well as a calculation of beam loading. The spatial and temporal stability of the PARMELA simulation was investigated by adjusting the mesh size and phase step to ensure minimum aliasing in the force calculations and solution stability over time. The mesh size for PARMELA's 3D convolution[26] space charge routine was varied from 0.08x0.08x0.12 mm^3 to 0.16x0.16x0.39 mm^3. The 3D convolution routine automatically adjusts its mesh size throughout the calculation to ensure all particles are within the mesh during acceleration and thus the mesh size quoted above is the initial mesh size. The time was incremented in phase steps from 0.9° to 5.4° per step in order to determine the Courant-Friedrichs-Lewy condition.[27] This condition simply requires the time to be small enough for information to propagate through the space discretization. Differences in energy were quantified as differences in the max and mean energy of the spectrum, while differences in the spatial distribution were quantified through the beam centroid and peak position.

With the optimal simulation parameters determined, PARMELA was used to quantify the effect of the coupling and port irises on the electron beam. PARMELA calculated the electron trajectories within the two waveguide geometries investigated (0.5 mm and 1.5 mm side cavity shift) as well as for a fictitious waveguide with no coupling. In order to simulate a waveguide with no coupling, the RF field within a non-coupled axisymmetric accelerating cavity was solved using the FEM and repeated many times to create the same number of cavities as the coupled system. A 15 keV cylindrical beam comprised of four million macroparticles, each representing $\approx 10^8$ electrons, was tracked through the linac for all PARMELA simulations over two RF periods. The maximum energy of the electrons incident on the target was set to 6 MeV and only the central electron bunch was used in the analysis disregarding the first and last half electron

bunches to remove all simulation end-effects so that the analyzed beam represented a stead-state electron bunch. In order to generate a sufficiently large phase space for the Monte Carlo studies, each PARMELA simulation was run 60 times (yielding roughly 40 million particles in total) with randomized electron injection locations within the cylindrical volume to ensure uncorrelated results.

3.2.6   Monte Carlo Simulations

A Varian 600C linac head (Figure 3.3) was modeled in the BEAMnrcMP 2007 (BEAM), which is based on the EGSnrc Monte Carlo code, according to information supplied from the manufacturer. However, the data supplied instructed the target to be modeled as a semi-infinite slab whereas the true target is known to be slightly larger than the waveguide beam tube. Thus a Monte Carlo investigation was performed to determine if there was any difference in results between the target modeled as a semi-infinite slab or as a smaller slab of 7 mm diameter.
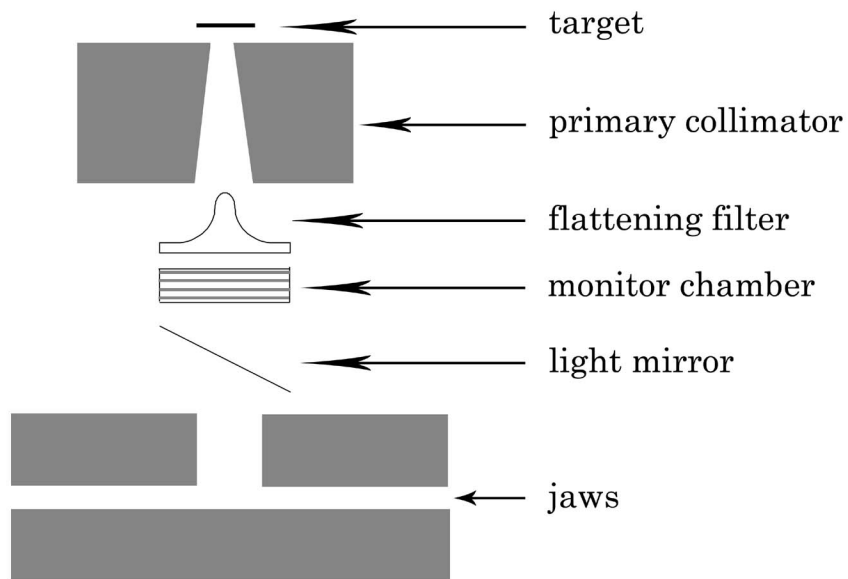
Figure 3.3: Schematic representation of the BEAMnrc linac model. All components modeled are outlined.

The EGSnrc parameters in the BEAM Monte Carlo simulations were as follows. Directional bremsstrahlung splitting was used with a source to surface distance of 100 cm, a splitting radius equal to the field size (40 cm for a 40x40 cm^2 field) and a splitting factor of 1000. Russian roulette was turned on with the splitting plane chosen to be 0.16 cm above the bottom of the flattening filter. The values of electron (ECUT) and photon (PCUT) transport cutoff energies were 0.70 MeV and 0.01 MeV respectively and range rejection was turned on with an ESAVE value of 0.7 MeV in the target and 2.0 MeV for the rest of the linac components with no photon forcing. If the electron has energy less than ESAVE, and its range will not allow it to cross a boundary, its energy is deposited locally. The smaller ESAVE value in the target allows for the electrons to be directly tracked down to lower energies for a more accurate estimate of the primary bremsstrahlung production (the generation of the X-ray beam). Elsewhere in the linac this constraint can be relaxed without significantly affecting the accuracy of the results.[28] With ESAVE and ECUT set to 0.70 MeV in the target less than 0.3% of the PARMELA phase space electrons were rejected. These parameters were used for all subsequent BEAM Monte Carlo simulations presented in this thesis.

The dose calculations were performed in DOSXYZnrc 2007 Monte Carlo code (DOSXYZ) and run in unison with BEAM using the *isource 9* option in DOSXYZ. A total number of 5x10^8 primary histories were run meaning the PARMELA target phase space was recycled approximately 12 times and the dose was scored in voxels of volume 1x1x0.5 cm^3 except in the penumbra where the voxel width was reduced from 1 cm to 0.2 cm. The ECUT and PCUT values were set to 0.70 MeV and 0.01 MeV for the DOSXYZ simulation, but this time no range rejection was used, and the dose profiles were normalized to the central axis dose (D_{CAX}).

3.3   RESULTS AND DISCUSSION

3.3.1   3D accelerating cavity and RF field solution benchmarking

Since our group does not have the resources to produce a cold model for verification of the RF field solution, validation was performed with a comparison against the benchmarked program Superfish for a single accelerating cavity, and with theory from the lumped-circuit model as seen later in this chapter. The results from the redesigned and optimized 2D accelerating cavity reproduced in 3D using COMSOL Multiphysics is seen in Table 3.1, where the important linac parameters (Q factor, shunt impedance, transit time factor and resonant frequency) are compared with those generated using Superfish. The results show a maximum discrepancy of 0.03% between the two methods of calculation showing excellent agreement. The tolerances given in Table 3.1 for the Superfish simulation were determined by reducing the average triangle area in steps down to a final value of 5.04×10^{-5} cm^2 (thus increasing the number of nodes to a maximum of 75 636) and calculating the difference in the parameters at each step. The same technique was used for the COMSOL simulations where the mesh size was decreased by roughly 5 times giving 338 360 elements (and 1.55 million nodes). The lower tolerances in the COMSOL solution can be understood due to COMSOL using isoparametric elements to better conform to the boundary and cubic shape functions for higher order interpolation.

Table 3.1: Computed values for some important linac parameters for both the 2D FD program Superfish and the 3D FEM program COMSOL Multiphysics. Note that there was no change to the transit time factor in either the Superfish or COMSOL simulation to the fourth decimal upon the maximum reduction in mesh size.

	Superfish	COMSOL	% difference
Q factor (rad)	17523±4	17521.3±0.1	0.01
Shunt Impedance (MΩ/m)	165.3±0.1	165.24±0.01	0.02
Transit Time Factor	0.8379	0.8381	0.03
Resonant Frequency (MHz)	3007.6±0.2	3007.23±0.01	0.01

3.3.2   Waveguide design

Superfish was used in the design and optimization of all aspects of the accelerating cavity except for the cavity diameter which was optimized using the 3D FEM to account for the frequency change due to the coupling irises. It was found that the resonant frequency of the uncoupled accelerating cavity needed to be 3007.2 MHz such that when coupled to side cavities with an overlap of *d=6 mm* (see Figure 3.1) the system of cavities, and hence the entire linac waveguide, would resonate at 2998.5 MHz. With the overlap between the side and accelerating cavities set to 6 mm, a coupling coefficient of 0.0112 was calculated in good agreement with previous simulations and measurement taken by Roy *et al.*[23]

With each accelerating and side cavity individually resonating at 2998.5±0.1 MHz, the waveguide system terminating in half cavities shown in Figure 3.2 resonated at 11 different frequencies corresponding to 11 different phase shifts per cavity for the TM_{010} mode. The 11 frequencies plotted against the 11 phase shifts per cavity produce a dispersion curve that was compared to the theoretical curve from lumped circuit theory[13] (Figure 3.4a) using the calculated coupling coefficient given above. The resonant frequencies, calculated using COMSOL's ARPACK[29] eigenfrequency solver, show excellent agreement with theory. From the dispersion curve, the phase and group velocities for the $\pi/2$ mode was determined to be speed of light *c* and 0.03*c* respectively, in agreement with values for a Varian 600C waveguide[1]. The axial field calculated within the waveguide of Figure 3.2 is given in Figure 3.4b.
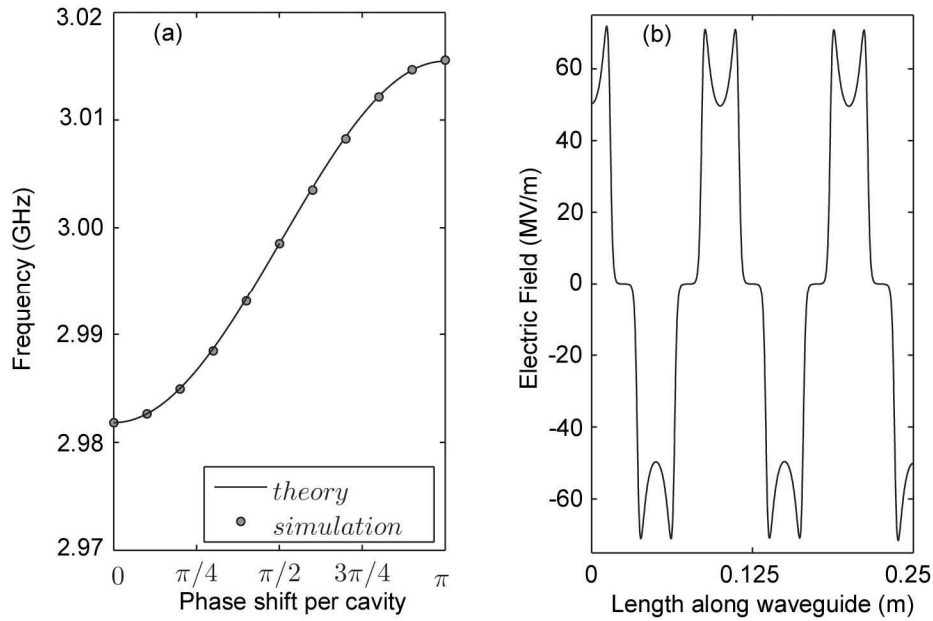
Figure 3.4: (a) The theoretical and simulated dispersion curves are shown for a side-coupled waveguide system terminating in half accelerating cavities as shown in Figure 3.2. (b) The axial electric field within the waveguide shown in Figure 3.2.

The design of the full end cavity and the cavities affected by the first side cavity shift were accomplished next in order to create a waveguide geometry that better represented a manufactured waveguide. For the end full cavity design it was found that an increase in the nose cone length of 0.145 mm increased the capacitance of that cavity enough to compensate for the single coupling iris and thus regain the nominal resonant frequency. A decrease in the RF field magnitude within the first half accelerating cavity was controlled by the magnitude of the first side cavity shift towards the front of the waveguide. Figure 3.5 shows the axial (z direction) electric field within the first half and second full cavity with a 0.5 mm side cavity shift and with a 1.5 mm side cavity shift. A clear drop in field magnitude is seen in the first half accelerating cavity for the 1.5 mm cavity shift compared to the 0.5 mm shift. The total energy contained within the first half accelerating cavity was calculated to be 0.163 J and 0.052 J for the 0.5 mm and 1.5 mm side cavity shifts respectively. However, the total energy contained within the first coupling cavity remained constant at around 0.001 J for either shift. The

larger coupling iris of the first half accelerating cavity caused an increased inductance, meaning a decreased capacitance was required to regain the nominal resonant frequency. For the 1.5 mm cavity shift, the decreased capacitance was obtained by shortening the first nose cone by 0.03 mm while for the 0.5 mm cavity shift no nose cone adjustment was required since the frequency change was less than 0.1 MHz. The side cavity also experienced an overall increase in inductance, so in order to decrease capacitance, the length of the posts were reduced by 0.03 mm for the 1.5 mm cavity shift geometry, while again no change was required for the 0.5 mm cavity shift.
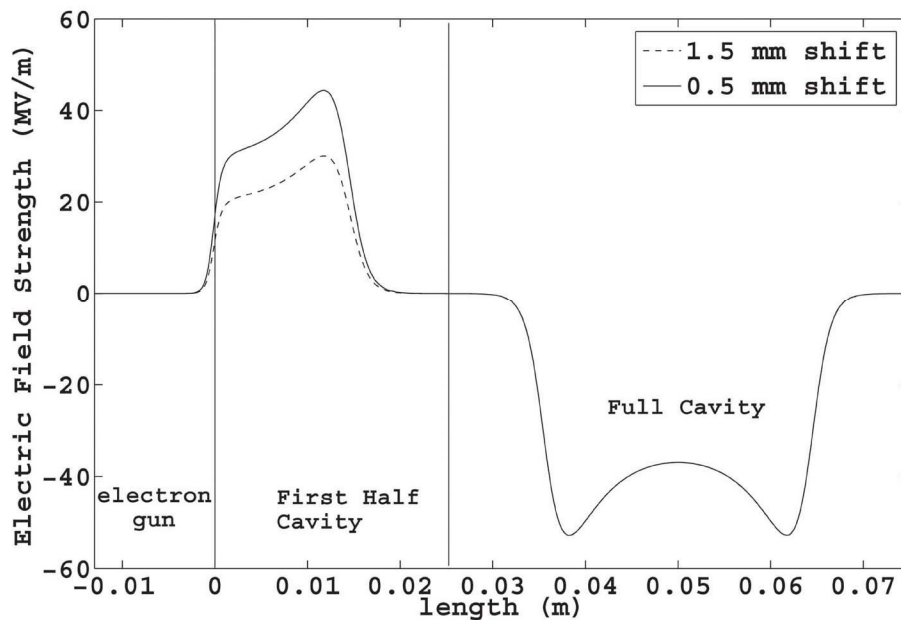
Figure 3.5: The axial electric field along the center of the waveguide for 0.5 mm and 1.5 mm cavity shifts are depicted. The larger cavity shift produced a lower electric field in the first accelerating cavity in order to maintain a node in the side cavity.

The input port cavity through which the power from the magnetron is fed required a redesigning of the accelerating cavity due to the introduction of the optimized port iris which gave a coupling coefficient of 2.09. The size of the input coupling port was different for the different side cavity shift geometries since the shifts changed the intrinsic impedance of the waveguide due to the different geometries. For the 1.5 mm cavity shift geometry with a coupling port area of

3.05 cm^2, the accelerating cavity diameter was decreased by 0.135 mm to recover the nominal resonant frequency since the addition of the port iris initially caused a 9.6 MHz decrease in frequency. Decreasing the diameter of this cavity had the effect of changing the intersection between it and the adjacent side cavities causing smaller coupling irises, but the effective change in iris size was found to be so minor that no significant change (> 0.1 MHz) in the resonant frequency of the side cavities was observed. For the 0.5 mm side cavity shift geometry with a coupling port area of 3.73 cm^2, the accelerating cavity diameter was decreased by 0.195 mm to compensate for the 13.8 MHz decrease in frequency and the side cavity's posts were decreased by 0.01 mm to recover the side cavity's nominal resonance frequency. The total energy within the port accelerating cavity was calculated to be 0.33 J while in the adjacent coupling cavities it was calculated to be 0.001 J for both the 1.5 mm and 0.5 mm side cavity shift designs. With all design optimizations completed, the RF field within the fully modeled waveguide was solved. Figure 3.6 shows the full 3D waveguide design together with the coupling port geometry while Figure 3.7 shows the axial (z direction) electric field FEM solution on axis along with the radial electric field at the beam tube edge for both side cavity shift in-line 6 MV linac waveguides. A summary of the waveguide dimensions along with optimization and design results are given in Table 3.2.

input coupling
port

h=2.05 (2.26) cm
w=1.49 (1.65) cm
r=0.318 cm
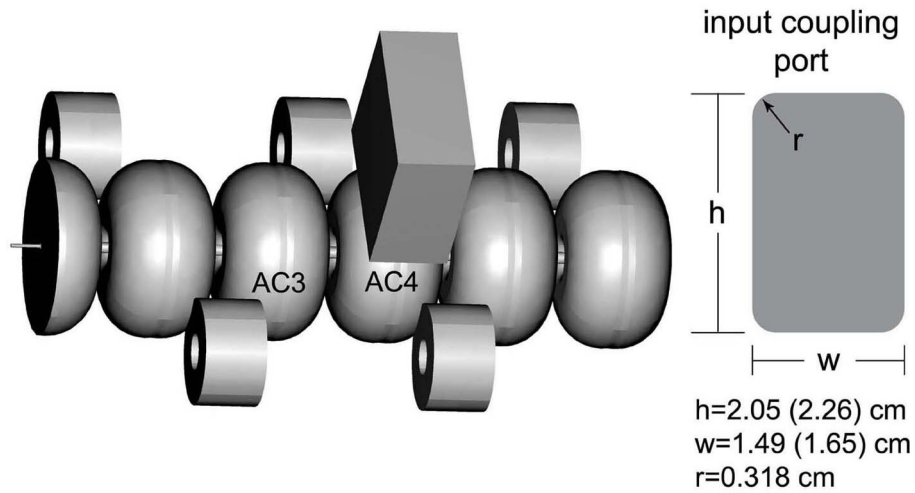
Figure 3.6: The geometry of the full waveguide with the third and fourth accelerating cavity (AC3 and AC4 respectively) locations outlined is given along with the dimensions for the input coupling port for the 1.5 mm (0.5 mm) shifts.
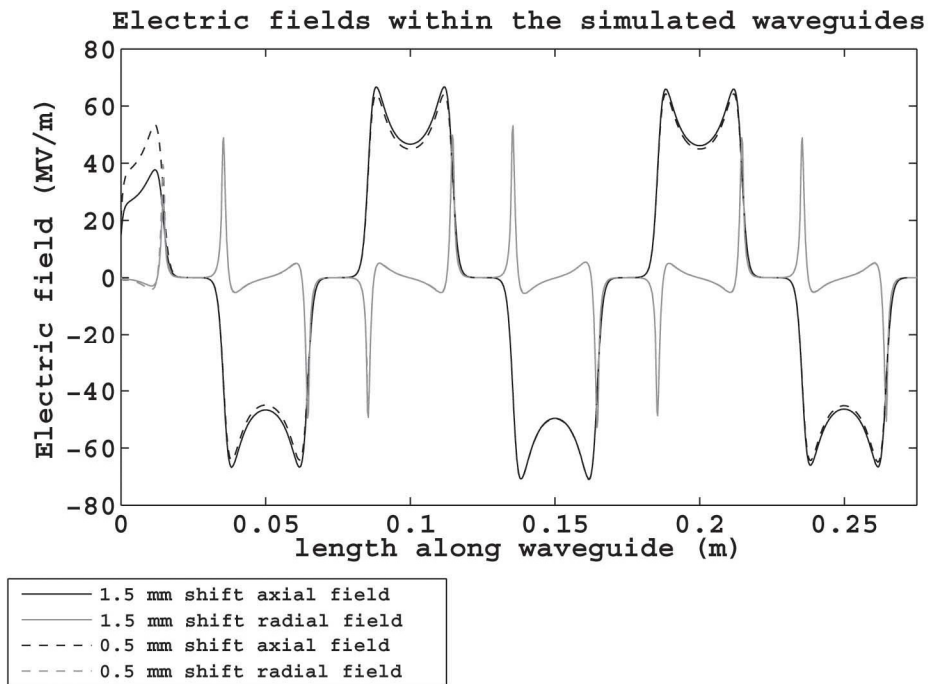
Figure 3.7: The electric field solution within the simulated in-line side-coupled 6 MV linac waveguide incorporating a 1.5 mm and 0.5 mm side cavity shift is given. The Axial electric fields were taken on the central axis while the radial electric fields were taken at the beam tube edge.

Table 3.2: A summary of all the waveguide dimensions that were optimized in the 1.5 mm (0.5 mm in brackets) cavity shift in-line side-coupled 6 MV linac model are given. The Greek letters refer to the dimensions outlined in Figure 3.1. Dimensions that were not changed are designated by a hyphen. These dimensions together with the dimensions in Figure 3.1 specify the entire waveguide.

	Optimized AC dimensions (mm)	first AC dimensions (mm)	port AC dimensions (mm)	End AC dimensions (mm)
Inner corner radius (β)	5.50	-	-	-
Cavity radius (γ)	38.46	-	38.325 (38.264)	-
Inner nose cone radius (δ)	1.00	-	-	-
Nose cone length (ε)	10.88	10.85 (-)	-	11.03 (-)
Beam tube diameter (ζ)	5.00	-	-	-
	Optimized CC dimensions (mm)	first CC dimensions (mm)	port CC dimensions (mm)	Coupling port area (cm^2)
Post length (α)	9.58	9.55 (-)	- (9.57)	3.05 (3.73)

3.3.3   Effect of side-coupling on RF field

The asymmetry in the RF field caused by the side and port coupling irises was investigated in the third and forth accelerating cavities shown as AC3 and AC4 in Figure 3.6. The third accelerating cavity (AC3) possesses two side coupling irises and the port cavity (AC4) possesses two side coupling irises along with the port iris. The frequency difference between the accelerating cavity (AC3) with and without coupling was calculated to be 8.75 MHz while the frequency difference for the port cavity was calculated to be 13.84 MHz (due to the reduced diameter required maintain the nominal resonance frequency with the port iris). It was determined through the COMSOL simulations that the magnitude of the differences caused by the different field distributions at different frequencies was an order of magnitude smaller than the results shown in Figure 3.8 – Figure 3.11. Thus, field differences caused by the different RF distributions at different frequencies can be neglected.
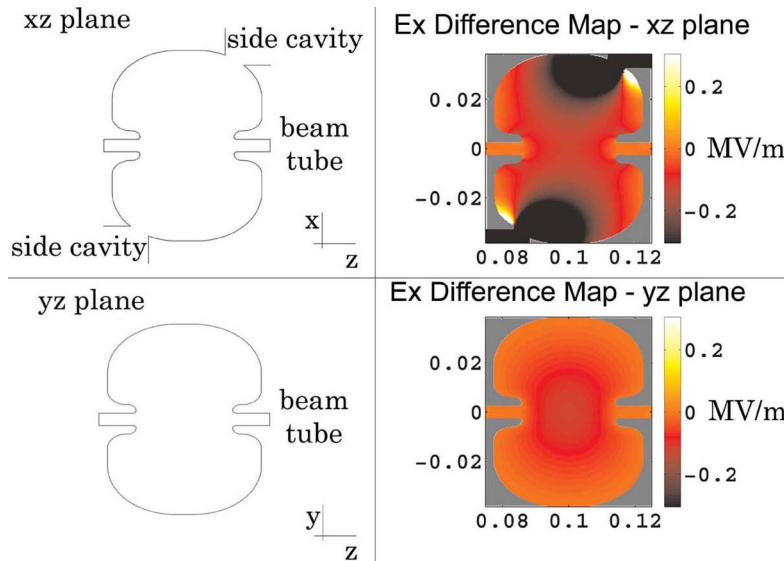
Figure 3.8: Electric field difference maps for the x component along the xz and yz planes for the third accelerating cavity (AC3). The left side of the figure shows a schematic drawing of the cavity whose difference map is shown on the right. The xz plane incorporates the coupling irises. The x component of the electric field was the only electric field component that had large differences in the beam tube where the electrons travel.
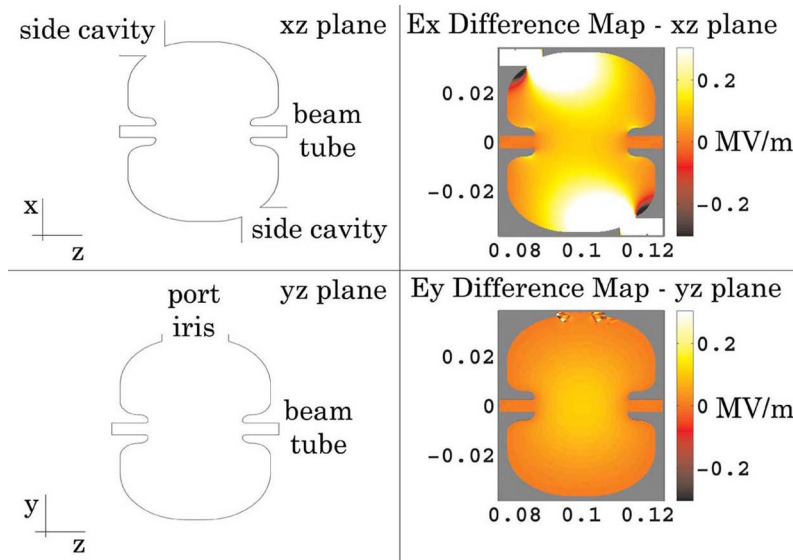
Figure 3.9: Electric field difference maps for the x component along the xz and yz planes for the port accelerating cavity (AC4). The left side of the figure shows a schematic drawing of the cavity whose difference map is shown on the right. The xz plane incorporates the coupling irises and the yz plane incorporates the input port. Only the x component of the electric field showed substantial differences in the beam tube. The polarity of the field is also reversed in this cavity (for the same RF phase as Figure 3.8) due to a reversal of the positions of the coupling irises.
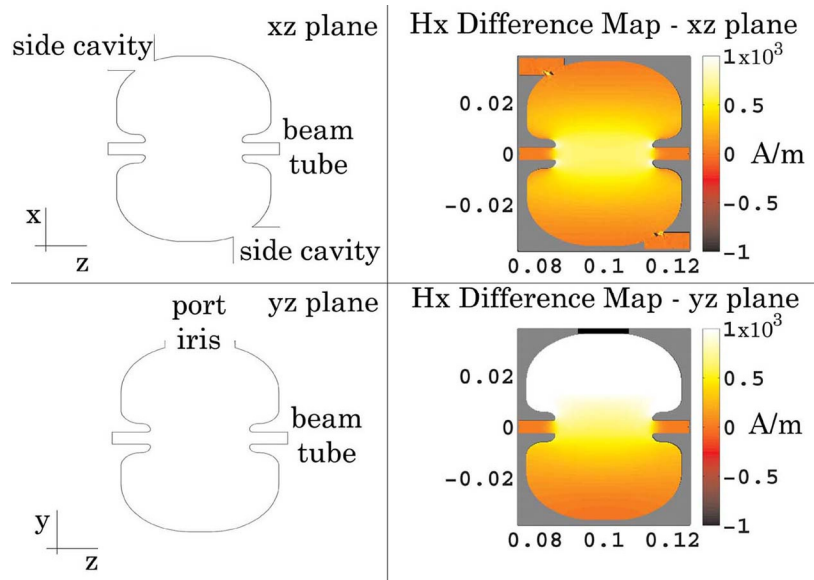
Figure 3.10: x component magnetic field difference maps along the xz and yz planes for the port accelerating cavity (AC4) are given. The other magnetic field components showed negligible differences in the beam tube. The left side of the figure shows a schematic drawing of the cavity whose difference map is shown on the right.
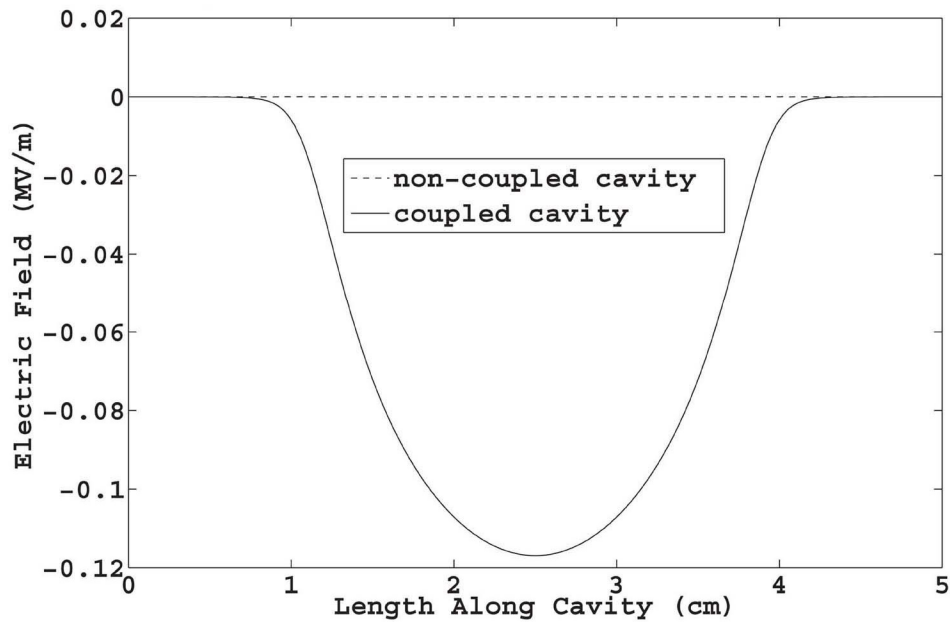
Figure 3.11: A plot of the true difference for the x component of the electric field in the third accelerating cavity is shown. The line plot was taken along the length of the accelerating cavity at the beam tube center.

Figure 3.8 and Figure 3.9 show the x component electric field difference maps in the xz and yz planes for the third and forth (port) accelerating cavities respectively and Figure 3.10 shows the x component magnetic field difference maps for the port cavity along the same planes. The xz plane shows the field differences in a plane including the coupling irises while the yz plane shows field differences in a plane not including coupling irises, but including the port iris for the port accelerating cavity. Only the x component electric field differences are shown for the third accelerating cavity (AC3) since all other components, including all magnetic field components, show negligible differences in the beam tube (less than 10^3 V/m). For the port cavity (AC4), the x component magnetic field difference map is shown in addition to the x component electric field map due to its large effect in the beam tube. As with AC3, the other field components are not shown since they yield negligible differences in the beam tube. In Figure 3.9 and Figure 3.10 some isolated numerical noise can be seen at the sharp edges caused by the intersection of the side cavity or port waveguide with the curved surface of the accelerating cavity. The sharp edges in the numerical model allow for a reduced number of mesh elements, significantly decreasing the memory and computational time requirements. In a manufactured linac, the edges would be smooth lowering the field concentration and reducing the probability of electrical breakdown.

In Figure 3.8 – Figure 3.10, the color scale was set such that field differences within the beam tube would be prominent while still showing changes throughout the entire cavity. The maximum magnitude of electric field difference in the beam tube was on the order of 10^5 V/m for both the third and port accelerating cavities while the maximum difference in the magnetic field was on the order of 10^3 A/m. In order to get a feel for the magnitude of the differences, the electric field strength in a typical accelerating cavity (Figure 3.7) is on the order of 5×10^7 V/m and the magnetic field strength is 1×10^4 A/m. To further illustrate the magnitude of these differences, Figure 3.11 shows the absolute difference for the x component of the electric field for the length of the third

cavity along the waveguide center. The non-coupled cavity has zero field magnitude of the x component electric field due to cylindrical symmetry, but side coupling introduces a maximum magnitude of just under -0.12 MV/m on axis.

In Figure 3.8 and Figure 3.11 it is clear that the x component of the electric field is more negative throughout the cavity as a result of the coupling. As the electron beam traverses the cavity, it experiences an extra negative transverse force in the x direction that is not present for non side-coupled structures. This leads to a shifting of the electron beam in the x direction, but the shift is not global since the differences introduced are asymmetric. For example, as seen in Figure 3.8, the change in the x component of the electric field due to coupling is different in the xz plane compared to the yz plane. In the xz plane, the change caused by the coupling irises leads to an increasingly larger difference going away from the axis of the waveguide. The opposite is true in the yz plane where the largest difference is on axis and becomes lesser near the beam tube edges. With a fully symmetric cavity, the electrons at ±x and ±y positions in the beam tube experience identical RF field magnitudes leading to a fully symmetric beam. The asymmetric differences seen in Figure 3.8 – Figure 3.10 mean that electrons at ±x and ±y positions in the beam tube no long experience the same RF field leading to a shift and skewing of the electron beam.

The effect of the asymmetries seen in Figure 3.8 and Figure 3.9 are minimized by the staggered location of the side cavities as seen in Figure 3.2. Two accelerating cavities are coupled with the side cavity on top of the waveguide and the next two accelerating cavities are coupled with the side cavity on the bottom of the waveguide. The x component of the electric field seen in Figure 3.8 is more negative due side-coupling, whereas it is less negative for the adjacent port cavity in Figure 3.9. Overall, the staggering of the side cavities along the top and bottom of the waveguide causes the polarity of these field asymmetries to be reversed in adjacent cavities for the same RF phase. However, a complete cancellation of the asymmetries is not expected since the effects on the

low velocity electrons at the beginning of the waveguide (γ=1.1) will be greater than at the end where they are traveling near the speed of light (γ=12.9).

The electric field differences in the port cavity show large changes in the cavity near the input port, but the effect is very small within the beam tube with the exception of the x component, and hence the electrons experience a nearly identical electric field in the port cavity compared to the non-port cavities. The effect of the port iris on the magnetic field however is non-negligible in the beam tube for the port cavity as seen in Figure 3.10. The x component of the magnetic field shows the largest changes due to the magnetic field's circumferential nature. The y and z components of the magnetic field are zeros or at least very nearly so at the port while the x component is near maximum. Thus the perturbations to the field will be most strongly experienced by the x component of the magnetic field. As seen in Figure 3.10, the changes in the field are asymmetric within the beam tube again causing an asymmetric force to be imparted to the electron beam predominantly in the y direction according to the Lorentz force.

3.3.4   Particle simulations

The results of the spatial, time and space charge analysis of PARMELA resulted in a determination of the optimal simulation parameters. Changing the mesh size in the 3D convolution space charge routine resulted in a 0.02% change in energy, 0.0002 mm change in the spatial distribution, and a 0.05 mA change in target current. The largest mesh size ran 5.8 times faster than the smallest. By changing the phase step from 0.9° to 5.4°, the maximum discrepancy in energy was found to be 0.2%, 0.01 mm in the spatial distributions and 1 mA in the target current. At the smallest phase step, the simulation ran 5.7 times slower than at the largest time step investigated. After applying an appropriate lateral shift of the electron target distribution with respect to the flattening filter (as done in linac commissioning) it was determined that all the discrepancies quoted above had no effect within statistical uncertainty on the Monte Carlo generated dose distributions. All subsequent particle simulations performed in PARMELA used

the 3D convolution space charge calculation with a mesh size of 0.08x0.08x0.12 mm^3, and a phase step of 3.6° as recommended by the PARMELA manual[30].

The particle simulations showed the expected shifting and skewing of the electron beam due to the asymmetric RF field within the side-coupled linac waveguide. For all particle simulations, a beam loading power of 1 MW was calculated with a target current of 180 mA. Figure 3.12 shows the spatial electron intensity distribution at the target in the x and y directions for the 0.5 mm and 1.5 mm side cavity shift simulations with coupling along with a simulation performed without the effects of coupling. The peak positions as well as the center of gravity of the x and y distributions are all zero for the fully symmetric, non-coupled waveguide simulation. When the 0.5 mm side cavity shift waveguide with coupling was modeled, the distribution peak and center of gravity positions were calculated to be 0.02 cm and 0.008 cm respectively in the x direction, and -0.004 cm and 0.005 cm respectively in the y direction. For the 1.5 mm side cavity shift waveguide, the peak and center of gravity positions changed to 0.01 cm for both in the x direction and -0.005 cm and -0.007 cm respectively in the y direction. From this analysis, at an input power of clinical relevance to a medical in-line side-coupled waveguide, the greatest effect on a cylindrical beam is due to the side coupling. An increasing input power would cause an increasingly larger beam shift in the y direction, but for an input power from the magnetron powering the 600C linac, the presented shift is the expected clinical output for an injected cylindrical electron beam. From Figure 3.12, it is also apparent that the larger RF field magnitudes in the first accelerating cavity cause a larger beam spot at the target. This may in part be due to a greater redistribution of the electron beam upon injection into the linac in order to shield the interior of the beam from the larger RF focusing forces.
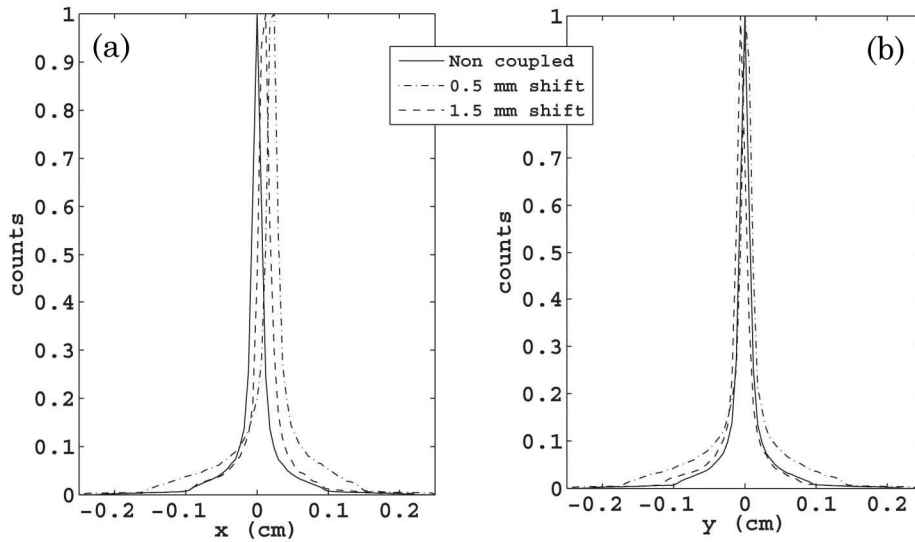
Figure 3.12: (a) The normalized x and (b) y electron spatial intensity distributions at the target are given. The effect on the electrons traversing the in-line side-coupled waveguide due to side and port coupling is shown. A noticeable shift and skewing of the electron distribution at the target is seen as a result of the RF field changes due to side and port coupling. The larger beam spot for the 0.5 mm side cavity shift waveguide is also seen due to the greater extent of electron blooming in the first accelerating cavity.

3.3.5   Dose distributions

The results of the target size investigation showed no difference when using either a semi-infinite slab, or a 7 mm diameter. Thus all subsequent simulations used the semi-infinite slab as instructed by the manufacturer.

The effect on the inline dose distribution from the small peak and center of gravity shifts of the electron beam due to side coupling is given in Figure 3.13. The statistical uncertainty in this and subsequent dose calculations was determined to be 0.6%. The dose distribution in the direction of the port iris (i.e. in the y direction) showed very little effect due to the port iris and is thus not shown here. Very little difference in the dose distributions for the waveguide designs between the 0.5 mm or 1.5 mm side cavity shift is seen, but the effect of side coupling as a whole exhibits itself as a 1% asymmetry in the profiles. This asymmetry is clinically acceptable, but in practice it is not seen after the linac has been properly commissioned. In the commissioning process, the waveguide is

translated laterally with respect to the flattening filter until symmetric dose distributions are achieved, correcting the small effect of side coupling in the process. Despite the peak shift being larger for the 0.5 mm side cavity shift, the total beam spot is larger with a greater number of electrons left of the main peak (-x direction in Figure 3.12) keeping the beam center of gravity similar to the 1.5 mm side cavity shift model. The similar beam center of gravities most likely causes the dose profiles to be similar. As seen in Figure 3.12 and Figure 3.13, the effect of the side-cavities and coupling port on a short in-line side-coupled linac has a very small effect on the dose distributions, which is easily removed during the commissioning process. For the linac modeled, and ones similar in design and length, the effect of the coupling can be, and is in practice ignored. However, longer waveguide structures like those for high energy medical beams cannot ignore these effects and in practice use solenoid focusing and steering coils to ensure the beam is not deflected to a large extent.
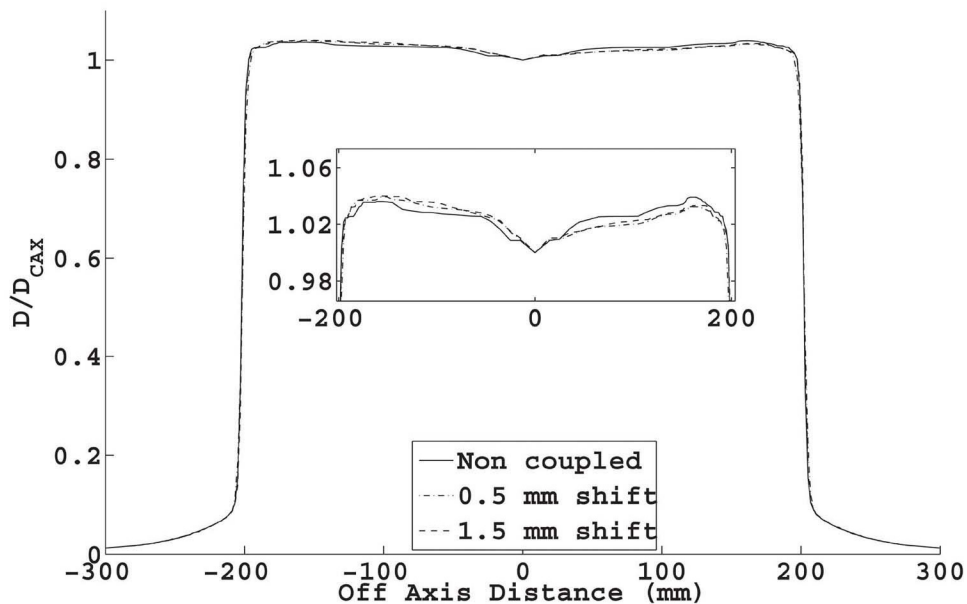
Figure 3.13: The inline dose profile (in the direction of the coupling cavities) shows a 1% asymmetry caused by the effects of the side-coupling cavities. The inset is a magnified view of the profile horns to show the asymmetry in greater detail. Little difference is seen between the 0.5 mm and 1.5 mm side cavity shift waveguide models.

The exact side cavity shift and proper electron injector design for this waveguide to more exactly emulate a Varian 600C requires the incorporation of various electrical measurements from a Varian 600C into the model and the Monte Carlo commissioning process[31, 32] to ensure the model waveguide and the Varian 600C are dosimetrically equivalent. The focal spot size can be adjusted by changing the first side cavity shift as explained above and the beam energy can be adjusted by changing the RF magnitude within the waveguide according to the constraint that the required power must not exceed what is available from clinically used magnetrons. With a fully commissioned 3D linac model, a better estimate of the extent of beam shifts due to the side-coupling and port irises of a Varian 600C will be known, as well as their effect on the dose distribution.

With a full 3D waveguide simulation, the electron trajectories can be accurately determined with and without the presence of an external magnetic field. In the pursuit of determining the maximum magnetic field in which the linac can operate, an analysis of asymmetries in dose profiles along with the extent of beam loss within the waveguide caused by an external magnetic field is required. If the shifting and skewing of the electron beam simply caused by the side and port coupling irises is not first taken into account, an underestimation of the effect of the external magnetic field is inevitable. The shift away from the central axis caused by an external magnetic field is increased due to the inherent effects of the side and port coupling irises. Thus the designed 3D simulation outlined here is able to quantify the true effect on the electron beam in a side-coupled medical linac waveguide in the presence of an external magnetic field.

3.4   CONCLUSIONS

A concise design for the generation of an accurate simulation of an in-line side-coupled 6 MV medical linac waveguide has been given. The design and optimization of the side-coupled waveguide given was designed to emulate a Varian 600C clinical waveguide. The 3D RF field solution within the reference cavity was shown to be highly accurate compared to the benchmarked program

Superfish, and the completed full waveguide simulation was able to incorporate the effects of side and port coupling. The effect of the side and port irises on the RF field have been quantified and have been shown to be predominantly in the electric and magnetic fields respectively. As expected for the $\pi/2$ operating mode, the total energy contained within the coupling cavities was orders of magnitude smaller than in the accelerating cavities, since these cavities contain the field nodes. Using the particle-in-cell program PARMELA, the electron trajectories within the simulated waveguide have been determined and have shown a slight shifting and skewing of the electron beam due to the effects of the side and port coupling irises. The dose profile in the direction of the coupling cavities was found to show the greatest change introducing a 1% asymmetry due to the side-coupling irises. However, in practice this asymmetry is removed in the proper commissioning of the medical linear accelerator.

3.5   REFERENCES

[1] C. J. Karzmark, C. S. Nunan, and E. Tanabe, *Medical electron accelerators* (McGraw-Hill, New York, 1993).

[2] D. Alesini, A. Falone, M. Migliorati, A. Mostacci, F. Palpini, L. Palumbo, and B. Spataro, "Design and RF measurements of an X-band accelerating structure for linearizing the longitudinal emittance at SPARC," Nucl. Instrum. Methods Phys. Res. Sect. A-Accel. Spectrom. Dect. Assoc. Equip., **554**, 1-12 (2005).

[3] D. Meidlinger, T. L. Grimm, and W. Hartung, "High-current SRF cavity design," Physica C, **441**, 151-154 (2006).

[4] A. Roy, J. Mondal, and K. C. Mittal, "RF properties of 1050 MHz, beta=0.49 elliptical cavity for high current proton acceleration," JINST, **3**, P04002 (2008).

[5] G. A. Loew, R. H. Miller, R. A. Early, and K. L. Bane, "Computer calculations of traveling-wave periodic structure properties," IEEE Trans. Nucl. Sci., **26**, 3701-3704 (1979).

[6] H. Halbach, and R. F. Holsinger, "Superfish - a computer program for evaluation of RF cavities with cylindrical symmetry," Part. Accel., **7**, 213-222 (1976).

[7] E. Jensen, "Computational tools for RF structure design" in Physics and technology of linear accelerator systems, (Long Beach, CA, 2002), pp. 155-179.

[8] L. Picardi, C. Ronsivalle, and B. Spataro, "Design development of the SCDTL structure for the TOP linac," Nucl. Instrum. Methods Phys. Res. Sect. A-Accel. Spectrom. Dect. Assoc. Equip., **425**, 8-22 (1999).

[9] S. Shin, E. S. Kim, H. S. Kim, and D. Son, "Design of a low-Q S-band cavity beam position monitor," J. Korean Phys. Soc., **52**, 992-998 (2008).

[10] S. Fu, and T. Kato, "RF-chopper for the JHF proton linac," Nucl. Instrum. Methods Phys. Res. Sect. A-Accel. Spectrom. Dect. Assoc. Equip., **440**, 296-306 (2000).

[11] H. Podlech, M. Grieser, R. von Hahn, S. Papureanu, R. Repnow, and D. Schwalm, "The 7-gap-resonator-accelerator for the REX-ISOLDE-experiment at CERN," Nucl. Instrum. Methods Phys. Res. Sect. B, **139**, 447-450 (1998).

[12] P. Balleyguier, "Losses in a multi-cell accelerating cavity: measurement against simulation," Nucl. Instrum. Methods Phys. Res. Sect. A-Accel. Spectrom. Dect. Assoc. Equip., **413**, 1-6 (1998).

[13] D. E. Nagle, E. A. Knapp, and B. C. Knapp, "Coupled resonator model for standing wave accelerator tanks," Rev. Sci. Instrum., **38**, 1583-1587 (1967).

[14] T. P. Wangler, *RF linear accelerators* (Wiley-VCH, Weinheim, 2008).

[15] J. C. Slater, *Microwave electronics* (D. Van Nostrand Company Inc., New York, 1950).

[16] E. A. Knapp, B. C. Knapp, and J. M. Potter, "Standing wave high energy linear accelerator structures," Rev. Sci. Instrum., **39**, 979-991 (1968).

[17] R. E. Collins, *Field theory of guided waves* (McGraw-Hill, New York, 1960).

[18] J. Gao, "Analytical formulas for the resonant frequency changes due to opening aperatures on cavity walls," Nucl. Instrum. Methods Phys. Res. Sect. A-Accel. Spectrom. Dect. Assoc. Equip., **311**, 437-443 (1992).

[19] H. A. Bethe, "Theory of diffraction by small holes," Phys. Rev., **66**, 163-182 (1944).

[20] U. Amaldi, P. Berra, K. Crandall, D. Toet, M. Weiss, R. Zennaro, E. Rosso, B. Szeless, M. Vretenar, C. Cicardi, C. De Martinis, D. Giove, D. Davino, M. R. Masullo, and V. G. Vaccaro, "LIBO - a linac-booster for protontherapy: construction and tests of a prototype," Nucl. Instrum. Methods Phys. Res. Sect. A-Accel. Spectrom. Dect. Assoc. Equip., **521**, 512-529 (2004).

[21] D. Davino, S. Falco, and V. G. Vaccaro, "Some relavent aspects in the design and construction of a 30-62 MeV linac booster for proton therapy" in LINAC, (Lubeck, Germany, 2004), pp. 336-338.

[22] T. Clauser, A. Raino, V. Variale, C. De Martinis, D. Giove, M. Mauri, A. D'Elia, M. R. Masullo, and V. G. Vaccaro, "A new tuning method for resonant coupling structures" in Particle Accelerator Conference, (Knoxville, Tennessee, 2005), pp. 973-975.

[23] R. Roy, and O. Shanker, "Calculation of intercavity coupling coefficient for side coupled standin- wave linear accelerator," IEEE Trans. Microwave Theory Tech., **41**, 1233-1235 (1993).

[24] J. Jin, *The finite element method in electromagnetics* (John Wiley & Sons Inc., New York, 2002).

[25] H. B. Zhao, R. Carter, C. D. Hannaford, P. Zhou, and E. A. Hughes, "The improvement of the output performance of a low-energy medical standing-wave accelerator," Nucl. Instrum. Methods Phys. Res. Sect. A-Accel. Spectrom. Dect. Assoc. Equip., **356**, 552-557 (1995).

[26] R. W. Hockney, and J. W. Eastwood, *Computer simulations using particles* (Taylor & Francis Group, New York, 1988).

[27] R. Courant, K. Friedrichs, and H. Lewy, "On the partial differential equations of mathematical physics," IBM J., **11**, 215-234 (1967).

[28] D. Sheikh-Bagheri, D. W. O. Rogers, C. K. Ross, and J. P. Seuntjens, "Comparison of measured and Monte Carlo calculated dose distributions from the NRC linac," Med. Phys., **27**, 2256-2266 (2000).

[29] R. B. Lehoucq, D. C. Sorensen, and C. Yang, "ARPACK Users' Guide: Solution of Large-Scale Eigenvalue Problems with Implicitly Restarted Arnoldi Methods", http://www.caam.rice.edu/software/ARPACK, 1997

[30] L. M. Young, "Parmela," *LA-UR-96-1835*, (L.A.N.L.,Los Alamos) 2005

[31] D. Sheikh-Bagheri, and D. W. O. Rogers, "Sensitivity of megavoltage photon beam Monte Carlo simulations to electron beam and other parameters," Med. Phys., **29**, 379-390 (2002).

[32] J. Pena, L. Franco, F. Gomez, A. Iglesias, R. Lobato, J. Mosquera, A. Pazos, J. Pardo, M. Pombar, A. Rodriguez, and J. Sendon, "Commissioning of a medical accelerator photon beam Monte Carlo simulation using wide-field profiles," Phys. Med. Biol., **49**, 4929-4942 (2004).

CHAPTER 4: An integrated 6 MV linear accelerator model from electron gun to dose in a water tank

4.1   INTRODUCTION

X-ray modeling of a linac for radiotherapy typically involves Monte Carlo simulation of radiation transport through a linac head comprised of a target, primary collimator, flattening filter, monitor chamber, secondary collimators, multileaf collimators (MLCs) and/or various accessories such as wedges using algorithms such as BEAMnrc[1-13], GEANT[14, 15], and PENELOPE[16-18]. In order to be accurate, these Monte Carlo simulations require precise knowledge of the initial electron energy and spatial intensity distribution at the target. One measurement made by the National Research Council of Canada (Winnipeg, Canada) on a linac which utilizes a bending magnet and energy slit, showed a Gaussian energy and spatial intensity distribution at the target[19]. However, it has also been shown that other linacs of varied energies and comprised of different beam-line components and electron injectors produce non-Gaussian intensity distributions at the target.[20, 21] Despite these discrepancies, Monte Carlo simulations of these linacs typically begin with an assumed Gaussian nominal electron intensity distribution at the target, as well as a Gaussian energy distribution. Commissioning of the simulated linac is then performed by adjusting the full width half maximum (FWHM) of the intensity distribution and the mean energy of the energy distribution until a 'best match' between measured and simulated dose distributions is reached.[2, 6-9, 11]

In contrast to simply assuming a Gaussian spatial intensity and energy distribution of the electrons at the target for the Monte Carlo studies, a better estimate can be determined through a full simulation of a linac including the modeling of an electron gun, solving for the electromagnetic field within the

waveguide, and particle simulations. In this type of linac simulation, the design of an electron gun geometry, determination of the electrostatic field solution within that geometry, and the electron phase space injected into the linac waveguide are all required. All of these can be obtained from numerical programs such as the 2D program EGN2w (formerly EGUN). EGUN has served as a tool to design electron guns and characterize the injection electron phase space for a variety of applications in the past.[22-27] The full linac simulation then uses the phase space generated from the electron gun simulation and the waveguide RF solution (chapter 3)[28] as inputs into a particle simulation program such as PARMELA which tracks electrons or ions as they accelerate through the linac.

From the full linac simulation (electron gun, linac RF field solution and particle simulation) an electron phase space is generated at the linac target. This phase space includes spatial intensity and energy distributions specific to the linac being modeled and Monte Carlo packages such as BEAMnrc and DOSXYZnrc can then be used to generate dose distributions in a patient, water tank, or phantom. Commissioning of the full linac simulation is performed in a similar way to what is currently practiced. However instead of changing the FWHM of the target Gaussian distributions, physical aspects of the gun and/or linac are adjusted. This chapter outlines the techniques and steps needed to create a full model of a linac (from gun to target), and the steps taken to commission it. With this information, a precise electron phase space can be determined at the target which is specific for the linac being modeled.

4.2   METHODS AND MATERIALS

4.2.1   Electron gun design and simulation

The initial stage in designing a Pierce-type electron gun requires the determination of desired injection beam properties. Laminar beams are a common design criterion for Pierce-type electron guns[29], where for medical accelerators a perveance of approximately 0.1×10^{-6} is common[30]. Incorporating these requirements, a beam described by Courant-Snyder parameters[31] of *α=±4.899*

(positive for a converging beam, negative for a diverging beam), $\beta=0.08$ mm/rad, and a normalized root-mean-square (rms) emittance of 0.47 π mm-mrad provided a good match to the stated perveance and measured gun current and cathode-anode potential; the results of the current and potential measurements are given in section 4.3.1. With the beam parameters set by the Courant-Snyder parameters, determining whether the laminar beam converged toward the central beam axis or diverged from it was the next design study. This was performed with the injection of a beam whose transverse phase space was described by the above given Courant-Snyder parameters. The waveguide model used for this study incorporated a 1.5 mm first side cavity shift as described by our previous work (chapter 3). This waveguide design was used due to the small RF field magnitude in the first half accelerating cavity minimizing the electron blooming and hence beam loss. The injected current and energy of the diverging and converging electron beams were set equal to the Varian 600C measurements given in section 4.3.1.

Upon the determination of the desired beam characteristics, a Pierce-type diode electron gun was designed using the 2D program EGN2w. EGN2w models the electron emission from the cathode as space charge limited and calculates the total current generated using Child's law given in eq. 2.84. The electron gun geometry was optimized to not only obtain the previously determined design criteria stated above, but also to match the gun current and cathode-anode potential measured from a Varian 600C linac. The final gun geometry was determined after numerous design iterations of cathode area and radius of curvature, anode aperture radius, anode nose cone length and curvature, focusing electrode shape and angle, and anode-cathode distance.

4.2.2   Electron trajectories within the linac waveguide

With the electron gun phase space calculated, PARMELA was used to calculate electron trajectories within the waveguide. The design of an in-line side-coupled 6 MV linac waveguide was outline previously in chapter 3, where the RF

field solution calculated was used as an input into PARMELA. Four million macroparticles were tracked through the linac over two RF periods and only the central electron bunch was used in the analysis disregarding the first and last half electron bunches. This removed all of the simulation end effects such that the analyzed beam represented a stead-state electron bunch. The size of the PARMELA phase space was increased by running EGN2w 60 times varying the number of electrons emitted off the cathode as well as their emission locations. This generated a total phase space of roughly 40 million particles.

Before the Monte Carlo simulations were performed, two different operations on the PARMELA generated phase space were required. The first involved a rotation of the PARMELA generated phase space. In a Varian 600C linac, the waveguide is rotated several degrees with respect to the inline and crossline axes such that the plane of the coupling cavities and port cavity does not fully lie along either axis. The simulated waveguide was thus also rotated by the same angle in order to accurately represent the effects of the side and port couplings in the inline and crossline profiles. The second operation involved a translation of the asymmetric electron intensity distribution with respect to the target coordinates to obtain symmetric dose distributions. The shifting was analogous to the commissioning of a medical linac where the waveguide is moved transversely with respect to the flattening filter until symmetric dose distributions are generated.

4.2.3   Monte Carlo linac head simulation with BEAM

The simulation of particle transport through a Varian 600C linac head (Figure 3.3) was performed using the Monte Carlo software package BEAMnrcMP 2007 (BEAM) from information provided from the manufacturer. All the BEAM parameters used in these simulations are identical to what was presented in Chapter 3, with the exception that roughly 3×10^8 initial histories were run requiring the PARMELA phase space to be recycled seven times. Field sizes of 40x40, 20x20, 10x10, and 5x5 cm^2 were simulated for this investigation.

4.2.4   Monte Carlo dose calculations with DOSXYZ

The dose distribution generated in water from the simulated linac was performed using the DOSXYZnrc 2007 Monte Carlo code (DOSXYZ). The number of particles simulated in DOSXYZ depended strongly on the field size. The 40x40 cm^2 field size required the largest number of particles to be simulated. The number of particles that would be required to be scored in the BEAM generated phase space file from initial $3x10^8$ histories run exceeded a 32 bit representation ($\approx 8x10^9$ particles generated). In order to overcome this problem, BEAM and DOSXYZ were run in unison using the *isource 9* input in DOSXYZ for the 40x40 and 20x20 cm^2 fields and thus no phase space was scored for these field sizes. Other Monte Carlo programs utilizing 64 bit representation (GEANT4) could overcome this, or, multiple smaller runs could have been combined, although this would add a significant amount of time to the simulations. The dose distributions for the 10x10 and 5x5 cm^2 field sizes were run by using a BEAM phase space file scored at a distance of 30 cm from the surface of the water tank. The total number of histories run in DOSXYZ was $7.8x10^9$, 2.0 x10^9, $2.0x10^9$ and $1.5x10^9$ for the 40x40, 20x20, 10x10 and 5x5 cm^2 field sizes respectively. The depth of the voxels for all depth dose (DD) simulations was 0.2 cm down to a depth of 1.5 cm and then 0.5 cm to a depth of 30 cm while the lateral dimensions were set to 1x1cm^2 for the two largest field sizes and 0.5x0.5 cm^2 for the two smallest field sizes. The total size of the water tank simulated was 66x66x48 cm^3, which approximated the size of the IBA Dosimetry (Bartlett, TN) water tank used for the measurements. The voxel sizes in which the dose was scored for the profiles varied in size depending on the field size that was simulated and were created such that the voxel width in the penumbra was 0.5 cm to approximate the volume averaging effect of the ion chamber used for the measurements. In order to ensure a sufficient number of points were obtained in the penumbra, all profiles were obtained through two simulations, with the voxel centers staggered to create points every 0.25 cm in the penumbra. The 40x40 and 20x20 cm^2 profiles had voxel dimensions of 1x1x0.5 cm^3 except in the penumbra

where the voxel size was reduced to 0.5x1x0.5 cm^3 while the 10x10 and 5x5 cm^2 profiles were generated using a uniform voxel size of 0.5x0.5x0.5 cm^3 for the entire profile. The ECUT and PCUT values were set to 0.70 MeV and 0.01 MeV for the DOSXYZ simulation, and no range rejection was used. All dose profiles were normalized to the central axis dose (D_{CAX}) while the DD curves were normalized to the dose at 10 cm depth (D_{10}).

In order to evaluate the goodness of agreement between the simulated and measured dose profiles, the simulated profiles were initially smoothed using a median filter, and a piecewise cubic interpolation was used. The comparison of the simulated and measured profiles was performed through the creation of a gamma index[32] with a 1%/1 mm acceptance criterion. The data preparation explained here and generating a gamma index is used for all subsequent dose comparisons in this thesis.

A flow chart summarizing the steps and programs used in the simulation process is shown in Figure 4.1.
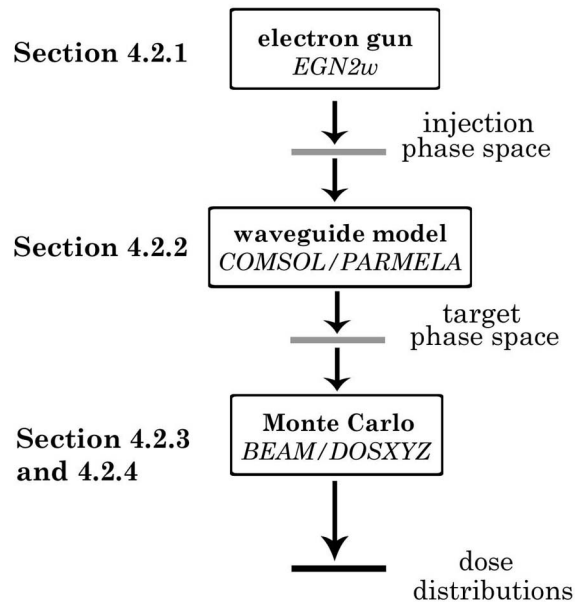
Figure 4.1: A flow chart showing the steps taken to simulate the linac is given. The grey lines represent electron phase space outputs, the black line represents the final dose distribution output, and all the simulation programs used are given in italics. The relevant sections describing each step are also shown in the flow chart.

4.2.5   **Measurements**

In order to design an electron gun with similar characteristics as the gun currently used in conjunction with the Varian 600C waveguide, and to ensure the simulated waveguide gun combination produced a similar capture efficiency, measurements of the cathode-anode potential, electron gun current and target current were made. The cathode-anode potential in a Varian 600C linac is dropped from ground to its maximum value in a pulsed fashion according to the duty cycle of the linac. The cathode-anode potential measurement was made through an oscilloscope with a Hewlett Packard (Palo Alto, CA) 35111A high voltage probe attached to the electron gun high voltage line. A correction factor of two was multiplied to the readout of the oscilloscope to account for the 1 MΩ input impedance of the oscilloscope and the 1 MΩ output impedance of the high voltage probe. The gun current was also measured on the high voltage line using a Stangenes Industries Inc. (Palo Alto, CA) 1-1.0 pulsed current transformer terminated in an impedance of 50 Ω at the oscilloscope. The output of the pulsed current transformer was designed to give 1 Amp / 1 Volt. The target current measurement was taken at the linac 600C console connected directly to the oscilloscope. The measurement was taken across a known resistance and the voltage measurement was converted to current using Ohm's law.

The dose measurements against which the Monte Carlo simulations were compared were taken using a Varian 600C linac with an IBA Dosimetry Scanditronix CC13 ion chamber with an active volume of 0.13 cm^3. The measurements for all field sizes were scanned with an IBA Dosimetry blue phantom water tank. All measured profiles were first centered using the D(50) values and then made symmetric by taking the mean value of two points equidistant from the central axis, and finally smoothed using Bezier smoothing[33]. This was all done within the OmniPro-Accept (Bartlett, TN) version 6.6B software package. The measured profiles were made symmetric (as explained above) in order to remove discrepancies in the comparison of measured and simulated profiles caused by slight asymmetries (within clinical standards) in the

measured profiles. In the Monte Carlo simulations, it was expected that the dose profile would be symmetric for a proper electron focal spot position with respect to the flattening filter, and any asymmetries would arise from some error in this focal spot positioning. Thus in the comparison of an ideal electron focal spot on the target, an 'ideal' measured dose profile was used. The measured dose profiles were normalized to D_{CAX} and the DD curves were normalized to D_{10} to avoid the uncertainty in the dose maximum measurement.

4.3   RESULTS AND DISCUSSION

4.3.1   Electrical measurements

The simulated electron gun was designed with a cathode-anode potential and a gun current matching measurements made on a Varian 600C linac. Figure 4.2a shows the measured electron gun current, Figure 4.2b shows the potential to which the cathode is dropped over the same time frame and Figure 4.2c gives the current measured at the target. The ordinate axis on Figure 4.2a reflects the pulsed transformers conversion of 1.0 Amps/Volt, the ordinate axis of Figure 4.2b reflects the correction factor of two accounting for the identical 1 MΩ impedances of the high voltage probe and oscilloscope and the ordinate axis in Figure 4.2c represents the result in Amperes after conversion of the measured potential over a known resistance using Ohm's law. The steady state electron gun current was determined to be 0.36±0.01 A as represented by the dotted line in Figure 4.2a. The value was determined near the end of the pulse to avoid the oscillations in current seen over most of the pulse. The cathode potential was determined to be -30.8±0.2 kV as represented by the dotted line of Figure 4.2b and was again taken near the end of the pulse and the target current was determined to be 0.134±0.003 A evaluated at the same time as the other measurements. The target current together with the cathode current measurement gave a capture efficiency of 37±2%.
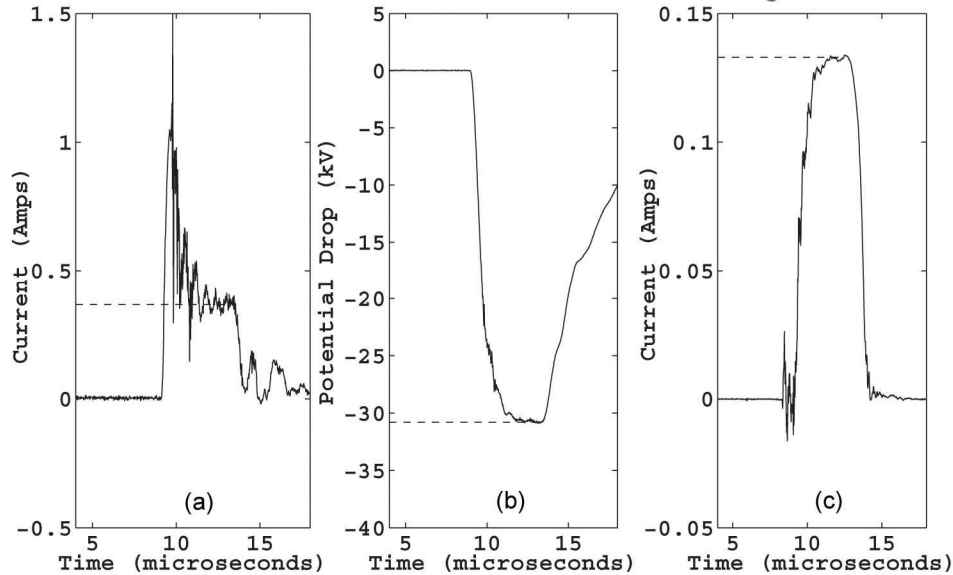
Figure 4.2: (a) The electron gun current with the ordinate axis converted to current using the pulsed transformer's conversion of 1.0 Amps/Volt. The dotted line reflects the current value measured on the electron gun and represents 0.36±0.01 A. (b) The potential drop at the cathode during the radiation pulse with the ordinate axis reflecting the correction factor required due to the 1 MΩ oscilloscope impedance. The dotted line represents the potential used for the electron gun simulations and represents -30.8±0.2 kV. (c) The target current of 0.134±0.003 A measured from a Varian 600C is shown with the ordinate axis changed to current using Ohm's law.

4.3.2   Electron gun simulations

Based on results from PARMELA simulations using an injection phase space described by the Courant-Snyder parameters, our electron gun was designed in order to achieve a converging beam. The results from these simulations showed that the diverging beam produced a capture efficiency of just 33%, eliminating it as a possibility since this value is below measurement. The converging beam however, produced a capture efficiency of 45%, meaning that through appropriate electron gun and first side cavity shift designs, a capture efficiency matching measurement could be obtained. Thus the electron gun designed in EGN2w was designed to achieve a laminar converging beam and produced a current of 0.358±0.002 A from a cathode potential of -30.8 kV. The final design of the

electron gun (Figure 4.3) was achieved through numerous geometric iterations in a trial and error fashion.

The complexity of the electron gun design process can be understood as follows: the cathode area and radius of curvature help define the initial electron trajectories as they are emitted from the metal, the focusing electrode angle and length further shape the beam shortly after emission. The length and diameter of the rounded edge of the focusing electrode help define the magnitude of convergence as does the radius of the anode. In effect all these geometries help determine the focal length of the system and hence the beam shape. All are required to be optimized to ensure a laminar converging beam. However, each alteration in the geometry changes the perveance, and hence the current (eq. 2.84) in a complex way. Thus numerous iterations were required to ensure all design parameters were met. Other geometries shown in Figure 4.3 not discussed here were simply designed to further adjust the perveance in a way to ensure all design parameters were met.
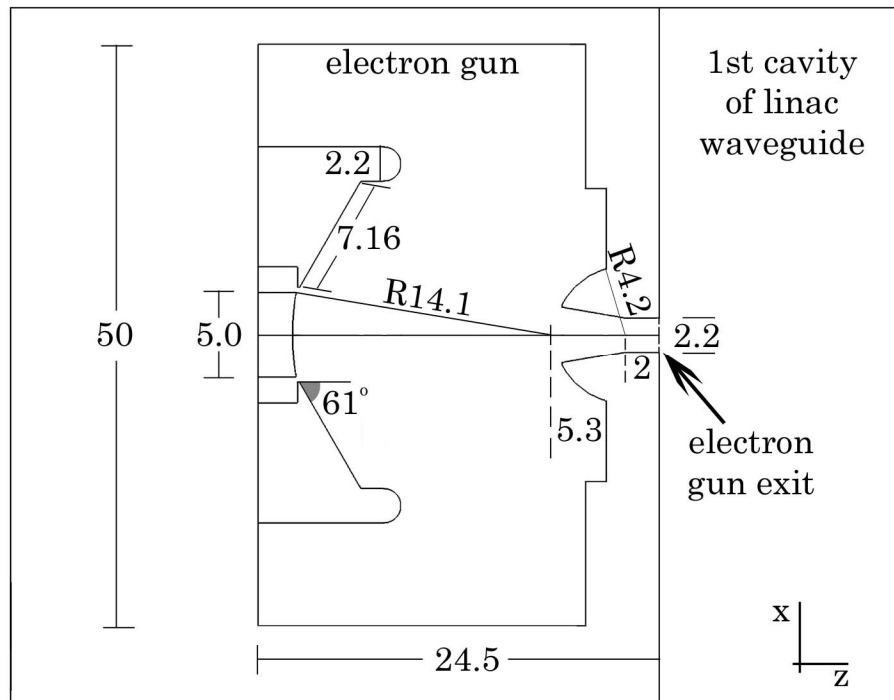
Figure 4.3: The electron gun design is shown in the xz plane. All dimensions are in mm.

The characteristics of the electron beam generated from the designed electron gun can be represented by the beam emittance and a transverse phase space plot taken at the electron gun exit (see Figure 4.3). Figure 4.4 shows the transverse phase space plot for the EGN2w model. The ordinate of the phase space plot given in Figure 4.4 is the transverse divergence coordinate x' which is a ratio of momenta p_x/p. The same is true for y' where the momenta ratio is p_y/p, but only the x component phase space plots are shown since the y plot is identical to the x plot. An ideal laminar beam has linearly increasing trajectory angles with increasing distance away from the cathode center. In an ideal laminar beam (which is never fully realized practically), particles near the cathode center travel with little angular deflection, while particles near the cathode edge have the largest angular deflection creating a beam with no trajectory crossings. However, in the simulations, the larger cathode area compared to the smaller injected beam cross section creates spherical aberrations causing the outer electrons to cross the paths of inner electrons producing some of the non-laminar aspects seen in the electron phase space of Figure 4.4. This effect may be a real effect, but can also be caused by the way space charge is allocated near the cathode edges[29]. An additional cause of the non-laminar portion of the injected electron phase space is due to non-linear electric forces on the beam.[34] The non-laminar aspects of the injected electron beam coming from non-linear electric forces were minimized through optimization of the cathode, anode, focusing electrode and anode radius designs. The emittance serves as a metric to measure the electron beam quality (a measure of how ordered and coherent a beam is), with an ideal laminar beam having the highest beam quality with a normalized rms emittance of zero. The electron beam from the EGN2w simulation gave a normalized rms emittance of 0.148 π mm-mrad.
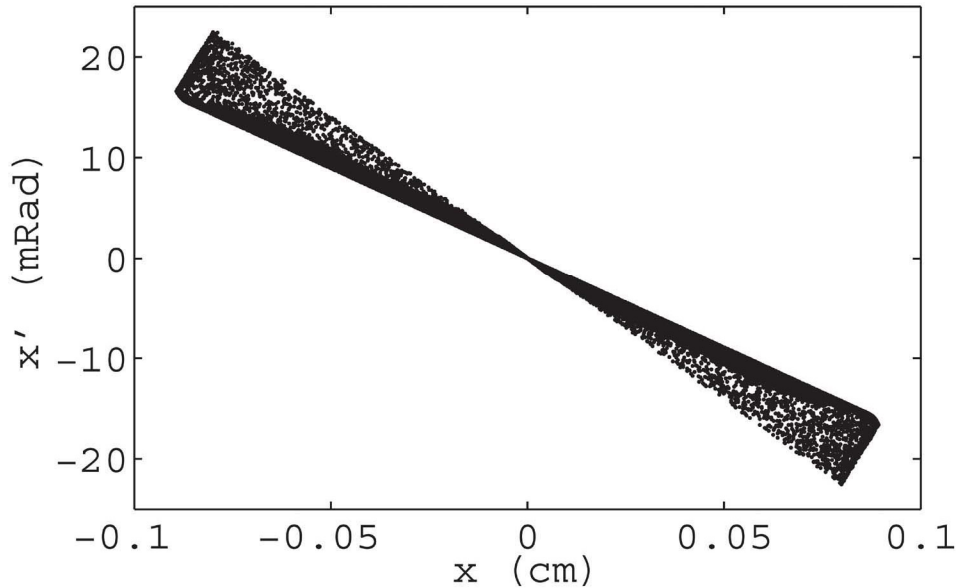
Figure 4.4: The transverse phase space for the EGN2w model.

4.3.3   Validation of the full linac simulation

4.3.3.1   Target focal spot size

The target focal spot size and the capture efficiency both were controlled by the magnitude of the first side cavity shift of the waveguide nearest the electron gun (chapter 3)[28]. It was found that a side cavity shift of 0.5 mm yielded a target current of 0.143±0.001 A (39.9±0.5% capture efficiency), 0.25 mm gave a target current of 0.136±0.001 A (38.0±0.5% capture efficiency), and no cavity shift gave a target current of 0.126±0.001 A (35.2±0.5% capture efficiency). From this it can be seen that a shift of 0.25 mm gives the correct capture efficiency and target current within error of the measurement. With a side cavity shift of 0.25 mm, the electron blooming created a beam diameter that was larger than the diameter of the beam tube diameter. Thus the maximum extent of the focal spot was restricted to the 5 mm diameter of the beam tube.

The spatial intensity distributions, in x and y, generated from the PARMELA runs are shown in Figure 4.5. The circular focal spot extends 5 mm and has a FWHM of 0.12 mm. As shown in chapter 3, the effects of side and port coupling causes the shifting and skewing of the electron distributions seen in

Figure 4.5. The peak shifts are -0.19 mm and -0.18 mm, and the center of gravity shifts are -0.09 mm and -0.06 mm for the x and y distributions respectively. The largest shift is seen in the x direction, but the largest skewing is in the y direction (as measured by the difference between the peak and the center of gravity). The simulation of the spatial intensity distribution at the target shown in Figure 4.5 is in direct contrast to the Gaussian distribution typically used in BEAM simulations of in-line linacs.
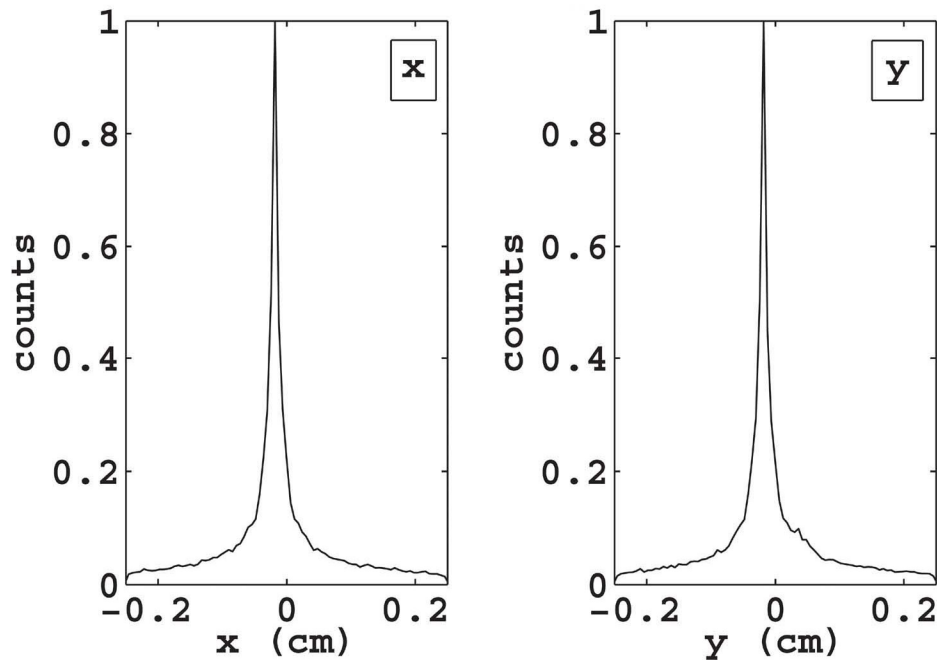
Figure 4.5: The x and y normalized spatial intensity distribution profiles at the target are given.

The phase space at the target generated from PARMELA was run through BEAM and DOSXYZ to produce 5x5 cm^2 profiles to validate the calculated focal spot size, since small-field profiles are very insensitive to energy changes but highly sensitive to the focal spot size[9]. It was found that by translating the PARMELA phase space by +0.08 mm in the x and y directions, symmetric dose profiles were obtained and the resulting 5x5 cm^2 inline and crossline profiles are shown in Figure 4.6a and Figure 4.6b respectively. Excellent agreement to measurement was found with 99.8% of all points meeting the 1%/1 mm

acceptance criterion. The shape of the focal spot seems to have a negligible impact on the dose profiles, considering a Gaussian intensity distribution typically used for BEAM simulations of low energy in-line linacs[11] show a similar agreement to measurement.
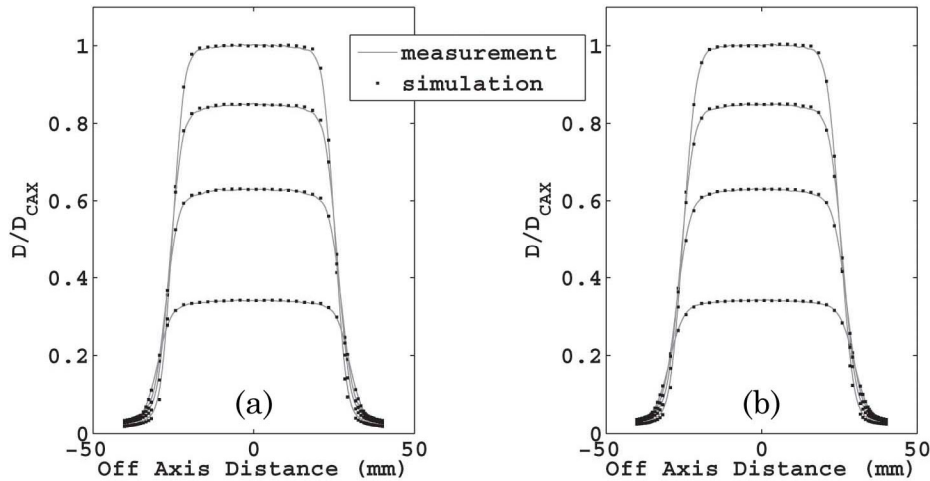
Figure 4.6: Measured and simulated (a) inline and (b) crossline 5x5 cm^2 profiles for the 0.25 mm cavity shift at 1.5, 5, 10 and 20 cm depths.

4.3.3.2   Electron beam energy

The COMSOL finite-element waveguide simulation does not to account for the real effects of power loss in the transmission waveguide, circulator, ceramic RF window separating the SF_6 gas and vacuum, manufacturing defects etc. so the exact power in the RF fields, and hence the exact electron beam energy is unknown. However, through the Monte Carlo commissioning process the electron beam energy can be determined. Wide field 40x40 cm^2 profiles have been shown to be sensitive to both the focal spot size and the electron beam energy[8] where a 0.2 MeV change in energy resulted in an approximately 2% change in the magnitude of the profile horn. Therefore, with the focal spot size verified using the 5x5 cm^2 field profiles, the wide field profile was used to determine the mean energy of the electron beam, and this energy was then verified by comparing DD curves. By adjusting the input power in the COMSOL FEM waveguide model by very small amounts, three different electron beams

with mean total energies (kinetic plus rest energy) of 5.4, 5.6 and 5.8 MeV incident on the target were simulated and used as input into BEAM and DOSXYZ to generate the three 40x40 cm^2 profiles shown in Figure 4.7. An energy spectrum giving a mean and maximum total energy of 5.6 and 6.3 MeV respectively provided the best match between simulation and measurement with 98.2% of all points meeting a 1%/1 mm acceptance criterion while the mean beam total energies of 5.4 and 5.8 MeV had only 50% and 60% of all points meeting the acceptance criterion respectively. The profiles shown in Figure 4.7 are also affected largely by the target thickness and density as well as the flattening filter shape and density. However, since these components were specified directly by the manufacturer, it not expected that they will lead to large errors in the dose profiles.
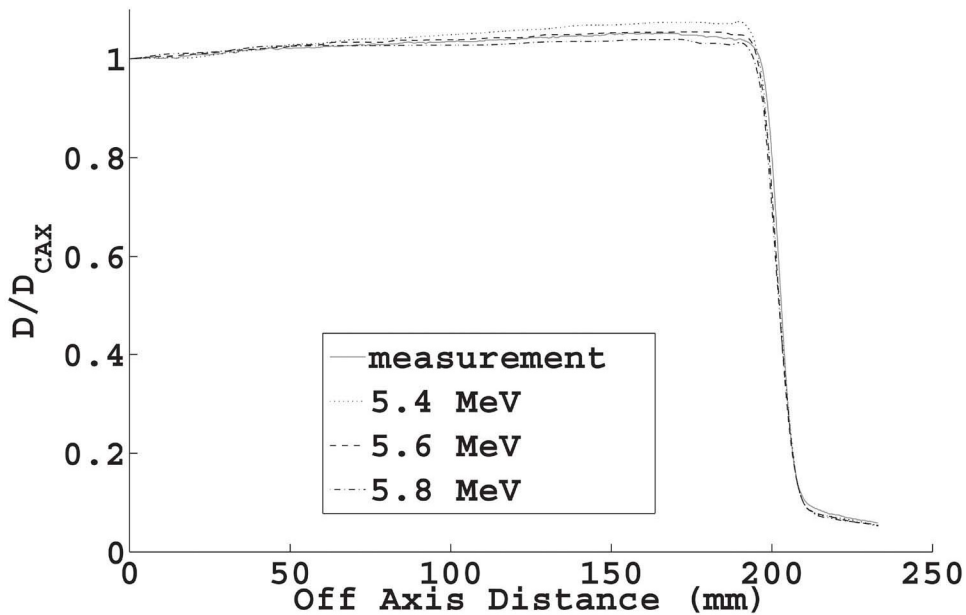
Figure 4.7: The crossline dose profiles for three different mean total energies of 5.4, 5.6 and 5.8 MeV were compared to measurement to determine the correct beam energy. Only this section of the profile is shown for visual clarity. The left half of this profile as well as the inline profile is identical to what's given above.

The electrons being injected over all RF phases gives the energy spectrum shown in Figure 4.8. The electrons with total energy greater than 5.8 MeV were

captured within an 'RF bucket', meaning they experience nearly the same RF phase in each accelerating cavity and hence the same field gradient in each cavity. The lower energy electrons experience a sequentially lower field gradient as they enter each accelerating cavity at different phases of the RF wave. Electrons that experience slightly different phases in each accelerating cavity gain slightly less energy, and those that experience drastically different RF phases in each accelerating cavity gain very little energy. In the extreme case, electrons can experience a decelerating field causing them to be lost outside the beam tube, or accelerated back toward the electron gun. This distribution of electrons accelerating at all phases of the RF wave produces the long low energy tail of the energy spectrum seen in Figure 4.8. The bimodal peaks of the total energy spectrum found at 5.8 and 6.3 MeV results from two stable but separate phases in the RF bucket for the captured electrons. The bimodal energy spectrum shown in Figure 4.8 again differs from the assumed Gaussian model used for in-line linacs. Since the results presented here were generated from a full linac simulation incorporating all of the relevant physics, these results are thought to be more accurate than the previously assumed Gaussian models.
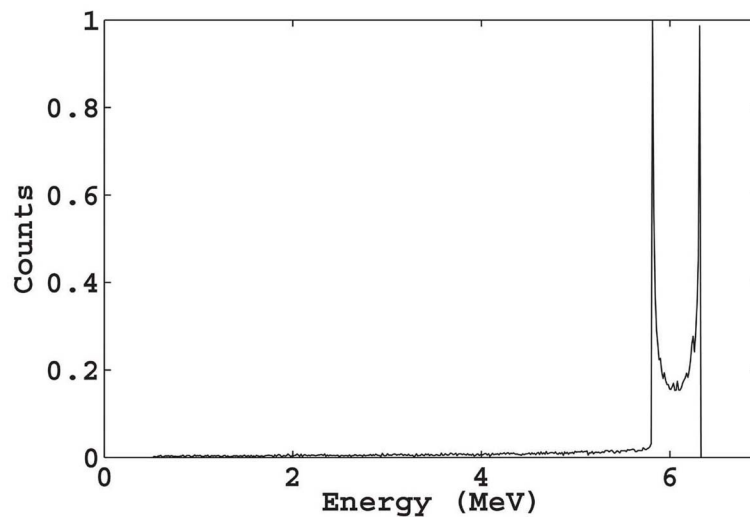
Figure 4.8: The optimal electron beam total energy spectrum for an in-line side-coupled 6 MV linac waveguide. The two large energy peaks correspond to total energies of 5.8 MeV and 6.3 MeV with the spectrum's maximum and mean total energy of 6.3 MeV and 5.6 MeV respectively.

The total power required from the linac simulation to accelerate the electrons to a total energy of 6.3 MeV did not exceed the power generated from clinically used magnetrons, which is roughly 2 MW for e2v technologies (Chelmsford, Essex, England) magnetrons at a frequency around 2998.5 MHz. The power required to accelerate the electrons to the given maximum energy was determined to be 1.3 MW from the FEM simulations. The power requirement for a manufactured clinical linac is however expected to be somewhat more than what was determined through the FEM solution since the simulation does not account for power loss in the transmission waveguide, circulator, ceramic RF window separating the SF_6 gas and vacuum, manufacturing defects etc.

4.3.3.3   *Dose distributions at various field sizes and depths*

The electron beam with the spatial intensity distribution and energy spectrum shown in Figure 4.5 and Figure 4.8 was used to generate DD curves for 40x40, 20x20, 10x10, and 5x5 cm^2 field sizes and profiles at the same field sizes at depths of 1.5, 5, 10, and 20 cm. Figure 4.9a shows the crossline profiles for all field sizes at a depth of 5 cm, Figure 4.9b shows the inline profiles for all field sizes at a depth of 10 cm, and Figure 4.10 gives the DD curves for all field sizes. The inline and crossline profiles for all field sizes and depths show similar symmetry and agreement to measurements, therefore only representative profiles at 5 and 10 cm depths are given in Figure 4.9. Greater than 99% of all points in the simulated profiles met the 1%/1 mm acceptance criterion for the 20x20, 10x10 and 5x5 cm^2 field sizes and greater than 98% of all points met the given acceptance criterion for the largest 40x40 cm^2 field size. It is expected that the penumbra of the largest field will have extreme sensitivity to differences between modeled and physical linac components, in particular in the flattening filter. The discrepancies for the DD curves at all field sizes also showed excellent agreement within statistical uncertainty with agreement to within 1% or less after a depth of 1.5 cm.

Despite the focal spot and energy spectrum presented here differing from an assumed Gaussian model (which is currently used in Monte Carlo simulations), the dose distributions presented show the same agreement to measurement as presented in the literature (within 1%). Thus, the exact nature of the electron phase space at the target does not have a large impact on the resulting dose distributions which is typically used to commission the simulated linac.
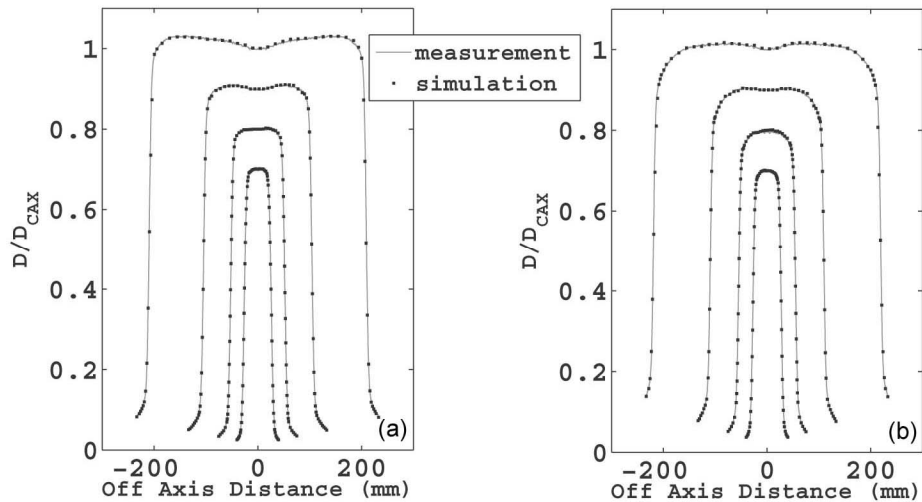
Figure 4.9: (a) Crossline profiles for 40x40, 20x20, 10x10 and 5x5 cm² field sizes at 5 cm depth. (b) Inline profiles for the same field sizes at a depth of 10 cm. The profiles were initially normalized to the D_{CAX} dose and then were scaled in the plots for visual clarity.
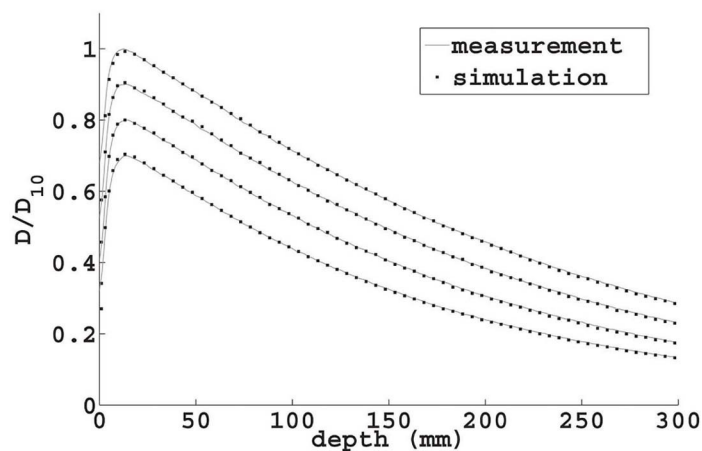
Figure 4.10: The DD curves for the 40x40, 20x20, 10x10 and 5x5 cm² field sizes were initially normalized at D_{10} and were then scaled for visual clarity. The uppermost DD curve is for the 40x40 cm² field and the bottommost DD curve is for the 5x5 cm² field size with the 20x20 and 10x10 cm² falling in between.

4.3.3.4   Sensitivity of the dose distributions on the electron gun parameters

A change in the cathode-anode potential of the electron gun directly affects the injection electron beam energy which in turn affects the shape of the electron energy distribution at the target, and the dose distributions. For example, a 15 kV reduction in the cathode anode potential, all else being constant, changed the bi-modal energy distribution into a single peak. This can be understood by the slower energy electrons being captured in a single stable phase of the RF as compared to the dual stable phases of the bi-modal energy peak. The 15 kV reduction in the injection energy corresponded to a 0.2 MeV reduction in the mean beam energy at the target which produced no change in the DD curve within statistical uncertainty, but showed an approximately 2% increase in the magnitude of the profile horns of the 40x40 cm^2 field. In addition, for a constant mean beam energy of 5.6 MeV, the DD curves resulting from using either a Gaussian, bi-modal, or single peaked electron energy spectrum showed less than 1% difference from each other. Thus the DD curves are very insensitive to changes in the cathode-anode potential and the shape of the electron energy spectrum at the target. However, since the bi-modal energy distribution was derived through the matching of electrical measurements as explained above, it is expected to be the best approximation of the energy spectrum for this linac waveguide.

Changes in the electron gun geometry will affect the divergence and beam diameter of the electrons injected into the waveguide (as explained in section 4.2.1), but not their energy. An example of this is a 0.1 mm reduction in the injected beam diameter changed the focal spot size at the target by about 0.3 mm which had no effect on the DD curves. However, this change resulted in a 1% increase in the magnitude of the dose profile horns for the 40x40 cm^2 field. Changes in the divergence of the injected beam largely affected the capture efficiency (section 4.3.2), but not the focal spot size (less than 1% change) or the DD curve within statistical uncertainty.

4.4   CONCLUSIONS

An integrated in-line side-coupled 6 MV linac model has been developed, benchmarked, and commissioned against measurements. A Pierce-type diode electron gun simulation was designed according to parameters measured from a Varian 600C. Specifically a cathode potential of -30.8 kV was modeled producing a fairly laminar converging electron beam at a current of 0.358±0.002 A. The designed electron gun was used together with a simulated in-line side-coupled waveguide incorporating a 0.25 mm first side cavity shift to obtain a target current of 0.136±0.001 A and a capture efficiency of 38.0±0.5%, matching measurement within error. The resulting focal spot size and designed mean beam energy of 5.6 MeV was used to generate simulated dose distributions through Monte Carlo. These simulated profiles were compared to measurements and showed excellent agreement with greater than 99% of all points meeting a 1%/1 mm acceptance criterion for the 20x20, 10x10, and 5x5 cm^2 field sizes at all depths with the exception of the largest 40x40 cm^2 field for which 98% of all points met the acceptance criterion. The simulated DD curves also matched measurement to 1% within uncertainty deeper than 1.5 cm.

4.5   REFERENCES

[1] D. W. O. Rogers, B. A. Faddegon, G. X. Ding, C. M. Ma, J. We, and T. R. Mackie, "BEAM - A Monte Carlo code to simulate radiotherapy treatment units," Med. Phys., **22**, 503-524 (1995).

[2] I. Chetty, J. J. DeMarco, and T. D. Solberg, "A virtual source model for Monte Carlo modeling of arbitrary intensity distributions," Med. Phys., **27**, 166-172 (2000).

[3] J. Deng, S. B. Jiang, A. Kapur, J. S. Li, T. Pawlicki, and C. M. Ma, "Photon beam characterization and modelling for Monte Carlo treatment planning," Phys. Med. Biol., **45**, 411-427 (2000).

[4] G. X. Ding, "Energy spectra, angular spread, fluence profiles and dose distributions of 6 and 18 MV photon beams: results of Monte Carlo simulations for a Varian 2100EX accelerator," Phys. Med. Biol., **47**, 1025-1046 (2002).

[5] P. Francescon, C. Cavedon, S. Reccanello, and S. Cora, "Photon dose calculation of a three-dimensional treatment planning system compared to the Monte Carlo code BEAM," Med. Phys., **27**, 1579-1587 (2000).

[6] P. J. Keall, J. V. Siebers, B. Libby, and R. Mohan, "Determining the incident electron fluence for Monte Carlo-based photon treatment planning using a standard measured data set," Med. Phys., **30**, 574-582 (2003).

[7] B. Libby, J. Siebers, and R. Mohan, "Validation of Monte Carlo generated phase-space descriptions of medical linear accelerators," Med. Phys., **26**, 1476-1483 (1999).

[8] J. Pena, L. Franco, F. Gomez, A. Iglesias, R. Lobato, J. Mosquera, A. Pazos, J. Pardo, M. Pombar, A. Rodriguez, and J. Sendon, "Commissioning of a medical accelerator photon beam Monte Carlo simulation using wide-field profiles," Phys. Med. Biol., **49**, 4929-4942 (2004).

[9] J. Pena, D. M. Gonzalez-Castano, F. Gomez, F. Sanchez-Doblado, and G. H. Hartmann, "Automatic determination of primary electron beam parameters in Monte Carlo simulation," Med. Phys., **34**, 1076-1084 (2007).

[10] L. L. W. Wang, and K. Leszczynski, "Estimation of the focal spot size and shape for a medical linear accelerator by Monte Carlo simulation," Med. Phys., **34**, 485-488 (2007).

[11] D. Sheikh-Bagheri, and D. W. O. Rogers, "Sensitivity of megavoltage photon beam Monte Carlo simulations to electron beam and other parameters," Med. Phys., **29**, 379-390 (2002).

[12] D. Sheikh-Bagheri, and D. W. O. Rogers, "Monte Carlo calculation of nine megavoltage photon beam spectra using the BEAM code," Med. Phys., **29**, 391-402 (2002).

[13] M. K. Fix, P. J. Keall, and J. V. Siebers, "Photon-beam subsource sensitivity to the initial electron-beam parameters," Med. Phys., **32**, 1164-1175 (2005).

[14] M. K. Fix, H. Keller, P. Ruegsegger, and E. J. Born, "Simple beam models for Monte Carlo photon beam dose calculations in radiotherapy," Med. Phys., **27**, 2739-2747 (2000).

[15] M. K. Fix, P. Manser, E. J. Born, R. Mini, and P. Ruegsegger, "Monte Carlo simulation of a dynamic MLC based on a multiple source model," Phys. Med. Biol., **46**, 3241-3257 (2001).

[16] J. Sempau, A. Sanchez-Reyes, F. Salvat, H. O. ben Tahar, S. B. Jiang, and J. M. Fernandez-Varea, "Monte Carlo simulation of electron beams from an accelerator head using PENELOPE," Phys. Med. Biol., **46**, 1163-1186 (2001).

[17] L. Blazy, D. Baltes, J. M. Bordy, D. Cutarella, F. Delaunay, J. Gouriou, E. Leroy, A. Ostrowsky, and S. Beaumont, "Comparison of PENELOPE Monte Carlo dose calculations with Fricke dosimeter and ionization chamber measurements in heterogeneous phantoms (18 MeV electron and 12 MV photon beams)," Phys. Med. Biol., **51**, 5951-5965 (2006).

[18] P. Carrasco, N. Jornet, M. A. Duch, L. Weber, M. Ginjaume, T. Eudaldo, D. Jurado, A. Ruiz, and M. Ribas, "Comparison of dose calculation algorithms in phantoms with lung equivalent heterogeneities under conditions of lateral electronic disequilibrium," Med. Phys., **31**, 2899-2911 (2004).

[19] D. Sheikh-Bagheri, D. W. O. Rogers, C. K. Ross, and J. P. Seuntjens, "Comparison of measured and Monte Carlo calculated dose distributions from the NRC linac," Med. Phys., **27**, 2256-2266 (2000).

[20] D. A. Jaffray, J. J. Battista, A. Fenster, and P. Munro, "X-ray sources for medical linear accelerators - focal and extra-focal radiation," Med. Phys., **20**, 1417-1427 (1993).

[21] P. Munro, J. A. Rawlinson, and A. Fenster, "Therapy imaging - source sizes of radiotherapy beams," Med. Phys., **15**, 517-524 (1988).

[22] F. M. Bieniosek, E. Henestroza, and J. W. Kwan, "Performance of the K+ ion diode in the 2 MV injector for heavy ion fusion," Rev. Sci. Instrum., **73**, 1042-1044 (2002).

[23] M. K. Hornstein, V. S. Bajaj, R. G. Griffin, and R. J. Temkin, "Efficient low-voltage operation of a CW gyrotron oscillator at 233 GHz," IEEE Trans. Plasma Sci., **35**, 27-30 (2007).

[24] F. M. Bieniosek, J. W. Kwan, E. Henestroza, and C. Kim, "Development of the 2-MV Injector for HIF," Nucl. Instrum. Methods Phys. Res. Sect. A-Accel. Spectrom. Dect. Assoc. Equip., **464**, 592-598 (2001).

[25] S. J. Park, S. H. Kim, Y. J. Park, J. S. Oh, S. H. Nam, C. H. Chung, M. H. Cho, and W. Namkung, "Development of a high-power klystron for radio-frequency linear accelerators," J. Korean Phys. Soc., **48**, 786-790 (2006).

[26] J. Reijonen, Q. Ji, T. J. King, K. N. Leung, A. Persaud, and S. Wilde, "Compact focusing system for ion and electron beams," J. Vac. Sci. Technol. B, **20**, 180-184 (2002).

[27] A. Kponou, E. Beebe, A. Pikin, G. Kuznetsov, M. Batazova, and M. Tiunov, "Simulation of 10 A electron-beam formation and collection for a high current electron-beam ion source," Rev. Sci. Instrum., **69**, 1120-1122 (1998).

[28] J. St. Aubin, S. Steciw, and B. G. Fallone, "The design of a simulated in-line side-coupled 6 MV linear accelerator waveguide," Med. Phys., **37**, 466-476 (2010).

[29] W. B. Herrmannsfeldt, "EGUN - An electron optics and gun design program," *SLAC-331-UC-28(A)*, 1988

[30] C. J. Karzmark, C. S. Nunan, and E. Tanabe, *Medical electron accelerators* (McGraw-Hill, New York, 1993).

[31] T. P. Wangler, *RF linear accelerators* (Wiley-VCH, Weinheim, 2008).

[32] D. A. Low, W. B. Harms, M. Mutic, and J. A. Purdy, "A technique for the quantitative evaluation of dose distributions," Med. Phys., **25**, 656-661 (1998).

[33] R. H. Bartels, J. C. Beatty, and B. A. Barsky, "Bezier Curves,"in *An Introduction to Splines for Use in Computer Graphics and Geometric Modelling* (Morgan Kauffman Publishers Inc., Los Altos, CA, 1987).

[34] S. Humphries, *Charged Particle Beams* (John Wiley & Sons, New York, 1990).

CHAPTER 5: Effect of transverse magnetic fields on a simulated in-line 6 MV linac

*A version of this chapter has been published. J. St. Aubin, S. Steciw, B.G. Fallone, "Effect of transverse magnetic fields on a simulated in-line 6 MV linac," Phys. Med. Biol., **55**, 4861-4869 (2010).*

5.1   INTRODUCTION

The work presented here builds on our work of a linac simulation (chapters 3[1] and 4[2]) by further investigating its operation in the presence of transverse magnetic fields. To date only one investigation has been published on the effects of magnetic fringe fields on a medical linac[3]. They investigated the effects of the magnetic fringe fields from a 1.5 T linac-MR system on 2 m long accelerating waveguides in adjacent vaults. The linear accelerators in that study were positioned 8 and 12 m away from the MR magnet, and the built in beam control systems, which correct for the changes in earth's magnetic field at different gantry angles, were exploited to correct the effects of the additional fringe fields from the MR. In contrast, the linac generating the X-rays for the linac-MR system is in close proximity to the MR imager with the target at approximately 1.5 m from the magnet isocenter. At this distance, the electron gun is expected to experience field strengths of 30 – 50 G, which increases to 80 – 100 G at the target for our low field linac-MR system. In addition, the linacs proposed for use with linac-MR systems do not include built-in beam control systems since they use much shorter in-line side-coupled 6 MV waveguides. Because our institute has limited access to dedicated research linacs on which magnetic field studies could be performed, magnetic field measurements on an actual in-line 6 MV linac were not possible. Thus the full in-line side-coupled 6 MV linear accelerator simulation designed and validated previously was used. Using the simulation has the added advantage of performing investigations on linac operation in the most extreme cases with field strengths resulting in 100% beam loss where measurements may be unpractical.

With no built-in beam control mechanism for the 6 MV linac, alternative solutions for correcting or avoiding any deleterious effects on the linac from the magnetic fringe fields are required. These solutions will only come after an understanding of 6 MV linac performance within an external magnetic field is obtained. The two proposed linac-MR systems[4, 5] are designed such that the magnetic fringe fields cross through the 6 MV linac perpendicular to its length. Our previously validated linac simulation incorporated the widely used 2D axisymmetric program EGN2w together with the finite element program (FEM) COMSOL and the particle-in-cell program PARMELA. However, EGN2w cannot be used directly for the investigation of linac performance in an external transverse magnetic field that crosses through the linac since it only allows for the addition of axisymmetric magnetic fields. Thus the fully 3D FEM electron gun program OPERA-3d/SCALA (Kidlington, UK) was used in its stead. An investigation was performed to determine the effects on the electron beam calculated at the target as well as the dosimetric effects caused by a transverse magnetic field.

5.2   METHODS AND MATERIALS

5.2.1   Simulation of the linac in the presence of transverse magnetic fields

The linac simulation used to investigate the effect of transverse magnetic fields was fully 3D in nature incorporating a 3D electron gun simulation using OPERA-3d/SCALA, 3D radio-frequency (RF) solution within the waveguide from COMSOL, and 3D particle tracking in PARMELA. The geometry of the EGN2w electron gun design presented in chapter 4 (Figure 4.3) was replicated in OPERA-3d to obtain the FEM electrostatic field solution and to calculate space charge effects with electron emission at the cathode set by Child's law (eq. 2.84). Transverse magnetic fields were added to the linac simulation in OPERA-3d/SCALA (hereafter referred to as SCALA) and PARMELA, and the electrons were tracked from the electron gun cathode to the target. As shown by work

performed previously (chapter 4), nominal linac operation inherently yields a 63±1% electron beam loss[2]. The subsequent beam loss percentages quoted throughout this chapter will refer to relative beam losses *above* the nominal 63%.

5.2.2   Dosimetric effects

Before Monte Carlo simulations were performed, the electron spatial intensity distribution at the target, generated from the PARMELA phase space, was translated laterally with respect to the center of the flattening filter. This translation was performed to ensure the dose profiles were symmetric as required for a clinical radiation beam and is analogous to the commissioning process performed when the waveguide is first installed in the linac head. A PARMELA generated phase space comprised of roughly 40 million particles was generated by running SCALA and PARMELA 60 times with random electron injection positions.

The geometry of the linac head (Figure 3.3) was modeled in BEAM from information on a Varian 600C supplied from the manufacturer. Roughly 5×10^8 initial histories were run recycling the PARMELA phase space 12 times. Field sizes of 40x40 and 20x20 cm^2 were simulated and all other BEAM parameters as explained in Chapter 3 were used for this analysis. BEAM and DOSXYZ were run in unison using the *isource 9* input in DOSXYZ and thus no phase space was required to be scored. All DOSXYZ parameters explained in Chapter 4 were used for this investigation. The dose profiles were normalized to the central axis dose (D_{CAX}) while the depth dose (DD) curves were normalized to the dose at 10 cm depth (D_{10}). Smoothing and interpolation of the dose profiles was performed as explained in Chapter 4 together with the generation of a gamma index[6] using a 1%/1 mm acceptance criterion. In order to evaluate the effect of the transverse magnetic fields on the simulated profiles, they were compared to the validated simulation profile given in chapter 4 at 0 G. By comparing to a validated simulation profile, only changes caused by the transverse magnetic fields are quantified. No magnetic fields were added to the Monte Carlo simulations in

order to solely investigate the effect of the magnetic field on the linac structure (electron gun and waveguide).

5.3   RESULTS AND DISCUSSION

5.3.1   Validation of the 3D SCALA electron gun

The geometry of the EGN2w electron gun[2] was replicated in SCALA (Figure 5.1) and the simulation results were compared. The emission current of the SCALA electron gun was determined to be roughly 20% greater than EGN2w predicted. Both programs determine the emission current from Child's law where the net potential at the cathode (which is the sum of the anode-cathode potential and the space charge potential) is zero. Thus the determination of emission current is critically dependent on the resolution of the electrostatic field at the cathode. SCALA uses isoparametric mesh elements to conform to curved geometries (such as the cathode). It also has the advantage of using quadratic basis functions in the determination of the electrostatic field solution and the space charge field creating a more accurate solution[7]. EGN2w on the other hand uses a square mesh and a finite difference approximation for the electrostatic field solution. The higher field resolution and conformal meshing of SCALA is expected to explain the differences in emission current between the two electron gun programs. The higher emission current in SCALA required a slight modification of the cathode to regain the measured emission current of a Varian (Palo Alto, CA) 600C linac of 0.36 ± 0.01 A[2]. The cathode radius was reduced by 7.6% from 2.5 mm to 2.31 mm giving an emission current of 0.361 ± 0.002 A. The emittance of the electron beam generated in SCALA was calculated to be 0.323 π mm-mrad compared to 0.148 π mm-mrad from EGN2w. The 3D SCALA electron gun was used as an input into our linac waveguide simulation at 0 G yielding a target current within measurement[2] of 0.131 ± 0.002 A. The linac simulation results using the 3D SCALA electron gun simulation were compared to the results previously presented using the 2D program EGN2w. This comparison showed a maximum discrepancy in electron energy and beam centroid at the target of 0.015 MeV and

0.01 mm respectively. When the 3D SCALA electron gun was used as an injector to our linac simulation and Monte Carlo simulations were performed, the simulated dose distributions were found to agree to measurement with the same accuracy as was presented in chapter 4.
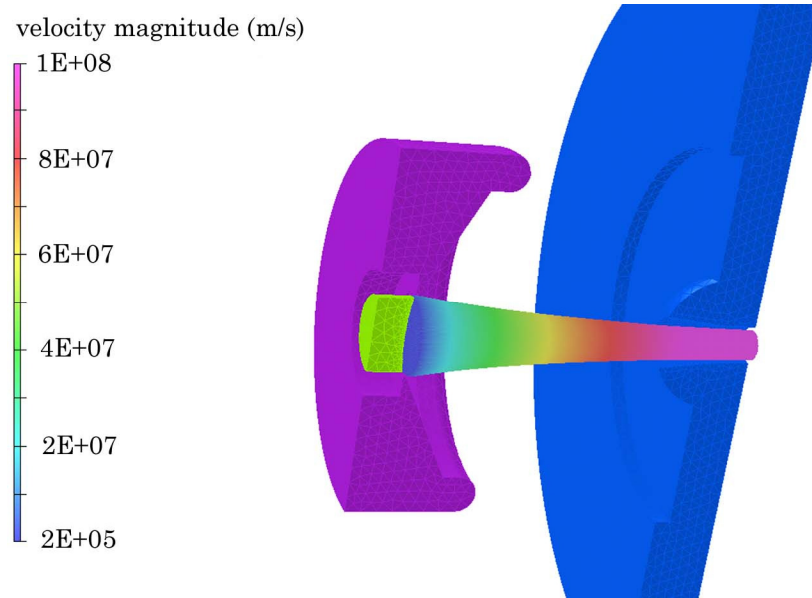
Figure 5.1: The geometry of the 3D SCALA electron gun with the beam colouring corresponding to the electron velocities. Only half of the geometry is shown with the anode on the right, the focusing electrode on the left, and the cathode defined by the location of electron emission.

5.3.2   Earth's Magnetic field

The validation of the simulation in the absence of magnetic field through the matching of the simulated electron gun and target currents, the electron gun cathode-anode potential, and dose distributions to measurements from a Varian 600C (section 4.3.1) is extended to simulation in earth's magnetic field. In Edmonton, Canada, the direction of earth's field is approximately 18° from vertical, so for the simulation 0.4755 G was directed along the length of the waveguide and 0.1545 G is directed transverse to the waveguide length through the coupling cavities (inline direction). With the addition of earth's magnetic field, the target current calculated was 0.131±0.002 A from an injection current of 0.361±0.002 A matching measured values from a Varian 600C. No changes in

energy were observed in this simulation compared to the validated linac simulation (section 4.3.2 and section 4.3.3). The only difference in the spatial distribution occurred in the y direction as seen in Figure 5.2, with the peak position shifted by -0.007 cm and the center of gravity shifted by -0.004 cm.
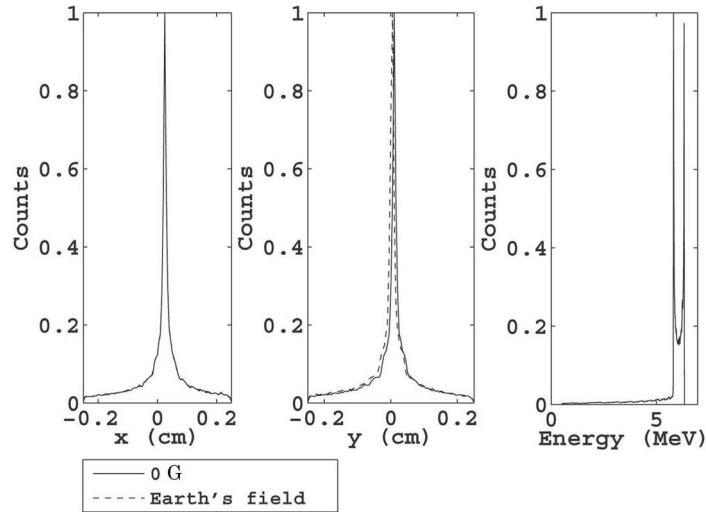
Figure 5.2: A comparison of the spatial intensity distribution and the energy spectrum of the electrons incident on the target for the linac simulation with and without earth's magnetic field. The results shown are normalized to the 0 G results and no differentiation between the two simulations in the figure is seen for the x spatial intensity distribution or the energy spectrum.

The dose distributions with the linac submersed in Earth's magnetic field showed excellent agreement to measurement. The DD curve was also found to agree within 1% of measurement giving the same results as section 4.3.3. Since the effect of a transverse field in the +x direction was observed in the y spatial distribution only (i.e. perpendicular to the coupling cavities), all subsequent dose analysis was focused on differences in the crossline 'y' profile. When the earth's magnetic field was added to the full linac simulation and the dose distributions were generated, it was found that greater than 99% of all points met the 1%/1 mm acceptance criterion for the 20x20, 10x10, and 5x5 cm^2 field sizes, and greater than 98% of all points met the same acceptance criterion for the 40x40 cm^2 field. Representative crossline dose profiles showing the goodness of agreement at 1.5 cm depth are given in Figure 5.3. The results described here are identical to what

was presented in our initial validation of the model (chapter 4). Since the short in-line side-coupled waveguide possess no built-in beam control systems to correct for Earth's magnetic field at different gantry angles, it is expected that earth's magnetic field has a very small effect on the short linacs.
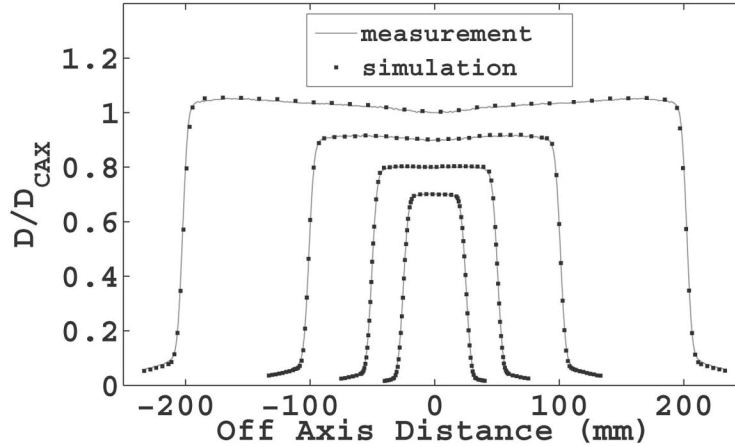
Figure 5.3: A comparison between the simulated and measured crossline dose profiles at 1.5 cm depth for all field sizes (40x40, 20x20, 10x10, and 5x5 cm^2) in earth's magnetic field is given.

5.3.3   Linac response to homogeneous transverse magnetic fields

The simulated linac responded to increasingly larger transverse magnetic fields by exhibiting increased beam loss. Homogeneous magnetic fields of 2, 4 and 6 G were added to the simulated linac and the resulting beam loss is shown in Figure 5.4a. The additional beam loss from the 2, 4 and 6 G transverse fields was determined to be 6±1 19±1 and 45±1% respectively. The first points left of the dotted line in Figure 5.4a at each magnetic field value correspond to beam losses within the electron gun. It is observed from Figure 5.4a that as the transverse field strength increases, less beam loss is experienced within the electron gun since the electrons which would normally be accelerated back towards the gun are lost elsewhere in the waveguide. Thus while the 6 G field contributes to the largest beam loss within the waveguide, it contributes to the least beam loss within the electron gun. The electron spatial distributions at the target for the 2, 4 and 6 G transverse field simulations are given in Figure 5.4b. Fields larger than 6 G

caused the electron distribution peak to be lost resulting in greater than 60% beam loss and a fairly flat distribution at the target. The 6 G field yields the most asymmetric spatial distribution at the target and thus has the largest effect on the dose distributions.
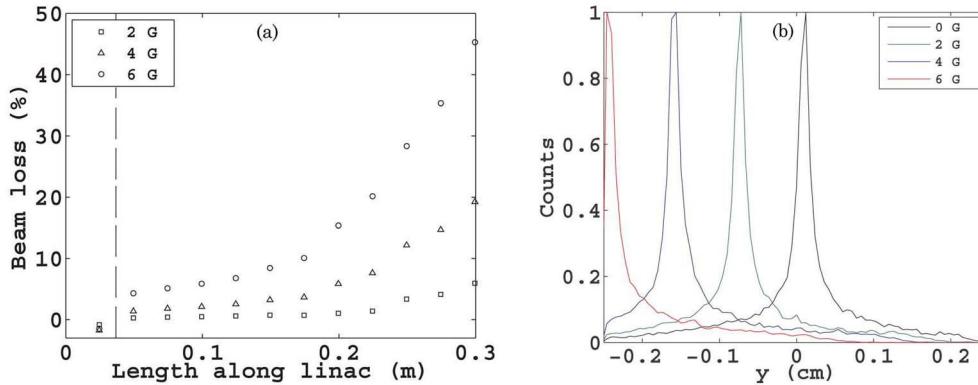
Figure 5.4: (a) The beam loss within the simulated linac is given for increasing homogeneous transverse magnetic field strengths with the intensities normalized to the 0 G intensity count. The first points in the figure left of the dotted line are beam loss values taken within the electron gun. (b) The electron spatial intensity distributions (normalized to 0 G) at the target resulting from the addition of the 0, 2, 4 and 6 G transverse magnetic fields are given.

The wide field dose distributions derived from the simulated phase space resulting from the addition of the 2, 4 and 6 G transverse magnetic fields is shown in Figure 5.5a-c along with the gamma index for a 1%/1 mm acceptance criterion. Since the peak shift away from center shown in Figure 5.4b becomes more drastic as the magnetic field is increased, a larger lateral translation of the spatial distribution at the target was required to maintain the profile symmetry. It was determined that a lateral translation of 0.07, 0.14, and 0.24 cm in the y direction for the 2, 4, and 6 G magnetic field simulations respectively was required to maintain the profile symmetry. The gamma index analysis found that 4.2, 10.8, and 14.4% of all points failed a 1%/1 mm criterion for the 2, 4 and 6 G field simulations respectively with nearly all the failed points positioned in the penumbra as seen in Figure 5.5a-c. When the acceptance criterion was changed to 3%/3 mm, all points for the 2, and 4 G magnetic field simulations met the new criterion while the 6 G field simulation had 0.9% of the points fail.
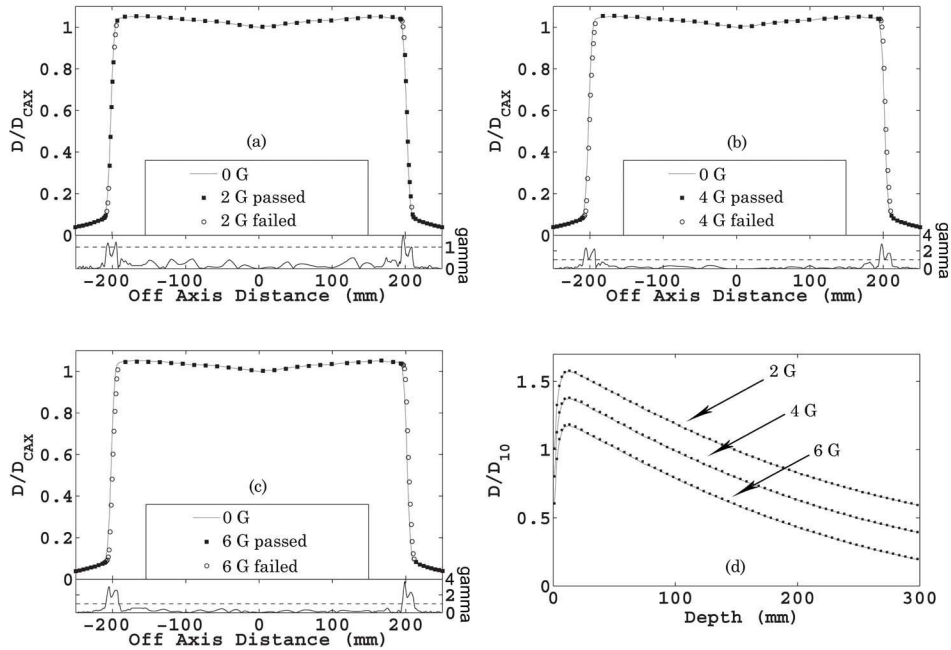
Figure 5.5: The crossline wide field dose profiles for 2, 4, and 6 G transverse field simulations are given in (a) – (c). The gamma index for a 1%/1 mm criterion is given below the profiles on the right axis with the gamma value of one depicted by the dashed line. (d) The DD curves for the increasing magnetic field simulations were initially normalized to D_{10} and then scaled for visual clarity.

The maximum energy of the electrons impacting the target showed no change with increasing magnetic field, but the mean energy increased slightly to 5.64 MeV, 5.71 MeV and 5.74 MeV for the 2, 4 and 6 G simulations respectively. The increase in mean energy is a result of more low energy electrons being lost as the transverse magnetic field increases. With these very small changes in the mean energy no differences greater than 1.3% were seen in the DD curves shown in Figure 5.5d. This is expected since the DD curves have been shown to be quite insensitive to small changes in the electron beam energy[8, 9].

The points failing the acceptance criterion were predominantly in the penumbra due to a lateral profile shift. The lateral shift in the dose profile as measured by the location of the 50% dose is directly caused by lateral shift in the focal spot due to the commissioning process (Figure 5.6). Thus if the symmetry is maintained it is at the expense of a laterally shifted dose profile. If on the other

hand there was no lateral shift in the profile (by not translating the spatial distribution at the target), the asymmetry in the 40x40 cm^2 field was calculated to be 13%, well outside of clinical specifications. As explained previously, homogeneous fields larger than 6 G cause the electron distribution peak to be lost within the waveguide resulting in a relatively flat and spatially homogeneous distribution at the target. Thus the largest effects on the dose distributions come from a homogeneous field of around 6 G. As an extension to the applicability of this study, any transverse magnetic field configuration (homogeneous or otherwise) that yields the beam centroid shifts shown in Figure 5.4b would yield the dosimetric results given in Figure 5.5. Thus the results presented here can be applied to various transverse magnetic field configurations.
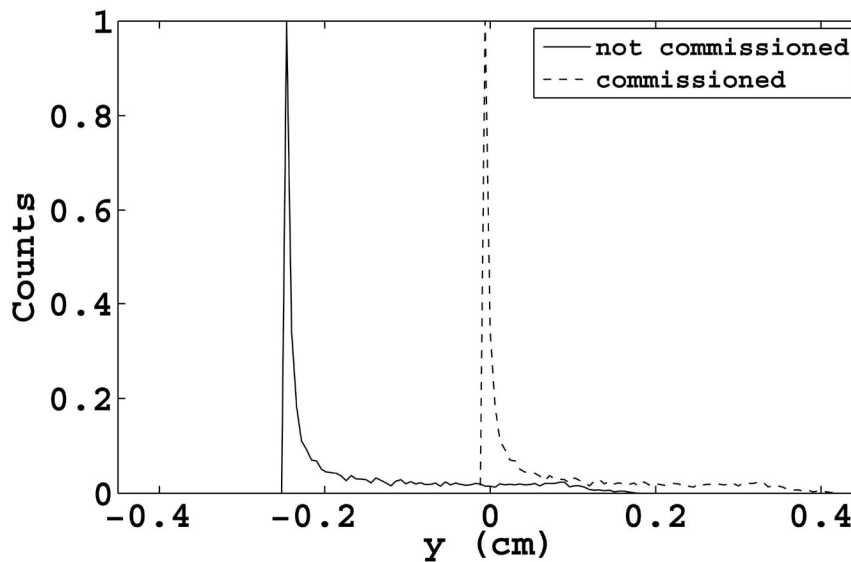
Figure 5.6: The non-translated (not commissioned) focal spot resulting from a 6 G transverse magnetic field together with the translated (commissioned) focal spot.

A further analysis was performed to determine the target current at increasingly larger field strengths for completeness. The results are presented in Figure 5.7 and show that by 14 G, all electrons are lost within the electron gun and waveguide and none reach the target.
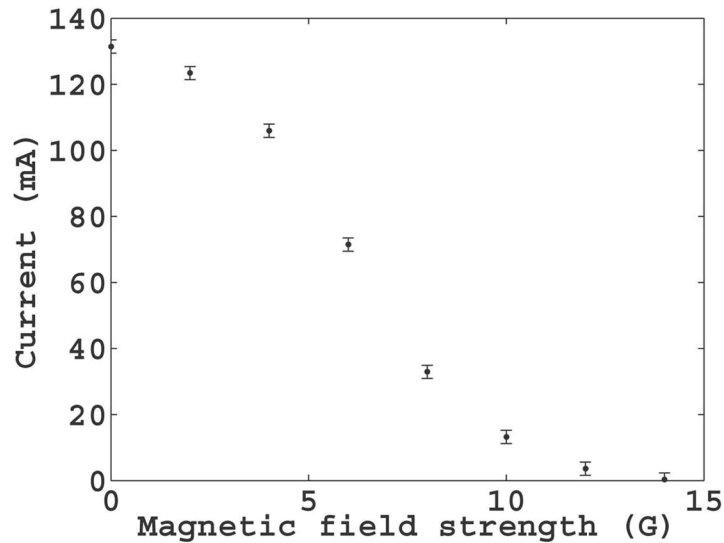
Figure 5.7: The reduction in target current for increasing homogeneous magnetic field strengths is given. At 14 G, none of the electrons are incident on the target.

5.3.4   Reduction of the magnetic field effect on the dose distributions

The lateral shift in the dose profiles seen in Figure 5.5a-c can be reduced significantly through the use of asymmetric jaw positions. The effectiveness of using asymmetric jaw positions for a 20x20 cm^2 field size is demonstrated in Fig. 6 to correct the largest lateral shift caused by the 6 G field. By changing the left and right jaw placements from -10 cm and 10 cm respectively to -10.15 cm and 9.85 cm (a shift of 1.5 mm to the left), the lateral shift seen in Figure 5.8a is almost completely removed (Figure 5.8b) with only 0.5% of the points failing the 1%/1mm criterion. Appropriate positioning of the x and y jaws can compensate the lateral shift even for collimator rotations. It should be noted that the multi-leaf collimators (MLCs) could also correct the lateral shift. However, the largest 40x40 cm^2 field cannot be used since the jaws are limited to a maximum position of ±20 cm, so the maximum field size must be slightly smaller, but only by a few millimeters at most.

As an alternative solution to using the jaws to compensate the dosimetric effects resulting from the transverse magnetic fields on the linac, beam control systems similar to a high energy unit may be added. These control systems would

be designed to redirect the electron beam to the target. Alternatively, passive or active magnetic shielding could reduce the magnetic fringe fields at the linac sufficiently to achieve minimal beam deflection.
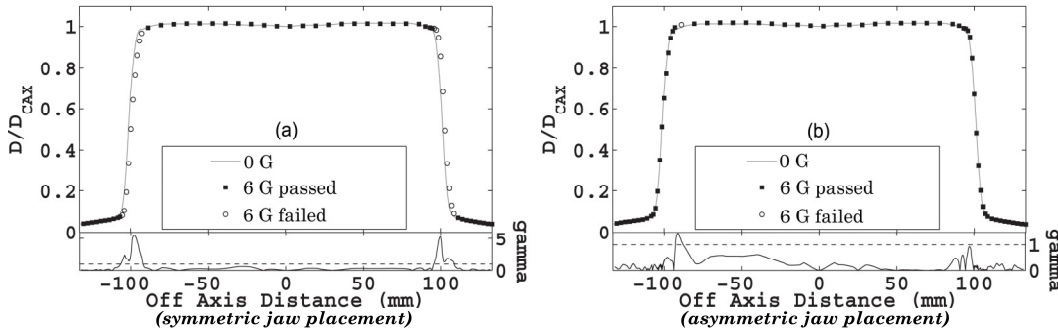
Figure 5.8: (a) A large lateral shift of the dose profile for the 6 G simulation is seen causing large discrepancies from a typical clinical profile as seen by the gamma index. (b) The use of asymmetric y jaw placements almost fully corrects the lateral shift.

5.4   CONCLUSION

The 2D axisymmetric electron gun program EGN2w was replaced by the 3D electron gun program OPERA-3d/SCALA in our validated linac simulation. The emission current from the 3D gun was found to be 20% larger than EGN2w calculated, requiring a 7.6% reduction in the cathode radius to ensure its output matched measurement. The linac simulation was revalidated using this updated design showing our previously achieved agreements to measurement. Upon the addition of increasing homogeneous magnetic field strengths, larger beam losses were calculated within the linac due to the increasing transverse electron deflections. The large electron deflections lead to a spatially shifted electron distribution at the target resulting in either clinically unacceptable profile symmetry, or if maintaining symmetry, a laterally shifted dose profile. The laterally shifted dose profiles at homogeneous fields of 4 and 6 G failed to meet a 1%/1 mm acceptance criterion with all points in the penumbra causing the failure. It was found that asymmetric jaw locations created an opposite shift that almost completely eliminated the lateral shifts in the dose profiles caused by the external

fields. It was also found that at a transverse homogeneous field of 14 G no electrons impacted the target resulting in 100% beam loss.

5.5 REFERENCES

[1] J. St. Aubin, S. Steciw, and B. G. Fallone, "The design of a simulated in-line side-coupled 6 MV linear accelerator waveguide," Med. Phys., **37**, 466-476 (2010).

[2] J. St. Aubin, S. Steciw, and B. G. Fallone, "An integrated 6 MV linear accelerator model from electron gun to dose in a water tank," Med. Phys., **37**, 2279-2288 (2010).

[3] J. G. M. Kok, B. W. Raaymakers, J. J. W. Lagendijk, J. Overweg, C. H. W. de Graaff, and K. J. Brown, "Installation of the 1.5 T MRI accelerator next to clinical accelerators: impact of the fringe field," Phys. Med. Biol., N409-N415 (2009).

[4] B. W. Raaymakers, J. J. W. Lagendijk, J. Overweg, J. G. M. Kok, A. J. E. Raaijmakers, E. M. Kerkhof, R. W. van der Put, I. Meijsing, S. P. M. Crijns, F. Benedosso, M. van Vulpen, C. H. W. de Graaff, J. Allen, and K. J. Brown, "Integrating a 1.5 T MRI scanner with a 6 MV accelerator: proof of concept," Phys. Med. Biol., **54**, N229-N237 (2009).

[5] B. G. Fallone, B. Murray, S. Rathee, T. Stanescu, S. Steciw, S. Vidakovic, E. Blosser, and D. Tymofichuk, "First MR images obtained during megavoltage photon irradiation from a prototype integrated linac-MR system," Med. Phys., **36**, 2084-2088 (2009).

[6] D. A. Low, W. B. Harms, M. Mutic, and J. A. Purdy, "A technique for the quantitative evaluation of dose distributions," Med. Phys., **25**, 656-661 (1998).

[7] J. Jin, *The finite element method in electromagnetics* (John Wiley & Sons Inc., New York, 2002).

[8] D. M. J. Lovelock, C. S. Chui, and R. Mohan, "A Monte Carlo model of photon beams used in radiation therapy," Med. Phys., **22**, 1387-1394 (1995).

[9] B. Libby, J. Siebers, and R. Mohan, "Validation of Monte Carlo generated phase-space descriptions of medical linear accelerators," Med. Phys., **26**, 1476-1483 (1999).

CHAPTER 6: Effect of longitudinal magnetic fields on a simulated in-line 6 MV linac

6.1   INTRODUCTION

Two proof-of-concept linac-MR systems have been presented previously that produce X-rays perpendicular to the main magnetic field of the MR imager.[1, 2] The existence of both of these proof-of-concept systems proves that all engineering difficulties relating to the transverse configuration linac-MR system can be overcome. However, despite overcoming engineering difficulties, the transverse case produces hot and cold spots at tissue-air interfaces in the treatment plan due to the significant deflection in low density media of the high energy electrons generated by Compton scattering etc.[3] At 1.5 T, these effects produce large deviations away from a nominal treatment plan with no magnetic field. However it has also been shown that at lower magnetic field strengths, such as 0.2 T, the hot and cold spots at tissue-air interfaces is largely reduced[3]. The minimization of electron deflections in low density media at lower field strengths is simply a result of a reduction in the transverse magnetic force on the particles.

The parallel design for a linac-MR system was first presented by our group in 2009.[4, 5] Our group has shown that in using the parallel design, there is a significant reduction in hot and cold spots at the tissue-air interface and that the highest magnetic field strength with minimum creation of hot and cold spots is approximately 0.5 T.[4, 6] The image quality at 0.5 T would be superior to that at 0.2 T. In addition, work has shown that a parallel configuration also results in a smaller penumbra.[6, 7]

Since an in-line side-coupled 6 MV linac is proposed to be the source of X-rays directed parallel to the main magnetic field of the MR imager, the accelerating electrons within the linac will be subjected to longitudinal magnetic

fringe fields. The longitudinal magnetic fields are not expected to deflect the electrons away from the target as a transverse field does, but the effects on the electron beam resulting from altered beam optics at the electron gun and throughout the waveguide require quantification. In addition to quantifying changes to the electron beam, the resulting changes on the dose distributions also require quantification.

6.2   METHODS AND MATERIALS

The outline of the work presented here is as follows. A continuous magnetic fringe field solution approximating discrete isoline data supplied by an open MR imager manufacturer was first generated. The reasoning and methodology behind this calculation is explained in section 6.2.1. The approximated continuous fringe field was then added to our linac simulation[8-10] as explained in section 6.2.1. Our linac simulation was previously validated against measurement as reported in Chapter 4[10] and Chapter 5[8]. The electron phase space at the linac target produced as a result of our linac simulation was then used as an input into a Monte Carlo simulation to calculate the associated dose distribution in a water tank which is discussed in section 6.2.2. Our Monte Carlo model of a linac was also validated against measurements as reported in chapter 4[10].

6.2.1   Magnetic fringe field calculations

The parallel linac-MR design (Figure 3.1) can be implemented with various commercial open MR imagers. Examples of open MR imagers include PARAmed MRopen™, GE Signa SP™, Phillips Panorama™, Siemens Magnetom Concerto™ and the Hitachi Elite™. As an example for what can be performed, an investigation of linac performance in a longitudinal magnetic field was performed using fringe field isoline data supplied by PARAmed for its MRopen™ system. The final location of the linac with respect to this MR imager is expected to lie within a target-isocenter distance ranging from 1 to 2.2 m.

Within this range of target-isocenter distances, the longitudinal magnetic field at the cathode of the electron gun is expected to range from 22 to 110 G.

It was necessary to approximate the discrete fringe field isoline data through the generation of a full magnetic field solution from the superposition of a single current loop. This was done because our linac simulation requires a fully continuous field solution, including vector components, and this cannot be adequately performed by simply inserting the provided discrete field values. The current I, separation h, radius a, and number of current carrying loops were optimized using a Monte Carlo technique to obtain the continuous field solution that matched the isoline data supplied from PARAmed. The analytic solution of the magnetic field in cylindrical coordinates for a single current loop is given in Eqs. 2.17b, 2.18 and 2.19. The cylindrically symmetric solutions given in these equations were transformed into Cartesian xyz coordinates by the transformations given in Eq. 2.20. Thus through a superposition of solutions from Eqs. 2.17b, 2.18 and 2.19 and the transformation of Eq. 2.20, the magnetic field from any number of current loops can be determined.

The current I, separation h, and radius a for the current loop pair were optimized in order to minimize the square root of the mean squared difference between the calculated magnetic field solution and the isoline data supplied from PARAmed using a Monte Carlo optimizer. An initial value for I, h, and a was input into the optimization algorithm and the square root of the mean squared difference between the calculated solution and the isoline data was determined. The Monte Carlo optimizer then used random numbers to make fluctuations in I, h, and a. By applying larger amplitude fluctuations to I, h, and a, the region around the minimized square root of the mean squared difference was first located. Once located, smaller amplitude fluctuations were used to find the minimized square root of the mean squared difference. Once the minimized square root of the mean squared difference was determined for a given number of current loop pairs, an additional loop pair was added to the model in an attempt to further minimize differences between the calculated solution and the isoline data.

The optimization of *I*, *h*, and *a* for each loop pair was then repeated. If the addition of a current loop pair reduced the square root of the mean squared difference by less than 1% of the previous solution, the optimization was completed and the model with the lower number of loop pairs was chosen as the optimal solution for simplicity. The use of a Monte Carlo optimizer on the current loop solution guarantees the divergence of the field to be zero (i.e. giving a physical solution). Regular fitting techniques such as chi-squared minimization or other polynomial based fitting techniques would not guarantee a physical solution.

The optimized continuous magnetic field solution was then added to our previously validated linac simulation[8-10] such that the field at the electron gun cathode was calculated to be 22, 46 and 110 G. These field strengths correspond to target-isocenter distances of 2.2, 1.6 and 1.0 m respectively. In addition to this investigation, homogeneous fields up to 2000 G were used to simulate the effects of other possible open split solenoid MR imagers which may have larger fringe fields due to poor or non-existent magnetic shielding.

6.2.2   6 MV linac simulation

Our validated linac simulation[8-10] consists of an electron gun simulated using the 3D finite element method (FEM) and space charge analysis electron gun program OPERA-3d/SCALA, a 3D FEM radio-frequency (RF) field solution within the waveguide from COMSOL Multiphysics, and the 3D particle tracking space charge calculation program PARMELA[11]. OPERA-3d/SCALA uses Child's law (Eq. 2.84) for electron emission off the cathode and calculates the space charge field. The initial design of the electron gun used was presented previously in chapter 4 with the slight cathode modification specified in chapter 5, and the design of the waveguide is given in chapter 3 and chapter 4.

6.2.3   Monte Carlo simulations

A Varian 600C linac head (Figure 3.3) was modeled in BEAMnrcMP 2007 (BEAM)[12] using information supplied from the manufacturer. Roughly $3x10^8$ initial histories were run in BEAM for a 40x40 cm^2 field size. A 40x40 cm^2 field size was chosen due to its sensitivity to changes in the electron focal spot size and energy.[13] All other BEAM and DOSXYZ parameters are as explained in Chapter 3.

6.3   RESULTS AND DISCUSSION

6.3.1   Effect of MRopen™ fringe magnetic fields on the linac

The results of the Monte Carlo optimization provided an accurate approximation of the 0.5 T MR when comparing magnetic fringe field isolines over the region where the linac is expected to be located using two current loop pairs. The continuous field solution derived from the discrete field values supplied for the MRopen™ system from PARAmed is shown in Figure 6.1. A maximum discrepancy of 12% was calculated at the 20 G field point. Elsewhere, the discrepancy was less than 2%.
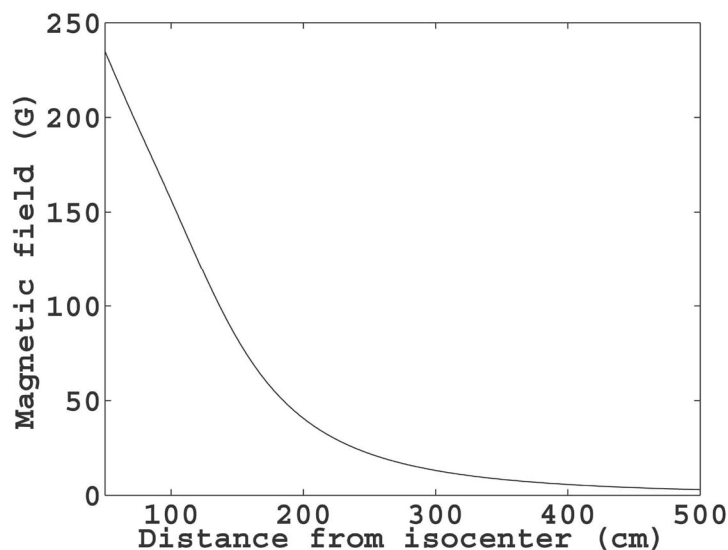
Figure 6.1: The derived magnetic fringe field solution resulting from Monte Carlo optimization of current loops. Two coil pairs were used to generate the above continuous field solution.

The longitudinal MR field was seen to have a large effect on the electron phase space at the exit of the electron gun as seen in Figure 6.2. The phase space becomes highly non-laminar prior to injection into the linac for all longitudinal field strengths investigated. The normalized root-mean-square (rms) emittance at the exit of the electron gun for the 0, 22, 46, and 110 G magnetic field simulations was calculated to be 0.358, 0.810, 1.573 and 3.255 π mm-mrad respectively. In addition to the non-laminar phase space, the diameter of the injected electron beam grew from 0.178 cm at 0 G to 0.183, 0.194, and 0.22 cm at 22, 46, and 110 G respectively. The changes in the electron beam at the electron gun are a result of the longitudinal magnetic field changing the optics of the electron gun which was originally designed for use in a nearly 0 G field environment. Despite the change in optics, at up to 110 G no beam loss was calculated within the electron gun.
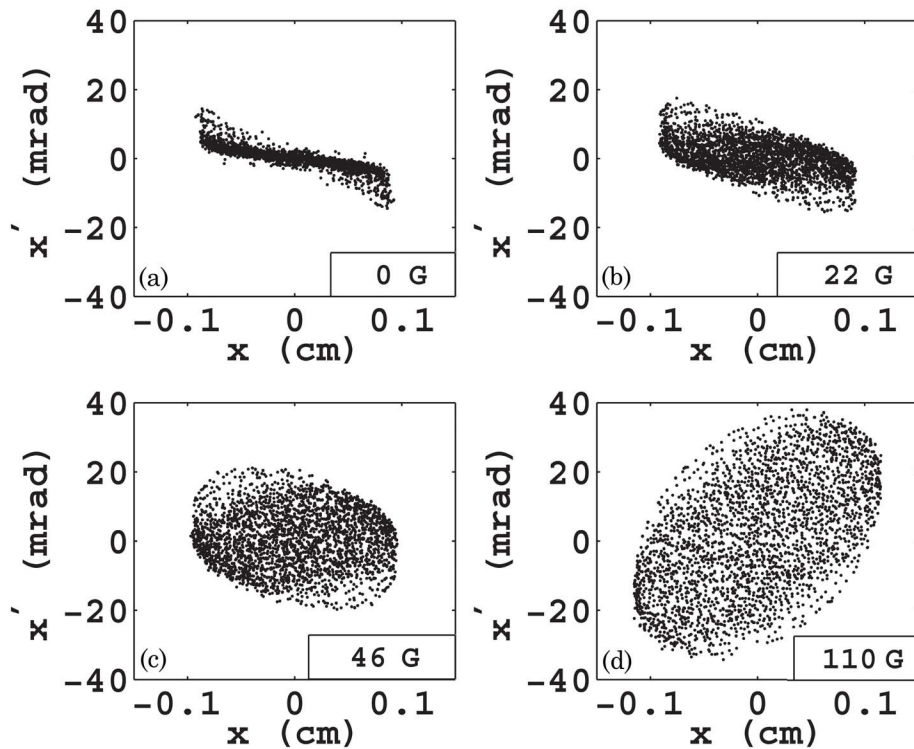
Figure 6.2: The transverse phase space at the exit of the electron gun is given when subjected to (a) 0 G, (b) 22 G, (c) 46 G, and (d) 110 G longitudinal magnetic fields.

The electron spatial intensity distribution and energy spectrum at the target resulting from the MR field are given in Figure 6.3. Beam losses above nominal (0 G) of 1±1, 2±1, and 16±1% were calculated for the 22, 46, and 110 G fields respectively. As can be seen, the spatial distribution changes drastically with the addition of longitudinal magnetic fields as quantified by the full width half maximum (FWHM). The FWHM of the spatial distribution, calculated to be 0.012 cm at 0 G, grew to 0.074, 0.143, and 0.254 cm for the 22, 46 and 110 G fields respectively. The maximum and mean energy of the electron beam incident on the target remained unchanged at 6.32 and 5.57 MeV respectively at 22 and 46 G. However, at 110 G, despite the maximum energy being unchanged, the mean energy increased slightly to 5.60 MeV. In order to separate the effects of the longitudinal magnetic field on the gun from those within the waveguide, a longitudinal magnetic field was placed on the electron gun only, and not on the linac waveguide and the target phase space was analyzed. The beam loss, energy spectrum and spatial intensity distribution was the same for these simulations compared to those with the field on both the electron gun and waveguide. This shows that the only effect of a longitudinal magnetic field (up to 110 G) on a linac is at the electron gun. The simulation results presented here are the same if the magnetic fringe field direction was reversed. A reversal of field direction would occur if the MR magnet poles were reversed with respect to the linac.
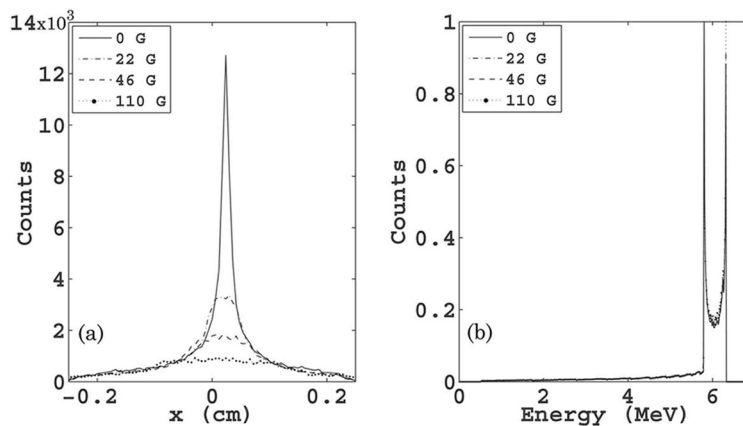
Figure 6.3: (a) Spatial intensity distribution and (b) energy spectrum at the linac target for simulations of 0, 22, 46 and 110 G longitudinal magnetic fields over the electron gun and linac waveguide.

Our Monte Carlo model of a Varian 600C linac, which was previously validated against measurements,[10] generated dose profiles and depth dose (DD) curves as seen in Figure 6.4. Figure 6.4a-c shows the inline 40x40 cm^2 dose profiles at 1.5 cm depth and Figure 6.4d shows the DD curves derived from the electron phase space at the linac target for the simulations in a 22, 46 and 110 G longitudinal magnetic field. Only the inline profiles are shown since the crossline profiles showed the same agreements. A comparison of the profiles at 22, 46 and 110 G to the 0 G profiles resulted in 96% of all points meeting a 1%/1mm acceptance criterion at all field strengths. The DD curves in longitudinal magnetic fields all matched the 0 G curve to within 1% at all depths down to 30 cm deep. Thus the addition of longitudinal magnetic fields does not have a large effect on the dose distributions in fields up to 110 G.
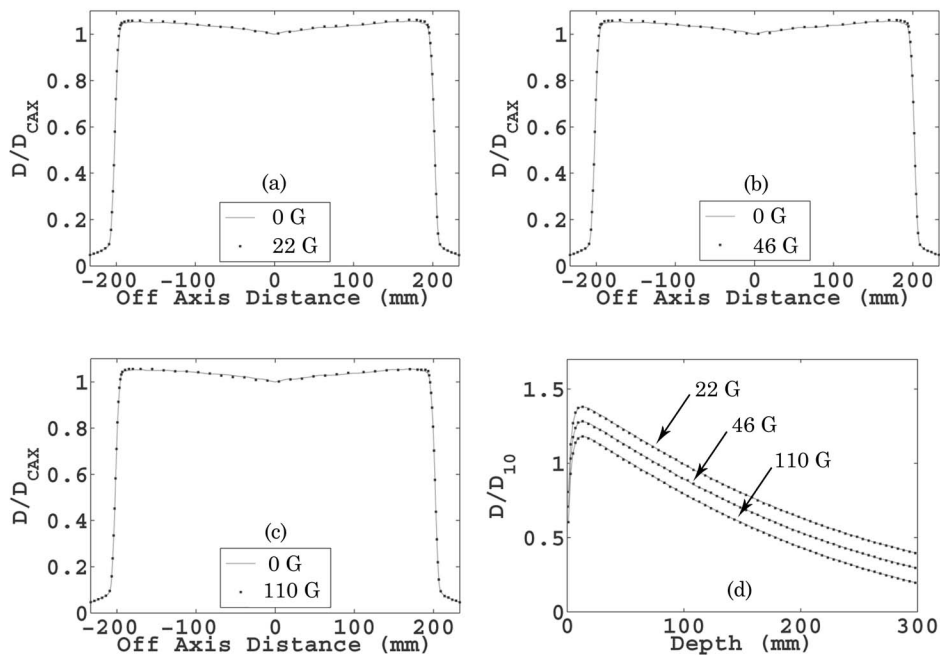
Figure 6.4: 40x40 cm^2 dose profiles at 1.5 cm depth and DD curves resulting from the linac operating in the presence of 22, 46 and 110 G longitudinal magnetic fields. The DD curves were initially normalized to D_{10} but scaled here for visual clarity.

An investigation was also performed to determine the linac sensitivity to lateral misalignments away from the symmetry axis of the MR imager. If the

linac is installed with a misalignment away from the central axis, it is subjected to larger transverse fields. A 1 cm misalignment corresponded to a maximum transverse field strength of 0.7 G, up from 0.17 G with no misalignment. At a target-isocenter distance of 1.0 m, a 1 cm misalignment in the x or y direction produced an 18±2% beam loss. The 2% increase compared to the simulation on the symmetry axis is a result of the larger transverse magnetic fields. The simulations incorporating the misalignments also produced a 0.012 cm shift of the beam centroid compared to no misalignment and a maximum discrepancy of 12 keV in the mean electron beam energy. After linac commissioning is performed by translating the target focal spot with respect to the flattening filter[10], these lateral misalignments for the MR imager modeled would have no effect on the dose distributions. Typical misalignments are expected to be on the order of a few millimeters at most, and not the exaggerated 1 cm offset investigated here. However, this investigation shows that even for a 1 cm misalignment, linac performance is minimally affected.

6.3.2   Effect of strong longitudinal magnetic fields on the linac

Other MR imagers of higher field strength or with less magnetic shielding could cause the magnetic fields at the linac to be greater than what was investigated previously. In addition, in order to achieve a full 40x40 cm^2 field at isocenter for the MRopen™ imager, which is not possible for the current design, the existing hole through which the radiation beam passes unattenuated may be required to be enlarged. Enlarging the hole may affect the magnetic fringe fields at the linac causing them to increase. Therefore, homogeneous longitudinal magnetic fields up to 2000 G were added to the linac simulation to investigate their effect on the electron gun as well as on the waveguide.

A slight increase in emission current which was calculated using Child's law, was observed for longitudinal fields of increasing field strength. This increase may be explained by a reduction in the space charge density near the cathode due to the larger beam diameter. A reduction in space charge density

means more current can flow from the cathode at the same cathode anode potential. The injection current saw the same increases up to around 120 G. However, further increases in field strength lead to a reduction in the injection current since the beam diameter became larger than the anode radius. The injection current dropped to its minimum value of 75±2 mA at 600 G (a 79% beam loss), but began increasing slowly at larger longitudinal field strengths due to greater beam collimation within the anode beam tube. Figure 6.5 shows the 3D electron gun model together with the calculated electron beam at 600 G field strength. Figure 6.6 highlights the results of the calculated emission and injection currents for increasing longitudinal magnetic field strengths up to 2000 G. The effects of the longitudinal magnetic field within the electron gun directly translate into a reduction in the linac target current as seen in Figure 6.7. Even though the injection current slightly increases up to 120 G, the target current is reduced over the same range. The changing beam characteristics quantified by the normalized rms emittance and shown in Figure 6.2 explain this drop. Changes in these characteristics of the injected beam have been shown previously to affect the overall capture efficiency of the linac.[10] At fields larger than 120G, the injection current decreases causing a further decrease in the target current where at 600 G the linac experiences a maximum beam loss of 92% corresponding to a target current of 28±2 mA. These large beam losses must be addressed before the linac can be subjected to strong longitudinal fields. Since the total beam loss over nominal has been shown to be largely due to losses within the electron gun, magnetically shielding the electron gun, or redesigning the electron gun optics to incorporate strong longitudinal magnetic fields of a known strength could minimize or eliminate these large losses.
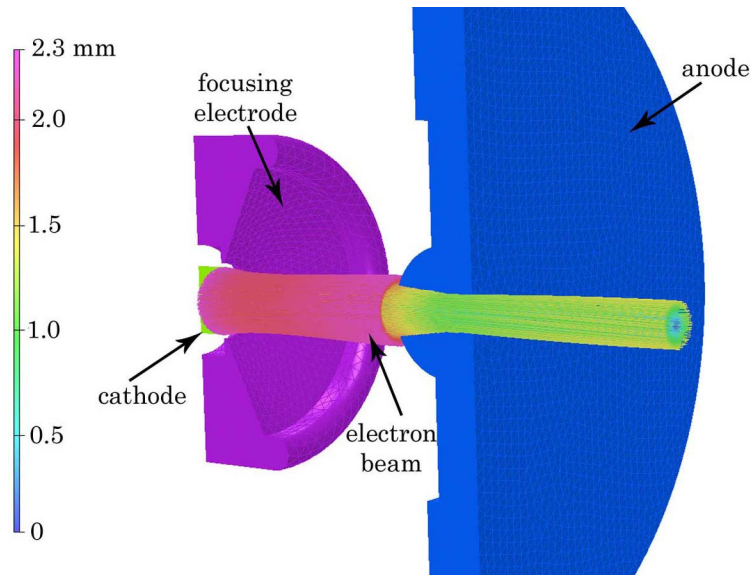
Figure 6.5: The 3D OPERA-3d/SCALA electron gun and trajectory solution in a 600 G longitudinal field is shown. The structure on the right is the anode, while the structures on the left are the focusing electrode and cathode (mostly hidden behind the electron beam). The electron beam color signifies its radius in mm. Much of the beam is incident on the anode at 600 G.
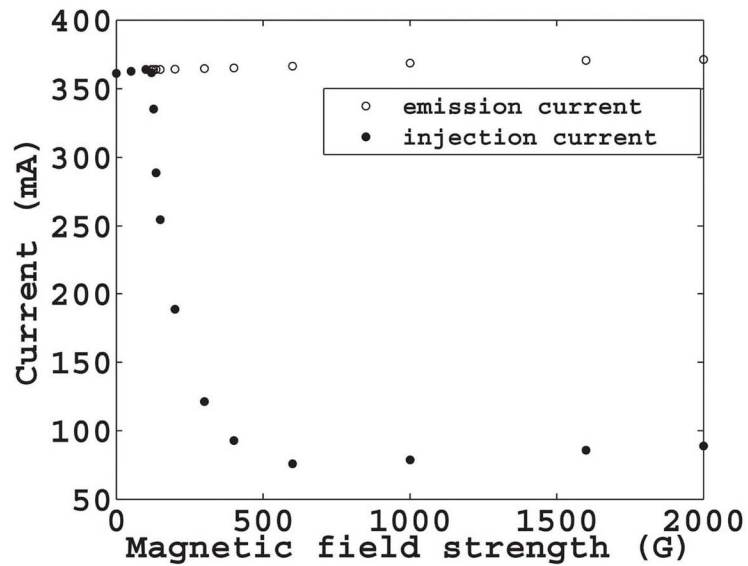
Figure 6.6: Calculated cathode emission current and injection current with increasing magnetic field strength using Opera-3d/SCALA is given. A very sharp decrease in injection current is observed after 120 G. At 600 G, the injection current is a minimum after which it slowly increases with increasing magnetic field due to beam collimation within the anode beam tube.
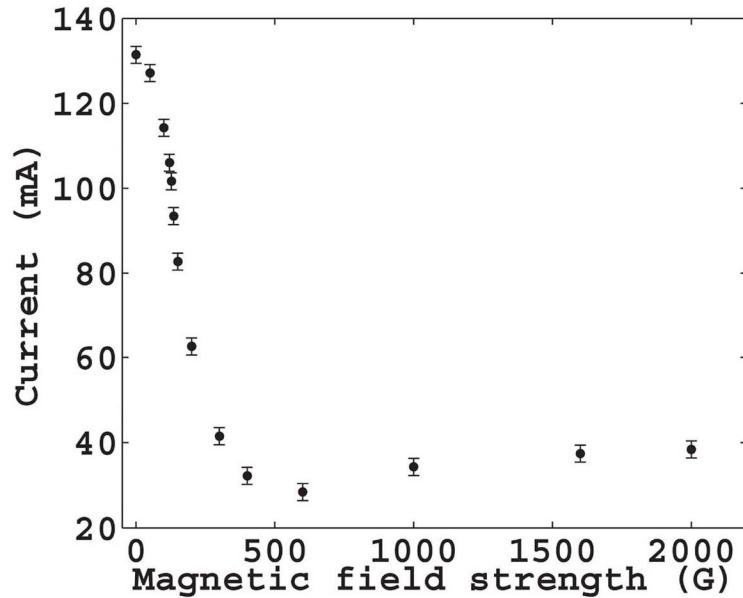
Figure 6.7: Calculated target current with increasing magnetic field strength. The target current decreases, even for increasing injection current up to 120 G due to a more non-laminar injected beam.

6.4   CONCLUSIONS

The next generation linac-MR system at the Cross Cancer Institute consists of a 6 MV linac coupled to a 0.5 T superconducting open MR imager. This configuration will allow for the X-ray beam to be generated in the same direction as the main magnetic field of the MR imager leading to a reduction of hot and cold spots in the dosimetry at tissue-air interfaces. As an example, depending on the final linac position, the longitudinal magnetic fringe fields at the cathode are expected to range from 22 to 110 G according to isoline data provided for an MROpen™ imager. A continuous field solution was optimized using Monte Carlo to match the fringe field isoline data for use in our in-line 6 MV linac simulation. The optimized longitudinal magnetic field on the linac has been shown to affect the electron optics of the electron gun creating an increasingly non-laminar electron beam with a larger beam radius being injected into the linac waveguide. This in turn causes a drastic reduction in the intensity of the peak of the electron spatial distribution and an increase in beam loss which was calculated to be 1±1, 2±1, and 16±1% at 22, 46, and 110 G respectively. However, the

altered electron focal spot at the target had little effect on the dose distributions with 96% of all points meeting a 1%/1mm acceptance criterion when compared to a 0 G distribution and an agreement of better than 1% in the DD curves at all depths. Fields larger than 110 G, representing a range of fringe field magnitudes for other open MR systems, produced large beam losses within the electron gun. Specifically, a sharp decline in injection current for the designed electron gun was observed for field strengths between 120 and 600 G at which point the injection current was a minimum of 75±2 mA. After 600 G, the injection current increased slowly due to increased beam collimation in the anode beam tube. The linac target current calculated was observed to follow a similar trend to the injection current with its minimum value of 28±2 mA achieved at 600 G. These excessive beam losses at the target need to be addressed by a modification of the electron gun optics, or in the form of magnetic shielding before the linac can be operated efficiently in strong longitudinal magnetic fields.

6.5 REFERENCES

[1] B. G. Fallone, B. Murray, S. Rathee, T. Stanescu, S. Steciw, S. Vidakovic, E. Blosser, and D. Tymofichuk, "First MR images obtained during megavoltage photon irradiation from a prototype integrated linac-MR system," Med. Phys., **36**, 2084-2088 (2009).

[2] B. W. Raaymakers, J. J. W. Lagendijk, J. Overweg, J. G. M. Kok, A. J. E. Raaijmakers, E. M. Kerkhof, R. W. van der Put, I. Meijsing, S. P. M. Crijns, F. Benedosso, M. van Vulpen, C. H. W. de Graaff, J. Allen, and K. J. Brown, "Integrating a 1.5 T MRI scanner with a 6 MV accelerator: proof of concept," Phys. Med. Biol., **54**, N229-N237 (2009).

[3] C. Kirkby, T. Stanescu, S. Rathee, M. Carlone, B. Murray, and B. G. Fallone, "Patient dosimetry for hybrid MRI-radiotherapy systems," Med. Phys., **35**, 1019-1027 (2008).

[4] B. G. Fallone, "Real-Time MR-Guided Radiotherapy: Integration of a Low-Field MR System," Med. Phys., **36**, 2774-2775 (2009).

[5] B. Fallone, B. Murray, S. Rathee, T. Stanescu, S. Steciw, S. Vidakovic, E. Blosser, and D. Tymofichuk, "First MR Images Obtained During Megavoltage Photon Irradiation From An Integrated Linac-MR System," **36**, 2745 (2009).

[6] C. Kirkby, B. Murray, S. Rathee, and B. G. Fallone, "Lung dosimetry in a linac-MRI radiotherapy unit with a longitudinal magnetic field," Med. Phys., **37**, 4722-4732 (2010).

[7] A. F. Bielajew, "The effect of strong longitudinal magnetic fields on dose deposition from electron and photon beams," Med. Phys., **20**, 1171-1179 (1993).

[8] J. St. Aubin, S. Steciw, and B. G. Fallone, "Effect of transverse magnetic fields on a simulated in-line 6 MV linac," Phys. Med. Biol., **55**, 4861-4869 (2010).

[9] J. St. Aubin, S. Steciw, and B. G. Fallone, "The design of a simulated in-line side-coupled 6 MV linear accelerator waveguide," Med. Phys., **37**, 466-476 (2010).

[10] J. St. Aubin, S. Steciw, and B. G. Fallone, "An integrated 6 MV linear accelerator model from electron gun to dose in a water tank," Med. Phys., **37**, 2279-2288 (2010).

[11] L. M. Young, "Parmela," *LA-UR-96-1835*, (L.A.N.L.,Los Alamos) 2005

[12] D. W. O. Rogers, B. A. Faddegon, G. X. Ding, C. M. Ma, J. We, and T. R. Mackie, "BEAM - A Monte Carlo code to simulate radiotherapy treatment units," Med. Phys., **22**, 503-524 (1995).

[13] J. Pena, L. Franco, F. Gomez, A. Iglesias, R. Lobato, J. Mosquera, A. Pazos, J. Pardo, M. Pombar, A. Rodriguez, and J. Sendon, "Commissioning of a medical accelerator photon beam Monte Carlo simulation using wide-field profiles," Phys. Med. Biol., **49**, 4929-4942 (2004).

CHAPTER 7: *Waveguide detuning caused by transverse magnetic fields on a simulated in-line 6 MV linac*

7.1   INTRODUCTION

Passive or active shielding designed to minimize the magnetic field strength intersecting the linac may not be 100% effective, with some magnitude of magnetic field strength persisting within the region the linac occupies. According to work presented previously in chapter 5, even small transverse magnetic fields on the order of 6 G can cause significant beam losses of 45±1%.[1] The linac waveguide is precisely designed to achieve a specified effective shunt impedance and energy gain for the electrons and any perturbation to the designed waveguide cavity geometry results in changes in the resonant frequency of that cavity[2, 3]. It is known that heating caused by radio-frequency (RF) power dissipation in the copper waveguide changes the resonant frequency of the linac and requires cooling.[4] Thus all medical linacs have cooling systems to eliminate thermal expansion of the waveguide due to heating. In transverse magnetic fields, electron deflections away from the beam axis cause the electrons to impact the copper waveguide creating another possible heating concern. If the temperature rises too much, the deformation in the copper structure could lead to a large enough change in the cavity's resonant frequency to cause the input RF field to be off resonance with the entire waveguide. This in turn could increase the electron beam loss above the expected value caused by a transverse magnetic field due to higher mode mixing and further RF power losses. Thus an investigation of waveguide detuning caused by these beam losses is necessary to obtain a better estimate of linac performance in transverse magnetic fields.

7.2   METHODS AND MATERIALS

The calculation of waveguide heating began with the beam loss per cavity calculated using our 6 MV waveguide and electron gun simulation as given in chapters 3[2], 4[5] and 5[6]. However, the particle-in-cell program PARMELA does not track electrons that are lost outside the beam tube, so the exact trajectories and locations where the lost electrons impact the waveguide are unknown. To estimate the increase in temperature and subsequent detuning of the copper waveguide, an assumption was made that all the lost electrons impact the waveguide nose cones which define the beam tube (Figure 7.1). Due to the high electric field concentration at the nose cones, they create a large fraction of the total capacitance of the cavity and small changes in their dimensions lead to large changes in the cavity resonant frequency as seen in chapter 3. The assumption that beam losses are concentrated on the nose cones thus represents a worst case scenario regarding cavity resonant frequency changes resulting from waveguide heating. Since trajectory information was unavailable, and as a simple approximation, the electrons are assumed to impact the nose cones perpendicular to their surface.
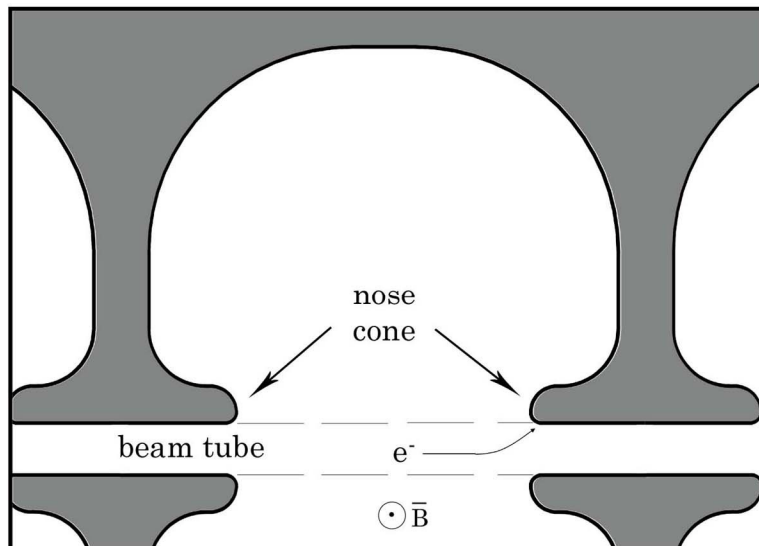
Figure 7.1: An accelerating cavity with the locations of the beam tube and nose cones is highlighted. The trajectory of electron deflection caused by a magnetic field out of the page is shown impacting the top half of the nose cone.

The energy deposited on the nose cones by the additional electron losses was investigated as follows. The number and mean energy of the electrons lost in each cavity was calculated using PARMELA. From the mean electron energy fluence incident on the nose cones, DOSRZnrc was used to calculate the total energy deposited in each cavity at each magnetic field strength investigated. In DOSRZnrc, a monoenergetic beam of electrons at the calculated mean energy was set to impact an annular ring of copper. The central region with a radius of 2.5 mm was modeled as vacuum representing the beam tube, and the nose cone was approximated by two annular copper rings of widths 1 mm and 2.5 mm. The geometry and the radial bin widths were kept identical for all cavities and all beam energies studied, but the voxel depths were adjusted depending on energy. The voxel depths varied from 0.001 mm for the lowest energy to 0.1 mm for the highest energy to obtain sufficient resolution of the energy deposition. The electron (ECUT) and photon (PCUT) transport cutoff energies were set to 0.521 MeV and 0.001 MeV respectively with no range rejection being used. The value of ECUT was chosen to explicitly simulate electrons with kinetic energies down to 10 keV in order to obtain sufficient resolution in energy deposition results despite the small electron ranges in Copper (e.g. 0.14 mm at 0.3 MeV).

The copper deformations and resulting change in accelerating frequency caused by the increased energy deposited (as calculated in DOSRZnrc) was determined next. The DOSRZnrc simulations resulted in the dose per voxel normalized to the planar electron fluence. Thus the total dose was calculated from all voxels and scaled to the fluence calculated from PARMELA under the assumption that the deflected electrons will predominately impact the nose cone (or annular ring) as seen in Figure 7.1. As seen previously, the largest beam losses occur when the linac is subjected to a transverse magnetic field. In the transverse magnetic field configuration investigated here, the electrons are assumed to impact one half of the total area of the nose cone since the electrons are deflected globally in one direction. From the known mass of copper in which the dose was deposited, the total energy deposited was calculated leading to a determination of

the rise in temperature using the specific heat capacity of copper. The copper deformation was calculated using the thermal expansion coefficient and the resulting cavity geometry was modeled with the finite element method (FEM) program COMSOL. The FEM simulation was performed on an accelerating cavity (AC) designed previously (chapter 3) in 2D using axisymmetry with the nose cones deformed according to the previous calculations. The change in the frequency of the π/2 accelerating mode caused by changes in the resonant frequency of each accelerating cavity was investigated using first order perturbation theory of *N+1* resonantly coupled cavities (Eq. 2.43)[7].

7.3   RESULTS AND DISCUSSION

The total beam loss caused by a homogeneous transverse magnetic field present in the linac, calculated as additional beam loss over nominal operation, is presented in Figure 7.2. The greater beam losses at larger field strengths are due to the larger electron beam deflections. The larger deflections cause the electrons to impact the copper waveguide inner structures, such as the nose cones, leaving less current at the target. At 14 G homogeneous field strength, no electrons are incident on the target and all are lost within the waveguide.
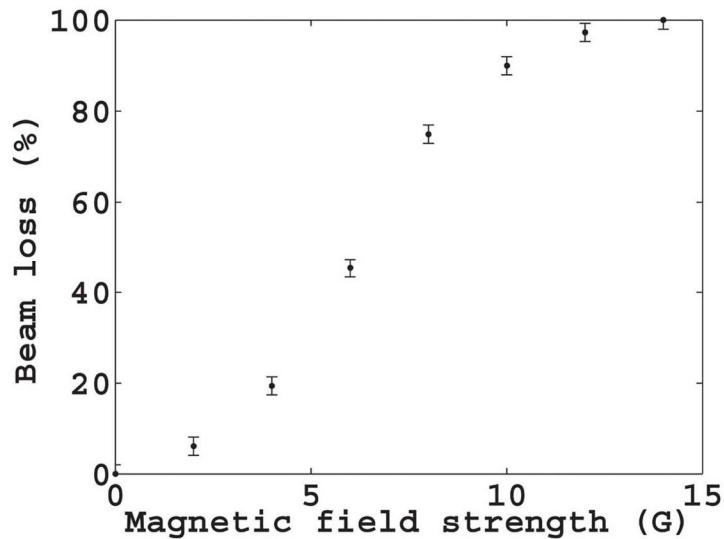
Figure 7.2: The beam loss over nominal operation caused by a homogeneous transverse magnetic field is given.

The results of the waveguide heating calculations are given in Figure 7.3 for 0, 6, 10 and 14 G field strengths while the electron fluence and mean energy calculated with PARMELA is given in Figure 7.4 and Figure 7.5 respectively for the same magnetic fields. The highest temperature increases were observed to be within the first or second accelerating cavity (AC). This is due to a combination of the electron fluence impacting the nose cones (Figure 7.4) as well as their mean energy (Figure 7.5). The error in the fluence and energy calculations performed with PARMELA was determined to be 0.1%. Thus data fluctuations are not expected to be caused by random or numerical noise. Significant beam losses are always seen in the first and second accelerating cavity, but at lower fields (up to 6 G) large losses are also calculated near the end of the waveguide. At fields up to 6 G, electrons near the central axis are deflected by a small amount causing them to be lost near the end of the waveguide. As the field strength increases up to 14 G, their deflection becomes greater and greater causing more and more beam loss at the beginning of the waveguide, and less and less near the end.
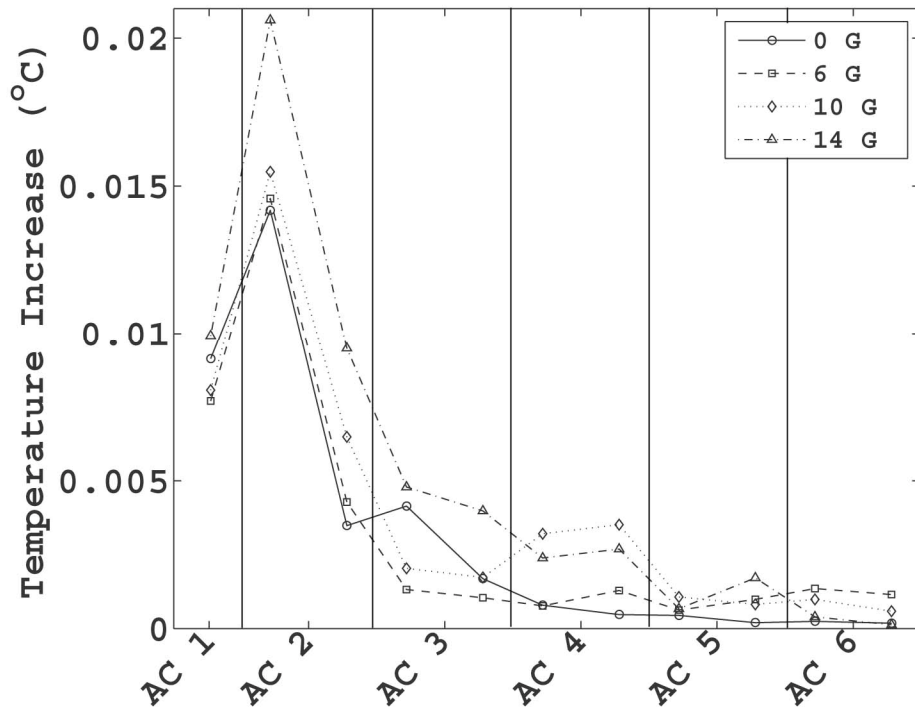
Figure 7.3: The temperature increase on the nose cones in each accelerating cavity (AC) is given at 0, 6, 10 and 14 G.
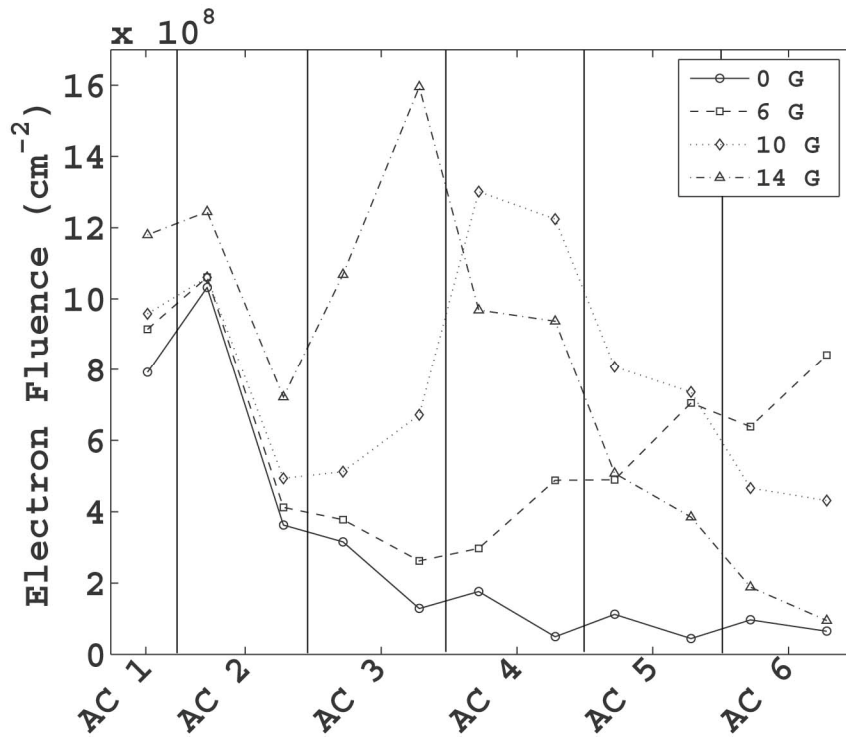
Figure 7.4: The electron fluence incident on the nose cones in each AC calculated by PARMELA is given for 0, 6, 10 and 14 G field strengths.
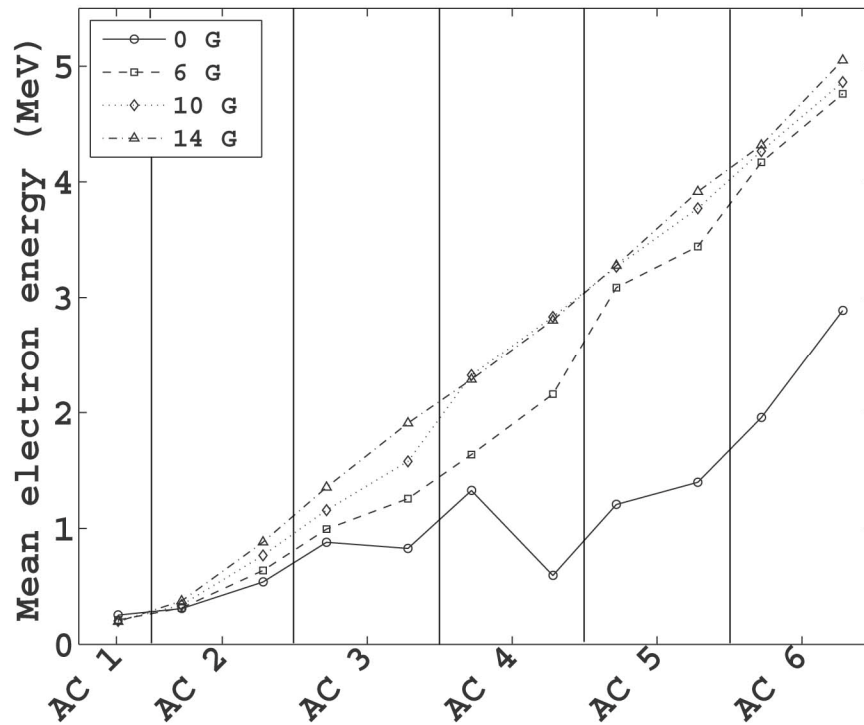
Figure 7.5: The mean energy of the electron beam impacting the nose cones in each AC as computed with PARMELA is given for 0, 6, 10 and 14 G field strengths.

Low energy electrons lose much of their energy in copper due to multiple elastic and inelastic collisions. The larger number of electron losses and greater collisional losses explain why the temperature increase is largest in the first and second accelerating cavity. The copper waveguide is maintained at a temperature of 40°C via water flowing through copper pipes attached to the exterior of the waveguide to dissipate RF heating and maintain a stable operating frequency. FEM simulations were conducted to investigate temporal heating effects in the waveguide; however the heat sink together with the high thermal conductivity of copper easily dissipates the instantaneous heating seen in Figure 7.3, resulting in no cumulative heating effects over time.

The resonant frequency changes for each cavity were calculated with COMSOL and Eq. 2.43 was used to determine their effects on the $\pi/2$ accelerating frequency. Table 7.1 summarizes the results for the cavity which experienced the greatest amount of heating leading to the maximum resonance frequency change together with the results of the perturbation analysis at each magnetic field strength investigated. For each beam loss scenario, the change in waveguide frequency is below a typical manufacturing tolerance of 10 kHz on the design frequency[8]. Thus changes in accelerating frequency less than 10 kHz is expected to have no serious effects. The maximum accelerating frequency change of 4.2 kHz was found to occur at 14 G corresponding to 100% electron beam loss.

Table 7.1: The electron beam loss over nominal, maximum cavity resonant frequency change ($\delta\omega_{on}$), and maximum change in the $\pi/2$ accelerating frequency ($\delta\omega_o$) is summarized for each transverse magnetic field strength investigated.

Field Strength (G)	2	4	6	8	10	12	14
Beam loss (%)	6.1	19.4	45.4	75.0	90.0	97.3	100.0
Max. $\delta\omega_{on}$ (kHz)	2.33	2.49	2.29	2.46	2.66	2.93	3.60
	(AC1)	(AC1)	(AC2)	(AC2)	(AC2)	(AC2)	(AC2)
$\delta\omega_o$ (kHz)	2.7	2.8	2.7	2.9	3.2	3.5	4.2

Beam losses elsewhere in the linac are not expected to have a great effect on the accelerating frequency of RF field magnitude. The beam loss within the electron gun could cause additional wear on the cathode, but has no effect on the RF operating frequency. In addition, the RF accelerating frequency (2998.5 MHz) is below the cutoff frequency of the beam tube (46 GHz) and so does not propagate inside. Thus beam loss within the beam tube is expected to have little effect on the resonance frequency of the cavity. Even with the results given in Table 7.1 representing a worst case scenario, the additional beam loss caused by transverse magnetic fields has been shown to have no serious effect on the linac accelerating frequency. Thus the detuning of the waveguide is negligible for any magnetic field strength that is not eliminated due to magnetic shielding. From this investigation, it can also be said that no resonance frequency effect is expected from a longitudinal magnetic field since it causes less beam loss overall. The beam losses that do occur are predominately in the electron gun thus having no effect on the waveguide resonant frequency.

7.4   CONCLUSIONS

Detuning of an in-line 6 MV linac waveguide in a transverse magnetic field caused by a larger number of electrons impacting the waveguide nose cones has been investigated. Beam losses were calculated in homogeneous magnetic fields of increasing strength up to 14 G where no electrons were incident on the target and all were lost in the waveguide. The resulting resonant frequency change in each cavity due to heating of the nose cones was determined to be below a manufacturing tolerance of 10 kHz and thus is expected to have no impact on accelerator efficiency. Thus any persistent magnetic field that is not eliminated due to passive or active shielding is not expected to affect the frequency of the waveguide operating mode. As an extension, no resonant frequency effects are expected with the linac subjected to a longitudinal magnetic field since there is less beam loss in the waveguide compared to the investigation given here.

7.5   REFERENCES

[1] J. St. Aubin, S. Steciw, and B. G. Fallone, "Effect of transverse magnetic fields on a simulated in-line 6 MV linac," Phys. Med. Biol., **55**, 4861-4869 (2010).

[2] J. St. Aubin, S. Steciw, and B. G. Fallone, "The design of a simulated in-line side-coupled 6 MV linear accelerator waveguide," Med. Phys., **37**, 466-476 (2010).

[3] J. C. Slater, *Microwave electronics* (D. Van Nostrand Company Inc., New York, 1950).

[4] J. M. Haughian, and R. M. Main, "An inexpensive method of cooling an RF cavity," IEEE Trans. Nucl. Sci., **NS16**, 395-396 (1969).

[5] J. St. Aubin, S. Steciw, and B. G. Fallone, "An integrated 6 MV linear accelerator model from electron gun to dose in a water tank," Med. Phys., **37**, 2279-2288 (2010).

[6] J. St. Aubin, S. Steciw, and B. G. Fallone, "Effect of transverse magnetic fields on a simulated in-line 6 MV linac," Phys. Med. Biol., (*under review*).

[7] D. E. Nagle, E. A. Knapp, and B. C. Knapp, "Coupled resonator model for standing wave accelerator tanks," Rev. Sci. Instrum., **38**, 1583-1587 (1967).

[8] L.A.N.L, "SNS coupled cavity accelerator RF cavity tuning requirements," *SNS-104040200-EQ0003-R02n*, (Los Alamos National Laboratory,Los Alamos) 2003.

CHAPTER 8: Brushed permanent magnet DC MLC motor operation in an external magnetic field

8.1 INTRODUCTION

Linac-MR systems have been proposed[1,2] as well as a cobalt-MR system[3] in order to achieve real-time image guided radiotherapy. Delivery of the radiotherapy treatment will be performed with the use of multileaf collimators (MLCs), not only allowing the execution of intensity modulated radiotherapy (IMRT), but also enabling real-time tumor tracking[4]. Various motors have been created for use in strong magnetic fields such as MR environments[5], but current Varian MLC technology uses brushed permanent magnet DC (BPMDC) motors. The close proximity of the MLCs to the MR imager can create artifacts in the MR imaging volume caused by RF noise from the BPMDC motors, as well as motor malfunction due to the large MR fringe fields. Our laboratory has shown that the negative effects of RF motor noise in MR images are mitigated through the use of appropriate RF shielding around the motors.[6] Magnetic interference would be entirely eliminated with use of MR compatible motors[5], but the purpose of this work is to investigate the effect of external magnetic field on the functionality of BPMDC motors such as those used in Varian MLC systems. The fringe magnetic fields from a linac-MR system will intersect the motors at various angles depending on the installation geometry as well as on collimator rotation. Therefore a characterization of Varian MLC BPMDC motor operation at various orientations in external magnetic fields is presented here.

8.2 METHODS AND MATERIALS

The motors were placed in the magnetic field of an EEV M4261 electromagnet (Chelmsford, England) capable of generating magnetic fields up to 2000 G and the field strengths were measured using a SENIS GmbH (Zurich, Switzerland) 3-axis magnetic field transducer. The BPMDC motors investigated were a MicroMO Electronics (Clearwater, FL) 20 V carriage motor, a MicroMO Electronics 24 V leaf motor used with Varian (Palo Alto, CA) 52 leaf MKII MLC systems, as well as Maxon Motor (Sachseln, Switzerland) 12 V half leaf and 12 V full leaf motors used with Varian 120 leaf Millennium MLC systems. The motors were assemblies consisting of a magnetic encoder for positional and speed information, the permanent magnet motor itself, and a gearbox. All the motors were tested in three orientations with the permanent magnet poles of the motors aligned 1) parallel to the electromagnet poles, 2) antiparallel to the electromagnet poles, and 3) perpendicular to the electromagnet poles. The one exception is for the carriage motor which was too large to place its permanent magnet poles perpendicular to the poles of the electromagnet, so no experiment was possible in this configuration. The three orientations mentioned above were investigated due to the MLC motor orientations with respect to the fringe magnetic fields of our bi-planar MR magnet. At a 0° collimator rotation (Figure 8.1), the magnetic fringe field will be aligned either parallel or antiparallel to the poles of the motors, while at a 90° collimator rotation (Figure 8.2), the magnetic fringe field will be perpendicular to the poles of the motors. Since our MR imager and linac rotate in unison[1], the change in motor orientation with respect to the fringe field is solely caused by collimator rotation. It is expected that even the alternate linac-MR or cobalt-MR designs proposed[2, 3] which incorporate a collimator rotation will have its MLC motors exposed to magnetic fringe fields in the directions being investigated. Due to axisymmetry of the magnets used in the other proposed designs, the fringe fields at the MLC are not expected to change upon azimuthal rotation of the treatment gantry with respect to the magnet.
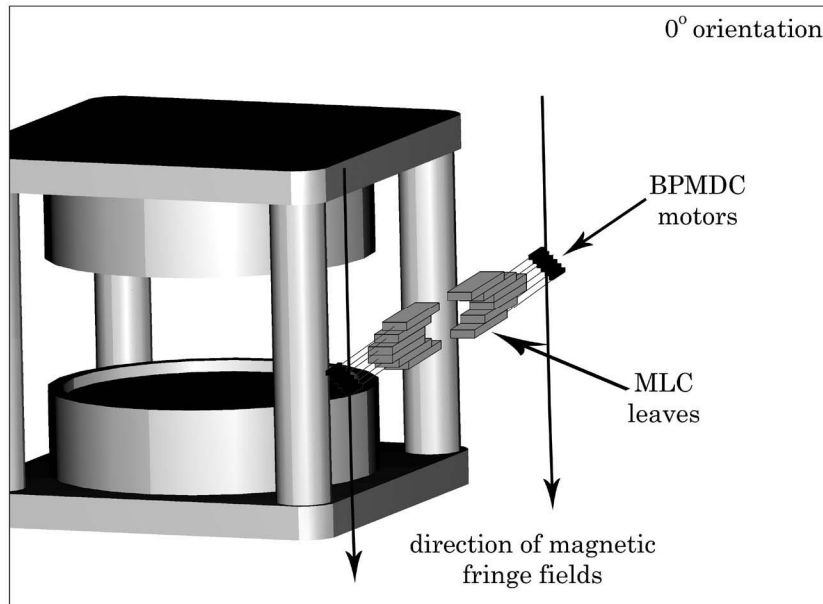
Figure 8.1: MLC and magnetic fringe field orientation for a 0° collimator rotation. The poles of the permanent magnet are aligned either parallel or antiparallel to the bi-planar magnet poles in this orientation.
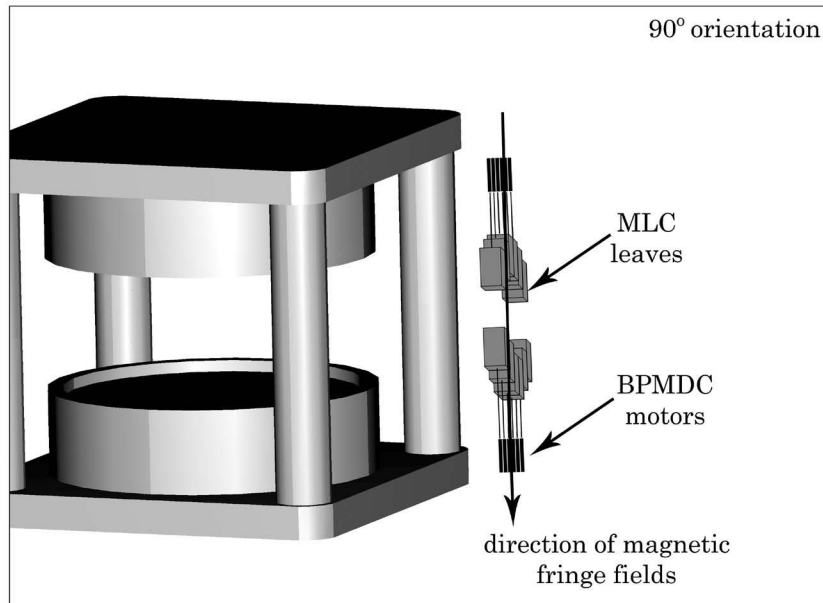
Figure 8.2: MLC and magnetic fringe field orientation for a 90° collimator rotation. The poles of the permanent magnet are aligned perpendicular to the bi-planar magnet poles in this orientation.

The motors were operated continuously for a minute both in the forward and reverse directions for each external magnetic field strength. The motors were

driven in magnetic fields of increasing strength until any one component of the motor (encoder, permanent magnet motor, or gearbox) failed at which point the entire motor was considered to have failed. An encoder failure was established when its output motor speed differed from an independent optical tachometer. Permanent magnet motor failure would indicate that more than the maximum manufacturer specified current was drawn. Excessive mechanical noise and wear was considered as gearbox failure. The motor characterization consisted of measuring motor speed in revolutions per minute (RPM) and current (mA) as the magnetic field strength increased. The changes in motor speed and current from those with no applied external field were measured as a function of external magnetic field strength. Two fixed loading scenarios were used when testing the motors: motors' self-load due to friction and gear box (i.e. no external load) and an equivalent external load to what the motors would experience in clinical use (i.e. clinical load). The clinical load was measured to cause an increase of 5 -10 mA in current drawn by the motors when driving a MLC leaf. All motors were driven using a variable voltage DC power supply. The motor speed was read from the motor's encoder using National Instruments (Austin, TX) MID-7654 4 axis servo motor driver integrated with their LabVIEW 8.5 software, and verified with a model 1726 Ametek digital optical tachometer (Largo, FL). Lastly, the current was read from a Uni-Trend Group Ltd. (Kwun Tong, Hong Kong) UT55 digital multimeter.

8.3   RESULTS AND DISCUSSION

In all orientations, with one exception, the magnetic encoder failed before the motor or gearbox when exposed to an external magnetic field. The field at which the encoder failed for each motor depended on the components, sensitivity and orientation of the encoder in the external magnetic field. In every case, failure of the encoder arose when the external field strength was large enough to saturate the Hall sensor of the encoder used for measuring the change in magnetic field as the armature rotated. The motor and gearbox assembly showed no increase in

temperature above the manufacturer's set limits (< 85 °C) as they were cool to the touch, nor did the current exceed the manufacturer's set limits in fields of up to 2000 G. The one exception where the permanent magnet motor itself failed before the encoder was the Maxon Motor 12 V full leaf MLC motor which was unable to maintain a consistent speed at 1500±10 G with its poles perpendicular to the electromagnet poles.

Considering that in normal operation the collimator can rotate the MLCs ±90° the minimum field strength at which the encoder fails between the parallel/antiparallel orientations and the perpendicular orientation sets the limit before motor failure. For example, in the case of the 24 V MicroMO electronics leaf motor, the encoder worked at a field of no greater than 450 G when its poles were perpendicular to the electromagnet poles. A ±90° rotation would place its poles in either a parallel or antiparallel orientation where the motor could sustain up to 800 G without encoder failure. However, the limit on this motor is 450 G set by the perpendicular pole orientation since the motor must operate clinically in either orientation. Table 8.1 illustrates the changes in current and motor speed for the maximum field strength after which the encoder failed.

Table 8.1: The maximum magnetic field strength the motors could sustain before failure is given together with the change in current and motor speed (in RPM) for each orientation tested.

	0 G		Field strength (±10 G)	Parallel pole alignment		Antiparallel pole alignment		Perpendicular pole alignment	
	RPM	Current (mA)		Δ RPM	Δ Current (mA)	Δ RPM	Δ Current (mA)	Δ RPM	Δ Current (mA)
24 V leaf motor	982	4.7	450	29±2	1.4±0.4	-14±2	0.7±0.4	32±2	1.6±0.4
20 V carriage motor	148	0.8 x10^2	2000	79±2	1.0±0.1 x10^2	4±2	0.3±0.1 x10^2	N/A	N/A
12 V half leaf motor	672	4.8	700	56±2	0.6±0.4	-15±2	0±1	63±2	11.2±0.4
12 V full leaf motor	614	18.0	600	45±2	4±1	-2±2	0±2	39±2	35±1

The results of the motor characterization in terms of changes in current and motor speed are presented in Figure 8.3 and Figure 8.4 for the MicroMo

electronics 24 V leaf and 20 V carriage motors respectively, while the results for the Maxon Motor 12 V half leaf and full leaf motors are given in Figure 8.5 and Figure 8.6 respectively. The results were identical within measurement error when the motors were run in forward or reverse directions, and the motors showed no sign of difficulty reversing direction in any magnetic field strength or orientation studied. The changes in motor speed and current were found to be identical in the clinical load or no-load experiments due to the relatively small loading of the MLC leaves. The trends seen in Figure 8.3 – Figure 8.6 are the result of a complicated interaction between the changes in backward electromotive force generated by the armature rotation and increases in mechanical and magnetic losses with increases in motor speed.
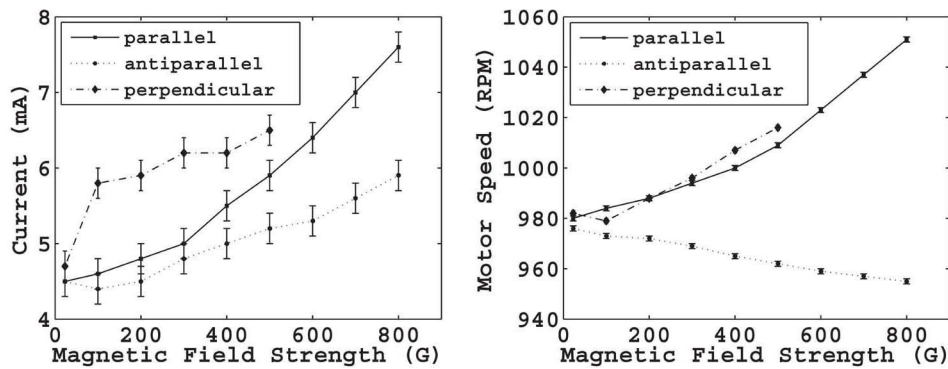
Figure 8.3: The changes in current and motor speed are given for the MicroMo electronics 24 V MLC leaf motor.
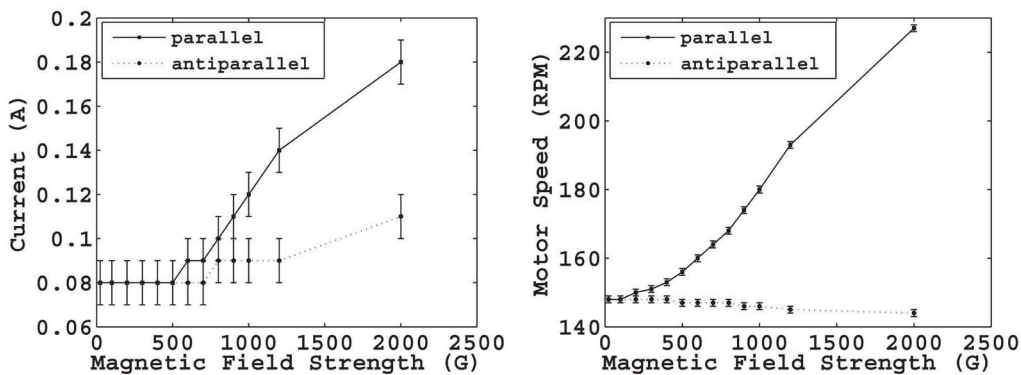
Figure 8.4: The changes in current and motor speed are given for the MicroMo electronics 20 V MLC carriage motor. The motor was larger than the bore of the electromagnet in the perpendicular orientation, so no data was obtained.
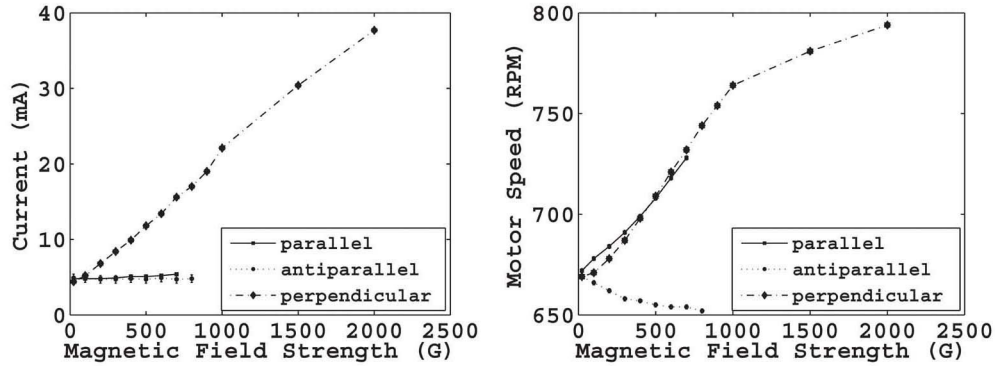
Figure 8.5: The changes in current and motor speed are given for the Maxon Motor 12 V half leaf MLC motor.
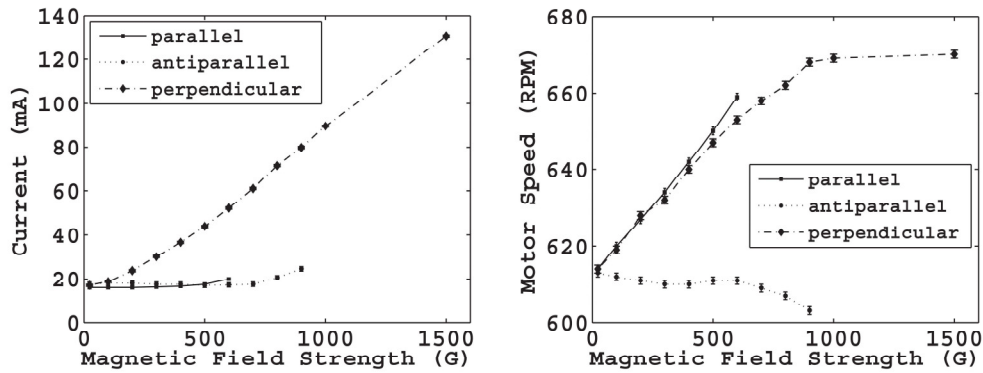
Figure 8.6: The changes in current and motor speed are given for the Maxon Motor 12 V full leaf MLC motor.

Any changes in motor speed would translate into an increasing or decreasing leaf speed. For example, from Table 8.1, the maximum increase of 63±2 RPM was observed for the 12 V half leaf motor which would translate into a 0.121±0.004 cm/s increase in leaf speed. In the antiparallel direction, a reduction of 15±2 RPM was observed translating into a 0.029±0.004 cm/s reduction in leaf speed. The Millennium MLC system, together with Varian Eclipse treatment planning software typically uses a maximum projected leaf speed of 2.5 cm/s at isocenter which translates into speed of around 1.3 cm/s at the carriage. It has also been shown that the motors are in fact able to drive the leaves with a projected speed of around 3.5 cm/s at isocenter[7] which translated into a leaf speed of around 1.8 cm/s at the carriage. Current MLC motor driver boards monitor each motor

position individually through the encoder, and modifies each leaf position individually over time maintaining a 1.3 cm/s motor speed as well as accounting for motor to motor variability due to manufacturing differences and wear. Thus changes in leaf speed quoted above caused by an external magnetic field would likely still be compensated by the MLC motor driver board.

The fact that the carriage motors and MLC leaf motors work together, the allowable magnetic field in which the MLC system as a whole can operate is limited by the motor with the lowest tolerance. This means that for the Millennium MLC system, the full leaf motor's field strength limit of 600 G restricts the entire system's operating limit. Therefore when a linac-MR system is designed, if the fringe magnetic fields at the location of the Millennium MLC system is greater than 600 G, appropriate magnetic shielding would be required. The strength of the magnetic fringe field at the location of the MLCs for linac-MR systems depends on the strength of magnetic field generated, their geometry as well as the effectiveness of their magnetic shielding, but it is expected that the MLC BPMDC motors can still be shielded to less than 600 G. By incorporating the previously determined requirement for RF shielding[6], and using appropriately designed magnetic shielding to ensure the BPMDC motors are not subjected to a magnetic field larger than the determined tolerances, current off-the-shelf Varian MLC systems can be used in a linac-MR system.

8.4   CONCLUSIONS

Four different brushed permanent magnet DC (BPMDC) motors used in Varian MLC systems were tested in magnetic fields of increasing strength at various orientations to determine an operational limit for each motor. No increase in temperature or current over the manufacturer's tolerances was observed for field strengths up to 2000 G. The magnetic encoder was observed to fail before the permanent magnet motor or gearbox which set the magnetic field tolerance of the whole motor assembly. Thus currently manufactured Varian MLC systems using the BPMDC motors tested could be used with linac-MR systems to provide

real-time tumor tracking, provided the necessary steps are taken to ensure the motor RF noise is shielded and the motors are below their field strength tolerances.

8.5   REFERENCES

[1] B. G. Fallone, B. Murray, S. Rathee, T. Stanescu, S. Steciw, S. Vidakovic, E. Blosser, and D. Tymofichuk, "First MR images obtained during megavoltage photon irradiation from a prototype integrated linac-MR system," Med. Phys., **36**, 2084-2088 (2009).

[2] B. W. Raaymakers, J. J. W. Lagendijk, J. Overweg, J. G. M. Kok, A. J. E. Raaijmakers, E. M. Kerkhof, R. W. van der Put, I. Meijsing, S. P. M. Crijns, F. Benedosso, M. van Vulpen, C. H. W. de Graaff, J. Allen, and K. J. Brown, "Integrating a 1.5 T MRI scanner with a 6 MV accelerator: proof of concept," Phys. Med. Biol., **54**, N229-N237 (2009).

[3] J. F. Dempsey, D. Benoit, J. R. Fitzsimmons, A. Haghighat, J. G. Li, D. A. Low, S. Mutic, J. R. Palta, H. E. Romeijn, and G. E. Sjoden, "A Device for Realtime 3D Image-Guided IMRT," Int. J. Radiat. Biol., **63**, S202-S202 (2005).

[4] B. Cho, P. R. Poulsen, A. Sloutsky, A. Sawant, and P. J. Keall, "First demonstration of combined kV/MV image-guided real-time dynamic multileaf-collimator target tracking," Int. J. Radiat. Biol., **74**, 859-867 (2009).

[5] G. Roger, Y. Akio, C. Dominique, D. Ludovic, B. Hannes, and B. Etienne, "Actuation methods for applications in MR environments," Concepts Magn Reson B Magn Reson Eng, **29B**, 191-209 (2006).

[6] M. Lamey, J. Yun, B. Burke, S. Rathee, and B. G. Fallone, "Radio frequency noise from an MLC: a feasibility study of the use of an MLC for linac-MR systems," Phys. Med. Biol., **55**, 981-994 (2010).

[7] K. Wijesooriya, C. Bartee, J. V. Siebers, S. S. Vedam, and P. J. Keall, "Determination of maximum leaf velocity and acceleration of a dynamic multileaf collimator: Implications for 4D radiotherapy," Med. Phys., **32**, 932-941 (2005).

CHAPTER 9: : Magnetic decoupling of the linac in a low field bi-planar linac-MR system

9.1   INTRODUCTION

The introduction of external magnetic fields on the linac have been shown in chapters 5 and 6 to cause large beam losses within the electron gun and waveguide.[1, 2] The linac-MR system in a transverse configuration showed the largest beam losses where at 14 G homogeneous field no electrons were incident on the target.[1] In contrast for the parallel configuration, 100% beam loss was never achieved even a fields of 0.2 T.[2] These investigations show that linac tolerance to transverse magnetic fields is substantially lower than for longitudinal magnetic fields. Thus it can be seen that magnetic shielding is an obvious requirement for the transverse case, but depending on the magnetic fringe field strength and tolerated beam loss, magnetic shielding may not be necessary for the parallel configuration.

The transverse configuration linac-MR system proposed by our group consists of a low field 0.2 T bi-planar magnet coupled to a 6 MV linac. This configuration currently has the linac to the side of the bi-planar magnets with the X-ray beam penetrating the open MR bore. As shown in chapter 5, transverse magnetic fields cause large electron deflections within the electron gun and linac waveguide leading to large beam losses. In order to minimize this deflection and beam loss, and in order to regain a usable radiation beam, passive or active shielding needs to be designed.

Passive shielding as a method to reduce the electron deflections within the electron gun and waveguide was initially presented by our group according to the constraint that the linac could only operate in a maximum 0.5 G field[3]. However, since that time investigations performed on linac operation within a transverse

magnetic field have shown the 0.5 G constraint to be overly restrictive[1]. The newly understood linac tolerances to an external transverse magnetic field allows for passive shielding designs to be re-optimized. The process of re-optimization allowed for a significant reduction in the shielding weight, a shorter target-to-isocenter distance, and reduced inhomogeneity of the main magnetic field. The larger linac tolerances to an external transverse magnetic field also admit simple active shielding designs as a method to reduce the magnitude of the magnet fringe fields where designs based on a strict 0.5 G net field limit would be extremely complicated or impossible. A study of the effectiveness of a simple passive shielding design to reduce the fringe magnetic fields at the linac culminating in an optimized design is presented. In addition to the presentation of an optimized passive shielding design, a study to determine the feasibility and effectiveness of the use of a simple active shielding design is performed. The results of these two studies show the ease in which the linac can be magnetically decoupled from the MR imager in a low field bi-planar linac-MR system.

9.2 METHODS AND MATERIALS

9.2.1 Linac operational tolerance

If the magnetic fringe fields at the location of the electron gun and waveguide are large enough to cause sufficient deflections of the accelerating electrons to cause an unusable X-ray beam, magnetic shielding would be required to shield the electrons from the external magnetic fields. In order to optimize magnetic shielding, a constraint dictating the maximum acceptable electron beam loss within the linac was chosen. The optimization of the passive magnetic shielding minimized of the amount of shielding required while meeting the chosen beam loss constraint. Less magnetic shielding translates into less perturbation of the main magnetic field of the MR imager. An operational constraint of the maximum beam loss acceptable was set to an additional 20% beam loss over nominal in this investigation. Asymmetry in the electron focal spot for an approximately 20% beam loss was presented previously in chapter 5.

After proper linac commissioning (see chapter 4), the lateral shift in the dose profile was calculated to be 1 mm. This is easily compensated by using appropriate jaw or MLC shifts. In addition to the ability to easily recover symmetric, non-shifted dose distributions, much of the 20% beam loss can be compensated by the yield and dose rate servos of the 600C; although this means running the linac outside of the manufacturer specifications. The calculation of beam loss was performed using the particle-in-cell program PARMELA.

It should be noted that the 2.10 m width of the bi-planar MR imager makes the minimum possible target-isocenter distance approximately 1.72 m. Thus including the dose rate reduction caused by the larger target-isocenter distance, the nominal 250 MU/min dose rate of a Varian 600C linac would be reduced to around 68 MU/min if no linac compensation was used. With linac compensation, the dose rate is expected to be around 85 MU/min. The focus of this investigation however is the reduction of magnetic field effects on linac operation, and these low dose rates are mostly a result of the target-isocenter distances dictated by geometry. Despite not being investigated here, the dose rate could be increased further by restricting the field size and making the flattening filter thinner, or by removing the flattening filter altogether and performing Intensity Modulated Radiation Therapy (IMRT). An increase in dose rate could also be achieved by interchanging the Varian 600C linac with a Varian 600C/D or 6EX whose nominal dose rates are up to 600 MU/min. However, since these other linacs have the same length and energy as the 600C, the same shielding requirements and designs presented here are expected to apply. No magnetic shielding was investigated in this work for the parallel configuration using the PARAmed MRopen™ MR imager since the largest beam loss expected at a 1 m target-isocenter distance was calculated to be within tolerance at 16±1%.

9.2.2   Finite Element Analysis and passive shielding

The finite element method (FEM) program COMSOL Multiphysics was used to simulate the magnetic fields of a low field (0.2 T) bi-planar magnet[4] used

in the transverse configuration linac-MR, and to optimize passive shielding designs. All FEM simulations were performed using Delaunay triangulation, quadratic basis functions and sufficient mesh elements in high gradient areas to ensure the maximum possible accuracy of the solution in the regions of interest. The low field 0.2 T MR imager modeled in Figure 9.1 was a permanent magnetic system, 1.98 m in height with a 2.10x2.10 m^2 base. This permanent magnet MR imager had a 0.7 m bore through with the X-rays would pass and where the patient would be positioned during treatment.

Passive shielding was designed as a 40 cm long and 80 cm inner diameter steel cylinder surrounding the multileaf collimators (MLCs) together with a 60 cm long and 36 cm inner diameter steel cylinder surrounding the linac electron gun and waveguide (seen in Figure 9.1). The steel mounting flange modeled (Figure 9.1) is axisymmetric with a radius of 29 cm and an equivalent thickness of 6 cm. It separates the waveguide and primary collimator from the rest of the linac components including the MLCs. The magnetic shielding is divided into two sections separated by the steel mounting flange. The first section closest to the magnet (MLC shield) is required to shield the MLC motors, but also encompasses the jaws and monitor chamber. The second section further back from the magnet (waveguide shield) is designed to shield the electron gun and waveguide, but also surrounds the primary collimator. The holes in the waveguide shield (Figure 9.1) are required to connect the wires from the electron gun to the modulator cabinet and feed the accelerating RF into the linac waveguide through a rectangular transmission waveguide. The hole in the MLC shield provides an opening for the X-ray beam to pass unattenuated. The addition of these holes is contrary to the optimal shielding design of a completely closed container drawing in the largest number of field lines and thus creating the maximum possible shielding effect. An investigation of the effectiveness of the cylindrical shielding design incorporating the required holes was performed by varying the cylinder thickness as well as its distance away from the magnet edge. The close proximity of the steel magnetic shielding and the MR imager causes increased inhomogeneity of the main

magnetic field over the imaging volume. By mirroring the shielding structure on the opposite side of the MR imager (as seen in Figure 9.1), the inhomogeneity can be reduced by creating a more symmetric distortion of the magnetic field. Large inhomogeneities would manifest as image distortions, reducing the accuracy in which the tumor or critical structure could be localized.
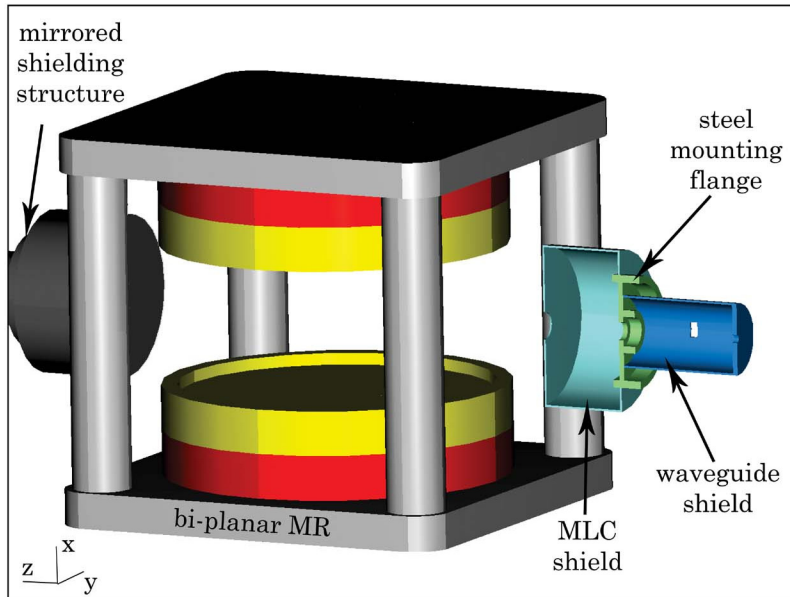
Figure 9.1: The design and configuration of the bi-planar magnet and a cutaway section of the proposed passive shielding. The presence of the shielding on the opposite side the bi-planar MR reduces the inhomogeneity of the main magnetic field.

The optimal passive shielding design was required to meet three major constraints. First, the waveguide shield was required to reduce the magnetic field throughout such that a maximum beam loss of 20% was not exceeded during linac operation. Second, the MLC shield was required to reduce the field at the MLC motors to below 600 G[5]. The third constraint imposed a minimum thickness of shielding at the shortest target-isocenter distance that yielded a pre-shim inhomogeneity of the main magnetic field below 300 ppm over a 30 cm diameter spherical volume (DSV). The maximum pre-shim inhomogeneity of 300 ppm was chosen after discussions with the National Research Council of Canada

(Winnipeg, Canada). From experience they consider a 300 ppm distortion over the 30 cm DSV manageable with current shimming methods.[6]

9.2.3   Active Shielding

Active shielding in the form of current driven independently through three or four coil pairs (Figure 9.2) was investigated as a possible alternative to passive shielding. The advantage of active shielding is the possible elimination of any electron beam loss within the linac. A disadvantage of active shielding however is the added complexity and cost. The design of the active shielding was constrained to three or four coil pairs. All coils in the 'three coil pair' configuration had diameters of 20 cm while the coils in the 'four coil pair' configuration had diameters of 10 cm. The vertical separation between two adjacent coils was set to 5 cm (Figure 9.2) in order to eliminate any possible physical overlapping of coils. The smallest separation between coils in a coil pair was 17 cm, just larger than the diameter of the waveguide including the coupling cavities, and the adjacent coil pair had a separation of 27 cm.
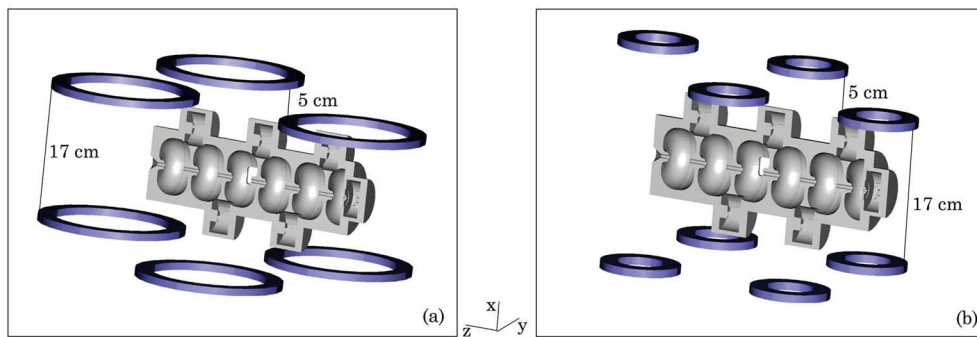
Figure 9.2: The active shielding designs surrounding a cutaway section of the linac electron gun and waveguide for (a) the three coil pair and (b) the four coil pair configurations.

The net active shielding magnetic field solution, normalized per unit current, was generated using superposition of the solution for a single current loop calculated from Eqs. 2.17b, 2.18 and 2.19. The cylindrically symmetric solutions given in these equations were transformed into Cartesian *xyz* coordinates using Eq. 2.20. Thus through a superposition of solutions from Eqs. 2.17b, 2.18 and

2.19 and the transformation of Eq. 2.20, the net active shielding field could be determined for the three or four coil pairs with varied lateral separations (z positions). The z location of each coil pair along the linac, together with the total current *nI* was optimized using the sequential quadratic programming routine in Matlab (Natick, MA) to create the best cancelation of the magnetic fringe fields. The total current *nI* represents the number of wire turns *n* and the driving current *I*.

9.3　　　RESULTS AND DISCUSSION

9.3.1　　　No shielding

　　　The magnetic fringe fields from the bi-planar MR imager are shown in Figure 9.3 and Figure 9.4. As shown in the inset of Figure 9.4, the electron gun experiences 33 G at the cathode and 92 G at the target. These fields create substantial electron deflections within the electron gun and waveguide resulting in all electrons impacting the electron gun and waveguide walls and none reaching the target. The FEM bi-planar magnet with its rose ring design provided a calculated pre-shim distortion of the main magnetic field of 81 ppm over a 30 cm DSV. The field strength at the location of the MLC motors (around 1.1 m from isocenter) was calculated to be 1273 G, well over their tolerance limit[5].
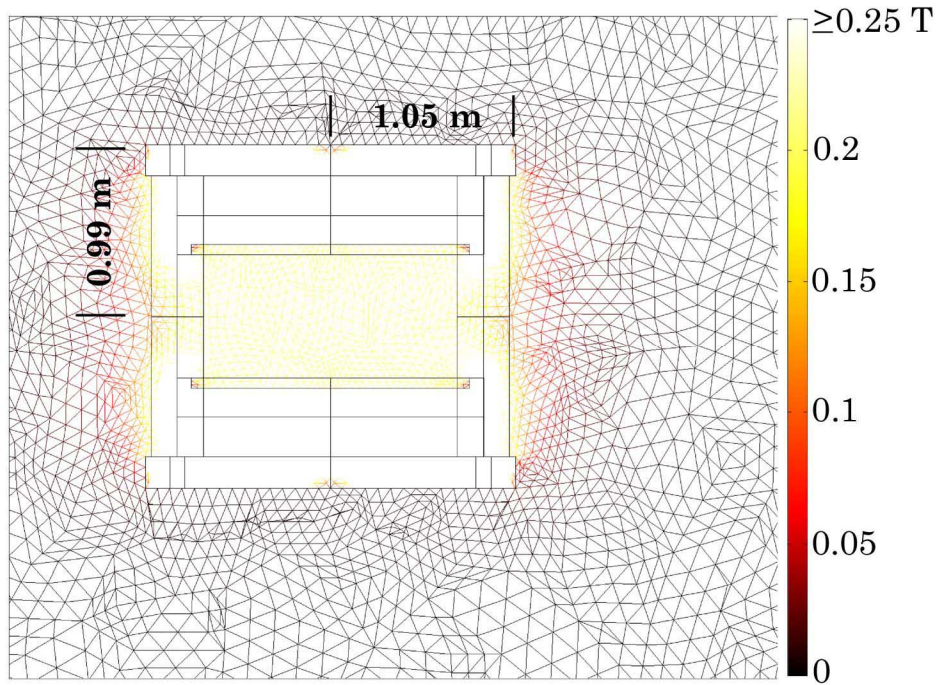
Figure 9.3: 2D magnetic field distribution for the bi-planar linac-MR system overlaid on the finite element mesh.
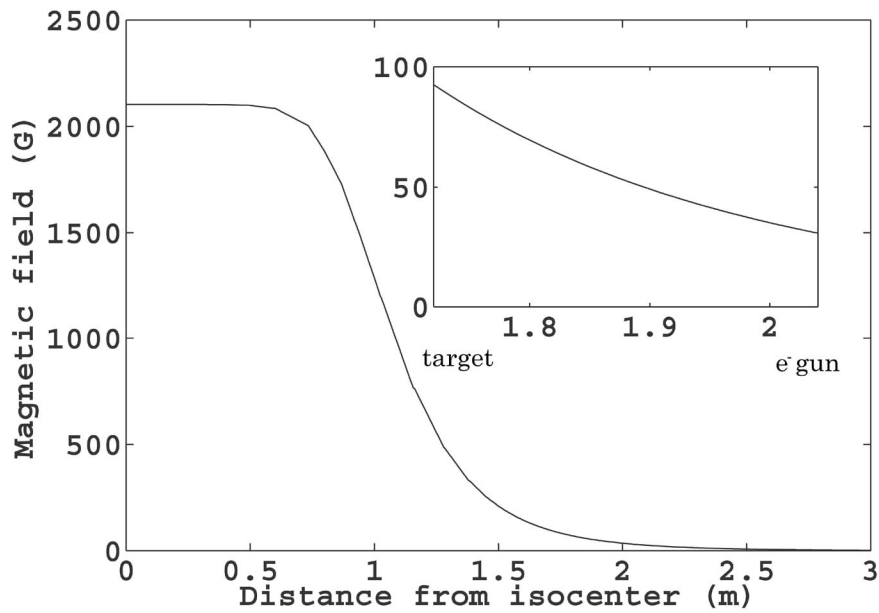
Figure 9.4: Bi-planar MR field extending from isocenter to 3 m. The inset shows the field over the length of the linac.

9.3.2   Passive shielding

The magnetic field strength in the waveguide calculated for different separations between the magnet edge and MLC shielding at various shielding thicknesses is given in Figure 9.5. The target-isocenter distance for a 0 m separation (Figure 9.5a) is 1.72 m. Figure 9.5 also clearly shows that the effectiveness of the passive shielding decreases as the field strength decreases. The field decrease observed by increasing the steel shielding thickness from 0.75 to 2 mm is larger than the decrease from 5 to 10 mm. Thus the difficulty of trying to restrict the magnetic field within the linac to less than 0.5 G becomes readily apparent. Very large slabs of steel and even the introduction of extremely high permeability material such as Mu-metal[TM] are required. Under the assumption that the entire linac required shielding to 0.5 G, our group initially presented a passive shielding design[3] resulting in a 2.1 m target-isocenter distance and a homogeneity of 321 ppm over a 30 cm DSV.
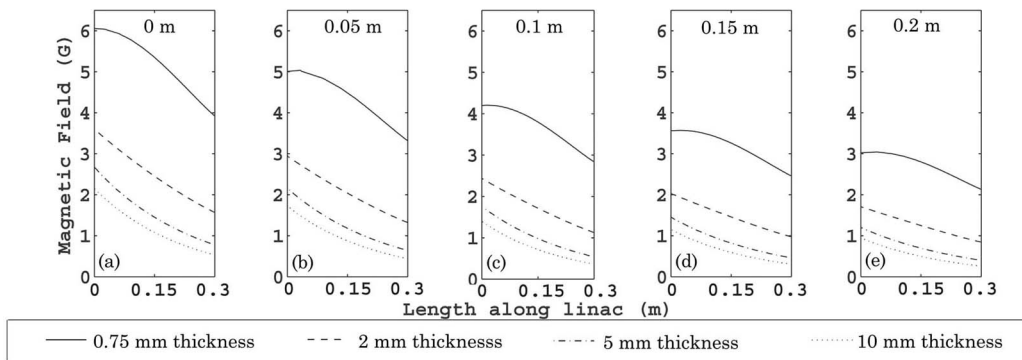
Figure 9.5: The magnetic field within the linac calculated for 0.75, 2, 5 and 10 mm thicknesses of the MLC and waveguide shield (Figure 9.1) at separations between the magnet edge and MLC shield of (a) 0, (b) 0.05, (c) 0.1, (d) 0.15, and (e) 0.2 m. The target is located at 0 m and the electron gun cathode at 0.3 m.

In contrast to the shielding design restricting the field to 0.5 G, a more optimal design can be determined with use of the known linac response to a transverse magnetic field[1]. According to the constraints listed in section 9.2.2, the optimal shielding configuration was determined to be a 0.9 mm thick waveguide shield together with a 0.75 mm thick MLC shield located 2.0 cm from the magnet

edge resulting in a target-isocenter distance of 1.74 m. Figure 9.6 gives the magnetic field distribution around the MR imager including the effects of the optimized shielding. Figure 9.7 shows the magnetic field at the linac within the optimized shielding. This shielding design resulted in a 447.2 G field at the MLC motors, an inhomogeneity of 298 ppm over a 30 cm DSV, and a 20±1% beam loss. This more optimal shielding design represents a three times reduction in shielding weight, and a 46% increase in dose rate cause by the closer target-to-isocenter distance compared to the initial design. A 0.75 mm thin MLC cylinder was the thinnest geometry that could be meshed while maintaining the accuracy of the solution resulted in the slight over shielding of the MLC.
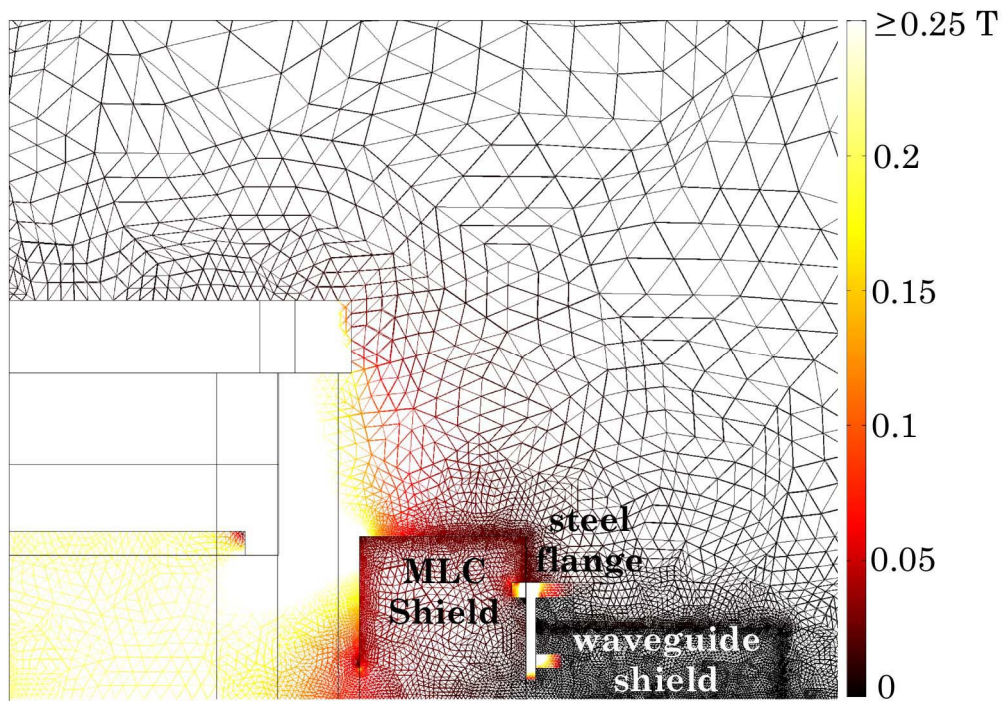
Figure 9.6: A 2D field map of the linac-MR system including the MLC optimized shielding overlaid on the finite element mesh.
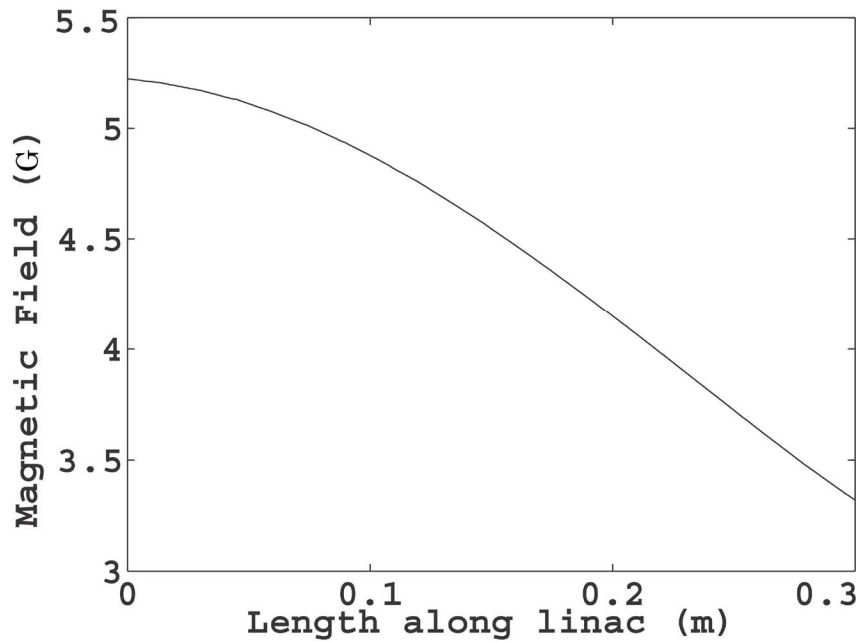
Figure 9.7: The magnetic field strength at the location of the linac resulting from the magnetic shielding. The target is located at 0 m and the electron gun cathode at 0.3 m.

The MLC shield was the main contributor to the inhomogeneity of the main magnetic field. Under the assumption that all magnetic parts of the MLC were changed to non-magnetic ones (e.g. the steel backplate changed to stainless steel), and by replacing the typical brushed permanent magnet DC MLC motors with motors designed for use in MR environments[7], there would be no need for MLC shielding. With no MLC shielding, the optimal waveguide shield thickness became 1.58 mm with no separation between the MLCs and the magnet edge yielding a 20±1% beam loss. This design represents a significantly reduced inhomogeneity which was calculated to be 85 ppm over a 30 cm DSV. It also provides an additional 10% reduction in weight, and with its target-isocenter distance of 1.72 m, it provides a further 2.3% increase in dose rate compared to the design with an MLC shield. Figure 9.8 gives the magnetic field distribution around the MR imager including the effects of the optimized shielding. Figure 9.9 shows the magnetic field at the linac within the optimized shielding.
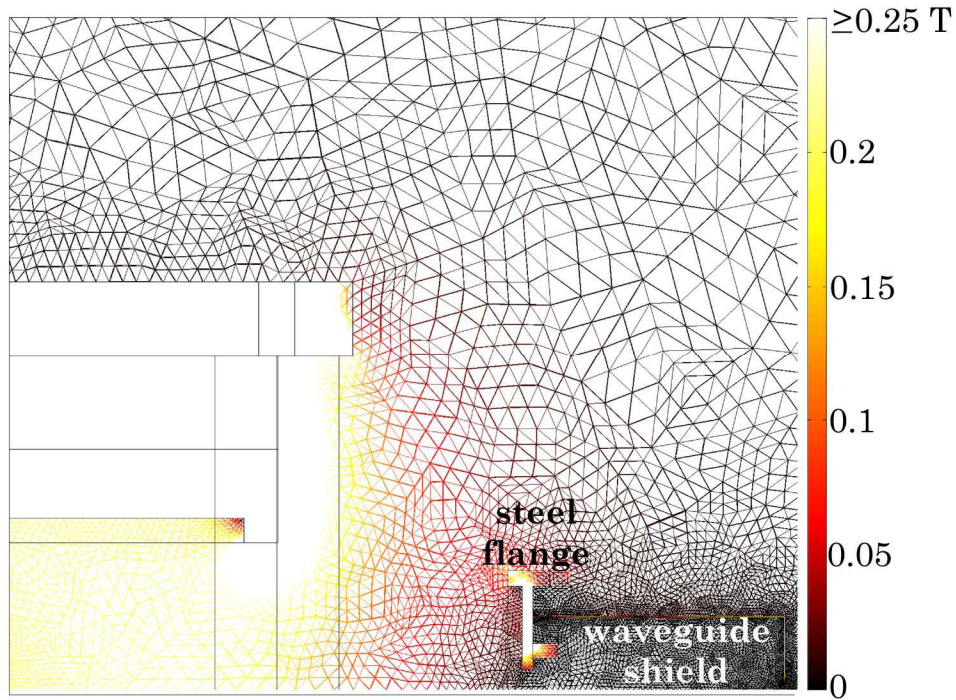
Figure 9.8: A 2D field map of the linac-MR system overlaid on the finite element mesh.
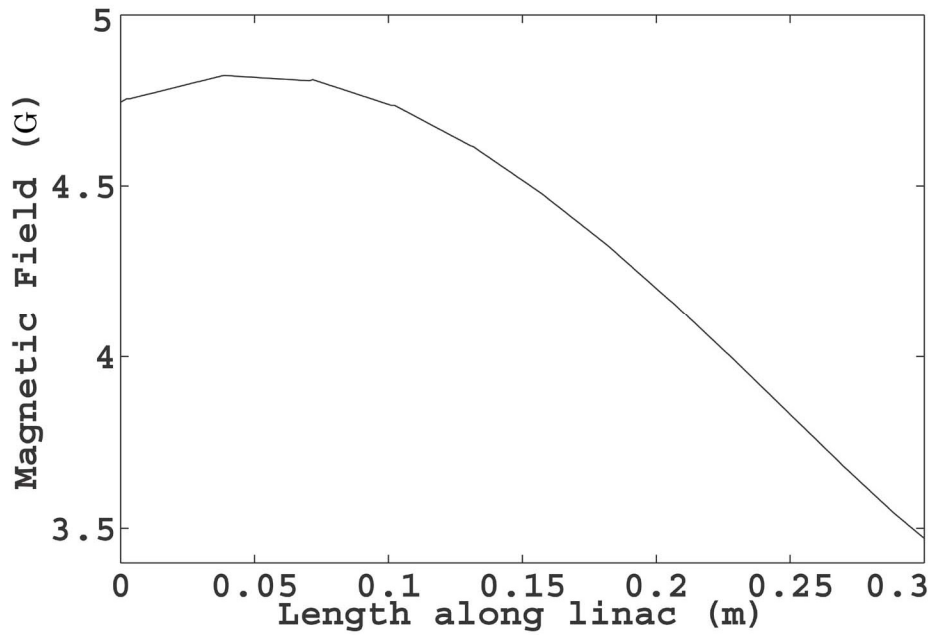
Figure 9.9: The magnetic field strength at the location of the linac resulting from the magnetic shielding. The target is located at 0 m and the electron gun cathode at 0.3 m.

Despite the presence of the steel shielding in very close proximity to the MR imager, eddy currents are not expected to be a large concern. Through initial calibration (gradient pre-emphasis) eddy currents generated in the steel structure of the MR imager (Figure 9.1) are already incorporated into the pulse sequences. However, the time varying magnetic fields of the gradients used to obtain spatial information in the MR image may extend to the steel shielding. Depending on the magnitude of eddy currents generated in the steel shielding, gradient pre-emphasis may be sufficient to minimize their effect. However, if gradient pre-emphasis is not enough, the steel shielding would need to be re-optimized to minimize eddy currents (by cutting the shielding up in sections separated by an insulator) while still ensuring the given magnetic shielding constraints are achieved.

9.3.3   Active shielding

Under the assumption that no MLC shielding was required, and the steel mounting flange was removed, active shielding was optimized to reduce the fringe fields within linac. The results from the optimization for the three and four coil pair active shielding are given in Figure 9.10 and Figure 9.11. The optimized locations and total currents for both active shield configurations are summarized in Table 9.1. Using the net field as an input into our linac simulation[8, 9], both the three and four coil pair configurations proved to provided sufficient cancellation of the fringe field such that no electron beam loss was observed. In addition, compared to our simulation in no magnetic field[9], the beam centroid at the target shifted by 0.01 and 0.001 cm for the three and four coil pair configurations respectively. These small beam centroid shifts have no impact on the dose distributions as presented previously[9] with Monte Carlo studies showing greater than 99% of all points meet a 1%/1 mm acceptance criterion at a 40x40 cm^2 field size. The four coil pair configuration provided the best cancellation of the fringe field as seen from the smaller beam centroid shift at the target and the smaller net magnetic field at the linac (Figure 9.11). Both three and four coil optimized configurations can be manufactured and require nothing but adequate ventilation

during use. After calculating the field variation caused by the active shielding fringe fields over the 30 cm DSV, the inhomogeneity is expected to be approximately 91 ppm for the 3 coil configuration and 87 ppm for the 4 coil configuration.
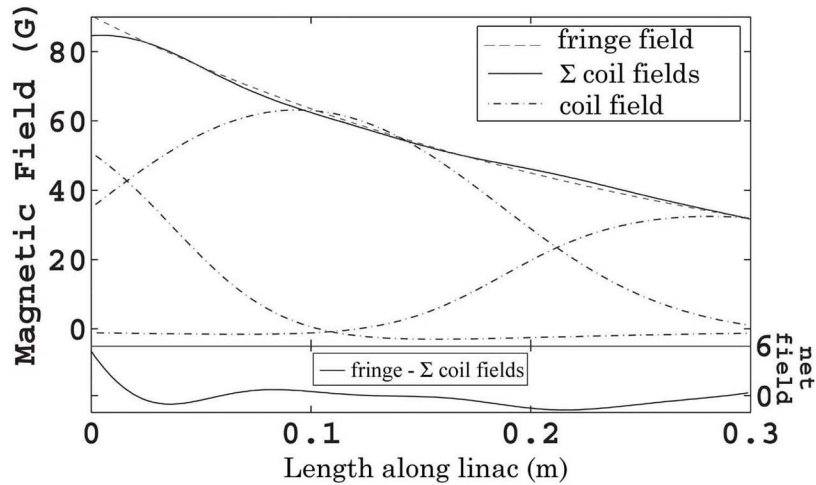
Figure 9.10: The fringe field of the bi-planar magnet, the individual coil magnetic fields and the sum of the coil fields are shown for the three coil pair configuration (Figure 9.2a). The net field within the linac is shown directly under the field plots. The target is located at 0 m and the electron gun cathode at 0.3 m.
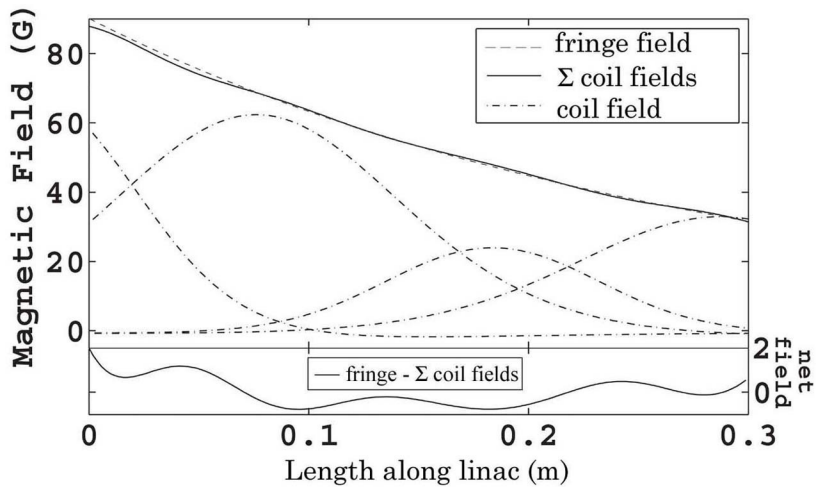
Figure 9.11: The fringe field of the bi-planar magnet, the individual coil magnetic fields and the sum of the coil fields are shown for the four coil pair configuration (Figure 9.2b). The net field within the linac is shown directly under the field plots. The target is located at 0 m and the electron gun cathode at 0.3 m.

Table 9.1: The optimized total current (*nI*) and location of each coil pair in both configurations shown in Figure 9.4 is given. The optimized locations are measured with respect to the target location at 0 m.

	3 coil pair configuration		
Total current (*nI*)	1111.3	2380.8	583.8	
Coil center location (m)	-0.0562	0.0938	0.2813	
	4 coil pair configuration			
Total current (*nI*)	2077.6	5909.2	728.7	3119.9
Coil center location (m)	-0.0260	0.0763	0.1851	0.2889

9.4   CONCLUSIONS

Simple and effective means of magnetically decoupling a 6 MV side-coupled linear accelerator for use in a bi-planar linac-MR system have been presented. Using current MLC systems which incorporate brushed permanent magnet DC motors, a 0.75 mm thick cylinder of steel was all that is required to allow the MLCs to operate in close proximity to a low field bi-planar linac-MR system. With this MLC shield in place, the steel mounting flange and a 0.9 mm thick cylinder around with waveguide and electron gun produced a 20±1% electron beam loss. With this MLC, flange, and waveguide shield combination, a pre-shim distortion of the main magnetic field of the MR imager was calculated to be 298 ppm over a 30 cm DSV. With the use of magnetically insensitive motors, no MLC shield would be required, and the thickness of the waveguide shield behind the steel flange grew to 1.58 mm maintaining a 20±1% electron beam loss. With only the steel flange and waveguide passive shield the distortion of the main magnetic field was calculated to be 85 ppm over a 30 cm DSV. As an alternative to passive shielding, with no MLC shield or steel flange, active shielding was optimized. The optimizations of coil current and location for the active shielding designs studied produced excellent results with no beam loss within the linac and a maximum distortion of the MR field of 91 ppm over a 30 cm DSV.

9.5 REFERENCES

[1] J. St. Aubin, S. Steciw, and B. G. Fallone, "Effect of transverse magnetic fields on a simulated in-line 6 MV linac," Phys. Med. Biol., **55**, 4861-4869 (2010).

[2] J. St. Aubin, D. M. Santos, S. Steciw, and B. G. Fallone, "Effect of longitudinal magnetic fields on a simulated 6 MV linac," Med. Phys., **37**, 4916-4923 (2010).

[3] S. Steciw, T. Stanescu, M. Carlone, and B. G. Fallone, "Magnetic shielding of a coupled MRI-Linac system," Med. Phys., **34**, 2623-2623 (2007).

[4] T. Stanescu, "Towards magnetic resonance imaging guided radiation therapy," Ph.D. Thesis in the *Department of Physics*, (University of Alberta, Edmonton, AB, 2007)

[5] J. Yun, J. St. Aubin, S. Rathee, and B. G. Fallone, "Brushed permanent magnet DC MLC motor operation in an external magnetic field," Med. Phys., **37**, 2131-2134 (2010).

[6] personal communication, A. Procca, and R. Tyson, (National Research Council of Canada, 2010)

[7] G. Roger, Y. Akio, C. Dominique, D. Ludovic, B. Hannes, and B. Etienne, "Actuation methods for applications in MR environments," Concepts Magn Reson B Magn Reson Eng, **29B**, 191-209 (2006).

[8] J. St. Aubin, S. Steciw, and B. G. Fallone, "The design of a simulated in-line side-coupled 6 MV linear accelerator waveguide," Med. Phys., **37**, 466-476 (2010).

[9] J. St. Aubin, S. Steciw, and B. G. Fallone, "An integrated 6 MV linear accelerator model from electron gun to dose in a water tank," Med. Phys., **37**, 2279-2288 (2010).

CHAPTER 10: Summary and conclusions

Real-time image guided radiation therapy has been proposed as a means to reduce the planning target volume (PTV). A reduction in the PTV is expected to minimize the severity of normal tissue complications and negative side effects inherent to external beam radiation therapy. The novel approach of coupling an in-line side-coupled 6 MV linear accelerator (linac) to a low field magnetic resonance (MR) imager has been proposed by our group with two separate designs. The first is a transverse configuration where the linac is to the side of the MR imager and is subjected to transverse magnetic fields. A small scale prototype linac-MR system in this configuration has been successfully built. The second design is a parallel configuration where the linac is placed on the symmetry axis of the MR imager and is subjected to longitudinal magnetic fields. The integration of the linac and MR imager poses many technical issues; one of which is the magnetic interference of the MR imager on the linac. The magnetic fringe fields of the MR imager intersect the linac and cause a change in the electron trajectories as they accelerate from the electron gun to the target at the end of the linac waveguide. The changes in electron trajectories and their effect on dosimetry in a water tank were investigated through the various simulations that were presented in this thesis.

The work began by modeling an in-line side-coupled 6 MV linac waveguide that emulated the commercial Varian 600C. The initial design was optimized to match various Varian 600C parameters and resonate at 2998.5±0.1 MHz. The optimized in-line 6 MV waveguide was generated as a 3D finite element method (FEM) radio-frequency (RF) field solution using COMSOL Multiphysics and was able to calculate the effects of side and port coupling. The 3D FEM solution was validated against a previously benchmarked program for a single accelerating cavity while the waveguide model was validated against a theoretical dispersion curve derived from lumped circuit theory. A reduction of the RF field magnitude in the first accelerating cavity was achieved by shifting the location of the first side-coupled cavity towards the electron gun. The side and

port coupling irises of the optimized waveguide were found to destroy axisymmetry causing asymmetric perturbations to the RF field. The asymmetric RF field created a shifted and skewed electron focal spot at the linac target resulting in a 1% asymmetry in the dose profiles.

Upon generation of a fully 3D waveguide simulation, an electron gun was designed using the 2D axisymmetric program EGN2w. The electron gun matched the measured electron gun current and cathode-anode potential of the gun used with a Varian 600C. The first side cavity shift was then set to match the Varian 600C capture efficiency and target current. The electron phase space at the linac target, calculated using the particle-in-cell (PIC) program PARMELA, was then used as an input into the Monte Carlo programs BEAMnrc and DOSXYZnrc to calculate the resulting dose distributions in a water tank. The simulated dose distributions, profiles and depth dose (DD) curves were found to agree with measurement to great accuracy with 98% of all points meeting a 1%/1 mm acceptance criterion for the profiles, and an agreement of 1% or better deeper than 1.5 cm for the DD curves. The validated linac simulation, from electron gun to target produced a non-Gaussian focal spot at the linac target and a non-Gaussian energy spectrum, contrary to current assumptions for Monte Carlo simulations.

Transverse magnetic fields were added to the validated linac simulation to investigate their effect on the electron beam, and the effect of the resulting electron phase space on the dosimetry in a water tank. EGN2w was replaced by the 3D FEM program OPERA-3d/SCALA to perform investigations of linac performance in non-axisymmetric transverse magnetic fields. The OPERA-3d/SCALA electron gun produced a 20% larger beam current than EGN2w, most likely due to the primitive finite-difference (FD) calculation used by EGN2w. A 7.8% reduction in the cathode radius of the OPERA-3d/SCALA model produced accurate results compared to measurements, and nearly identical to EGN2w. OPERA-3d/SCALA was used for all further investigations. The linac showed a low tolerance to transverse magnetic fields since the magnetic force caused a global deflection of the beam away from the beam axis. From 2 to 6 G an

increasingly asymmetric focal spot at the linac target was calculated with beam losses ranging from 5±1 to 45±1% respectively. Fields larger than 6 G caused the main intensity peak of the electron spatial distribution to be lost resulting in a fairly homogeneous focal spot. Thus at 6 G, the focal spot at the linac target had the greatest asymmetry and thus produced the most asymmetric dose profiles. Upon 're-commissioning' the linac by translating the focal spot laterally with respect to the flattening filter, symmetric dose profiles were regained, but they were shifted laterally. It was shown however that by using asymmetric jaw (or MLC) positions, the lateral profile shift could be almost fully corrected. At a 14 G transverse field, it was determined that no electrons were incident on the linac target, and all were lost within the electron gun and waveguide.

Longitudinal magnetic fields did not deflect the electron beam away from the beam axis, but did change the optics of the electron gun substantially. Using the isoline data of the MRopen™ imager from PARAmed as an example of an expected longitudinal magnetic fringe field, a 16±1% beam loss was calculated for a 110 G field measured at the electron gun cathode. Longitudinal magnetic fields on the linac caused the full width half maximum (FWHM) of the electron focal spot to increase from 0.012 cm at 0G to 0.254 cm at 110 G. The 110 G field value corresponded to an ideal 1.0 m target-isocenter distance. For longitudinal magnetic fields up to 110 G, the resulting dose distributions showed excellent agreement to a 0 G profile with greater than 96% of all points meeting a 1%/1 mm acceptance criterion, and all DD curved agreeing within 1%. An increasingly non-laminar electron beam upon injection into the waveguide resulted from increasing longitudinal magnetic field strengths. Magnetic fields larger than 110 G caused the optics of the electron gun to change drastically enough that large beam losses within the electron gun were calculated. At 600 G, the maximum electron beam loss was calculated. Fields greater than 600 G caused a collimation of the electron beam within the anode beam tube resulting in a slight reduction in beam loss. Beam loss caused by a longitudinal magnetic field was determined to be solely the result of the changing electron gun optics.

An investigation into how the additional electron beam loss within the linac waveguide caused by transverse magnetic fields affected the waveguide resonant frequency was also investigated. DOSRZnrc was used to calculate the energy deposition in copper from the beam losses calculated in PARMELA. The resulting rise in temperature and spatial distortion of copper was calculated under the assumption that the electrons impacted the waveguide nose cones. COMSOL was then used to calculate any change in cavity resonant frequency and first order perturbation theory from lumped circuit theory was used to determine the effect on the waveguide as a whole. Even at the worst case scenario of 100% beam loss (resulting from a 14 G transverse field), the maximum resonant frequency change was calculated to be 4.2 kHz, below the 10 kHz tolerance.

The feasibility of using current off the shelf Varian MLC systems with a linac-MR system was investigated. Varian MKII and millennium MLC systems use brushed permanent magnet DC (BPMDC) motors incorporating magnetic encoders in their MLC assemblies. By subjecting the motors to increasingly larger magnetic fields at various orientations, their tolerance and functionality was investigated. Each motor was determined to have a different magnetic field tolerance and functionality depending on orientation in the magnetic field. The 120 leaf millennium MLC system was found to tolerate a maximum of 600 G. Since the fringe field of the low field MR imagers at the location of the MLCs is expected to be higher than 600 G, magnetic shielding is required for these motors.

Magnetic shielding of the electron gun, linac waveguide and MLCs was designed to magnetically decouple the sensitive linac components from the MR imager. A 20% beam loss tolerance was set for the Varian 600C since it is theoretically able to compensate a 15% loss through the dose rate servo and may compensate a bit more through the yield servo. At a 20% beam loss tolerance, no magnetic shielding is required for a linac-MR system subjected to longitudinal fringe fields similar in magnitude to the PARAmed MRopen™ imager. However, some form of magnetic shielding is required for the transverse configuration using a low field 0.2 T permanent magnet MR imager. If a Varian millennium MLC

assembly is used, MLC and waveguide shielding are both required in addition to the existing 600C steel mounting flange. In this case, a 0.75 mm thick cylinder surrounding the MLCs and jaws together with a 0.9 mm thick cylinder surrounding the waveguide and electron gun separated by a steel mounting flange provided sufficient shielding of the MLCs, maintained a 20±1% beam loss, and a shimmable homogeneity of the MR imager. If magnetically insensitive motors were used in the place of the BPMDC motors in the MLC assembly, no MLC shielding is necessary and the waveguide shielding grew to 1.58 mm behind the steel flange. Active shielding was also designed by optimizing the current and location of three or four current carrying coil pairs. By using the optimized active shielding with no MLC shield or steel flange, beam loss within the electron gun and waveguide caused by the transverse magnetic field was completely eliminated. Thus a thorough investigation of linac performance in an external magnetic field was performed culminating in a magnetic shielding design that magnetically decouples the linac from the MR imager in a low field linac-MR system.

Future work would include performing detailed measurements of linac performance in external magnetic fields. In the work presented here, a dedicated medical linac submersed in a nearly 0 G magnetic field environment was unavailable. However, in the future, when the next generation linac-MR system is built, there may be a possibility to take these measurements. The general methodology for these measurements may be as follows. First, a system to generate known magnetic fields that do not fluctuate over time would be calibrated. An example may be a Helmholtz coil. With the magnetic field generator calibrated, various orientations would be used to yield both transverse and longitudinal magnetic fields on the linac. The target current would then be measured as a validation of one of the simulation results. Further, dosimetric measurements could be made to quantify the changes in depth dose (DD) curves as well as the dose profiles resulting from the addition of a magnetic field. These measurements could be used to directly validate the results presented in chapters 5

and 6. Lastly, the optimized active and passive magnetic shielding designs could be manufactured and placed at the locations given in chapter 9 to test the efficiency of the shielding.